DYNAMIC MODELING OF ORGANIC RANKINE CYCLE POWER SYSTEMS

ADRIANO DESIDERI
2016

Dynamic modeling of organic Rankine cycle power systems

PhD Thesis
submitted the 15th of October 2016
and defended the 6th of December 2016
Universitè de Liège

for the degree of Doctor of Philosophy

by
Adriano Desideri

under suggestion of:
Associate Professor Vincent Lemort (Ulg), main supervisor
Lecturer Sylvain Quoilin (Ulg), co-supervisor

and under recommendation of:
Associate Professor Sotiris Karellas, National Technical University of Athens, examiner
Associate Professor Assaad Zoughaib, Mines Paristech, examiner
Associate Professor Martijn van den Broek, Ghent University, examiner
Associate Professor Pierre Dewallef, University of Liège, examiner
Associate Professor Grégoire Léonard, University of Liège, examiner

PhD Thesis
On the cover: Le Creuset brisé - Constantin Meunier
Font: Utopia typeset with LaTeX 2_ε

Ulg Aerospace and Mechanical Engineering
Thermodynamics laboratory
Universitè de Liège

Campus du Sart-Tilman
BAT. B49 Thermodynamique appliquée
chemin des Chevreuils, 7
B-4000 Liège 1
Belgium
Phone: (+45) 4525 4131
Fax: (+45) 4525 4325
www.labothap.ulg.ac.be/cmsms/

To Susanna, Sandro, Fabio,
Martina

Preface

The present thesis was prepared at the Thermodynamics laboratory, Department of Aerospace and Mechanical Engineering, University of Liège (Ulg). It is submitted as a partial fulfilment of the requirements for the degree of Doctor of Philosophy and is written as a monograph.

The work was carried out for four years, from November 2012 to August 2016, under supervision of Associate Professor Vincent Lemort (Ulg) and co-supervision of Dr. Eng. Sylvain Quoilin (Ulg).

An external research stay was undertaken at the Section of Thermal Energy, Department of Mechanical engineering, Technical University of Denmark (DTU), under guidance of Associate Professor Fredrik Haglind, from May 2015 to October 2015.

The funding was ensured by the IWT SBO-110006 project The Next Generation Organic Rankine Cycles (www.orcnext.be), founded by the Institute for the Promotion and Innovation by Science and Technology in Flanders. Support was also received from the BRICKER project (www.bricker-project.com) founded by the European Union's Seventh Framework Programme for research, technological development and demonstration under grand agreement No. 6090701.

31st August 2016 Adriano Desideri.

Acknowledgements

This manuscript is the result of some years of work that I carried out with the help of many people at the University of Liège. I would like to thank my two advisers Vincent Lemort and Sylvain Quoilin for their help, support and experienced guidance.

The cooperation with UGent[1], DTU[2] and FBK[3] allowed to accomplish most of the work presented in this manuscript. The experience of Martijn and Sergei was fundamental for the experimental work carried on at the ORC unit facility at UGent, and I would like to thank them together with Andres for the many discussions we had. I also had the privilege to spend some of my time at the Section of Thermal Energy at DTU, and I would like to thank Fredrik for giving me this opportunity together with Jorrit, Torben, Martin and all the other team members of the group for welcoming me in Denmark, you have made the experimental work at DTU intense and fun.
I am also very thankful to all my colleagues at the Thermodynamic laboratory of the University of Liège.

Finally I want to thank my friends and my family for their support throughout these years. Special thanks go to Martina for her patience and her smile.

[1] Ghent University
[2] Denmark University of Technology
[3] Fondazione Bruno Kessler

Abstract

There are several factors worldwide that are creating an increasing potential for renewable energy technologies. The need to reduce greenhouse gases emissions, the need for sustainable power growth in developing countries, the need for distributed power generation in rural areas. In this context, energy conversion systems based on the organic Rankine cycle (ORC) technology can play a relevant role in the energy sector transitioning process from traditional fossil-fuel based power plant towards a distributed renewable technologies based system. The scientific contributions presented in this thesis are related to the dynamic modelling of small-thermodynamic systems, with a focus on ORC power units for waste heat recovery applications. The aim of this work consisted in developing a reliable and validated methodology to simulate the dynamics of low capacity, say tens of kW_{el}, organic Rankine cycle power systems. This work covered several aspects of small ORC power systems. It can be considered divided in three main parts: (i) experimental investigation of small ORC system (ii) development and validation of an open-source software for dynamic modelling simulations (iii) application of the developed software on a real trigeneration unit.

In order to identify and understand the main physical phenomena characterizing the transients of small ORC power unit, an 11 kW_{el} ORC unit equipped with a screw expander was tested at different working conditions. The obtained experimental data allowed drawing general conclusions about the performance of small systems and were used to derive simplified semi-empirical laws describing the behaviour of the main components. As the main dynamics of these power systems are mainly concentrated in the two-phase heat exchangers, evaporator and condenser, and given the lack of experimental data investigating the evaporation heat transfer performance for low critical temperature organic fluids, a second experimental campaign on a brazed plate heat exchangers test-rig was performed. The acquired results allowed characterizing the heat transfer performance of low critical temperature organic fluids at typical evaporation temperature for ORC application and a preliminary semi-empirical correlation to predict the heat transfer coefficient and the pressure drop was proposed.

Regarding dynamic modelling simulation a reusable and reliable software for dynamic modelling of low capacity ORC power systems was developed in the object-oriented Modelica code: the ThermoCycle library. The ThermoCycle library aims at providing a robust framework to model small-capacity thermodynamic cycles. It has been designed to provide an integrated and fully open-source solution ranging from the thermophysical substance properties, using

CoolProp to the simulation of complex systems with their control strategy. In comparison with alternative libraries dedicated to power plants (ThermoPower, ThermoSysPro, Thermal Power), the ThermoCycle library includes various models dedicated to the modelling of smaller-scale thermal systems, such as volumetric compressors models used for the simulation of heat pump or refrigeration cycles. A thorough validation of the main models included in the library comprising the validation of a complete ORC systems were performed against experimental data acquired on three different facilities, namely an library models As most of the works available in the literature on 11 kW_{el} ORC unit available at Gent University, an heat exchanger test-rig at the Technical University of Denmark and a parabolic through collector field at the Plataforma Solar de Almeria in Spain.

The final part of this manuscript presents a methodology based on dynamic modelling to investigate the performance of a trigeneration system under construction in Spain in the framework of the EU founded BRICKER project. A flexible modelling approach is presented allowing to investigate the performance of the system on a daily and annual basis. The proposed methodology and tool are virtually applicable to any combined heat and power systems.

Keywords. Organic Rankine Cycle, waste heat recovery, dynamic modelling, dynamic validation, Modelica, concentrated solar power, hybridization.

Papers and Presentations

Part of the work performed during the PhD project resulted in peer-reviewed publications and presentations, which are listed hereafter in the order of acceptance and by category. They are directly or indirectly related to the main topics of this thesis.

Peer-review journal article

Desideri A, Zhang J, Kærn MR, Ommenb TS, Wronski J, Lemort V, Quoilin S, Haglind F. Low critical temperature organic fluids vaporization inside brazed plate heat exchanger for organic Rankine cycle power systems. (submitted for publication)

Desideri A, Hernandez, A, Gusev S, Broek MVD, Lemort V, Quoilin S. Steady-state and dynamic validation of a small-scale waste heat recovery system using the ThermoCycle Modelica library. Energy 2016;

Desideri A, Dechesne B, Wronski J, Broek MVD, Sergei G, Lemort V, et al. Comparison of Moving Boundary and Finite-Volume Heat Exchanger Models in the Modelica Language. Energies 2016;:1–17doi:10.3390/en9050339.

Guillaume L, Legros A, Desideri A, Lemort V. Performance of a radial-inflow turbine integrated in an ORC system and designed 47 for a WHR on truck application: An experimental comparison between R245fa and R1233zd. Applied Energy 2016;(March). doi:10.1016/j.apenergy.2016.03.012.

Hernandez A, Desideri A, Ionescu C, De Keyser R, Lemort V, Quoilin S. Real-Time Optimization of Organic Rankine Cycle Systems by 50 Extremum-Seeking Control. Energies 2016;9(5):334. doi:10.3390/en9050334.

Desideri A, Gusev S, Broek MVD, Lemort V, Quoilin S. Experimental comparison of organic fluids for low temperature ORC systems for waste heat recovery applications. Energy 2015;97:460–9. doi:10.1016/j.energy.2015.12.012

Quoilin S, Bell I, Desideri A, Dewallef P, Lemort V. Methods to increase the robustness of finite-volume flow models in thermodynamic systems. Energies 2014;7(3):1621–40. doi:10.3390/en7031621.

Refereed Conferences

Desideri A, Kærn MR, Ommen TS, Wronski J, Quoilin S, Lemort V, Haglind F. Experimental results for hydrocarbon refrigerant vaporization in brazed plate heat exchangers at high pressure. In: The 29TH International Conference on Efficiency, Cost, Optimization, Simulation and Environmental Impact of Energy Systems. 2016.

Andritsos G, Desideri A, Gantiez Clé ment, Lemort V, Quoilin S. Steady state and dynamic modelling of a 1 MW_{el} commercial waste heat recovery ORC power plant. In: The 29TH International Conference on Efficiency, Cost, Optimization, Simulation and Environmental Impact of Energy Systems. 2016.

Ziviani D, Desideri A, Lemort V, De Paepe M, van den Broek M. Low-order models of a single-screw expander for organic Rankine cycle applications. In: IOP Conference Series: Materials Science and Engineering; vol. 90. 2015, p.42 012061. doi:10.1088/1757-899X/90/1/012061.

Hernandez A, Desideri A, Ionescu C, Quoilin S, Lemort V, Keyser RD. Experimental study of Predictive Control strategies for optimal operation of Organic Rankine Cycle systems. In: European Control Conference (ECC). ISBN 9783952426944; 2015, p. 2259–64.

Hernandez A, Desideri A, Ionescu C, Quoilin S, Lemort V, De Keyser R. Towards the optimal operation of an organic Rankine cycle unit by means of model predictive control. Proceedings of the 3rd International Seminar on ORC Power Systems 2015;:1–10doi:10.1109/ECC.2015.7330874.

Dickes R, Desideri A, Lemort V, Quoilin S. Model reduction for simulating the dynamic behavior of parabolic troughs and a thermocline energy storage in a micro-solar power unit. In: The 28TH International Conference on Efficiency, Cost, Optimization, Simulation and Environmental Impact of Energy Systems. 2015.

Desideri A, Dechesne B, Wronski J, Broek MVD, Sergei G. Comparison of moving boundary and finite-volume heat exchanger models in the Modelica Language. In: Proceedings of the 3rd International Seminar on ORC Power Systems. 2015, p. 1–10.

Desideri A, Amicabile S, Alberti F, Vitali-nari S, Quoilin S. Dynamic modeling and control strategies analysis of a novel small CSP biomass plant for cogeneration applications in building. In: ISES Solar World Congress. November; 2015, p. 8–12.

Buch QA, Dickes R, Desideri A, Lemort V, Quoilin S. Dynamic modeling of thermal systems using a semi-empirical approach and the ThermoCycle Modelica Library. In: The 28TH International Conference on Efficiency, Cost, Optimization, Simulation and Environmental Impact of Energy Systems. 2015.

Ireland M, Orsoz M, Desideri A, Quoilin S. Dynamic modeling and control system definition for a micro-CSP plant coupled with thermal storage unit. In: Proceedings of ASME Turbo Expo 2014: Turbine Technical Conference and Exposition. 2014.

Hernandez A, Desideri A, Ionescu C. Increasing the efficiency of Organic Rankine Cycle Technology by means of Multivariable Predictive Control. In: IFAC world congress. 2014, p. 2195–200.

Dickes R, Desideri A, Bell I, Quoilin S, Lemort V. Dynamic modeling and control strategy analysis of a micro-scale CSP plant coupled with a thermocline system for power generation. In: EuroSun. September; 2014, p. 16–9.

Desideri A, Broek MVD, Gusev S, Lemort V, Quoilin S. Experimental campaign and modeling of a low-capacity waste heat recovery system based on a single screw expander. In: 22nd International Compressor Engineering Conference at Purdue. 2011; 2014, p. 1–10.

Contents

1 Introduction

1.1 Energy scenario

In the last three decade anthropogenic global warming has been accepted worldwide [1–3]: from the United Nations Framework Convention on Climate Change in 1992 ratified by 50 states, through the Kyoto Protocol in 1997 signed by 84 governments to the recent agreement at the Paris Climate Conference in December 2015 (COP21) involving 195 nations.
The COP21 agreement main objective is to keep the world temperature rise below 2°C and possibly limit it to 1.5°C by reducing the greenhouse gas (GHG) emissions from 2015 to 2030 [4]. To reach this goal a series of actions and appropriate financial flows towards a low carbon, renewable energy-based future are required. Nowadays two thirds of the world's GHG emissions are due to energy production. It is thus clear that the energy sector must play a crucial role in reducing global emissions. The COP21 Paris agreement sent a powerful signal to the world that a low-carbon future has been chosen as the common path for humanity. At the same time what matters are the specific policies put in place to implement the deal and it can be safely stated that as long as fossil fuels appear to be the cheapest fuels available, they will be continued to be burned.
In the last years effective actions have been taken by the governments worldwide towards a green energy economy, and the coupling between energy-related emissions and economic growth has significantly weaken. Thanks to the policies adopted, solar photovoltaic (PV) and wind energy technology have reached large-scale deployment. In 2014, half of the total world installed capacity was based on renewable energy solutions. Carbon-free energy technologies are becoming increasingly cost competitive, but public subsidies are still required for many applications.
The International Energy Agency (IEA) recently presented a series of measures in the energy sector that should serve as a general guidelines for the nations worldwide in order to meet the 2°C temperature rise limit [5]. In the short term measures to increase the energy efficiency in the industry sector, reducing fossil-fuel subsidies and closing the least-efficient coal-fired power plants should be promoted. In the long term, a strategy fostering the development of an integrated, decentralized renewable-based energy system is presented as the most effective solution.
To the author's opinion, the organic Rankine cycle (ORC) technology can play a significant role in the foreseen energy transition process. Proven to be a mature, flexible and commercially

viable for standard power capacities, say from hundreds of kW_{el} up to a few MW_{el}, ORC power systems have been successfully employed for converting thermal energy from geothermal reservoirs, biomass combustion, waste heat from industrial processes and concentrated solar energy into electricity and heat. The ORC technology entails the same basic components of a traditional steam Rankine cycle, but an organic fluid is employed at the place of water. The fluid gets fully evaporated at high pressure and it is further expanded through an expansion machine to a lower pressure. It is then condensed and returned to its initial state, from where it is pumped to the high pressure line. During the expansion phase the energy of the fluid is converted into mechanical energy and further into electricity by means of a generator. The different thermo-physical characteristics of organic fluids allow for efficiently exploiting low quality thermal energy sources with respect to the traditional steam Rankine cycle. The organic fluids are normally characterized by an higher saturation pressure than water at the same temperature. As a consequence an ORC unit normally operates at a pressure close or higher than the atmospheric one with a low condensing volume flow. A simple and very compact layout for a Rankine-based power system is therefore often possible when employing an organic fluid. ORC systems are thus an interesting technology to look at for low temperature small-scale applications. In particular, in a decentralized and integrated energy based scenario small ORC systems can provide a modular and flexible solution for exploiting renewable energy sources which are often at a temperature lower than the one characterizing the combustion of fossil fuels.

1.2 State of the art and motivation

The first recorded attempts of replacing water with a non-conventional media as working fluid for a steam engine dates back to the 19th century [6] with the most well-known example being the development of a naptha engine to power small launch, an open motorised pleasure boat popular at the time, by Frank Ofeldt [7].
In the 20th century the ORC technology potential was investigated in the thirties and forthies with the pioneering work of Professor Mario Dorning and Professor Luigi D'Amelio [8] exploiting solar energy at low temperature followed by the commercialization of the SOMOR solar pump [9]. In the 1960s and 1970s several engines employing organic fluids, mainly refrigerants, were built based on solar, waste heat and geothermal as energy sources [10]. ORC power systems started to be seriously considered in the 1980s with the studies of Lucien Bronicki [11], Professor Angelino and his collegues Mario Gaia and Ennio Macchi [12].
In the last decade, as Society has been investing into renewable-based energy solutions to replace the traditional carbon-based ones, the ORC technology has experienced a renewed interests manifested both at research and industrial levels. As shown in figure 1.1a, since 2004 the installed ORC electrical capacity has been growing with an exponential trend driven by geothermal and biomass installations. In the same years the scientific publications covering ORC systems have been characterized by a comparable tendency (see figure 1.1b).
As far as scientific work is concerned, the number of publications focusing on the identification of suitable approaches for fluid selections is remarkable [15–18]. This is related to the high number of available organic fluids in the industry. An organic media can be defined as

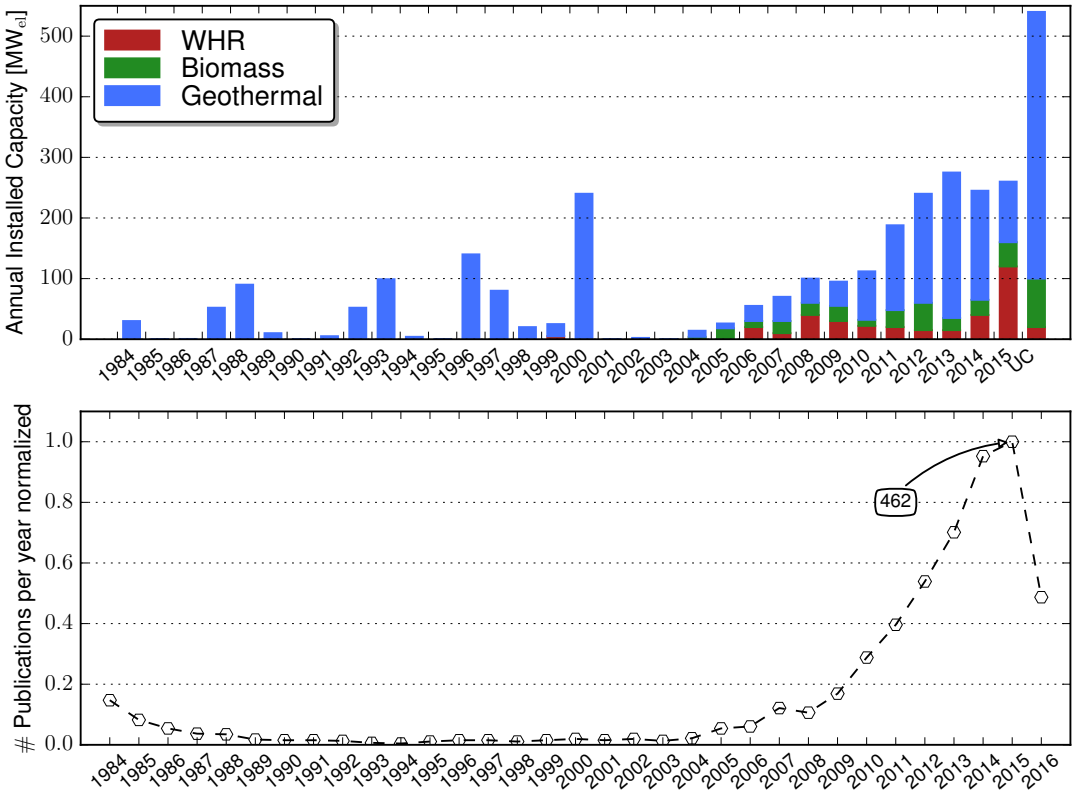

Figure 1.1 – (a) Installed capacity per year and per applications, rearranged from [13]. UC: under construction. (b) Number of publication matching the word 'organic Rankine cycle' from Scopus [14]. The values are normalized with respect to the maximum values, indicated in the plot.

any composts, not necessarily present in living organisms, containing a significant quantity of carbon [6]. Examples of these fluids used in the power industry are: Hydrocarbons, Fluorocarbons, Hydrofluoroolefin and Siloxanes. Up to now no universal fluid selection technique has been identified, and the most recent publications covering this subject present methodologies based on molecular design-technique [19].

The large number of working fluids available for ORC system applications call for a reliable, efficient and comprehensive software for the computation of the thermo-physical and transport properties. In the industry the proprietary REFPROP software developed by the National Institute of Standard and Technology (NIST) of the United States of America is the standard [20]. Other commercial softwares are FluidProp [21] and TIL Media Suite [22] which has been built specifically for dynamic simulations. There exist a number of open-source libraries which have been traditionally characterized by limited capacity compared to the proprietary ones [23]. Recently the open-source CoolProp fluid properties database has been developed as a joint effort between the University of Liège and the Technical University of Denmark [24]. The library allows for pure, pseudo-pure, mixtures and incompressible fluid properties calcu-

lation using high-accuracy Helmholtz energy formulations, cubic equation of state and fitting algorithms. The library also provides access to tabulated properties interpolation boosting the computational efficiency of the fluid properties calculation process. For these reasons the CoolProp library has been used throughout the development of the presented work.
Among the large amount of scientific literature related to ORC systems, very recently two reviews have been published by Colonna et al. [25] and Quoilin et al. [26] presenting an overview of the different ORC applications from the first installations and the exemplary state of the art systems to the possible next generation machines. The former focused on turbine-based ORC systems while the latter investigated smaller system equipped with volumetric expander. Both studies underlined the potential of ORC technology in converting localized and low temperature renewable energy sources into electricity, cooling and heating from few kW_{el} to tens of MW_{el} and concluded that further research and development is required for small-scale applications before reaching the commercialization stage.
Due to the intrinsic non-constant nature of the harvested energy resources, specific control strategies ensuring safe and optimal operation of the ORC unit during working conditions are required. In this regard dynamic modelling can play a key role in enabling the application of small-scale ORC systems for non-constant energy sources, as it allows accounting for transient phenomena from the early design stages [27] [28]. Dynamic modelling can be adopted to support plant maintenance and supervision (e.g. by suppressing disturbances unavoidable in the real systems in order to isolate particular effects), to evaluate and optimize the response time of a system under transient boundary conditions, to test dangerous working conditions, to support tuning of the controller, to develop and test control strategies.
Small capacity ORC systems are characterized by faster dynamics compared to large power plants given the lower volumes of the components. In particular the thermal inertia of the heat exchangers, often of the brazed plate type (BPHX), determines the main dynamics of the unit [28] [29]. In an ORC power system, the evaporator heat transfer performance is a key aspect in defining the system overall efficiency. As it operates at the highest cycle temperature far from the ambient conditions, ensuring a good heat transfer allows reducing the entropy production leading to higher expander inlet temperature and thus better cycle efficiency. Accurate evaporating heat transfer correlations are therefore deemed necessary from the early design stage to the development and testing of efficient model-based control strategies. Despite the broad use of BPHXs for small ORC systems, the available literature covering the performance of brazed plate type exchangers at typical evaporating temperatures and pressures of ORC power units for low temperature applications is scarce. Most of the published correlations are derived from water-based experiments [30] [31] or refrigeration studies [32] [33] where the working conditions are far away from those characterizing low temperature ORC systems. In this regard, there is a need to experimentally characterize the evaporation of low critical temperature working fluids for ORC power units, in order to validate existing correlations or derive new ones.
In the power industry, dynamic modelling and simulations originally gained attentions in the nuclear power field and gradually spread to the rest of the industry [34] [35]. Several software have been developed since the 60's in order to handle the modelling of systems described

by ordinary differential equations and discrete events. At the end of the 21th century, the increasing interests towards dynamic modelling simulations lead a group of scientists to gather together in an effort to define an object-oriented language for physical modelling, which resulted, in December 1999, to the release of the open-source Modelica programming language [36]. Since then, given the flexibility of the language, several Modelica-based libraries have been developed to model thermodynamic and thermal systems [27, 37]. Nowadays a number of libraries are available to model steam and gas cycles (e.g. ThermoSysPro, Power Plants, Thermal Power, ThermoPower, etc.) or refrigeration systems (TIL, AirConditioning, etc.). However, not all of them are open-access, and few are able to handle non-conventional working fluids which are used in ORC power systems, this lead to the effort partly documented in this thesis: the development of an an open-source Modelica-based library, ThermoCycle, focusing on the modelling of small thermal-power systems.
As most of the published literature related to dynamic modelling of ORC power units focuses on the application rather than the model validation [38][39][40], no dynamic experimental data of low-capacity ORC systems are available for a systematic comparison with results from model simulation. There is the need here for further research in order to provide means to validate the modelling approaches adopted in the ThermoCycle library components for the simulation of small capacity ORC systems.

1.3 Objectives

The aim of this work is to develop a reliable and validated methodology to simulate the dynamics of low capacity, say tens of kW_{el}, organic Rankine cycle power systems with a focus on low quality waste heat recovery applications.
This thesis evolved covering different aspects of small thermal power cycles. Low capacity installations are characterized by faster and different dynamics compared to large power plants. Identifying and understanding the main physical phenomena characterizing the behaviour of small ORC power units for different working conditions is the first step towards the development of a reliable modelling methodology. In particular given the lack of experimental data investigating the evaporation heat transfer performance of low critical temperature organic fluids at typical pressures and temperatures for waste heat recovery power systems, a specific experimental campaign is carried out to gain knowledge on the phenomena driving this process. The second aspect deals with the development of a reliable, flexible and accessible software for the dynamic modelling of small power systems based on the knowledge gained through the performed experimental campaigns. A comparison against experimental data is required both at a component and at a system level to validate the developed modelling tool. The last step focuses on the investigation of the software potential in assisting the development of a real case project. The results obtained through the performed experimental campaigns and the numeric dynamic-based investigations provide a contribution towards the optimal design and control of low capacity ORC power systems for low quality waste heat recovery applications.
The different steps carried out throughout this project can be listed as follows:

- Characterize the working conditions of a low capacity ORC power unit through a dedicated experimental campaign.
- Identify and validate heat transfer correlations for low temperature organic fluids at typical pressures and temperatures for low quality power generations with a focus on vaporization.
- Provide a reusable and accessible software for dynamic modelling of low capacity ORC power systems.
- Design and perform suitable experimental tests to validate the dynamic modelling software both at a component and at a system level.
- Investigate and test the potential of the developed software in providing valuable insights during the early project phase of an ORC-based trigeneration systems for building applications.

1.4 Thesis Outline

This thesis is divided in 5 main chapters covering the aspects outlined in the above sections. A brief overview of each chapter is provided hereunder:

Chapter 2 describes the experimental campaign carried out on a small organic Rankine cycle power unit for stationary low quality waste heat recovery applications available at the Ghent University, campus Kortrijk. The performance of the different components are analysed in a wide range of working conditions for two low critical temperature organic fluids. A comparison between the two fluids allows drawing general guidelines on the development of low capacity organic Rankine cycle power systems.

Chapter 3 reports an overview of available correlations for heat transfer and pressure drop of plate heat exchangers. Dedicated experimental tests carried out on a test-rig available at the Technical University of Denmark are presented. The acquired data are used to validate existing heat transfer correlations for typical pressures and temperatures of organic Rankine cycle-based applications targeting low quality power generation.

Chapter 4 presents a Modelica-based software for the modelling of low capacity thermal power systems: the ThermoCycle Modelica library. An overview of the software structure is provided. The implementation of the different heat exchangers modelling approaches are presented in detail.

Chapter 5 deals with the validation in steady-state and dynamic regime of the developed dynamic models. A comparison of the heat exchanger models against experimental data collected on the test-rig available at the Technical University of Denmark is shown. An organic Rankine cycle model based on the ThermoCycle models is validated with dynamic data acquired on the test rig presented in Chapter 2. Guidelines to design and perform effective dynamic experiments are provided.

Chapter 6 shows how the developed models can be used to assist the design of a real organic Rankine cycle-based tri-generation systems for building applications exploiting the thermal energy from a biomass boiler and a parabolic through concentrated solar power system.

Chapter 7 summarizes the main findings of this contribution, analysing the main objectives stated at the beginning of this work. Furthermore suggestions are given for future work.

2 Organic Rankine Cycle Experimental Set-Up

Abstract In this chapter the performance of a low capacity ORC system for stationary bottoming WHR application operating with two different working fluids, SES36 and R245fa are analysed. The test rig is a regenerative cycle equipped with a single screw expander modified from a standard compressor characterized by a nominal shaft power of 11 kW_{MECH}. A total of 36 and 43 steady-state points are collected for SES36 and R245fa respectively, over a wide range of operating conditions by changing the expander rotational speed, the pump frequency and the cooling condenser flow rate. The performances of the ORC components are individually evaluated. A maximum expander isentropic efficiency of 62% is reached using SES36 at 3000 rpm, and a value of 52% is reached with R245fa at 3000 rpm. However, for a given pressure ratio the expander output power is higher with R245fa than with SES36. The overall performance of the ORC unit are investigated in terms of first and second law efficiencies and net output power for the two fluids. The results experimentally demonstrate the correlation between the working fluid critical temperature and the ORC unit working characteristics for low temperature waste heat recovery applications. Open experimental data are provided for both fluids.

2.1 Introduction

The deployment of ORC systems for low temperature small-scale applications is still at a research stage. In order to identify the performance of these power systems, experimental data is of utmost importance. Working fluid and expander machine selection plays a major role in ORC system performance and economy. The working fluid selection process has been widely investigated in several studies [41] but no universal optimal fluid is indicated since the choice is highly dependent on the target application. A detailed list of the guidelines and indicators that should be taken into account when selecting an organic fluid for power generation is reported in [26] and in [42]. In general the critical temperature of the selected fluid should be slightly higher than the target evaporation temperature. For low quality waste heat recovery, refrigerants are often selected due to the low critical temperature value [41]. As far as the expander is considered there are two possible choices: turbo and positive displacement machines. In the micro power range (3 - 20 kW_{el}) the latter are often preferred over turbo-generators for the following characteristics: low flow rate, low rotational speed, high single-state expansion ratio [43]. In addition, displacement machines can handle two-

phase flow, a condition that can appear at the expander outlet when operating with 'wet fluids'. Despite these advantages, the market suffers a lack of commercial expanders for the micro power range [44] and the majority of positive displacement machines that have been used up to now are prototypes often derived from existing compressors in order to be cost-effective [26] [45] [46]. Among the displacement expander technologies, the screw expander represents a promising candidate for ORC systems. In recent years Leibowitz et al. [47] presented a 20 kW_{el} ORC system for low grade heat source application based on a screw expander demonstrating the economical feasibility of the system with an installation cost in the range of 1500 to 2000 \$/kW_{el} and a predicted adiabatic shaft efficiency in the order of 70%. Field data from a commercial ORC power plant recovering low waste heat in Sweden are reported in [48]. The plant is equipped with a twin screw expander and uses ammonia as working fluid reaching a thermal efficiency of 8 to 9% at capacities from 50 to 100%. Experimental studies of screw expander machines handling 2-phase expansion has been published in the literature. Öhman and Lundqvist [49] presents test data of a 50 KW_{el} screw expander with controlled 2-phase conditions at machine inlet, showing a maximum efficiency of up to 92%. The test results are compared with the most relevant experimental data available in the literature and a correlation for a first estimation of the adiabatic efficiency during 2-phase conditions, underling the interesting potential of screw machines for 2-phase expansion processes, is derived. Recent studies have reported experimental performance of in-house built single screw expanders for low power capacity. The single screw expander allows for a simplified configuration, low vibration, low leakages and balanced loading of the main screw [50]: characteristics that make this machine an interesting choice over twin screw expander. A 5 kW_{el} single screw machine with a measured isentropic efficiency of 59% is presented in [51]. A 22 kW_{el} single screw expander was built and tested by He et al. [52] reaching a maximum efficiency of 55% at 2800 rpm. The impact of the gaterotor/shell and the screw/shell gap has been analyzed by [53] concluding that the machine with a medium gap achieved the best performance with an output power of 5 kW_{el} and an isentropic efficiency of 60%. The working fluid employed in the cited contributions is compressed air.

To the author's knowledge at the present time there is a lack of experimental data for single screw expander operating with different organic fluids. In this chapter the author investigates the performance of an ORC system for low grade waste heat recovery application equipped with a single screw expander under the adoption of two low critical temperature organic fluids SES36 and R245fa. A preliminary comparison of the performance of the test rig operating with the two fluids is presented in [54] while a steady-state semi-empirical model of the expander was developed by Desideri et al. [55]. The results presented are devoted to the development of small capacity ORC systems equipped with single screw expander for low temperature waste heat-recovery applications. The recorded experimental data set allows to evaluate the potential of a low-capacity system working with two different organic fluids, to derive and calibrate semi-empirical models of the different components of the ORC unit and to gain insights on the main thermodynamic phenomena characterizing the systems.

2.2 ORC experimental set-up architecture

The front view and the process flow diagram of the ORC test rig are shown in figure 2.1. The system is a regenerative cycle equipped with a single screw expander characterized by a nominal shaft power of 11 kW. The expansion machine is obtained by modifying a single screw compressor to run in expansion mode with a calculated built-in volume ratio of 6 [50]. Oil with a mass concentration of 3.23% is added to the cycle to lubricate the rotor while the bearings are lubricated through a by-pass pipe that goes from the pump outlet to the expander as shown in figure 2.1b. The vertical variable speed multistage centrifugal pump and the screw expander, through the asynchronous generator, are both connected to two inverters that allow controlling the rotational speed of the machines, a 4-quadrant inverter is selected for the expander asynchronous machine, to be able to run both in motor and generator modes. The evaporator is insulated with a glass wool layer of 180 mm thickness. A liquid receiver is placed at the condenser outlet. The tank imposes a saturated liquid state to avoid sub-cooling at the condenser outlet [29]. Looking at the bottom left of figure 2.1b, it is possible to recognize the liquid receiver. From there (1), the working fluid is pumped through the recuperator, where it is pre-heated from (2) to (3), and then it enters the evaporator, where it undergoes a transition from liquid to vapour state (4), before expanding in the single screw expander machine. The superheated vapour leaving the expander enters the recuperator (5) and the condenser (6) . The fluid in saturated liquid condition is then accumulated in the liquid receiver. A summary of the main ORC components characteristics is reported in table 2.1.

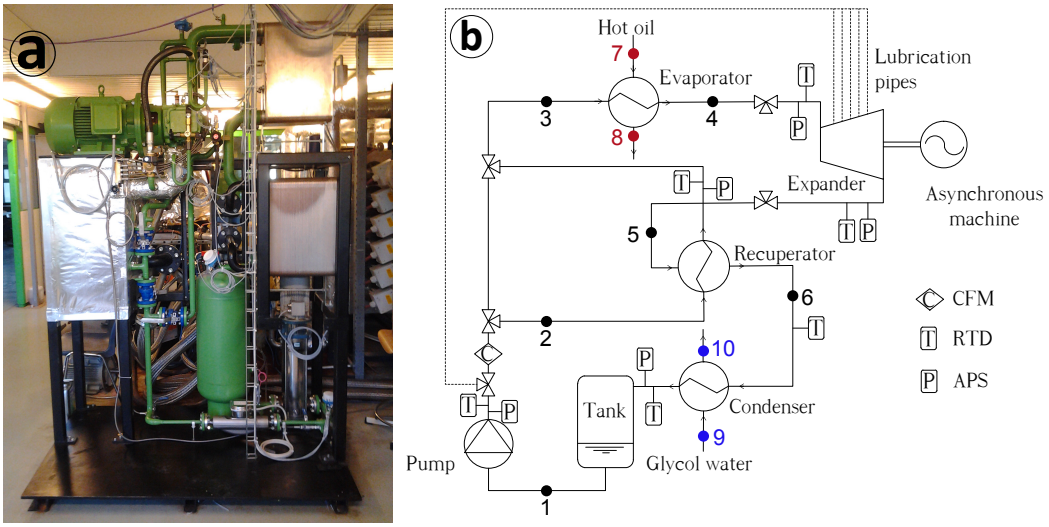

Figure 2.1 – (a) Front view of the ORC test rig. (b) Process flow diagram with the relative sensors position of the ORC test facility.

Table 2.1 – Summary of the specifications of the main ORC unit components.

System component	Specifications
Evaporator, condenser, recuperator	Brazed plate type - 150 plates
Pump	Vertical centrifugal pump 14 stage 2.2 kW motor, 2900 rpm max, p_{max} 14 bar
Expander	Single screw type, $r_V = 6$

2.2.1 Heating loop

The low-capacity waste heat thermal energy source is represented by means of an electrical boiler where thermal oil, Therminol66, is pumped through to temperatures of up to 125°C. The boiler has a maximum power of 250 kW_{th}. A proportional integral (PI) controller is implemented to maintain the temperature of the oil at the inlet of the evaporator constant during transient in the ORC test rig (e.g. change of ORC pump rotational speed).

2.2.2 Cooling Loop

A variable flow rate of glycol water, 32% vol. ethylene glycol, is used as heat sink to cool down the working fluid in the condenser. The thermal energy absorbed by the cooling fluid is rejected to the ambient by means of an air cooler. A by-pass of the air cooler allows controlling the condenser temperature by means of an adjustable solenoid valve.

2.2.3 Data Aquisition System

Absolute pressure sensors (APS) and resistance temperature detectors (RTD) at the inlet and at the outlet of the different components allow the determination of the energy balance for each component and the management of the plant. The working fluid mass flow rate is measured by means of a Coriolis flow meter (CFM) installed at the turbo-pump outlet. The cooling loop is equipped with two RTDs to measure the temperature of the cooling fluid at the inlet and at the outlet of the condenser and an ultrasonic flow-meter is used to measure the flow rate of glycol water. In the heat source circuit, the temperature of Therminol66 is measured at the inlet and at the outlet of the evaporator and a pressure difference transmitter is used to calculate the oil mass flow rate. The expander electrical power after the 4-quadrant inverter is measured by means of a wattmeter. The data acquisition system is done with a PLC, and a laptop with LabView is used for data visualization. The characteristics of the measurement devices are reported in table 2.2.

2.3 Working fluid selection

In the ORC technology field, the fluid selection is a fundamental aspect of the system design stage. Different studies focus on the characteristics required by the fluid in order to retrieve

Table 2.2 – Range and precision of the measurement devices. k: coverage factor.

Variable	Device type	Range	Uncertainty (k=2)
$\dot{m}$	CFM	0 kg s^{-1} to 1.8 kg s^{-1}	± 0.09%
T (ORC)	RTD	50°C to 300°C	± 0.2K
T (heat sink)	RTD	0°C to 150°C	± 0.2K
T (heat source)	RTD	30°C to 350°C	± 0.2K
p	APS	0 bar to 16 bar	± 0.016 bar
$\dot{W}_{el}$	Wattmeter	0 to 100 kW	± 0.1%

the highest efficiency or power out of the given thermal energy source [41][26][42]. In general the fluid should have a low critical pressure and a critical temperature slightly higher than the target evaporation temperature. For low quality waste heat recovery, the choice of the working fluid is often restricted to the refrigerant fluid family because of their low critical temperatures and pressures. Among null ozone depletion potential (ODP) refrigerants, R245fa and SES36 are selected since they are well known fluids in the power industry, currently used by the main industrial ORC manufacturers [42]. This criterion ensures that the fluids are not toxic, not flammable and easily available on the market. The properties of R245fa and SES36 are compared in table 2.3.

Table 2.3 – Fluid properties of R245fa and SES36.

Fluid property	R245fa	SES36
Molar mass [kg kmol^{-1}]	134	184.85
Critical pressure [bar]	36.51	28.49
Critical temperature [°C]	154.01	177.55
GWP [-]	950	3710
Boiling point at 1 bar [°C]	14.8	35.34

2.4 Results and analysis

This section reports the analysis of the experimental results. At first an overview of the collected set of experimental data is provided. Secondly, the thermodynamic performance of the different components of the ORC test rig is reported. The thermal energy balance over the heat exchangers is investigated, to cross-check the precision and the quality of the measurements. This step, although often overlooked, is of primary importance because of the numerous measurement issues that can arise in experimental campaigns. The rotary machines performances are then analyzed by comparing the isentropic efficiency and the power consumed or delivered under the different test conditions. Finally the cycle thermodynamic performances for the two selected fluids are assessed.

2.4.1 Experimental Investigation

A total of 36 and 43 steady-state points are collected for SES36 and R245fa respectively. These points are obtained by keeping the system at a stable condition (RTD temperature variations below 1 K) for a minimum of 10 minutes and by averaging the measurements over a period of 3 minutes [49]. During the experimental campaign the oil temperature at the inlet of the evaporator is kept constant at 125°C for both fluids. Its mass flow rate varies between 3.1 to 3.4 kg s^{-1}. The glycol water temperature in the condenser mainly depends on the ambient (external) temperature. It varies between 14°C and 43°C for SES36 and R245fa. The condenser pressure varies between a value of 0.9 and 1.7 bar for SES36 and between 1.2 and 2.1 bar for R245fa and is adjusted by controlling the cooling flow rate. In order to investigate the effect of the expander rotational speed on the single screw machine performance, its value has been set to 2000 and 3000 rpm for both fluids. For each expander speed value, different operating conditions are obtained by varying the pump rotational speed which imposes the working fluid flow rate through the unit. On-line signal plotting is used to ensure that a steady state condition is achieved before any change is imposed to the system. The minimum and maximum performances obtained during the measurement campaign for R245fa and SES36 are reported in table 2.4.

Performance	ε_{cycle} (%)	$\varepsilon_{s,exp}$ (%)	$\varepsilon_{s,pu}$ (%)	$p_{su,exp}$ bar	$r_{p,exp}$ -	ΔT_{sc} (K)	ΔT_{sh} (K)	PP_{eva} (K)	PP_{cd} (K)	ΔP_{LP} (bar)	ΔP_{HP} (bar)
					SES36						
Min	0.2	13.25	12.3	4.5	3.12	9	1	0.1	0.1	0.06	$0.4{\cdot}10^{-3}$
Max	9.8	62	35	10.2	10.97	26	29	0.7	1	0.17	0.09
					R245fa						
Min	0.3	12.21	10.9	5.66	3.5	2.5	15.83	0.1	0.1	0.09	0.14
Max	8.5	51.92	21.3	12.3	7.3	4.79	56.54	0.7	4	0.15	0.24

Table 2.4 – Min/Max performances achieved during the measurement campaigns for SES36 and R245fa. Pressure drops are evaluated from turbine outlet to pump inlet, ΔP_{LP}, and from pump outlet to turbine inlet , ΔP_{LP}.

Very low pressure drop and pinch point (PP) values are registered in the condenser and the evaporator for both fluids, which is due to the oversizing of the heat exchange area which causes a high heat exchange efficiency. A large value of the subcooling at condenser outlet is measured for the SES36 tests. This can be explained by the presence of non-condensable gases in the test rig due to the sub-atmospheric value of SES36 condensing pressure for some of the operating conditions [29]. This explanation is strengthened by the results obtained with R245fa, where the condensing pressure is always higher than the atmospheric pressure and a low value of subcooling is registered. Maximum cycle efficiencies of 9.8% and 8.5% are reached for SES36 and R245fa respectively. The maximum expander electrical isentropic efficiency is 65%. The pump is characterized by electrical isentropic efficiencies lower than 35% under the reported test conditions.

2.4.2 Heat exchangers thermal energy balances

The thermal energy balances over each component of the ORC test rig can be computed in order to check for possible unbalances. Significant residuals can indicate measurement issues or unconsidered parasitic phenomena such as ambient losses. The temperature difference between the inflow and the outflow of the pump and the liquid receiver is in the order of 1-2 K. Furthermore the temperature values characterizing the fluid flow in these two components are in the order of magnitude of the ambient temperature, leading to small thermal energy losses to the ambient. For these reasons they are not considered in the following analysis. The working fluid enthalpy flow to or from a component is calculated as follows [56]:

$$\dot{Q} = \dot{m} \cdot (1 - \alpha_{\mathrm{lo}}) \cdot (h_{\mathrm{I}} - h_{\mathrm{II}}) + \dot{m} \cdot \alpha_{\mathrm{lo}} \cdot c_{\mathrm{p,lo}} \cdot (T_{\mathrm{I}} - T_{\mathrm{II}}) \tag{2.1}$$

where h_{I}, T_{I} and h_{II}, T_{II} are the inlet (I) and the outlet (II) temperature and enthalpy values of the different components. Enthalpies are computed using the open-source CoolProp library [24]. α_{lo} and $c_{\mathrm{p,lo}}$ are the mass fraction and the specific heat capacity of the lubricant oil present in the working fluid circuit. In figure 2.2 the energy flows, computed on both sides of the evaporator for both fluids are depicted. The Figures show a fairly constant unbalance

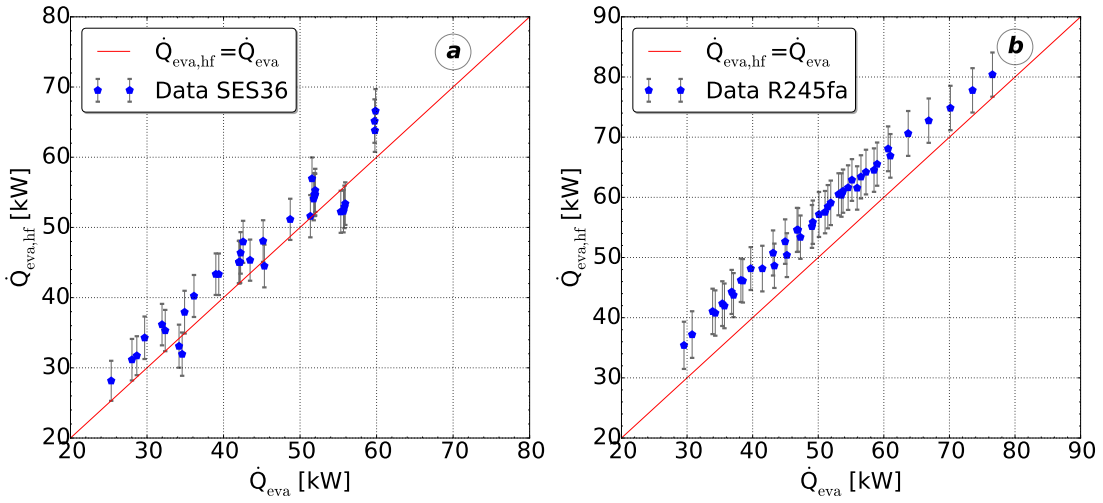

Figure 2.2 – Thermal energy balance over the evaporator for SES36 (a) and R245fa (b) with the relative error bars. $\dot{Q}_{\mathrm{eva}}$: thermal power absorbed by the working fluid. $\dot{Q}_{\mathrm{eva,hf}}$: thermal power transferred by the hot source.

between the thermal energy flows of the secondary fluid, $\dot{Q}_{\mathrm{eva,sf}}$ and the working fluid, $\dot{Q}_{\mathrm{eva}}$, for both fluids. This trend can be explained either by energy losses or by measurement imprecision. The latter option is checked by means of an uncertainty propagation analysis. For most of the points the error bars, indicating the standard error over the difference between the secondary and the primary fluid thermal energy flows, are of the same order of magnitude as the thermal energy difference. The thermal energy transfer to the ambient can be considered as the main cause of the unbalance. As far as the low pressure line is concerned, for most

of the tests the measured recuperator outlet temperature is characterized by a value similar or even lower than the saturation temperature at the condensing pressure. This allows to state that condensation starts in the recuperator. As a consequence a thermal energy balance accounting for both recuperator and condenser is performed. The results are reported in Figure 2.3 with the relative uncertainty propagation analysis to examine the sensor imprecision. The thermal energy absorbed by side2 (s2), which comprises the condenser cooling fluid side and recuperator liquid side, results higher than the one delivered by side1 (s1), which accounts for the condenser working fluid side and the recuperator vapor side. As it is possible to see the uncertainty is of the same order of magnitude as the unbalance for both fluids leading to the conclusion that measurement imprecision causes the energy unbalance in the recuperator and condenser.

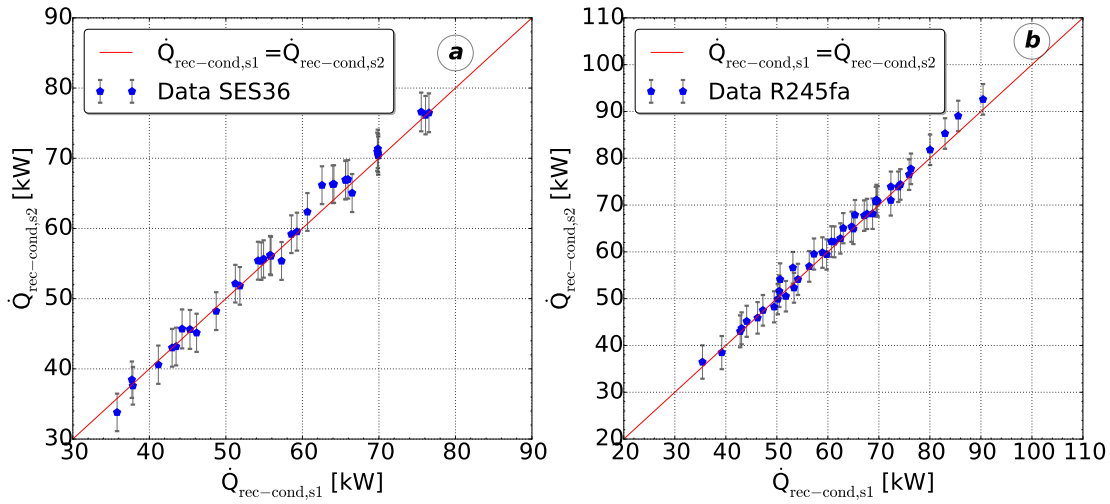

Figure 2.3 – Recuperator and condenser thermal energy balance for SES36 (a) and R245fa (b) with the relative error bar. $Q_{rec-cd,s1}$: thermal energy transferred by the condenser working fluid side and the recuperator hot side. $Q_{rec-cd,s2}$: thermal energy absorbed by the condenser cooling fluid side and the recuperator cold side.

2.4.3 Pump performance

The pump performance is analyzed in terms of the electrical isentropic efficiency, defined in equation 2.2 [57], and the consumed electrical power.

$$\varepsilon_{pu,s} = \frac{\dot{m} \cdot (h_{ex,pu,s} - h_{su,pu})}{\dot{W}_{pu,el}} \tag{2.2}$$

The two variables are plotted in figure 2.4 with respect to the delivered mass flow rate. The pump electrical isentropic efficiency is characterized by similar low values for both SES36 and R245fa at a given mass flow rate. The cause of the scattering for SES36 could not be determined with certitude. It might be due to pump cavitation or to the presence of bubbles of non-condensing gases. The second hypothesis is supported by the fact that the phenomenon

disappears with R245fa, which is less subject to non-condensing gases issues. For most of the collected measurements, the electrical isentropic efficiency does not exceed 22%. Such a low value is in line with the available data in the literature [26] and it can be partly explained by the fact that it accounts for the motor efficiency. Power consumption is also very similar for both fluids and increases linearly with the delivered mass flow rate as shown in figure 2.4b. In the R245fa case with expander speed at 3000 rpm a fairly constant trend of the electrical pump power is registered at 0.6, 0.7 and 0.8 kW_{el} for mass flow values comprised between 0.2 and 0.3 $kg.s^{-1}$. For each of these sets of experimental points, the pump is running at the same speed, and the slight difference in the mass flow rate is due to different pump inlet conditions imposed by the thermodynamic state at condenser outlet. For higher mass flow rate values, the consumed power increases linearly as the pump speed is raised.

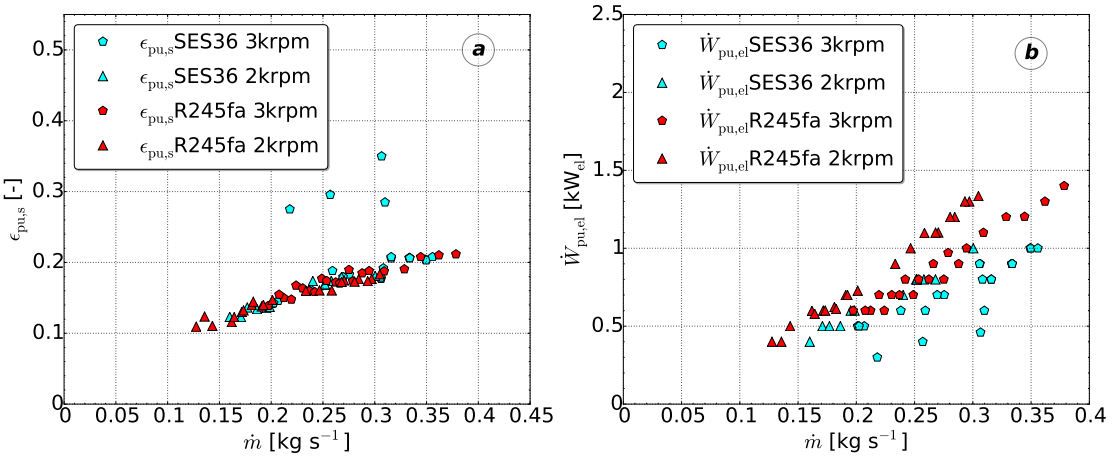

Figure 2.4 – (a) Pump isentropic efficiency, $\varepsilon_{pu,s}$, and (b) pump consumed power, $\dot{W}_{pu,el}$, as a function of the working fluid mass flow rate for SES36 and R245fa at an expander rotational speed of 2000 and 3000 rpm.

2.4.4 Expander performance

In figure 2.5 the expander isentropic efficiency and the generated expander power are plotted as a function of the pressure ratio for both fluids. The isentropic efficiency is calculated according to Declaye's recommendations to avoid the effect of ambient heat losses [46]:

$$\varepsilon_{exp,s} = \frac{\dot{W}_{exp,el}}{\dot{m} \cdot (h_{su} - h_{ex,is})} \tag{2.3}$$

In figure 2.5a, the isentropic efficiency trend for SES36 shows a maximum that it is not present in the case of R245fa. The maximum is due to a fixed built-in volume ratio of the expander. The pressure ratio applied to the expander differs from the optimal pressure ratio corresponding to the built-in volume ratio for most of the tests. This leads to over/under expansion losses whose impact is minimized when the pressure ratio matches the internal pressure ratio of the expander. This optimal pressure ratio could not be reached in the case of R245fa due to

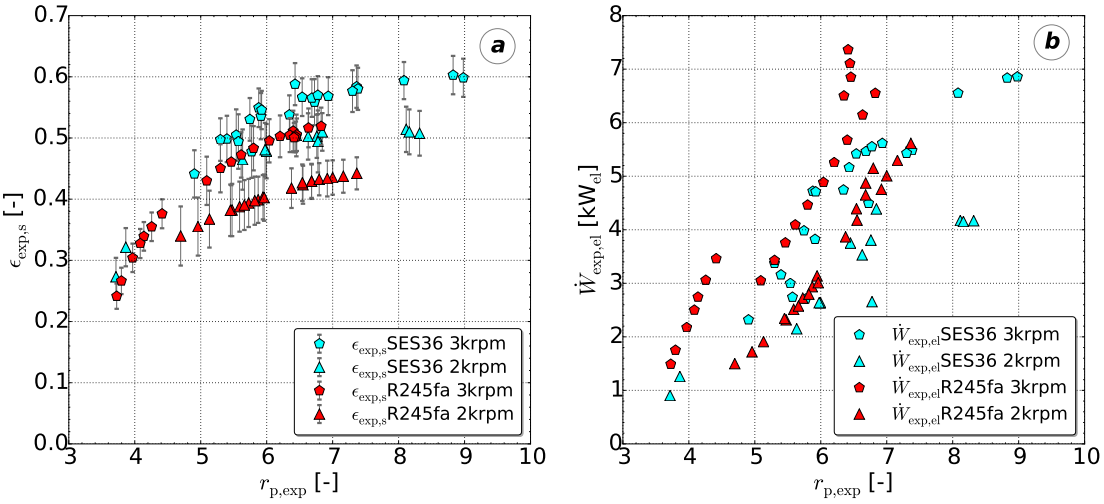

Figure 2.5 – (a) Expander isentropic efficiency, $\varepsilon_{exp,s}$, and (b) expander output power, $\dot{W}_{exp,el}$, as a function of the expander pressure ratio, $r_{p,exp}$, for SES36 and R245fa at an expander rotational speed of 2000 and 3000 rpm.

the higher condensing pressure, which explains the growing trend of the R245fa isentropic efficiency. For pressure ratios in the range of 5 to 9 for SES36 and from 5 to 7.7 for R245fa, the isentropic efficiency at 3000 rpm is about 11% higher than at 2000 rpm. For lower pressure ratio this difference tends to disappear. These results are in line with the numerical results of Lemort et al. [45] according to which the impact of leakages on the performance of the expander is predominant at low rotating speed and high pressure difference. Comparing the expander performance for the two fluids, for pressure ratio values ranging from 5 to 7.7, and a given rotational speed the SES36 isentropic efficiency is 22% higher than the R245fa one. This could be explained by the high inlet pressure in the R245fa tests (see table 2.4), close to the maximum allowable expander pressure, that would cause an increase of leakage losses. The maximum expander isentropic efficiency ranges from 51% at 2000 rpm to 62% at 3000 rpm for SES36 and from 44% at 2000 rpm to 52% at 3000 rpm for R245fa. The pressure ratio that maximizes the isentropic efficiency is 6.8 at 2000 rpm and 7.7 at 3000 rpm for SES36. This shift can be due to the relative effect of leakage losses as explained above. At high pressure ratios, under-expansion occurs, as described in [45]: the built-in volume ratio is too low for the imposed expansion ratio and the efficiency decreases.
The trend of the shaft power differs from the one of the isentropic efficiency, displaying a monotonically increasing function of the pressure ratio as shown in figure 2.5b. This could be explained by the generation of additional work during the discharge process if the outlet pressure is decreased, even if the pressure ratio is higher then the internal expansion ratio. The scattering characterizing the plot for both fluids is due to the variations of additional operating conditions not displayed in the plot, such as small variations in the inlet expander pressure. In particular in the case of R245fa at 3000 rpm two distinct trends can be recognized. One for a pressure ratio between 3.5 to 4.5 and the second for values comprises between 5 to 7.

The data for R245fa at an expander speed of 3000 rpm, where recorded on two different days, characterized by different weather conditions. The influence of the air-cooled condenser on the expander outlet condition leads to the two depicted tendencies. Comparing the overall expander power trend for the two fluids, it can be noted that for a given pressure ratio and rotational speed the power generated with R245fa is higher than in the SES36 case. This is explained by the higher density, and thus higher mass flow rate for the same volume flow rate, at the inlet of the expander in case of R245fa. A maximum power of 7.1 kW_{el} is reached for a pressure ratio of 8.5 for SES36 at 3000 rpm while a value of 7.3 kW_{el} is reached for a pressure ratio of 6.2 for R245fa.

2.4.5 Cycle performance

An experimental comparison of the cycle performance of the test-rig running with the two fluids is performed by analysing the first and second law cycle efficiencies as a function of the saturation temperatures difference between evaporator and condenser, ΔT_{ORC}, where the evaporating temperature is a function of the evaporating pressure which is calculated as the arithmetic mean between the measured inlet and outlet evaporator pressures, and the condensing temperature is a function of the condensing pressure that is set equal to the measured pressure at the outlet of the expander. The first and second law efficiency are defined respectively in equation 2.4 and 2.5 [58].

$$\varepsilon_{I} = \frac{\dot{W}_{net}}{\dot{Q}_{eva,hf}} \tag{2.4}$$

$$\varepsilon_{II} = \frac{\dot{W}_{net}}{\dot{E}x_{hf}} \tag{2.5}$$

where $\dot{W}_{net}$ is the net output power:

$$\dot{W}_{net} = \dot{W}_{exp,el} - \dot{W}_{pu,el} \tag{2.6}$$

and $\dot{E}x_{hf}$ is the hot fluid exergy flow:

$$\dot{E}x_{hf} = \dot{m} \cdot [(h - h_0) - T_0(s - s_0)] \tag{2.7}$$

with a dead (reference) state defined by a pressure value, p_0, set to 1 bar and by a temperature value, T_0, set to 25°C. As shown in figure 2.6a, the second law thermodynamic efficiency is higher for R245fa than for SES36 at a given ΔT_{ORC}. This is explained by the higher power generated by the expander with R245fa as reported in figure 2.5, while the pump consumption is characterized by similar values for both fluids. On the other hand both fluids exhibit similar values of the first law thermodynamic efficiency at a given ΔT_{ORC} as shown in figure 2.6b meaning that the R245fa is absorbing more thermal energy from the heat source in the evaporator. A maximum first law efficiency of 9% is obtained for SES36 and of 8% is obtained for R245fa. The maximum value of the second law efficiency is around 8% for both fluids. As the ORC test-rig design was not optimized for none of these two fluids, these

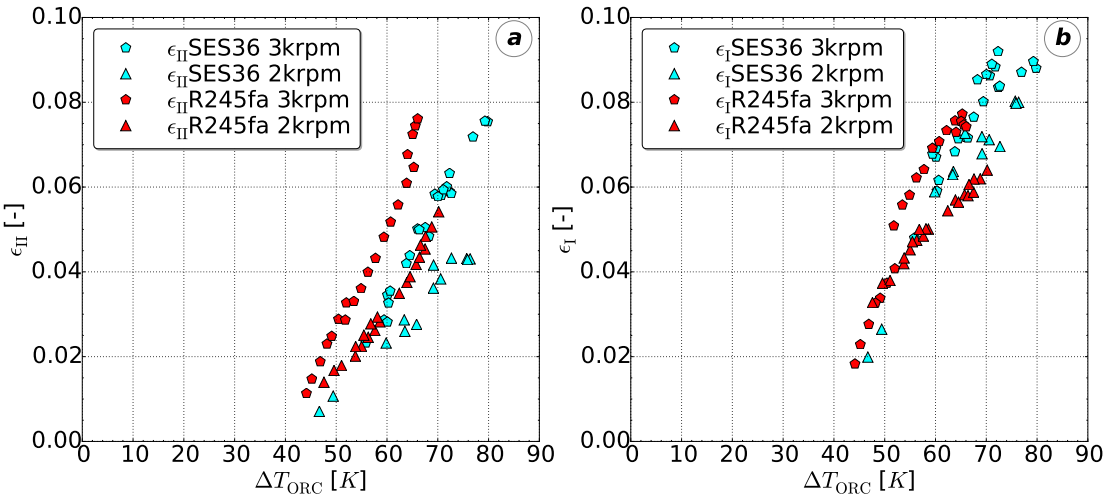

Figure 2.6 – (a) Second law efficiency, $\varepsilon_{\mathrm{II}}$, and (b) first law efficiency, $\varepsilon_{\mathrm{II}}$, as a function of the saturation temperature difference between evaporator and condenser, ΔT_{ORC}, for R245fa and SES36 at an expander rotational speed of 2000 and 3000 rpm.

quantitative results have to be considered as indicative and related to the different components performances of the unit. In figure 2.7a and 2.7b the net output power is plotted versus the

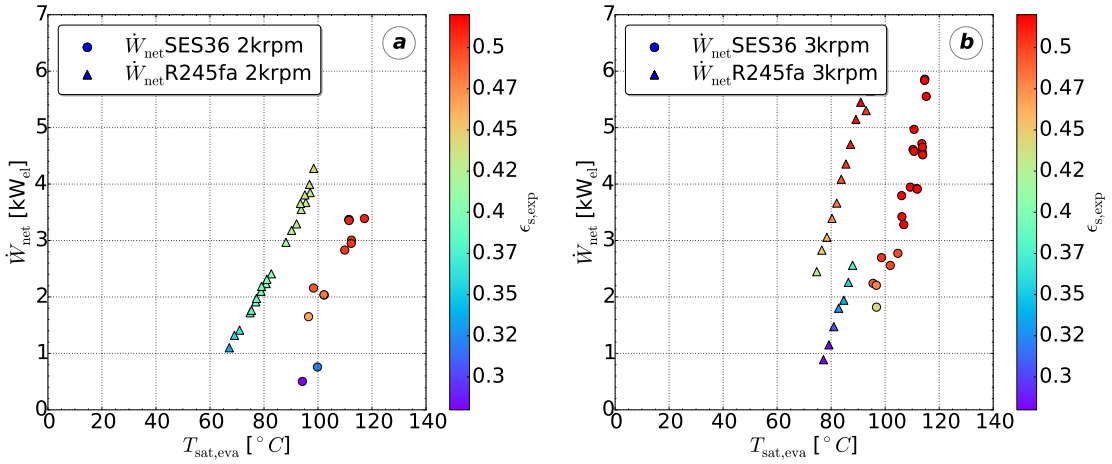

Figure 2.7 – Net output power, $\dot{W}_{\mathrm{net}}$, as a function of the evaporating temperature, $T_{\mathrm{sat,eva}}$ for SES36 and R245fa at an expander rotational speed of 2000 rpm (a) and 3000 rpm (b). The contour is representative of the expander isentropic efficiency.

evaporating temperature for R245fa and for SES36. A clear trend is detected at 2000 and 3000 rpm of the expander rotational speed for both fluids. For a given evaporating temperature, $T_{\mathrm{sat,eva}}$, the net output power is higher in the case of R245fa than in the case of SES36. This is explained by the fact that at a given $T_{\mathrm{sat,eva}}$ the density of R245fa is higher than for SES36. As a consequence, given a certain evaporating temperature and a volume flow rate, fixed by the

rotational speed of the expander, more mass flow goes through the evaporator leading to more power generation in the case of R245fa than in the case of SES36. This experimentally proves that for low temperature heat source the expander for R245fa can be designed with a smaller swept volume compared to the one that SES36 would need leading to a more compact less expensive system in case of R245fa. The performance of the two fluids is further analyzed by examining the T-s diagram for the steady-state point corresponding to the maximum power achieved during the experimental campaign, plotted in figure 2.8. The temperature of the thermal oil at evaporator inlet, point 7, is 125°C for both fluids and the temperature of the water-glycol mixture at the condenser inlet, point 9, is 22.7°C for R245fa and 22°C for SES36. The expander rotational speed is set to 3000 rpm. The net output power corresponds to 6 kW_{el} for R245fa versus 5.6 kW_{el} for SES36. The secondary fluid side evaporator temperature glide, ΔT_{hf}, has a value of 13.5 K for R245fa and of 10.7 K for SES36. R245fa is characterized by a lower evaporating temperature, T_{eva}, than SES36, leading to an higher amount of recovered thermal energy and lower first law efficiency compared to SES36. As shown in figure 2.8a for an evaporating pressure of 8.9 bar the SES36 evaporating temperature is 115.2°C which leads to a superheating of only 4 K. In the case of R245fa, for an evaporating pressure of 12

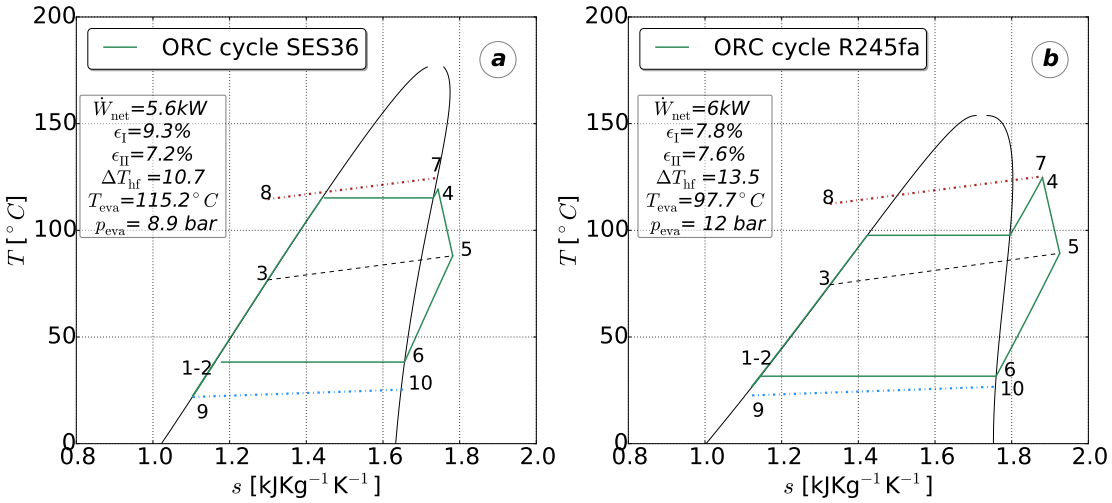

Figure 2.8 – Temperature entropy diagram for for SES36 (a) and R245fa (b). The heat source mass flow is set to 3.1 kgs^{-1} with an evaporator inlet temperature of 125 °C (point 7). The heat sink is set at a condenser inlet temperature of around 22°C (point 9). ΔT_{hf}: heat source temperature gradient in the evaporator(from point 7 to point 8).

bar corresponds an evaporating temperature of around 98°C which leads to a superheating of around 27 K. To produce more power in both cycles it would be necessary to increase the mass flow rate circulating in the system by increasing the pump speed. This would also cause an increase of evaporating pressure/temperature. In the case of SES36, due to the already quite high value of the evaporating temperature, such an action would lead to a two-phase condition at the inlet of the expander which can not be sustained. In other words for the given heat source condition the SES36 cycle is operating at a point close to its optimum. On the

other hand, in the case of R245fa, given the high value of superheating, there is still room for improvement of the cycle performance by increasing the evaporating temperature. During the experimental campaign, it was not possible to proceed in this direction because of the technical characteristic of the pump that limited the maximum operating pressure to around 12 bar. This analysis experimentally demonstrates that for the given test-rig R245fa represents a better choice compared to SES36 for waste heat recovery of a low temperature thermal energy source. The second law efficiency results slightly higher for R245fa than for SES36 for a given ΔT and expander rotational speed. A maximum net output power value of 5.94 kW_{el} is achieved with R245fa at a ΔT of 66 K and an expander rotational speed of 3000 rpm. A slightly smaller value of 5.8 kW_{el} is reached with SES36 for a ΔT of 80 K at 3000 rpm.

2.5 Conclusions

Small scale ORC systems can play a key role for low grade waste heat recovery applications. In this chapter an experimental investigation of a small capacity ORC system equipped with a single screw expander using two well-known fluids in the state of the art of ORC applications, SES36 and R245fa, has been presented. In the first part the different components are investigated. The heat exchanger performances are checked by analysing the thermal energy balance over each of them. Condensation is found to start in the recuperator vapour side for both fluids. An uncertainty propagation study is performed on the heat exchangers thermal energy balance. Thermal energy transfer to the ambient may explain the evaporator unbalance. In light of the experimental data analysis the following conclusions are drawn:

- The experimental analysis leads to identify the presence of non-condensable gases as the cause of the high level of sub-cooling measured for the SES36 tests, due to the sub-atmospheric value of the SES36 condensing pressure. This result is strengthened by the low value of sub-cooling measured for R245fa which is characterized by a super-atmospheric condensing pressure.

- The very low performance characterizing the pump, with a maximum isentropic efficiency of around 22% for both fluids, leads the authors to suggest that the design of pump systems for organic fluids is crucial for increasing the thermal efficiency of small ORC systems.

- The performances exhibited by the expander are in line with the data available in the literature using compressed air as working fluid. A maximum electrical isentropic efficiency of 62% is obtained for SES36 at 3000 rpm and a pressure ratio of 6.8. An electrical isentropic efficiency of 52% is registered for R245fa at 3000 rpm and a pressure ratio of 7.7. The results highlight the potential of the single screw machine as an interesting solution for small capacity ORC unit for low temperature applications.

- In terms of electrical power output the expander performance results show that R245fa allows to generate a higher power for a given rotational speed and pressure ratio, because of the higher density provided at the inlet of the expander machine with respect to SES36. A maximum power of 7.3 kW_{el} is reached with R245fa at a pressure ratio of 6.2 at 3000

rpm while a value of 7.1 kW_{el} is reached using SES36 with a pressure ratio of 8.5 at 3000 rpm. On the other hand, the expander isentropic efficiency is lower for R245fa. A possible explanation has been identified in high leakage losses due to the working pressure value approaching the maximum value allowable by the expander. Additional work produced during the discharge process when the pressure ratios is higher than the internal expansion ratio may explain the monotonically increasing trend of the expander power as a function of the pressure ratio. Additional empirical support would be needed to prove this conclusions.

- At a given ΔT_{ORC}, more power is generated with R245fa than with SES36. On the other hand, the first law efficiency is characterized by similar values for both fluids. These experimental results are in line with the study presented in [59] where it is numerically shown that the first law efficiency is a weak function of the critical temperature.

- For the same volumetric expansion machine, at a given evaporating temperature, the fluid with the lower critical temperature, R245fa, is characterized by an higher operating pressure than the fluid with an higher critical temperature, SES36. This results in an higher density for R245fa which leads to more mass flow flowing through the expander and to more power production. The fluid characterized by the lower critical temperature allows to generate more power.

  From the last two points, it follows that for low temperature waste heat recovery applications with an intermediate oil loop, an optimally designed SES36 ORC system would perform better than an R245fa one. On the other hand, the SES36 system will be characterized by bigger components (e.g. expander with higher swept volume) resulting in a more costly system compared to an R245fa one. This analysis experimentally proves that when selecting an organic fluid for the design of an ORC system, additional parameters taking into account the practical design of the system have to be considered, in particular the expansion machine characteristic as shown in [60]. Furthermore, to our best knowledge, this work is the first one to propose a fully open experimental dataset with two different working fluids on the same machine. This data opens a broad range of possibilities for further investigation, such as model calibration or validation, cycle analysis or fluid comparison.

Nomenclature

Acronyms		
WHR	=	waste heat recovery
ORC	=	organic Rankine cycle
ODP	=	ozone depletion potential
PI	=	proportional integer
APS	=	absolute pressure sensor
RTD	=	resistance temperature detectors
CFM	=	Coriolis flow meter
PP	=	pinch point
Subscripts		
su	=	supply
ex	=	exit
hf	=	hot fluid
cf	=	cold fluid
lo	=	lubricant oil
s	=	isentropic
sc	=	sub-cooled
sh	=	super-heated
eva	=	evaporator
exp	=	expander
rec	=	recuperator
pu	=	pump
cd	=	condenser
el	=	electrical
LP	=	low pressure
HP	=	high pressure
r	=	reduced
l	=	liquid
v	=	vapour

Symbols

α	=	mass fraction (-)
p	=	pressure (bar)
T	=	temperature (°C)
r_V	=	volume ratio (-)
r_p	=	pressure ratio (-)
h	=	specific enthalpy (kJ kg^{-1})
$\dot{Q}$	=	thermal power (kW)
$\dot{W}$	=	electrical power (kW)
$\dot{m}$	=	mass flow (kg s^{-1})
c_p	=	specific heat capacity (kJ kg^{-1} K^{-1})
$\dot{E}x$	=	exergy flow (kW)
ε	=	efficiency
Δ	=	difference

3 Plate Heat Exchanger Performance Investigation

Abstract In this chapter the results of an experimental campaign to characterize vaporization heat transfer and pressure drop of low critical temperature organic fluids is presented. The two tested fluids are HFC-245fa and HFO-1233zd. The experiments were carried out at saturation temperature of 100, 115 and 130 °C and inlet and outlet qualities ranging between 0.1-0.4 and 0.6-1 respectively. In the first part of the chapter the fundamentals about two-phase heat transfer and pressure drop in brazed plate heat exchangers are briefly addressed. It follows a description of the experimental facility and the results obtained during the experimental campaign. In the last part the experimental heat transfer coefficients and frictional pressure drop are compared with well-known correlations and new correlations for frictional pressure drop and two-phase heat transfer coefficients are proposed.

3.1 Introduction

Small capacity ORC systems are often equipped with brazed plate heat exchangers (BPHX) which allows for efficient heat transfer with a compact design. In an ORC power system, the evaporator heat transfer performance is a key aspect in defining the system overall efficiency. As it operates at the highest cycle temperature, far from the ambient conditions, ensuring an effective evaporating heat transfer allows reducing the entropy production leading to higher expander inlet temperature and thus better cycle efficiency.

In a small scale ORC systems, the brazed-plate evaporator is typically a once-through heat exchanger covering the phase transition and the adjacent single phase regimes. Thus when modelling the evaporator component the liquid, two-phase and vapour domains need to be taken into account. The single phase heat transfer coefficient inside BPHX has been extensively study over the last decade. The correlations derived by Muley and Manglik [30] and by Martin [61] have been validated by different studies and are recommended for modelling single phase heat transfer phenomena for non-conventional organic fluids. However, most of the thermal energy is transferred in two-phase. Thus validated evaporation heat transfer correlations for ORC systems are necessary from the early design stage to the development and testing of efficient model-based control strategies.

Despite the broad use of BPHXs for small ORC systems, the available literature covering the performance of these devices at the typical evaporating working temperatures of ORC power

units for low quality waste heat recovery (WHR) is scarce. Most of the literature reporting heat transfer characteristics for plate heat exchangers with non-conventional fluids are related to the refrigeration field where the vaporization conditions are far away from the ones characterizing ORC power units. Longo et al. [32] presented experimental data for HFC-134a, 410a and 236fa vaporization inside BPHX at typical evaporation temperature for traditional heat pump applications. To the author's knowledge the only published work investigating the heat transfer performance of fluids for ORC systems is focusing on supercritical architectures and does not provide experimental data [62]. At the present time there is a lack of experimental data assessing the evaporation performance of low critical temperature non-conventional fluids inside BPHXs for ORC systems.
This led to the effort partially documented in this chapter: a first step towards an experimental database comprising experimental data of low critical temperature non-conventional fluids vaporization at typical evaporating conditions for ORC power systems. In particular the heat transfer and pressure drop performance during evaporation in small brazed plate heat exchanger of two low critical temperature organic fluids HFC-245fa and HFO-1233zd are investigated. The first one is a well-known hydrofluorocarbon used in the majority of the recently introduced small capacity low temperature ORC systems [63], the latter is a hydrofluroolefin which has been lately brought to the market as a low GWP alternative to HFC-245fa [64]. The experimental data was collected on a test-rig equipped with seven BPHXs that has been recently built at the Mechanical Engineering Department of the Technical University of Denmark (DTU). The facility allows running experimental tests to characterize the thermal phenomena driving the vaporization and condensation of non-conventional low critical temperature fluids in the working conditions characterizing high temperature heat pumps and low temperature ORC systems. Preliminary experimental results with HFC-134a as working fluids are presented in [65]. More detailed experimental data covering the vaporization of HFC-134a, HFO-1234yf and HFO-1234ze are presented in [66].

3.2 Geometry specifications

Brazed plate heat exchanger is a device used to transfer thermal energy between two media by an indirect method: thermal energy is transferred from one medium through a partition to the second medium. BPHX is composed by a pack of stainless-steel plates stacked in a frame. The number of plates contained in the frame varies depending on the BPHX size. Supporting points on the plate design narrow channels among the plates. The media enter and leave the channels through holes at the corner of the plates. Open and blind holes define the route of the fluids through the different channels. An exploded view of a brazed plate heat exchanger is shown in figure 3.1.
The plates are corrugated in pattern designed in order to enhance the heat transfer mechanism. Over the years many patterns have been proposed and tested, and the herringbone or Chevron pattern proved to be the most efficient in terms of heat transfer and mechanical strength and nowadays it is the predominant choice [67].
In Figure 3.2, a schematic representation of a plate heat exchangers with the relative geometric characteristics is reported. The inclination of the corrugation pattern is denoted with ϕ and it

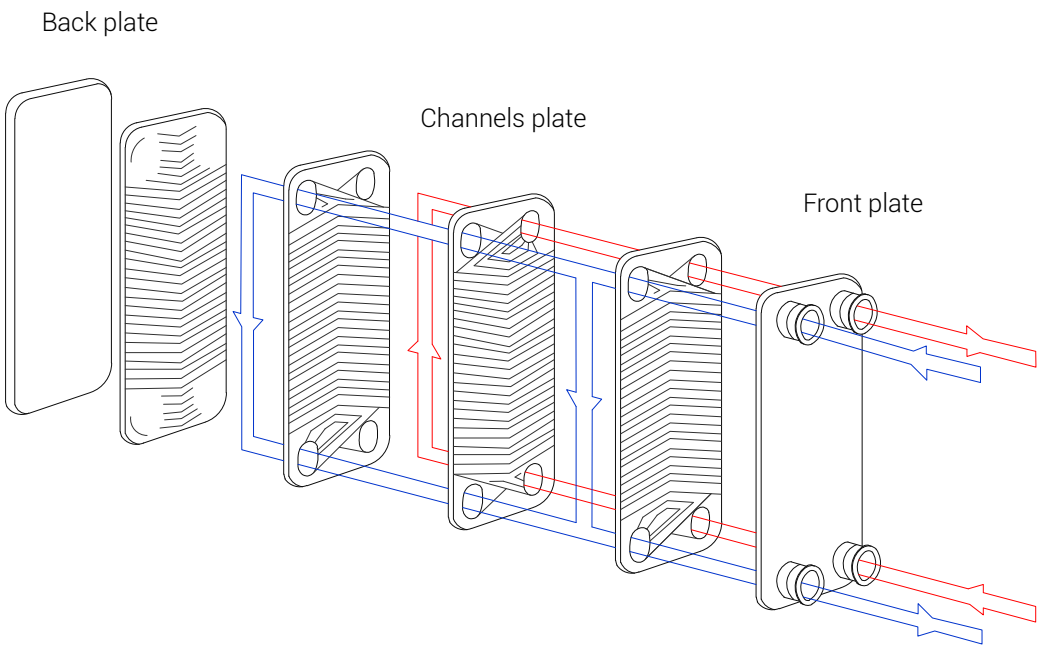

Figure 3.1 – Schematic exploded view diagram of a brazed plate heat exchanger.

changes from 0° for corrugation parallel to the flow direction to 90° for corrugation normal to the flow direction. Typical ϕ values are in the range of 40° to 70°.
The Chevron corrugation pattern is defined by two geometric characteristics, the amplitude of the sinusoidal corrugation denoted with $\hat{a}$, and the phase or wavelength denoted with Λ.
Other important geometric characteristics of BPHX which are used in the computation of heat transfer correlations are:

- l_p the thickness of the plate.
- $X = \frac{2\cdot\pi\cdot\hat{a}}{\Lambda}$ the dimensionless corrugation parameter or wave number
- $\Phi \approx (1+\sqrt{1+X^2}+4\cdot\sqrt{1+X^2/2})/6$, the surface enhancement factor defined as the ratio between the real surface area with respect to the projected area (Typical values are 1.22).
- L_p the vertical length of the plate measured between the center of the upper and lower port holes.
- L_{tot} the total vertical length of the plate.
- B_p the total width of the plate.

The characteristic linear dimension used in the formulations of several non dimensional number (e.g. Reynolds) is defined either as the hydraulic diameter, d_h, or the equivalent diameter, d_e, computed as reported in equation 3.1.

$$d_h = \frac{4\hat{a}}{\Phi} \qquad d_e = 4\hat{a} \tag{3.1}$$

In this work the hydraulic diameter is used throughout the reduction process of the acquired experimental data.

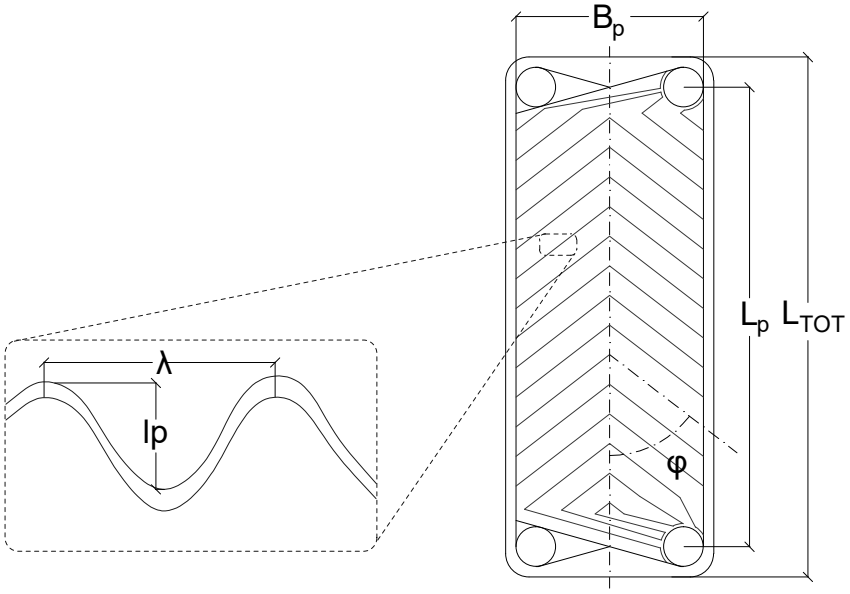

Figure 3.2 – Schematic view of the plate with the relative geometric characteristics.

3.3 Vaporization heat transfer and pressure drop models

3.3.1 Heat transfer coefficient

Before addressing the different mechanisms driving the two-phase heat transfer phenomena in a plate heat exchanger the terms *vaporization*, *evaporation* and *boiling* are defined. The first one comprises any process that leads to liquid-vapour transition due to heat addition. The last two are specific types of the vaporization process. *Boiling* refers to the creation of vapour bubbles at the heated wall. *Evaporation* occurs when the liquid vaporizes at the liquid-vapour interfaces within the flowing fluid. For natural convective condition the vaporization heat transfer is mainly governed by the temperature difference between the fluid and the solid, the fluid physical properties and the wall roughness.
Vaporization of a fluid which is flowing through a channel is called internal forced convection vaporization. In this condition flow is due to a direct motion of the fluid and to the buoyancy effects. Formation of vapour bubbles is strongly related to the fluid velocity. A variety of two-phase patterns characterize this phenomenon: bubbly flow, plug flow, stratified flow, wavy flow, slug flow, annular flow, droplet flow. In corrugated channels, annular flow pattern is expected to dominate [68]. Such a pattern is characterized by a gas core with a film of fluid in liquid state on the wall and allows reaching an high heat transfer coefficient.
It is generally accepted by the scientific community that two fundamental mechanisms drive the overall two-phase thermal energy transfer :

1. Convective heat transfer (α_{cb}): thermal energy transfer occurs due to the bulk fluid motion and the random motion of fluid molecules (conduction or diffusion). The same phenomenon that characterize heat transfer in single-phase systems.

2. Nucleate heat transfer (α_{nb}): thermal energy transfer occurs due to the creation of vapour bubbles. The creation of vapour bubbles tends to increase the thermal energy transferred which in turns suppress the nucleation.

In the nucleate regime the heat transfer coefficient is dependent on the heat flux but almost independent of quality and typically the liquid velocity tends to suppress this phenomena. In the convective regime the heat transfer is dependent on quality and mass flow but almost independent on heat flux.
Depending if convective or nucleate boiling are predominant the vaporization mechanism is referred to as convective evaporation or nucleate pool boiling respectively. If both phenomena occur simultaneously the heat transfer is described as convective evaporation.
To estimate the heat transfer coefficients during forced convection vaporization, three different models have been proposed in the past, namely the superposition, the asymptotic and the enhancement approaches [69]. The superposition, originally proposed by Chen [70], assumes that the two phase heat transfer coefficient results from the sum of the nucleate and the convective evaporation terms as:

$$\alpha_{tp} = (S \cdot \alpha_{nb} + F \cdot \alpha_{cb}) \tag{3.2}$$

where the S factor accounts for the suppression of nucleate boiling effects and the F factor accounts for the enhancement of the convection term due to higher velocity of the vapour flow with respect to the liquid.
The asymptotic model is an extension of the superposition approach where an exponent, n>1, is added to the nucleate and convective terms, it was firstly introduced by Kutateladze [71] and it assumes the form of:

$$\alpha_{tp} = (\alpha_{nb}^{n} + \alpha_{cb}^{n})^{1/n} \tag{3.3}$$

The enhancement method, initially proposed by Shah [72], considers the two-phase heat transfer coefficient as a function of the single phase heat transfer coefficient multiplied by an 'enhancement factor' which is a function of the boiling, Bo, and convection number, Co. These methods were originally proposed to describe in tube two-phase heat transfer phenomena but have been employed for BPHX by applying different single phase correlations and new empirical constants.
Thonon et al. [68] proposed a method to identify the transaction between the two boiling regimes and suggested that the nucleate phenomenon is expected to dominate the evaporation heat transfer at high pressures in brazed plate heat exchangers. The experiments performed by Palm et al. [31] with HFC-134a and by Longo [33] with isobutane, propane and propylene supported this assumption.

3.3.2 Frictional pressure drop

Three main models are presented in the literature to describe frictional pressure drop during fluid vaporization inside a corrugated channel.
To characterize the significant increase of the pressure drop due to two-phase flow the Chisholm correlation can be used [73]. The equation correlates the friction pressure gradient to the Lockhart-Martinelli parameter, X_{tt}, as follows:

$$\Delta p_{f,tp} = \phi_l^2 \cdot \Delta p_{tp} \tag{3.4}$$

$$\phi_l^2 = 1 + \frac{C}{X_{\mathrm{tt}}} + \frac{1}{X_{\mathrm{tt}}^2} \tag{3.5}$$

$$X_{tt} = \left(\frac{(1-x_m)}{x_m}\right)^{0.9} \cdot \left(\frac{\rho_v}{\rho_l}\right)^{0.5} \cdot \left(\frac{\mu_l}{\mu_v}\right)^{0.1} \tag{3.6}$$

where C is an experimental parameter that is mainly influenced by the flow regime. The second model is based on the calculation of a two-phase Fanning friction factor, f_{tp}, as:

$$\Delta p_{f,tp} = \frac{2 \cdot f_{tp} \cdot G^2 \cdot L_p}{d_h \cdot \rho_m} \tag{3.7}$$

The third one, introduced by [74], is based on the kinetic energy per unit of volume as follows:

$$\Delta p_{f,tp} = \Gamma \cdot \frac{G^2}{2 \cdot \rho_m} \tag{3.8}$$

where Γ is a parameter evaluated experimentally, and ρ_m is the average two-phase density between evaporator inlet and outlet. Assuming homogeneous flow it is calculated as:

$$\rho_m = \left(\frac{x_m}{\rho_{\mathrm{v}}} + \frac{1-x_m}{\rho_{\mathrm{l}}}\right)^{-1} \tag{3.9}$$

where x_m is the average quality in the evaporator.

3.3.3 Review of selected prediction methods

A variety of correlations for two-phase heat transfer coefficient and frictional pressure drop have been derived over the years. In what follows a description of the prediction methods selected for comparison with the experimental data collected in this study are reported. These correlations will be used later in section 3.6.
As far as two-phase heat transfer prediction methods are concerned, the Gungor-Winterton superposition method [75] is selected for further analysis as it is based on a large database of refrigerants and organic fluids experimental data. In their study they found that the Shah enhancement-based model [72] produced the second best results besides their own formulation. For this reason the Shah correlation is also chosen for comparison. As nucleate boiling is expected to dominate the evaporation heat transfer at high pressure [68], the Cooper [76] and the Gorenflo equation [77] are also selected. Developed for nucleate pool boiling inside a pipe, the two equations were recently validated for refrigerant vaporization inside BPHXs at

low evaporating temperature by Palm et al. [31] and Longo et al. [32]. In recent years several correlations based on two-phase vaporization experiments with plate heat exchangers have been derived. Among those the Han [78] and Amalfi [79] correlations have been selected. The former is largely used in the refrigeration field as it was one of the first to account for the effects of the plate geometry [80]. The latter is derived with a dimensional analysis coupled with a multiple regression approach (DACMR) on a large number of published experimental data from thirteen sources related to vaporization of refrigerants in plate heat exchangers.
As far as two-phase frictional pressure drop is concerned, four correlations based on the Fanning friction factor model are selected for comparison against the experimental results. The Ayub correlation [67] derived from experimental data from a variety of commercial plate heat exchangers in operation between 1992 and 2001 with HFC-22 and ammonia as working fluid is selected. The Amalfi [81] correlation based on a large database of experimental data including different refrigerants is chosen. Amalfi [81] compared different two-phase friction pressure drop correlations against a large database and found that the Khan [82] correlation gave the second best results. For this reason this correlation is also selected. Finally the recently developed Vakili-Farahani [83] correlation valid for HFC-245fa at low evaporating temperature is chosen.
The characteristics of the selected correlations for heat transfer coefficient and frictional pressure drop prediction are summarized in Table 3.2 and 3.1.

Table 3.1 – Summary of models for two-phase friction pressure drop.

Investigators	Year	Geometry	Fluids	Characteristics
Ayub [67]	2003	PHX	Ammonia,HFC-22	β=30-65°,T_{sat} = -35 to 5°C
Khan et al. [82]	2012	PHX	Ammonia	β=60°, d_h=3.9 mm, T_{sat}=-2 to -25°C, $\dot{q}$= 21 to 44 kW m^{-2}
Vakili-Farahani [83]	2014	PHX	HFC-245fa	β=65°,T_{sat} = 19 to 35°C, x=0.05-0.8, G=10-40 kg m^{-2} s^{-1}
Amalfi et al. [79]	2015	PHX	Refrigerants, Water, Ammonia	Refrigerants: T_{sat} = -3 to 35°C, Water: T_{sat} = 20 to 105°C, 1501 experimental data from 13 studies

Table 3.2 – Summary of models for vaporization heat transfer coefficient.

Investigators	Year	Geometry	Fluids	Characteristics
Shah [72]	1982	Pipe	Water,R-11,R-12,R-113,Cyclohexane	Enhancement method;x=0.1-1;d=2.9-64.5 mm
Cooper [76]	1984	Pipe	Water	Nucleate boiling, 250 points from 5 sources, p = 0.25-71 bar, d=5-32 mm $\dot{q}$=0.3-15 kWm^{-2}
Gungor-Winterton [75]	1986	Pipe	Water,Refrigerants,Ethylene-Glycol	Superposition, 3693 saturated boiling data from 29 studies
Gorenflo [77]	1988	Pipe	Refrigerants, Cryogenics, Hydrocarbon	Nucleate pool boiling
Han et al. [78]	2003	PHX	HFC-410A,HFC-22	Homogeneous flow model, β=45°-55°-70°,T_{sat}=5-10-15°C
Amalfi et al. [79]	2015	PHX	Refrigerants, Water, Ammonia	DACMR method; 1930 experimental data from 13 studies

3.4 Experimental facility

The process flow diagram and the front view of the heat exchanger (HX) test-rig are shown in Figure 3.3 and 3.4 respectively. The experimental rig comprises three loops: the working fluid, the cooling and the heating loop. Six brazed plate heat exchangers connected in series are installed in the working fluid loop. A seventh BPHX, HX-G, is installed on the set up between the heating and the cooling loop. The heat exchanger was used to derive the heat transfer coefficients of the heat transfer fluid employed in the heating loop through Wilson-plot [84] based experiments as explained in section 3.5.

The cooling and heating circuits are closed loops where water and thermal oil Texatherm 22 (TX22) [85] are used as heat transfer fluids respectively. In the cooling loop a volumetric pump ensures a stable water flow rate which rejects the thermal energy absorbed in HX-G,-D,-E,-F to

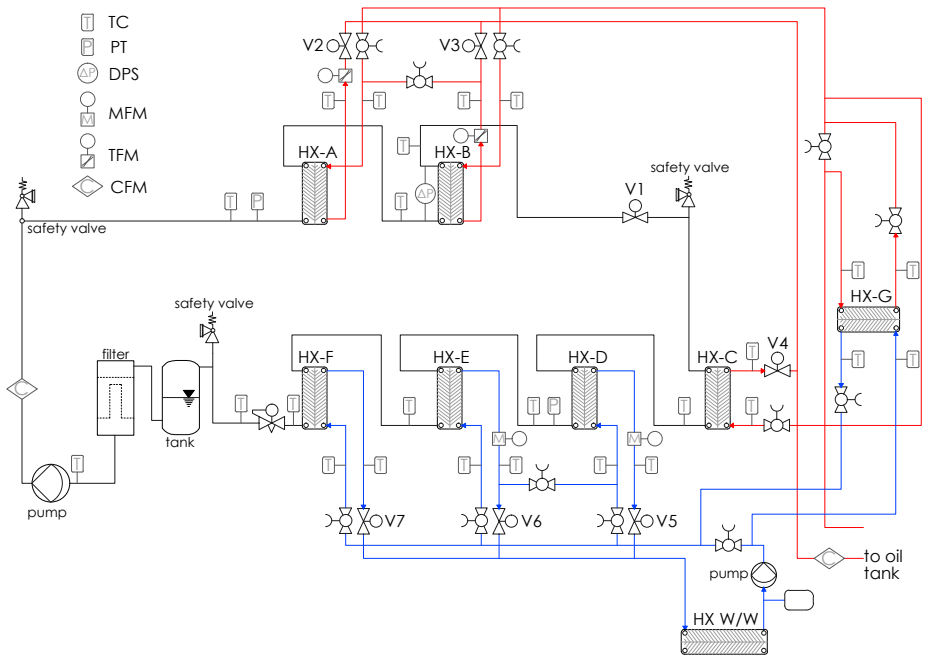

Figure 3.3 – Process flow diagram and sensor position of the HX test rig. CFM: Coriolis flow meter. TFM: turbine flow meter. MFM: Magnetic flow meter. TC: Thermocouple. PT: pressure transmitter. DPS: differential pressure sensor.

the cooling network system via the brazed plate heat exchanger HX W/W, while an expansion tank ensures a constant pressure in the circuit. Three automatic valves (V5-V6-V7) installed at the outlet of HX-D,-E and-F allow controlling the mass flow rate, while five manually controlled valves give extra flexibility to the system allowing for different loop configurations (i.e. phase out one or more HXs or set the HXs in series or parallel).
The heating loop comprises a tank where six electrical heaters supply the thermal energy to the thermal oil. A variable speed centrifugal pump circulates the oil through HX-A,-B,-C and -G. Three electronic valves (V2-V3-V4) installed at the outlet of HX-A,-B and-C allow controlling the oil mass flow rate, while six manual valves allow for different loop configurations.
Referring to the bottom left side of figure 3.3 the refrigerant was pumped from the receiver tank through the pre-heater HX-A and the evaporator HX-B where it was partially evaporated to get a defined value of vapour quality. The fluid was then flashed by the expansion valve V1 and entered the low pressure evaporator HX-C, the de-superheater HX-D, the condenser HX-E and the sub-cooler HX-F. The fluid in liquid phase was stored in the receiver tank at the outlet of HX-F. A filter placed at the pump inlet protects the machine from any solid residues present in the fluid. The variable speed volumetric pump allowed controlling the working fluid flow rate. The evaporating pressure was regulated by the expansion valve, V1, the pump speed and the temperature and mass flow of the thermal oil. In the cooling circuit, the volumetric pump was run at full speed and the mass flow was regulated acting on the automatic valves V5-V6-V7. The oil mass flow rate was regulated varying the centrifugal pump

flow rate and the automatic valves V2-V3-V4. Calibrated T-type thermocouples were used to

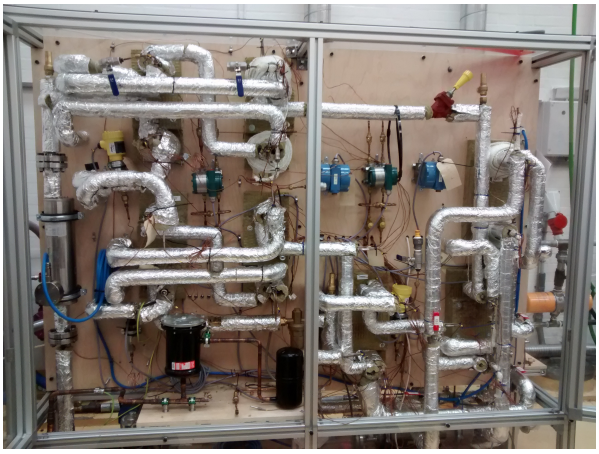

Figure 3.4 – Front view of the HX test rig.

measure the temperature of the working fluid, the cooling water and the thermal oil at the inlet and the outlet of each component. The working fluid pressure at the inlet of the pre-heater was measured by a pressure transmitter, whereas the refrigerant pressure drop through the evaporator was measured with a differential pressure sensor. The working fluid mass flow rate and density were measured at the pump outlet with a Coriolis flow meter. Two turbine volume flow meters were used to measure the oil volume flow at the outlet of HX-A and -B. A Coriolis flow meter installed on the return pipe from the test-rig to the oil tank measured the TX22 mass flow rate and density. The water volume flow rate was measured at HX-D and HX-E outlets by two magnetic volume flow meters. The uncertainty of the sensors are reported in Table 3.3. The sensors signal outputs are acquired via the National Instrument (NI) 9208

Table 3.3 – Range and precision of the measurement devices. k: coverage factor. CFM: Coriolis flow meter. TFM: turbine flow meter. MFM: magnetic flow meter. TC: thermocouple. PT: pressure transmitter. DPS: differential pressure sensor.

Variable	Device type	Model	Range	Uncertainty (k=2)
$\dot{m}_{wf}$	CFM	Siemens 2100 DI6	0-0.15 kg s^{-1}	± 0.06%
$\dot{m}_{hf}$	CFM	Siemens 2100 DI15	0-0.8 kg s^{-1}	± 0.02 %
$\dot{V}_{oil}$	TFM	GL flow - LX13	2-20 l min^{-1}	± 0.1 %
$\dot{V}_{cf}$	MFM	Yokogawa RXF015G	0-20 l min^{-1}	± 1 %
T	TC	Omega Type T	20-180 °C	± 0.19 K
p	PT	Vegabar82	1-51 bar	± 0.45 %
Δp	DPS	Yokogawa EJX110A	5-400 mbar	± 0.038%

module for current input and the NI 9214 thermocouple module. A NI cDAQ-9188XT chassis is used to pass the signal via USB connection to a laptop where LabView2013 is used for data visualization.

The uncertainty of the NI 9214 thermocouple module has been taken into account during the calibration process of the thermocouple.
The NI 9208 current input module is characterized by the following uncertainty:

$$\begin{aligned} Un_{\text{gain}} &= 0.76\% \text{ of reading} \\ Un_{\text{offset}} &= 0.04\% \text{ of range} \\ Un_{\text{NI}} &= Un_{\text{gain}} \cdot \text{reading}/100 + Un_{\text{offset}} \cdot \text{Range}/100 \end{aligned} \tag{3.10}$$

The uncertainty of the current module is taken into account using the theory of uncertainty propagation as follows:

$$Un_{\text{sensor,tot}} = \sqrt{Un_{\text{sensor}}^2 + Un_{\text{NI}}^2} \tag{3.11}$$

where, Un_{sensor}, is the uncertainty of the sensors reported in Table 3.3. Thermodynamic calculations were performed in real-time via the CoolProp-Labwiew wrapper [24].
The heat exchangers are of the brazed plate type. The pre-heater and evaporator consist of 8 and 10 plates respectively, 76 mm in width and 317 mm in length with an herringbone corrugation. The main geometrical parameters of the BPHXs are reported in Table 3.4. A summary of the characteristics of the test-rig components is reported in Table 3.5. During

Table 3.4 – Geometrical characteristics of the brazed plate used for the BPHXs.

Parameter	Symbol	Value
Total length (mm)	L_{tot}	317
Plate width (mm)	B_p	76
Port diameter (mm)	d_p	16
Plate thickness (mm)	l_{co}	0.3
Wave length (mm)	Λ	7
Corrugation depth (mm)	a_{co}	1
Corrugation type (-)		Herringbone
Corrugation angle (°)	ϕ_{co}	65
Area of the plate (m^2)	A_p	0.02329
Wall heat conduction ($W\,K^{-1}m^{-1}$)	k_{wall}	16.2

the experiments, the pre-heater, HX-A, and evaporator, HX-B, were connected in parallel on the secondary fluid side, and were fed with a varying thermal oil mass flow rate at a constant temperature. In order to bring the system in steady-state condition, in the cooling loop water was pumped to the inlet of HX-D,-E and -F with a constant mass flow rate and temperature. The system was considered in steady-state when the oscillations characterizing all the temperature readings exhibited an amplitude lower than 0.5 K for 120 seconds. Once this condition was reached, all the measures were recorded for 120 seconds and averaged over this time.

Table 3.5 – Summary of the specifications of the main heat exchanger test-rig components.

System component	Model	Specifications
HX-A,G	SWEP- B8T M pressure	Brazed plate type - 8 plates
HX-B,C,E,F	”	Brazed plate type - 10 plates
HX-D	”	Brazed plate type - 16 plates
$Pump_{wat}$	GRUNDFOS Alpha2 25-60 180	Volumetric pump 5-45 W power consumption
$Pump_{wf}$	WANNER-DG03-I E(Not sure)	Volumetric pump $p_{su,max}$ = 17 bar, 1750 rpm max

3.5 Data reduction

3.5.1 Working fluid heat transfer coefficient

In the evaporator, HX-B, the overall heat transfer coefficient U is equal to:

$$U = \frac{\dot{Q}}{A_{HX}\Delta T_{ln}} \tag{3.12}$$

where the thermal power $\dot{Q}$ was calculated from the oil side of the heat exchanger as:

$$\dot{Q} = \dot{m}_{oil} \cdot c_{p,oil} \cdot \Delta T_{oil} \tag{3.13}$$

The heat transfer area, A_{HX} was computed as:

$$A_{HX} = A_p \cdot n_{ch,min} \cdot 2 \tag{3.14}$$

where $n_{ch,min}$ is the minimum number of channel between the two BPHX sides and A_p is the area of one plate calculated as shown in Equation 3.15:

$$A_p = L_{tot} \cdot B_p - \pi \cdot d_p^2 \tag{3.15}$$

As the refrigerant passed through the evaporator in two-phase flow with no phase transition, the logarithmic mean temperature difference was calculated as:

$$\Delta T_{ln} = \frac{T_{oil,su} - T_{oil,ex}}{ln\left(\frac{T_{oil,su} - T_{sat}}{T_{oil,ex} - T_{sat}}\right)} \tag{3.16}$$

where T_{sat} is the refrigerant saturation temperature at the evaporating pressure $p_{HXB,su}$. The average heat transfer coefficient of the refrigerant in HX-B was then computed as:

$$\alpha_{wf} = (1/U - R_{wall} - 1/\alpha_{oil})^{-1} \tag{3.17}$$

where R_{wall} is the metal wall thermal resistance defined as the ratio of the plate thickness, l_p, to the metal thermal conductivity, k_{wall}, computed at the wall average temperature $T_{wall,m}$ defined as:

$$T_{wall,m} = \frac{T_{oil,su} + T_{oil,ex} + T_{wf,su} + T_{wf,ex}}{4} \tag{3.18}$$

The working fluid vapour quality at the inlet, $x_{HXB,su}$, and outlet, $x_{HXB,ex}$, of the evaporator, HX-B, were calculated from the temperature and pressure at the inlet of the pre-heater, HX-A, adding the oil thermal power exchanged in HX-A, $\dot{Q}_{HXA,oil}$ and HX-B, $\dot{Q}_{HXB,oil}$ as follows:

$$x_{\mathrm{HXB,su}} = f(h_{\mathrm{HXB,su}}, p_{\mathrm{HXB,su}}) \tag{3.19}$$

$$h_{\mathrm{HXB,su}} = h_{\mathrm{HXA,su}} + \frac{\dot{Q}_{\mathrm{HXA,oil}}}{\dot{m}_{\mathrm{wf}}} \tag{3.20}$$

$$x_{\mathrm{HXB,ex}} = f(h_{\mathrm{HXB,ex}}, p_{\mathrm{HXB,ex}}) \tag{3.21}$$

$$h_{\mathrm{HXB,ex}} = h_{\mathrm{HXA,su}} + \frac{\dot{Q}_{\mathrm{HXB,oil}}}{\dot{m}_{\mathrm{wf}}} \tag{3.22}$$

3.5.2 Oil heat transfer coefficient by the Wilson plot method

In order to solve Equation 3.17, the oil side heat transfer coefficient, α_{oil}, is required. A specific oil to water experimental campaign was carried out on heat exchanger G to determine a correlation for the oil heat transfer coefficient applying the Wilson plot technique. The Wilson plot method allows determining the individual resistances of the heat exchanger from the overall resistance. The original method is subjected to a series of restrictions and several modified approaches have been developed to relax these limitations [84]. In this study the original Wilson plot technique (WPO) and the modified Briggs and Young method (WPBY) were employed to identify the oil heat transfer coefficient.
In a heat exchanger the overall heat transfer coefficient can be expressed as:

$$\frac{1}{U} = \frac{1}{\alpha_{\mathrm{oil}}} + \frac{t_{\mathrm{wall}}}{k_{\mathrm{wall}}} + \frac{1}{\alpha_{\mathrm{wat}}} + R_{\mathrm{f,oil}} + R_{\mathrm{f,wat}} \tag{3.23}$$

where t_{wall} and k_{wall} are the thickness and the thermal conductivity of the plates respectively, α_{wat} is the water side heat transfer coefficient and $R_{\mathrm{f,oil}}$ and $R_{\mathrm{f,wat}}$ are the oil and water fouling resistances respectively. For the original Wilson Plot, if fouling resistances, wall resistance and the heat transfer coefficient of the water side are kept constant than the resistance balance reported in equation 3.23 can be expressed as a function of the oil Reynolds number:

$$\frac{1}{U} = \frac{1}{C \cdot Re^{0.8}} + b \tag{3.24}$$

Equation 3.24 is of the linear form. The constant 1/C and so a correlation for the Nusselt number can be identified by linear regression.
The Briggs and Young method accounts for variable fluid property effects, assuming a power-

law relation between Nusselt, Reynolds and Prandtl expressed as:

$$Nu = C_0 \cdot Re_{\text{oil}}^{a} \cdot Pr^{1/3} \tag{3.25}$$

Based on equation 3.25, equation 3.23 can be reformulated as:

$$\left[\frac{1}{U} - \frac{t_{\text{wall}}}{k_{\text{wall}}}\right] \cdot \left[\text{Re}_{\text{wat}}^{a} \cdot \text{Pr}_{\text{wat}}^{1/3} \cdot k_{\text{wall}}/d_{\text{h}} (\mu_{\text{wat}}/\mu_{\text{wall,wat}})^{0.14}\right] = \frac{1}{\text{C}_{\text{oil}}} \cdot \frac{\text{Re}_{\text{wat}}^{a} \cdot \text{Pr}_{\text{wat}}^{1/3} \cdot k_{\text{wall}}/d_{\text{h}} (\mu_{\text{wat}}/\mu_{\text{wall,wat}})^{0.14}}{\text{Re}_{\text{oil}}^{a} \cdot \text{Pr}_{\text{oil}}^{1/3} \cdot k_{\text{wall}}/d_{\text{h}} (\mu_{\text{oil}}/\mu_{\text{wall,oil}})^{0.14}} + \frac{1}{\text{C}_{\text{wat}}} \tag{3.26}$$

which is of the linear form. The Reynolds, Re and Prandtl, Pr, number are defined as:

$$Re = \frac{G \cdot d_{\text{h}}}{\mu} \qquad Pr = \frac{c_p \cdot \mu}{k} \tag{3.27}$$

where μ is the dynamic viscosity and k is the thermal conductivity. An iterative linear regression on the experimental data allows to identify the coefficient $1/C_{\text{oil}}$ and the Reynolds exponent a.
In order to minimize the uncertainties of the Wilson plot results the guidelines presented in [86] were followed.

Two Wilson plot experimental tests were performed by setting two different values of the oil and water temperature at the inlet of HX-G. Steady-state experimental data were acquired for a range of thermal oil flow rates, by keeping constant the inlet temperature and mass flow rate on the water side and the inlet temperature on the oil side as described in [84]. The tests comprised 15 steady-state points each and the operating conditions are summarized in Table 3.6. During the experiments the thermal energy balance of HX-G was characterized by an

Table 3.6 – Operating conditions in the heat exchanger HX-G during the two experimental tests for Wilson plot technique.

Tests	Runs	$\dot{m}_{oil}$ [kg s^{-1}]	$T_{oil,su}$ [°C]	$T_{wat,su}$ [°C]	Re_{oil} [-]	Pr_{oil} [-]
I	15	0.061-0.119	135	20	79.5-200	76.27-96.5
II	15	0.029-0.107	125	45	30.7-173	78.91-117

error below 4.5% for all the recorded data as shown in Figure 3.5 and 3.6. The thermodynamic properties of the two fluids were determined at the average HX-G fluid temperature. The wall temperature was computed as the average between the inlet and outlet of both fluids and fouling resistances were neglected. The results for the ⟨I⟩ and ⟨II⟩ datasets are plotted in Figure 3.7 and 3.8 respectively. The regressions were performed applying a least-square error method weighted on the uncertainties of the ordinate data [87]. The co-ordinates of the

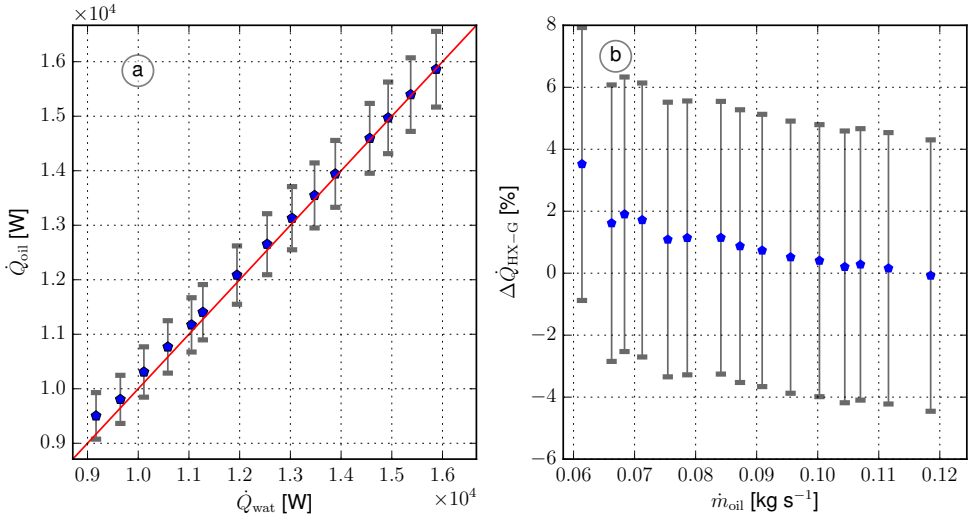

Figure 3.5 – Steady-state results for the ⟨I⟩ dataset of the HX-G experimental campaign. (a) Parity plot for the thermal energy exchanged in HX-G (b) thermal energy balance percentage error, $\Delta\dot{Q}_{HX-G}$ for each steady-state point.

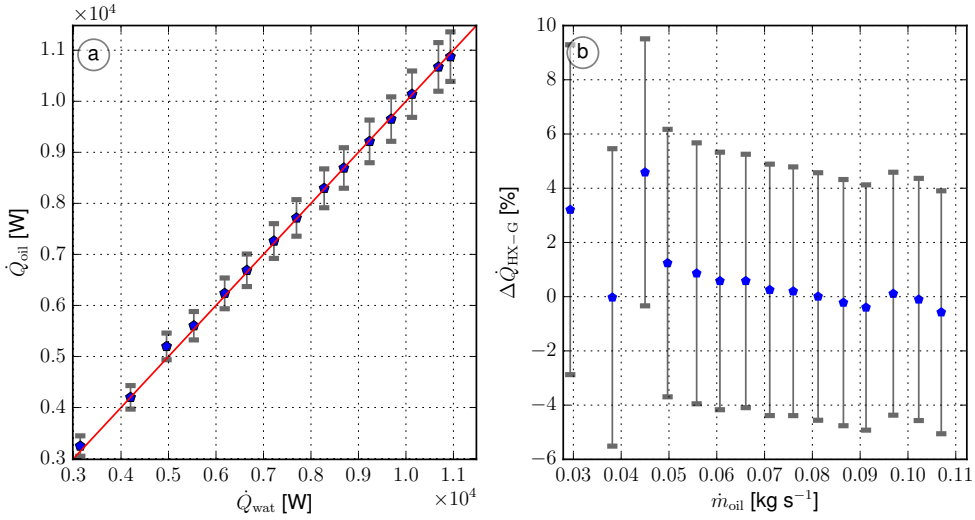

Figure 3.6 – Steady-state results for the ⟨II⟩ dataset of the HX-G experimental campaign. (a) Parity plot for the thermal energy exchanged in HX-G (b) thermal energy balance percentage error, $\Delta\dot{Q}_{HX-G}$ for each steady-state point.

modified Briggs and Young method shown in Figure 3.7b and 3.8b were defined as:

$$YY = \left[\frac{1}{U} - \frac{t_{wall}}{k_{wall}}\right] \cdot \left[\mathrm{Re}_{wat}^{0.8} \cdot \mathrm{Pr}_{wat}^{1/3} \cdot k_{wat}/d_h (\mu_{wat}/\mu_{wall,wat})^{0.14}\right] \tag{3.28}$$

$$XX = \frac{\mathrm{Re}_{wat}^{0.8} \cdot \mathrm{Pr}_{wat}^{1/3} \cdot k_{wat}/d_h (\mu_{wat}/\mu_{wat,wall})^{0.14}}{\mathrm{Re}_{oil}^{0.8} \cdot \mathrm{Pr}_{oil}^{1/3} \cdot k_{oil}/d_h (\mu_{oil}/\mu_{wall,oil})^{0.14}} \tag{3.29}$$

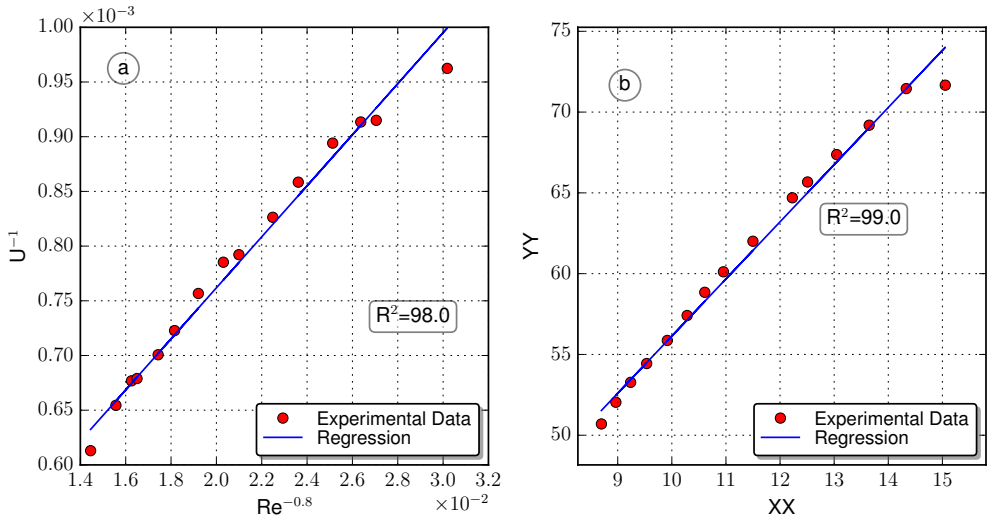

Figure 3.7 – (a) Original Wilson plot (WPO) and (b) modified Briggs and Young Wilson plot (WPBY) results for the ⟨I⟩ dataset of the HX-G experimental campaign. R^2: Coefficient of determination.

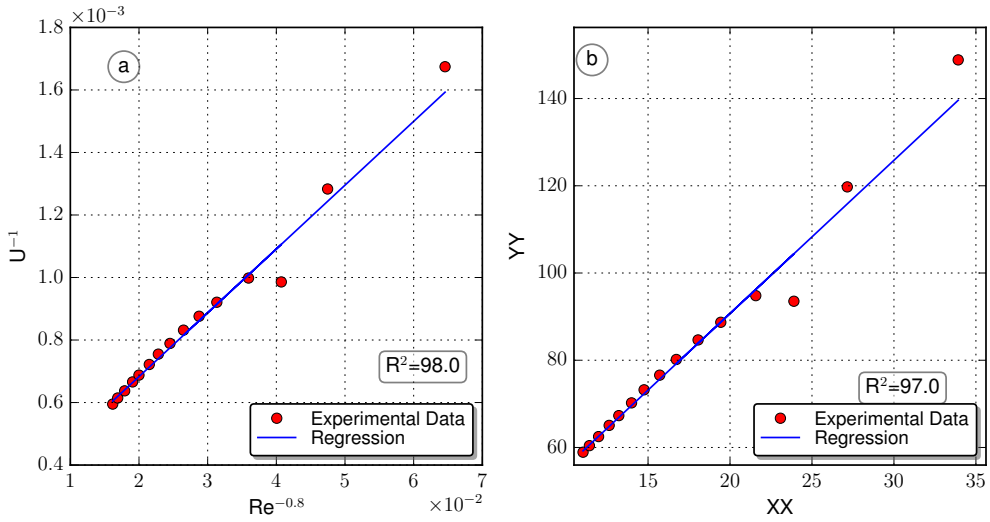

Figure 3.8 – (a) Original Wilson plot (WPO) and (b) modified Briggs and Young Wilson plot (WPBY) results for the ⟨I⟩ dataset of the HX-G experimental campaign. R^2: Coefficient of determination.

where the oil and water Reynolds exponent resulted from an iterative process as reported in [84]. The slopes of the linear regressions shown in figure 3.7-3.8 are the constant of the power law-type calibration correlations defining the oil Nusselt number. The coefficients of the four derived calibration equations are reported in Table 3.7.

Table 3.7 – Constants values for the original Wilson plot (WPO) and the modified Briggs and Young Wilson plot (WPBY).

Tests	$Nu_{\mathrm{WPO}} = C_0 Re^a$ (3.30)	$Nu_{\mathrm{WPBY}} = C_{oil} Re^a Pr^{1/3} \left(\frac{\mu_{\mathrm{oil}}}{\mu_{\mathrm{wall,oil}}}\right)^{0.14}$ (3.31)
I	$C_0 = 1.13 \pm 0.08$ a=0.8	$C_0 = 0.283 \pm 0.028$ a=0.8
II	$C_0 = 1.29 \pm 0.05$ a=0.8	$C_0 = 0.285 \pm 0.014$ a=0.8

The Wilson plot-based oil Nusselt equations are plotted in Figure 3.9 against the oil Reynolds number together with existing correlations available in the literature for the ⟨II⟩ experimental dataset. For a given oil Reynolds number the Wilson plot-based equations exhibited Nusselt values which were up to two times higher than the one predicted with existing correlations. This can be explained by the fact that the tested single phase correlations were mainly derived from experiments employing water, a fluid characterized by thermophysical properties which significantly differ from the ones of a thermal oil specifically synthesized to have enhanced heat transfer features. As it possible to see in Figure 3.9 the WPO and the WPBY correlations

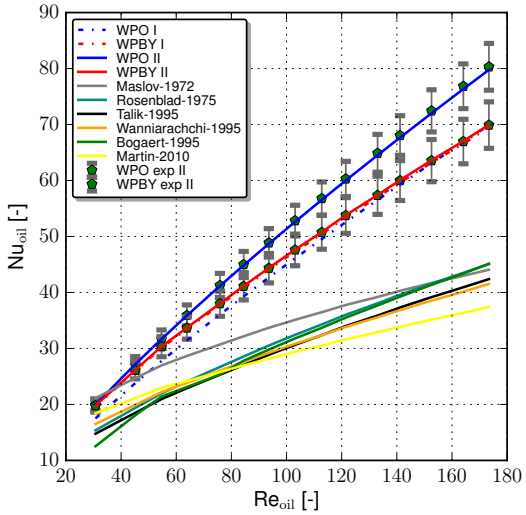

Figure 3.9 – Comparison between the developed Oil Nusselt number equations versus Reynolds number for the developed equations and a number of existing correlation. I and II refer to the two different set of experiments. Maslov-1972 [88]; Rosenblad-1975 [89]; Talik-1955 [90, 91]; Wanniarachchi-1995 [92]; Bogaert-1995 [93]

based on the ⟨II⟩ dataset were characterized by a diverging trend. This can be explained by modest changes of fluid properties during the tests which are not taken into account in equation 3.30. As WPBY method allowed to relax this limitation, the correlation derived from

the Briggs and Young approach was selected for predicting the oil Nusselt number. The final calibrated equation is expressed as:

$$Nu = 0.283 \cdot Re_{\text{oil}}^{0.8} \cdot Pr_{\text{oil}}^{\frac{1}{3}} \cdot (\mu_{\text{oil}}/\mu_{\text{wall,oil}})^{0.14} \qquad 31.6 < Re < 205 \ \Lambda \ 76 < Pr < 117 \tag{3.32}$$

It is worth mentioning that the validity of Equation 3.32 is restricted to the specific test facility over the reported range of Reynolds and Prandtl number.

3.5.3 Frictional pressure drop

The frictional pressure drop during refrigerant vaporization, Δp_f, was evaluated based on the measured pressure drop subtracting the momentum, Δp_{mom}, the gravity, Δp_g, and the manifolds and port, Δp_{mp}, pressure drops following the guidelines reported in [94]. As the pipes connecting the evaporator working fluid inlet and outlet channels to the differential pressure drop sensor were characterized by different length, a term, $\Delta p_{g,conn}$, accounting for the elevation difference was considered. The frictional pressure drop equation was therefore computed as:

$$\Delta p_{f,tp} = \Delta p_{meas} - \Delta p_{mom} - \Delta p_g - \Delta p_{mp} - \Delta p_{g,conn} \tag{3.33}$$

In particular the momentum pressure drop is defined as:

$$\Delta p_{mom} = G_{\text{wf}}^2 \cdot \left(\frac{1}{\rho_{\text{tp,ex}}} - \frac{1}{\rho_{\text{to,su}}}\right) \tag{3.34}$$

where G_{wf} is the working fluid mass flux in the evaporator channels and $\rho_{\text{tp,ex/su}}$ is the two phase density at the outlet/inlet of the evaporator defined as:

$$\rho_{\text{tp,ex/su}} = \frac{x_{\text{ex/su}}}{\rho_{\text{v}}} + \frac{(1 - x_{\text{ex/su}})}{\rho_{\text{l}}}) \tag{3.35}$$

The gravity pressure drop results in:

$$\Delta p_g = \text{g} \cdot \rho_{\text{m}} \cdot L_{tot} \tag{3.36}$$

The manifolds pressure drop is estimated using the port mass flux of HX-B as:

$$\Delta p_{mp} = 1.5 \cdot \frac{G_{\text{wf,port}}^2}{2 \cdot \rho_{\text{m}}} \tag{3.37}$$

where $G_{\text{wf,port}}$ is the mass flux computed at the port cross section of HX-B. The correction due to the different elevation of the connecting lines from the evaporator to the differential pressure sensor is computed as:

$$\Delta p_{g,conn} = g \cdot L_{\text{diff}} \cdot \rho_{\text{l}} \tag{3.38}$$

where L_{diff} is the difference in meter between the two connecting lines as shown in Figure 3.10. For all the performed calculations, the refrigerant, thermal oil and water properties were

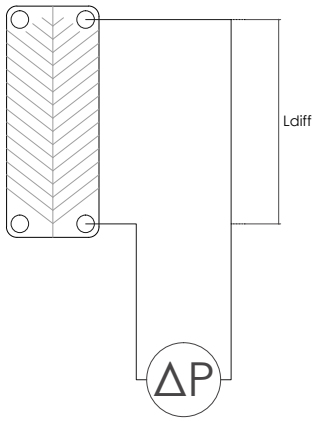

Figure 3.10 – Schematic layout of the pressure drop sensor connection to the evaporator, HX-B.

computed based on the open-source CoolProp library [24]. Incompressibility was assumed for the thermal oil model, being the fluid always in liquid phase.

3.6 Results and analysis

A set of 70 and 80 steady-state points have been collected for HFC-245fa and HFO-1233zd respectively at three different saturation temperatures (100, 115, 130 °C) with varying inlet and outlet vapour conditions and for mass flux varying between 62 and 103.5 kg.s^{-1} m^{-2}. In Table 3.8 the working conditions are reported for the two fluids. The maximum uncertainties for the main computed variables are reported in Table 3.9. The error analysis was based on [95] and indicated a maximum uncertainty of 9.5 and 6 % for the refrigerant average heat transfer coefficient and the pressure drop respectively.

Table 3.8 – Operating conditions in the evaporator HX-B during the experimental tests for HFC-245fa and HFO-1233zd.

Fluid	runs	p_{eva} [bar]	x_{su} [-]	x_{ex} [-]	G_{wf} [kg s^{-1}m^{-2}]	G_{oil} [kg s^{-1}m^{-2}]	$\dot{q}$ [kW m^{-2}]
HFC-245fa	70	12.51-23.85	0.05-0.39	0.48-1	62.8 - 103.5	72.7 - 136.6	13.2 - 36
HFO-1233zd	80	10.33-19.35	0.14-0.39	0.53-1	62.0 - 102.8	51.3 - 149.7	9 - 37

3.6.1 Heat transfer coefficient analysis

In Figures 3.11a and 3.12a, the average heat transfer coefficient, computed based on Equation 3.17, is plotted versus the average evaporator quality for HFC-R245fa and HFO-1233ZD respectively. For all the analysed conditions the heat transfer coefficients varied between a maximum of around 4500 and a minimum of around 2800 for both fluids. In the performed experiments

Table 3.9 – Maximum uncertainty of the main calculated variables for the evaporator.

Variables	Maximum uncertainty (k =2)
Geometrical parameters	
Area HX-B	± 0.0028 m^2
Heat transfer and pressure drop parameters	
Heat flux	± 3 %
Average vapour quality	± 5 %
Overall heat transfer coefficient	± 3.5 %
Refrigerant heat transfer coefficient	± 9.5 %
Pressure drop	± 6 %

the heat flux and the outlet vapour quality were coupled, i.e. in order to increase/decrease the evaporator outlet vapour quality the heat flux was increased/decreased. It was therefore not possible to clearly identify the effects of the two parameters on the heat transfer coefficient trend. As shown in figure 3.11a and 3.12a, the heat transfer coefficient values were characterized by an increasing trend as the mean vapour quality increased up to a certain value where they experienced a decrease. At low mean quality the convective and nucleate boiling phenomena are expected to co-exist, as the heat flux and so the quality increases both phenomena are enhanced and this could explain the increasing trend [96]. The decrease of the heat transfer coefficients at around x_m=0.55-0.6 could be related to local occurrence of dry-out in accordance with [97] and [98]. A weak sensitivity to saturation temperature was found in accordance with [33] for both fluids.
In Figure 3.11b and 3.12b the average heat transfer coefficients at a saturation temperature of 115 °C for different mass fluxes is plotted versus the average evaporator quality for HFC-245fa and HFO-1233zd. To an higher mass flux corresponded a slightly higher heat transfer coefficient. The increase was partly clearer for HFC-245fa than for HFO-1233zd results, but in both cases is well within the maximum uncertainty. It can be concluded that for both fluids a weak sensitivity of the heat transfer coefficients with respect to the mass flux was found. The scatter for a mass flux of 68 kg s^{-1} m^{-2} for the HFO-1233zd was related to small changes of the operating pressure.

In order to investigate the dominant heat transfer regime during vaporization the criterion proposed by Thonon et al. [68] was applied. It is based on the product of the Boiling number , B_0, and the Lockart-Martinelli parameter, X_{tt}, and it is expressed as:

$$B_0 X_{tt} > 0.15 \cdot 10e^{-3} \quad \textit{Nucleate boiling regime} \tag{3.39}$$

$$B_0 X_{tt} < 0.15 \cdot 10e^{-3} \quad \textit{Convective boiling regime} \tag{3.40}$$

where B_0 is defined as follows:

$$B_0 = \frac{\dot{q}_{HXB}}{(G_{wf} \cdot \Delta h_{vap})} \tag{3.41}$$

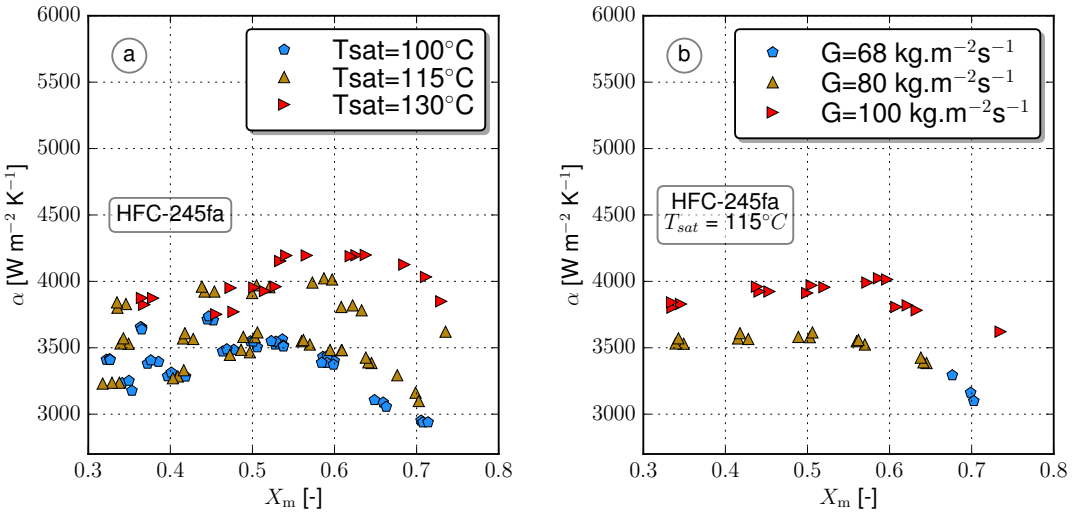

Figure 3.11 – (a) HFC-245fa average heat transfer coefficient versus mean quality (b) Mass flux dependence of HFC-245fa average heat transfer coefficient for T_{sat} = 115 °C.

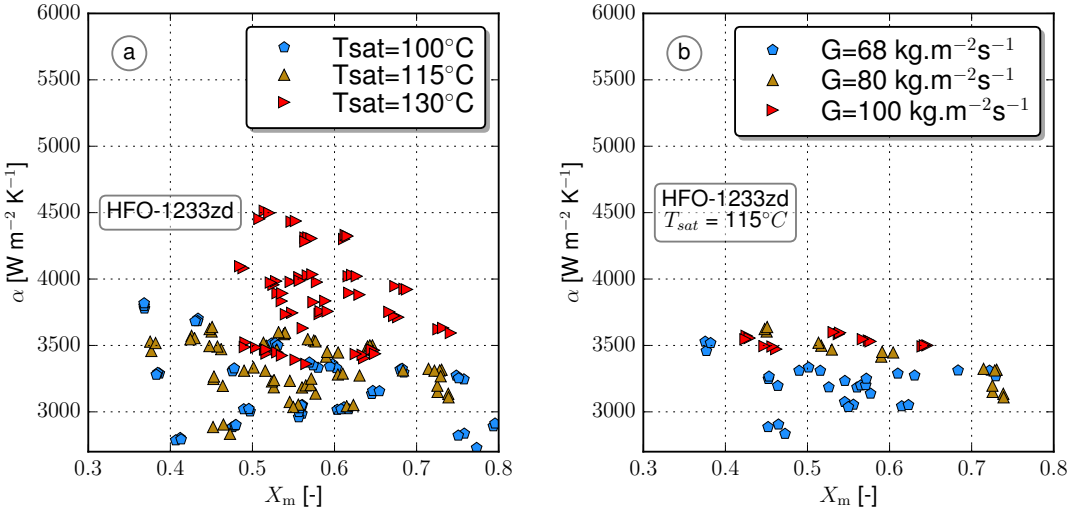

Figure 3.12 – (a) HFO-1233ZD average heat transfer coefficient versus mean quality (b) Mass flux dependence of HFO- 1233ZD average heat transfer coefficient for T_{sat} = 115 °C.

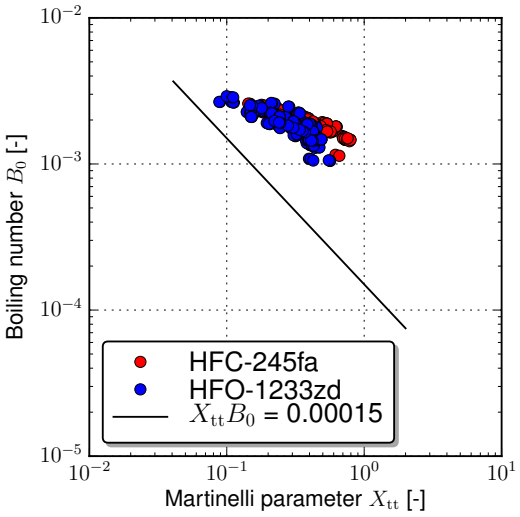

Figure 3.13 – Thonon et al. criterion [68] to investigate the heat transfer regime for R245fa and R1233ZD.

The results, reported in Figure 3.13 for both fluids, indicated the nucleate boiling as the leading phenomena for all the measured steady-state points for HFC-245fa and HFO-1233zd. These results should be taken as indicative only, as the method does not take into account the effects of heat exchanger geometrical parameters changes [68].

3.6.2 Two-phase pressure drop analysis

The frictional pressure drop values, calculated based on Equation 3.33, are plotted versus the average quality in the evaporator in Figure 3.14 for HFC-245fa and HFO-1233zd. The values were comparable for the two fluids ranging from few kPa.m^{-1} to a maximum of around 45 kPa.m^{-1}. In Figures 3.15a-b the frictional pressure drop for a mass flux of 100 kg.m^{-2} s^{-1} is plotted versus the average quality in the evaporator for the two fluids. From the Figure it is clear how the frictional pressure drop monotonically increased with the average quality in accordance with the data recorded by [98, 99] for HFC-134a. This can be explained by an increase of the vapour mass velocity as the quality rose. Furthermore, the higher the saturation temperature the lower the pressure drop. This trend resulted by the change of thermo-physical properties, density and viscosity, with respect to the saturation temperature. In particular as pressure decreases, the liquid to vapour density ratio increases leading to higher frictional losses.

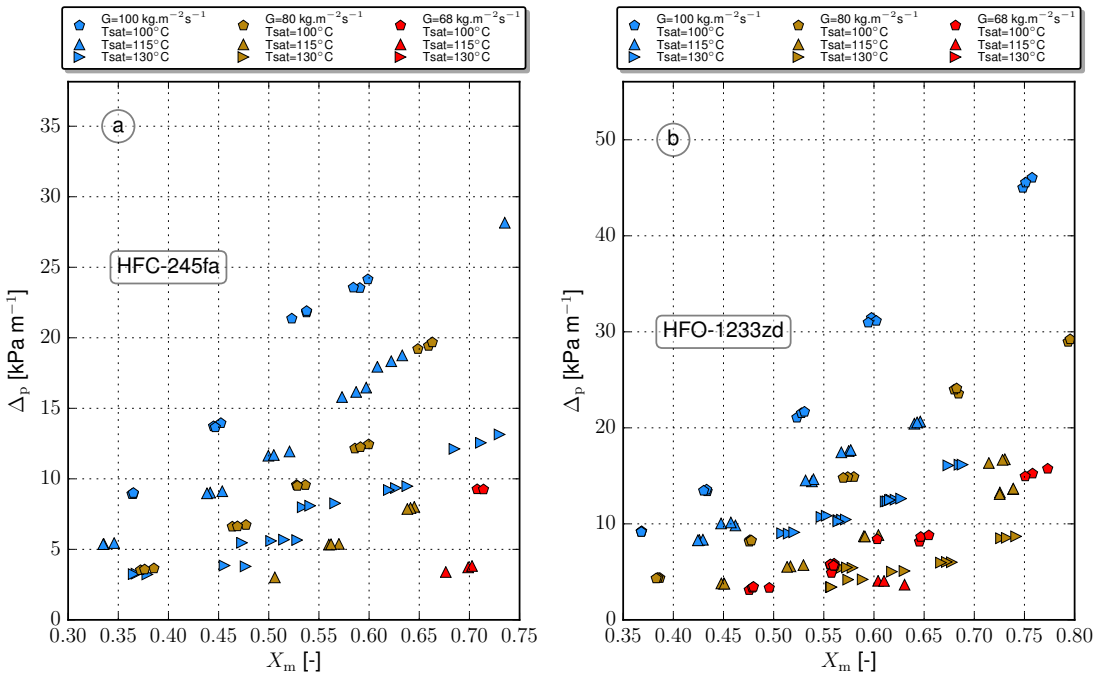

Figure 3.14 – Pressure drop for HFC-245fa and HFO-1233zd versus average quality in the evaporator for all the measured data for (a) HFC-245fa and (b) HFO-1233zd.

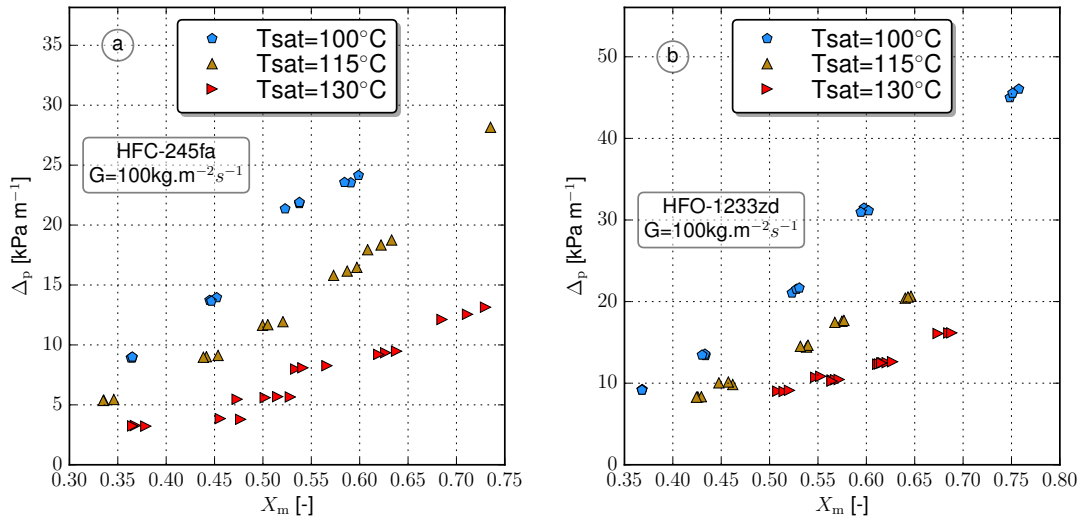

Figure 3.15 – Frictional pressure drop versus average evaporator quality for a mass flux of 100 kg m^{-2} s^{-1} for (a) HFC-245fa and (b) HFO-1233zd.

3.6.3 Comparison of prediction methods to the experimental data

In order to assess the capability of the selected correlations to predict the experimental data derived in this work, the percentage mean absolute error, θ, was computed as reported in equation 3.42.

$$\theta = \frac{1}{n} \cdot \sum_{i=1}^{n} \frac{|Y_{\text{exp,i}} - Y_{\text{pred,i}}|}{Y_{\text{exp,i}}} \tag{3.42}$$

where n is the total number of available data, and $Y_{\text{exp,i}}$ and $Y_{\text{pred,i}}$ are the i-th experimental and predicted values respectively. In Figure 3.16 the selected heat transfer coefficient prediction methods are graphically compared against the recorded experimental data. Shah [72] and Gungor-Winterton [75] correlations exhibited a trend which drastically differs with the experimental data and were characterized by a θ of around 60%. The prediction methods proposed by Han et al. [78] and Amalfi et al. [81] allowed for a slightly better forecast of the experimental data and were characterized by a θ value above 40%. It is interesting to notice how the Cooper [76] correlations was able to predict the results with a much smaller error compared to the Gorenflo correlation [77], although both have been developed for nucleate pool boiling phenomena. It is worth noticing that, despite the low mean absolute error, the trend predicted by the Cooper correlation does not match with the experimental data.
The parity plots comparing the selected frictional pressure drop prediction methods against the experimental data are reported in Figure 3.17. All the selected methods significantly over-predicted the pressure drop and presented an extremely high percentage mean absolute error. This can be explained by the much lower evaporating temperature characterizing the experimental data on which the selected methods was based. As two-phase frictional pressure drops are inversely proportional to the saturation temperature, the data measured in this study were characterized by much lower values than the ones predicted with published correlations that are mostly based on low saturation temperatures as shown in Table 3.1.

3.6.4 Two-phase heat transfer and frictional pressure drop prediction methods

Given the poor agreement of most of the tested heat transfer and frictional pressure drop correlations with respect to the experimental data, new correlations were derived.
As far as the heat transfer coefficient is concerned, a similar prediction method to the one proposed by Amalfi et al. [81] was employed. The method consists in three subsequent steps. First the independent variables affecting the heat transfer coefficient are defined as reported below:

$$\alpha = f(d_h, k_l, c_{pl}, \rho_l, \rho_v, \rho_m, u_l, u_v, u_m, (\rho_l - \rho_v) \cdot g, \mu_l, \mu_v, \dot{q}, \sigma, \Delta h_{vap}) \tag{3.43}$$

where σ is the surface tension, Δh_{vap} is the latent heat of vaporization, $u_{l/v/m}$ are the saturated liquid, vapour and mean velocity respectively and $(\rho_l - \rho_v) \cdot g$ accounts for the buoyancy force. A non dimensional analysis is then performed to express Equation 3.43 in dimensionless form.

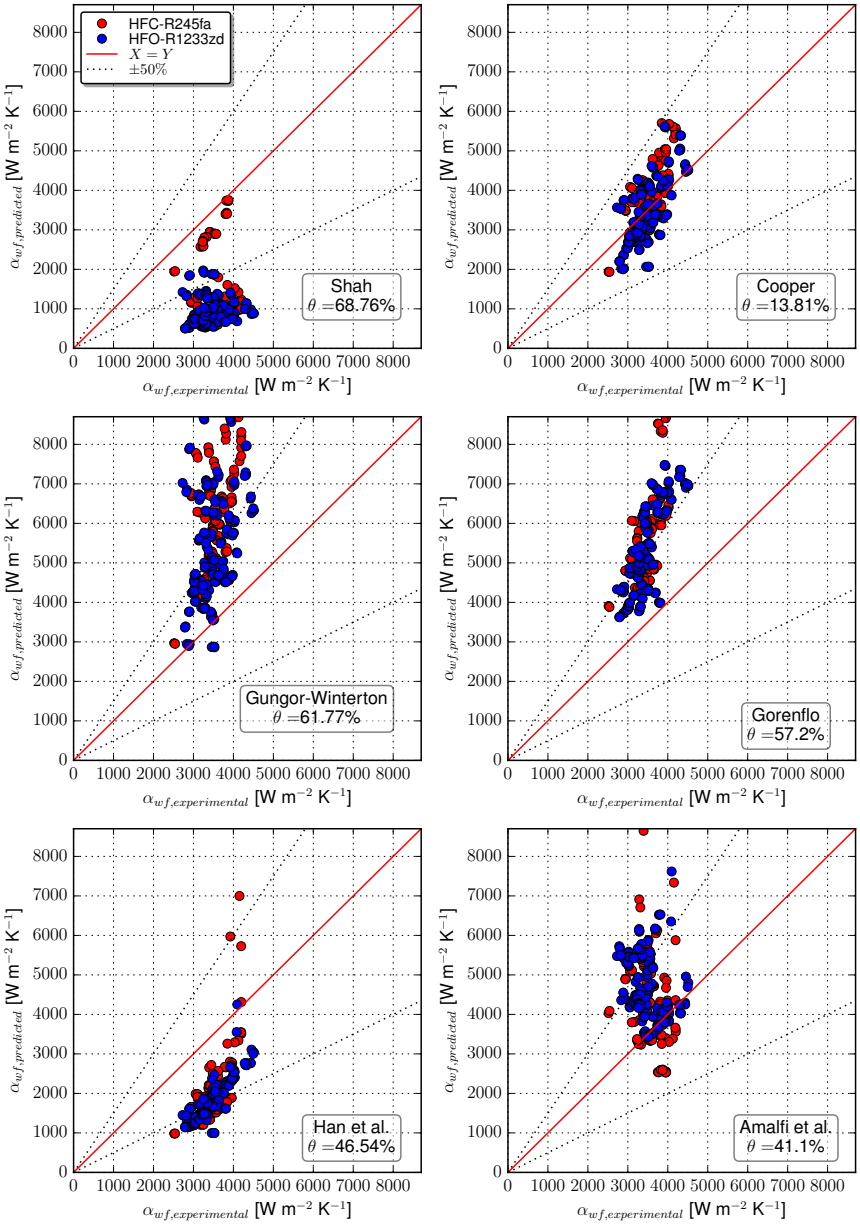

Figure 3.16 – Heat transfer coefficient parity plot between the selected prediction methods and the experimental data for HFC-245fa and HFC-1233zd. Shah [72]; Cooper [76]; Gungor-Winterton [75]; Gorenflo [77]; Han et al. [78]; Amalfi et al. [81].

By arithmetic manipulation the following non-dimentional groups are obtained:

$$\alpha = (We, Re_l, Re_v, Bo, Bd, \rho^\star) \tag{3.44}$$

$$We = \frac{G^2 \cdot d_h}{\rho_m \sigma} \tag{3.45}$$

$$Bd = \frac{(\rho_l - \rho_v) \cdot g d_h^2}{\sigma} \tag{3.46}$$

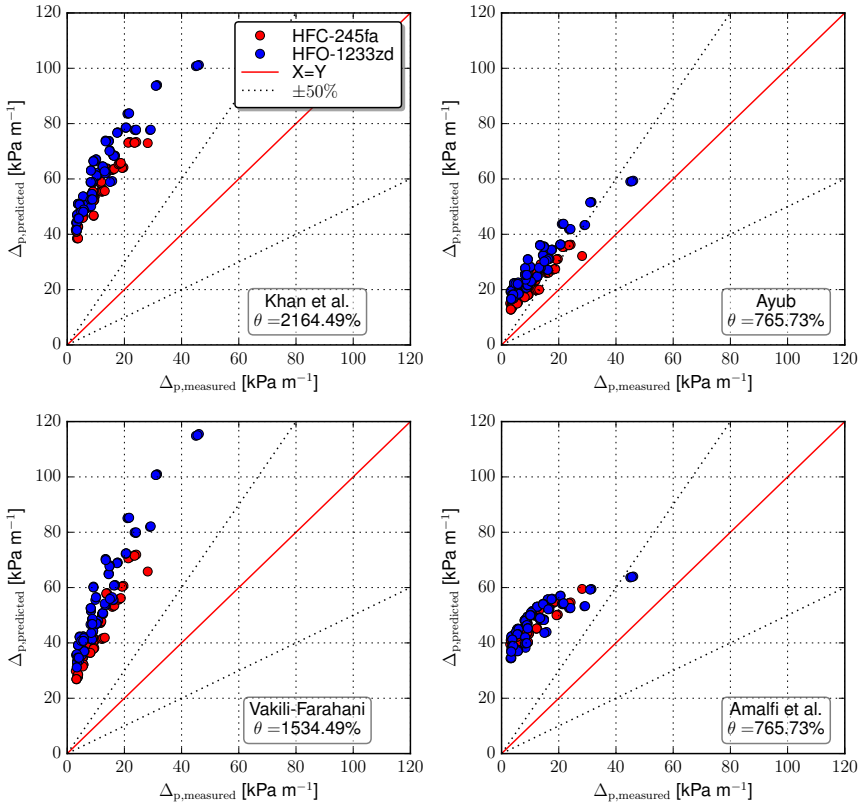

Figure 3.17 – Two-phase frictional pressure drop parity plot between the selected prediction methods and the experimental data for HFC-245fa and HFO-1233zd. Khan et al. [82]; Ayub [67]; Vakili-Farahani [83]; Amalfi et al. [81].

where $\rho^{\star}$ is the ratio between saturated liquid and vapour density, We is the Weber number which accounts for the inertia forces with respect to the tension forces, Bo is the boiling number, accounting for the effect of the heat flux, the mass flux and the latent heat, and Bd is the Bond number which characterizes the bubble behaviour in the BPHX.
Each non-dimensional group was used to fit with a power law the experimental data. Based on the fitting results, the non-dimensional groups exhibiting the lowest mean absolute error were selected and the ones adding limited gain in accuracy were discarded for the sake of conciseness and simplicity. Following this approach, the two-phase heat transfer coefficient could be predicted as follow:

$$\alpha_{\text{pred}} = 2.06e3 \cdot We^{-1.45e-2} \cdot \rho^{\star -3.62e-1} \cdot Re_l^{4.14e-1} \cdot Bd^{-4.87e-1} \tag{3.47}$$

The correlation allowed predicting the experimental data with a coefficient of determination, R^2, of 77 % and a mean absolute error $\theta = 4.21\%$ employing four non-dimentional numbers. It is graphically compared against the experimental data in Figure 3.18a. Despite the derived equation is valid only for the proposed test-rig, it is characterized by a simple layout and can

be easily coded in a software for simulation purposes.
As far as frictional pressure drops are concerned, a different approach was employed. Friction pressure drop can be considered mainly dependent on the laminar and turbulent phenomena of the flow rate. These can be mathematically identified as:

$$\Delta p_{laminar} = k \cdot \dot{V} \quad \Delta p_{turbulent} = \frac{1}{A^2} \cdot \frac{\dot{m}^2}{2 \cdot \rho_m} \tag{3.48}$$

As the working fluid flow regime was turbulent over the performed experiments only $\Delta p_{turbulent}$ was considered. The parameter A was identified by linear regression and the results are graphically compared against the experimental data in figure 3.18b. The correlation was characterized by a coefficient of determination, R^2, of 72 % and a mean absolute error $\theta = 30\%$, which can be considered satisfactory for modelling purposes. The obtained frictional pressure drop correlation is reported in equation 3.49.

$$\Delta p_{\mathrm{f,tp}} = 3.38e8 \cdot \frac{\dot{m}^2}{2 \cdot \rho_m} \tag{3.49}$$

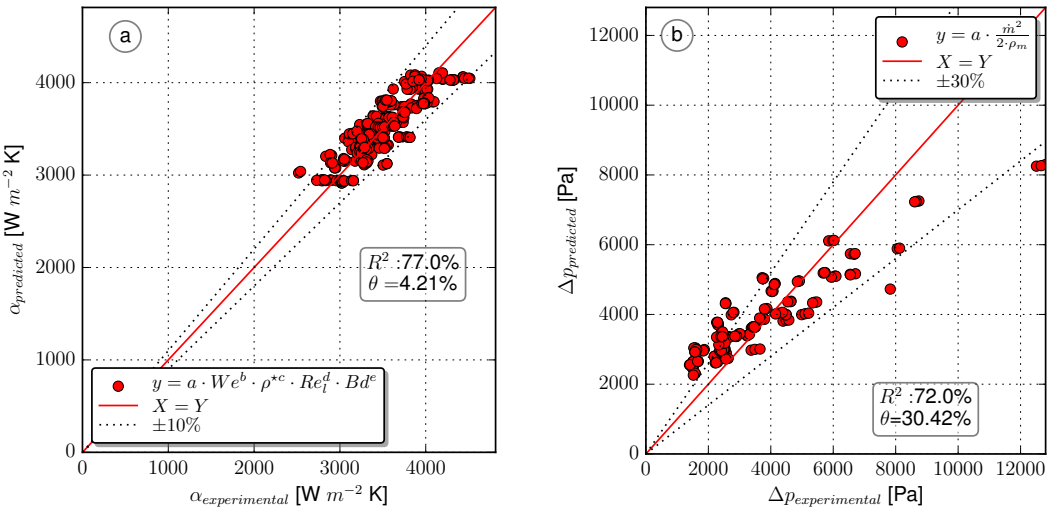

Figure 3.18 – (a) Predicted vaporization heat transfer coefficient versus the experimental data for HFC-245fa and HFO-1233zd (b) Predicted two-phase frictional pressure drop versus the experimental data for HFC-245fa and HFO-1233zd .

3.7 Conclusions

In this chapter, an experimental investigation of the vaporization phenomena characterizing HFC-245fa and HFO-1233zd low critical temperature organic fluids inside brazed plate heat exchanger at typical evaporating conditions for ORC power systems has been presented. The experimental results were reported in terms of average working fluid heat transfer coefficient and frictional pressure drop. The effects of saturation temperature, mass flux, inlet and outlet quality conditions on heat transfer and pressure drop during vaporization inside BPHX were analysed. In particular the fluids were tested at saturation temperatures of 100, 115 and 130 °C, mass fluxes of 62 - 102 kg $m^{-2}s^{-1}$, heat fluxes of 9 - 37 kW m^{-2} and outlet vapour qualities of 0.5 - 1. The main experimental findings are outlined hereunder:

- The Wilson plot method was used to derive the thermal oil single phase heat transfer coefficient. It was experimentally demonstrated how the modified Briggs and Young Wilson plot method [100] allows deriving more reliable results than the original Wilson plot approach as it takes into account the thermophysical properties variations of the tested fluids.
- The heat transfer coefficient values were characterized by an increasing trend as the evaporator mean vapour quality increased up to a certain value where they experienced a decrease. A possible explanation of the decreasing trend starting from a mean quality, x_m, of 0.55-0.6 was given by local occurrence of dry-out in accordance with [97, 98]. Furthermore weak sensitivity to the saturation temperature and to mass flux was found in agreement with [33].
- The frictional pressure drop was found to increase linearly with the increase of vapour quality in accordance with [98, 99]. The experimental data clearly showed the inverse proportionality of frictional pressure drop and saturation temperature.
- The average heat transfer coefficients and the two-phase frictional pressure drop were found to be of comparable magnitude for the two fluids. This would allow to replace HFC-245fa with HFO-1233zd in existent ORC power systems without experiencing major variation in the heat exchangers performances.
- The Thonon method [68] was applied to identify the leading heat transfer mechanism during the vaporization of the two fluids. It was found that the nucleate boiling process was predominant in all the recorded data in accordance with [32, 33]. This result has to be considered as indicative only, as the Thonon method was developed without taking into account the geometrical parameters of the heat exchanger.
- Six two-phase average heat transfer coefficient correlations available in the literature have been tested to predict the measured experimental data for HFC-245fa and HFO-1233zd. For the tested conditions, only the Cooper correlation [76] was found to be able to reproduce the experimental average heat transfer coefficient with good accuracy despite showing a different overall trend. In lack of a validated correlation the Cooper approach is suggested to predict the heat transfer coefficient of low critical temperature organic fluids during vaporization at high pressures in BPHX.
- Four two-phase frictional pressure drop correlations were compared to the experimental data of the two fluids. All the correlations considerably over-predicted the measured

frictional pressure drop. The low saturation temperatures, on which the selected correlations were developed, explain these results.

- A two-phase heat transfer correlation for predicting the presented experimental data of HFC-245fa and HFO-1233zd has been developed following the prediction method proposed by Amalfi [81]. The power law-type correlation was based on four non-dimensional number and presented an accuracy suitable for engineering modelling purposes with a coefficient of determination, R^2, of 77 %.
- A two-phase frictional pressure correlation based on a quadratic term accounting for turbulent phenomena and assuming homogeneous flow was proposed. The equation allowed predicting the experimental data of the two fluids with a coefficient of determination, R^2, of 72 %..

A first step towards an experimental database comprising experimental data of low temperature organic fluids vaporization at typical evaporating conditions for ORC power systems has been set. Additional experimental data at high pressures using the same test rig with HFC-134a, HFO-1234yf, HFO-1234ze fluids can be found in [66]. Further work is necessary to enlarge the database and make it as comprehensive as possible. In this regard experimental campaigns entailing the study of mixture vaporization and the investigation of brazed plate heat exchangers geometrical parameters have been planned at the Technical University of Denmark.

Nomenclature

Acronyms	
HFC	hydrofluorocarbon
HFO	hydrofluoroolefin
WHR	waste heat recovery
ORC	organic Rankine cycle
BPHX	brazed plate heat exchanger
HX	heat exchanger
TC	thermocouple
PT	pressure transmitter
DPS	differential pressure sensor
CFM	Coriolis flow meter
TFM	turbine flow meter
MFM	magnetic flow meter
Subscripts	
su	supply
ex	exit
wf	working fluid
wat	water
eva	evaporator
meas	measured
m	mean
p	plate/port
e	equivalent
h	hydraulic
ln	logarithmic
ch	channel
v	saturated vapour
l	saturated liquid
sat	saturation
f	friction
vap	vaporization
exp	experimental
pred	predicted

Symbols

d	diameter (m)
l_p	plate thickness (m)
L_p	plate vertical length (m)
B_p	plate width (m)
ϕ	corrugation angle (°)
$\hat{a}$	Sinusoidal corrugation amplitude (m)
Λ	Wave length (m)
α	fluid heat transfer coefficient (W m^{-2} k^{-1})
U	overall heat transfer coefficient (W m^{-2} k^{-1})
f_{tp}	Fanning friction factor (-)
X_{tt}	Martinelli parameter (-)
x	vapour quality (-)
A	area (m^2)
t_{wall}	wall thickness (m)
p	pressure (bar)
T	temperature (°C)
h	spec. enthalpy (J kg^{-1})
ρ	density (kg m^{-3})
u	velocity (ms^{-1})
μ	viscosity (Pa s)
k	thermal conductivity (W m^{-1} k^{-1})
σ	surface tension (J m^{-2})
$\dot{Q}$	Thermal power (W)
$\dot{q}$	Thermal flux (W m^{-2})
$\dot{m}$	mass flow (kg s^{-1})
G	mass flux (kg s^{-1} m^{-2})
c_{p}	spec. heat capacity (J kg^{-1} K^{-1})
Δ	difference
θ	mean absolute error
Un	uncertainty

4 Object Oriented Dynamic Modelling of Small Power Systems

Abstract In this chapter the main features of the ThermoCycle library are reported. The library is based on the open-source modelling language Modelica and is focusing on the modelling of small thermo-hydraulic systems. In the first part a review of existing Modelica libraries for modelling thermodynamic systems together with an analysis of the reasons why modelling and simulations are extensively used in the engineering fields are reported. The structure and the main characteristics of the ThermoCycle library are described. The library comprises many different models. For the sake of conciseness only the models that are used in the next chapters are described in details. In the last section a description of the various numerical methods implemented in the library to increase model robustness is reported.

4.1 Introduction

Software for dynamic modelling and simulation have been successfully applied in the power system field for the past 40 years with the first programs being developed in the late 1950s [101]. The early applications involved the modelling of nuclear and fossil-based power plants [34]. Digital dynamic models of power units allowed to facilitate the use of advanced control algorithm, to train the personnel, to investigate the behaviour of the plant in off-design condition and to improve plant operation and maintenance. Understanding boiler dynamic effects and controlling the drum level were among the first problems dynamic modelling tools were applied to [102][103].

In the last decade the attention towards the dynamics of power generation plants has been significantly growing to respond to the needs of an energy industry relying more and more on intrinsically unstable renewable energy technologies [104]. This led to the release of several commercial and open-source software specific for dynamic modelling analysis [105].

Depending on the investigated issue two classes of dynamic models characterized by different level of details (LoD) can be identified: low order models and detailed physics-based models. The former are generally employed to simulate global plants with the main goal of capturing the gross dynamics of the system, to implement general control strategies, to investigate how the interaction of the various components can be optimized or to develop reliable technical and economical predictions of a power system in an early project phase. These models are based on low order approximations with drastic modelling assumptions. Formulated as block

diagrams based either on characteristic lines and/or transfer functions they often require data input from the real system. The simple modelling paradigms on which they rely on lead to ease of comprehension and high computational efficiency. They are usually linear models suited for long time frame simulation, e.g., yearly-based analysis.
The second category comprises detailed models based on the first and second principle laws (conservation of mass, energy and momentum) in order to accurately predict the dynamic behaviour of a component or a whole power plant possibly in working conditions far away from the nominal one. They are normally used to investigate how the system responds to specific transients in the boundary conditions over a limited time frame that usually ranges from some minutes to several hours. These models are suited for the development and testing of advanced model based control especially when new plants or innovative control strategies are considered. Their complexity calls for a modular modelling framework and makes simulations over long periods impractical. Combination of the two modelling paradigms to address specific problems are often employed.
In general these models are mathematically expressed by a set of coupled differential algebraic equations (DAE). Solving a DAE system requires a robust solver and is subject to different numerical problems and challenges [27, 106, 107]. Various specialized techniques and tools supporting dynamic modelling and simulations have been developed during the past years [101][108].
In 1997 the object-oriented, declarative, multi-domain language Modelica was released, opening new possibilities for component-oriented modelling of complex systems [109]. In recent years, the Modelica language has gained momentum for the dynamic modelling of a wide range of physical systems. It allows describing continuous and discrete components in a physical way by writing self-consistent sets of causal and a-causal equations, that are then transformed by a simulation environment software (e.g. Dymola [110], OpenModelica [111], et al.) into an optimized set of hybrid differential-algebraic equations [107]. Various Modelica libraries are available to model thermodynamic and thermal-hydraulic systems [112][113] with a focus on steam and gas cycles (e.g. ThermoSysPro [114] , Thermal Power [115], ThermoPower [37] etc.) or refrigeration systems (e.g. TIL Suite [116], Buildings [117] etc.). Some of these libraries are open-access and only few of them are able to handle thermo-physical properties of non-conventional working fluids used in organic Rankine cycle (ORC) systems. Fluid property calculations require solving complex equations of state (EoS) and are normally implemented in ad-hoc libraries accessed on a per-call basis. In the Modelica language the Modelica standard library allows the computation of thermophysical properties of (moist) air, water and a limited number of organic fluids. To the author's knowledge when modelling thermodynamic systems in the Modelica language the only two libraries allowing the computation of a wide range of non-conventional fluids are the TIL Suite and ThermoPower. The former is a suite of commercial libraries for steady-state and dynamic simulation of thermodynamic systems [116]. It includes TILMedia a model library providing thermophysical properties of organic fluids using custom high performance EoS, fast table based bicubic spline interpolation and an interface to RefProp [20]. TILMedia is not compatible with the Modelica Media standard but provides an interface to the Modelica.Media library.

The latter is an open-source library focusing on the modelling and simulation of large power plants, including ORC power systems [118]. Thermophysical properties calculation of non conventional fluids is achieved by coupling ThermoPower with FluidProp [21], a thermodynamic property library which is freely available but not open-source. The coupling between ThermoPower and FluidProp is accomplished by the ExternalMedia library [119].
The lack of a completely open-source software package for dynamic modelling and simulation of thermo-hydraulic systems led to the effort partially documented in this chapter: the development of the ThermoCycle Modelica library [120]. The library has been built for the simulation of thermal plants (heat pumps, steam and gas cycles, etc.) with a focus on smaller-capacity systems. It aims at addressing three typical challenges inherent to the modelling of thermo-flow systems:

1. Computing the thermophysical substance properties of working fluids
2. Computational efficiency
3. Robustness during initialization and integration

Several numerical methods have been developed and implemented in order to enhance the robustness and the simulation speed of the models during initialization and integration. Furthermore, the computation of the working fluid thermophysical properties is achieved by a strong coupling with the open-source thermodynamic properties database Coolprop [24]. The interface between CoolProp and the ThermoCycle library is achieved by modifying the existing ExternalMedia library [119].

4.1.1 Modelling and simulation: fundamentals

Before addressing the main characteristics of the ThermoCycle library and of the dynamic models used in the framework of this thesis, an attempt to summarize what a model and a simulation is and why modelling and simulations are extensively used in the field of engineering is made.
In modelling and simulation any problem that is codable as a computer program can be conceived as composed by a system S to be simulated, an abstract model M of the system and a computer C on which the simulation is carried on [121].
The concept of a "system" has been introduced in the 19th century and can be defined as a list of interacting and/or independent variables. Another definition of the term system is [122]:

A system is a potential source of data.

A system can be observed and controlled and its interactions with the surrounding environment allow to classify its variables in inputs and outputs. The former are generated by the environment and influence the behaviour of the system, the latter are determined by the system and in turn influence the behaviour of the environment.
The process of gaining knowledge on a given system is defined as experiment. By applying a set of external conditions to the accessible inputs of a system its reaction can be observed,

leading to the identification of the causes and the effects.
As reality is complex, a model of a system is often developed to help in the process of gaining knowledge about a given system. As defined by Marvin Minsky [123]:

To an observer B, an object $A^\star$ is a model of an object A to the extent that B can use $A^\star$ to answer questions that interest him about A.

Depending on the question to be answered about a given system, different models can be developed. This entails that there is no such thing as a perfect model and on the contrary there is no such a thing as an invalid model. A model of a system can be valid for an experiment, i.e., for answering a certain question, but invalid for another. A model is not intrinsically related to a system but rather to the sequence system and experiment. Once the model is developed, it can be simulated, i.e., experiments can be performed on it. Simulation tools can then be used to exercise the model as a real system is tested in a laboratory.
The process of organizing the knowledge gained about a system through experiments in a structured way defining the causes and the effects and placing the observation in a temporal and spatial order is defined as modelling. Given this definition, modelling is the thing in common in all discipline of science and engineering. Modelling and simulation techniques have been increasingly adopted in the engineering practice in the last decades, exploiting the increasing capability of computing machines. Several reasons drove this trend, an attempt to list the main ones is reported hereunder:

1. A simulation is generally cheaper and safer than conducting a real experiments. For example it could be that the system to be studied is used 24/7 and putting it off-line to perform the test would cost too much.

2. The real system can be characterized by a time constant which is not compatible with the one of the experimenter. The time constant could be in fact too small that it can hardly be experienced by a human being or too big that the experiment is too slow. In these cases simulation would allow to slow down or speed up the real system time constant.

3. In a real system not all the state variables or system parameters are always accessible, on the contrary a simulation allows accessing to all inputs and outputs of the model. Furthermore a simulation allows manipulating the model out of the feasible range of the system at no extra cost.

4. Simulations allow eliminating any disturbances or second-order effects that in real systems would make challenging to measure and understand certain processes.

Finally it is worth mentioning that modelling and simulation are goal driven, i.e., the purpose of the potential model should be known before creating it.

4.2 The ThermoCycle Modelica library

4.2.1 Basic ideas

The ThermoCycle library aims at providing a robust framework to model small-capacity thermal systems. It has been designed to provide an integrated and fully open-source solution ranging from the thermophysical substance properties, using CoolProp [24], to the simulation of complex systems with their control strategy. In comparison with alternative libraries dedicated to power plants (ThermoPower, ThermoSysPro, Thermal Power), the ThermoCycle library includes various models dedicated to the modelling of smaller-scale thermal systems, such as volumetric compressors models used for the simulation of heat pump or refrigeration cycles. When designing a library compromises between flexibility and ease of use or between numerical efficiency and simplicity of the models are inevitable. The key features of the ThermoCycle library are the following:

- Designed for system level simulations
- Full compatibility (connector-wise) with libraries such as Modelica Standard library or ThermoPower, use of stream connectors
- Ability to handle reverse flows and flow reversals
- Various numerical robustness strategies implemented in the components and accessible through Boolean parameters
- High readability of the models (limited levels of hierarchical modelling)

The ThermoCycle library has been designed to provide components that can be as generic as possible trying to minimize the overall complexity. Lumped models and distributed parameter models limited to one-dimensional discretization are included in the library. Different types of discretization grid are available for selection to the user. In general the models included in the library can be classified as flow and control volume models. The former comprise all the equipment that in a thermohydraulic system is characterized by small volumes and high power density [27], i.e., rotary machines, valves etc., the latter refer to large volume components such as heat exchangers, tanks, pipes etc. . In the library the control volume models are generally characterized by a dynamic mass and energy balance while a static momentum balance is always considered. In case incompressibility is assumed in the fluid model no dynamic is taken into account in the mass balance as well. As the thermal phenomena are the prevailing ones in thermo-hydraulic system simulations, the flow models are described by static conservation equations and by different type of correlations to predict the off-design trends.

4.2.2 Library structure

The ThermoCycle library is built following the basic concepts of the object-oriented modelling language Modelica. It is organized into different packages, including:

1. *Components*, is the central part of the library. It is divided in three sub packages: FluidFlow, HeatFlow and Units. It contains all the models available in the library from the

simple cell model for fluid flow to complete models of heat exchangers, expanders and control units.

2. *Examples*, contains simulation models where the components of the library are tested. It includes several ORC plant models and it also provides a step by step package where the procedure to build an ORC power unit and an heat pump system is described in detail.

3. *Functions*, includes the empirical correlations used to characterize some of the library models as well as general purpose mathematical functions.

4. *Interfaces*, contains the connectors used for the library components.

5. *Media*, predefines a list of the fluids available in the library.

An illustration of the main packages and sub-packages characterizing the ThermoCycle library is presented in Figure 4.1. A limited and careful use of the inheritance, the class parametriza-

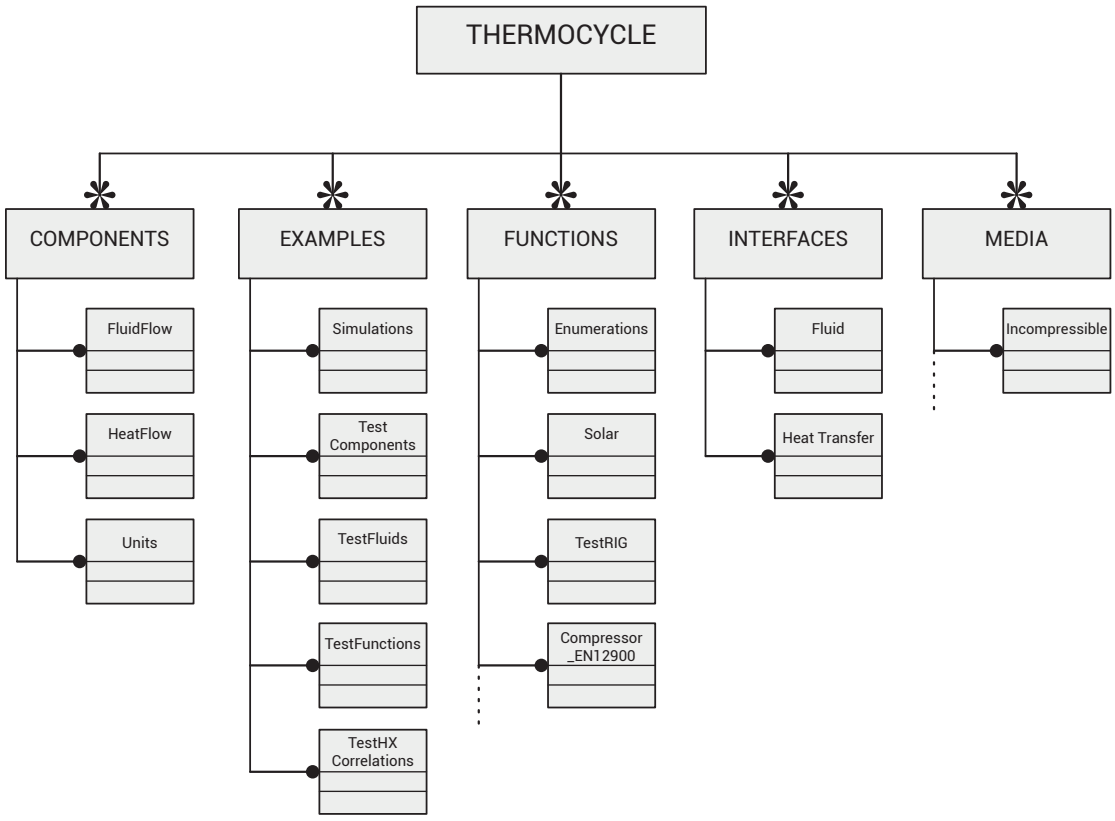

Figure 4.1 – Schematic representation of the structure of the ThermoCycle Modelica library.

tion and the enumeration features characterized the development of all the models included

in the library.
The inheritance allows reusing codes that have already been written by extending it in another model. An extensive use of this feature often leads to Matryoshka-type models irrationally increasing the complexity of the model. The class parametrization consists in defining a general class inside a model which can be replaced by different models. The inheritance feature has been limited to the heat transfer mechanism while a slightly larger use of the class parametrization has been made.
The enumeration is adopted in the library to a greater extent. This feature allows defining an ordered collection of items that can be selected by the user changing the general behaviour of the model. In the Library examples of the enumeration technique can be found in the distributed one-dimensional model, where it is used to define the type of discretization grid, or in the lumped rotary machine models to characterize the component performances. This approach avoids to have specific models suitable only for one particular component or type of geometry increasing the flexibility of the library and allowing to use the same model for different types of simulations.
In the case of heat exchanger models, the user is free to select detailed heat transfer correlations or simplified laws depending on the required needs. As an example, the same model can readily be used for shell & tubes or plate heat exchangers only be modifying the law computing the heat transfer coefficient. In Figure 4.2, the icons of the ThermoCycle models described in this chapter from the graphical user interface of Dymola are reported.

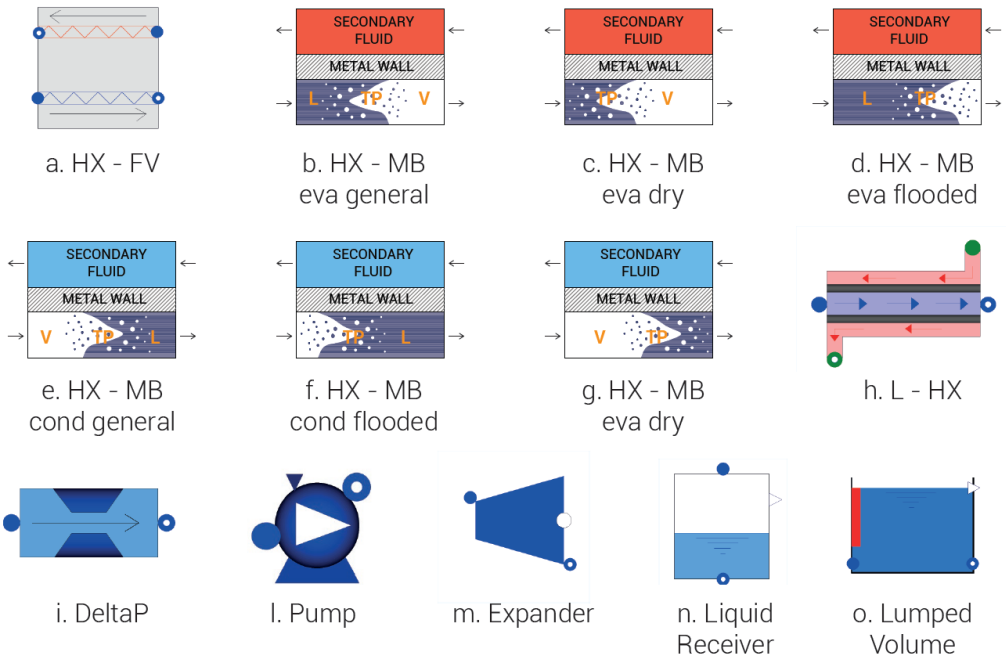

Figure 4.2 – Representation of the ThermoCycle models described in this chapter from the Dymola graphical user interface (GUI).

4.3 Heat exchanger modelling

When modelling low capacity thermo-hydraulic systems, the governing dynamics are usually mainly concentrated in the heat exchanger (HE). For this reason particular care has been taken in the ThermoCycle library for the modelling of HE component. In the case of heat exchangers involving phase transitions, the two commonly adopted modelling approaches are the finite volume (FV) and the moving boundary (MB) [124]. Both methods are based on the conservation laws of energy, mass and momentum over a defined control volume. In a moving boundary model the fluid flow in the HE is divided in as many control volumes as the states (e.g. liquid, two-phase, vapour) in the fluid flow (from one to three). The size of the control volumes varies in time during transients, following the saturated liquid and the saturated vapour boundaries. The finite volume approach consists in discretizing the HE volume in a number of equal and constant control volumes. The conservation laws are then applied in each of the control volumes.
In the ThermoCycle library three types of heat exchanger models have been implemented: the finite volume (FV), the moving boundary (MB) and a novel model characterized by a simplified lumped-parameter approach (L-HX) based on the logarithmic mean temperature difference (LMTD). In what follows the main common assumptions and a description of the three modelling approach is reported.

4.3.1 Assumptions

The fluid flow through the control volume of one of the two fluid sides of an heat exchanger can be described with a mathematical formulation of the conservation laws of physics:

- The mass of the fluid is conserved.
- The rate of change in momentum equals the sum of the forces on a fluid particles (2nd law of Newton).
- The rate of change of energy is equal to the sum of the rate of thermal energy addition to and the rate of work done on a fluid particle (1st law of thermodynamics).

For developing the general conservation equation, a small element of fluid is analysed with sides ∂x, ∂y and ∂z. The fluid is considered as a continuum. The analysis of the fluid trend is carried out at macroscopic scale length (from 1 µm and larger). As a consequence the fluid molecular structure and motion can be ignored. The evolution of the fluid is described in terms of macroscopic properties i.e. pressure, temperature, density and velocity and their space and time derivatives. Defining with **u** the velocity vector in three dimensions, the general form of mass energy and momentum balance are reported hereunder:

$$\frac{\partial \rho}{\partial t} + div(\rho \mathbf{u}) = 0 \tag{4.1}$$

$$\rho \frac{DE}{Dt} = -div(\rho \mathbf{u}) + div(kgradT) + S_E \tag{4.2}$$

$$\rho \frac{Du}{Dt} = \frac{\partial(-p + \tau_{xx})}{\partial x} + \frac{\partial \tau_{yx}}{\partial y} + \frac{\tau_{zx}}{\partial z} + S_{Mx} \tag{4.3}$$

where *div* is the divergence vector operator (i.e. the extent to which the vector field flow behaves like a source at a given point), *grad* is the gradient of the vector (i.e. a generalization of the concept of derivative in x dimensions, 3 in our case x,y,z), and $\frac{D}{Dt}$ is the total or substantive derivative which is defined as, letting ϕ be the value of a property of the fluid per unit of mass:

$$\frac{D\phi}{Dt} = \frac{\partial\phi}{\partial t} + \mathbf{u} \cdot grad\phi \tag{4.4}$$

For the sake of conciseness, the momentum balance is expressed only for the x-direction. Starting from Equations 4.1-4.3, as the developed heat exchanger models are conceived to be integrated into a system model, the following general assumptions for the fluid elements and the metal wall element are considered:

- The heat exchanger is considered as a 1-dimensional tube (z-direction) in the flow direction. Energy and mass balances are expressed considering the dynamic contribution. Given the low time constant characterizing the propagation of pressure throughout the heat exchanger compared to those related to mass and thermal energy transfer, a static momentum balance is assumed.
- Kinetic energy, gravitational forces and viscous stresses are neglected.
- No work is done on or generated by the fluid in the control volume.
- The cross section area is assumed constant throughout the heat exchanger length.
- The velocity of the fluid is uniform over the cross section area (homogeneous two-phase flow).
- Pressure drop through the heat exchanger are neglected (homogeneous pressure).
- Axial heat conduction is neglected in the fluid element.
- The rate of thermal energy addition by radiation is neglected in the fluid element.
- The rate of thermal energy exchanged with the ambient by convection is considered in the fluid element.
- Thermal energy accumulation is considered for the metal wall of the tube.
- Thermal energy conduction in the metal wall is neglected in the flow direction and considered static and infinite in the circumferential direction (the wall cross section area has a uniform temperature).

Other assumptions, depending on the heat exchanger modelling technique, i.e., FV - MB - L-HX, are reported in the specific sections of each model.

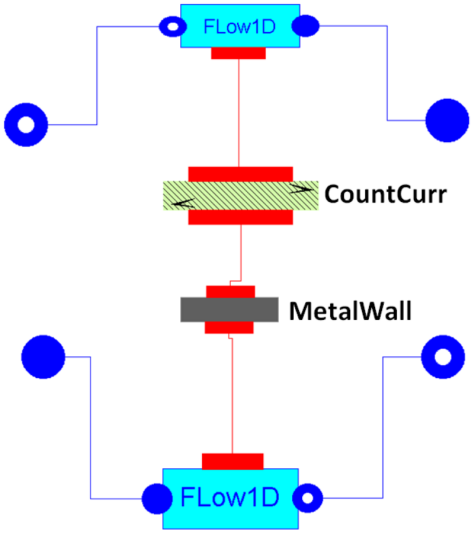

Figure 4.3 – Representation of the finite volume from the Dymola graphical user interface (GUI).

4.3.2 Finite volume method

The finite volume heat exchanger model is object oriented, its structure being shown in 4.3. It is based on the connection of different subcomponents from the ThermoCycle library. Two fluid components simulating the flows in the two sides of the heat exchanger, *Flow1D*, and one wall component, *MetalWall*, accounting for thermal energy accumulation in the metal wall. A forth component *CountCurr* allows switching between parallel and counter flow configuration. The conservation laws are derived by integrating the general one-dimensional (1-D) form of equations 4.1-4.3 over a constant volume. Considering the above mentioned assumptions, their final formulation for each CV is reported in Equations 4.5 to 4.7, taking pressure, p, and specific enthalpy, h, as dynamic state variables [125].

$$\frac{dM}{dt} = \dot{m}_{su} - \dot{m}_{ex} \quad \text{with} \quad \frac{dM}{dt} = V \cdot \left(\frac{\partial \rho}{\partial h} \cdot \frac{dh}{dt} + \frac{\partial \rho}{\partial p} \cdot \frac{dp}{dt} \right) \tag{4.5}$$

$$V \rho \frac{dh}{dt} = \dot{m}_{su} \cdot (h_{su} - h) - \dot{m}_{ex} \cdot (h_{ex} - h) + V \frac{dp}{dt} + A_l \cdot \dot{q} \tag{4.6}$$

$$p_{su} = p_{ex} \tag{4.7}$$

where $\frac{\partial \rho}{\partial h}$ and $\frac{\partial \rho}{\partial p}$ in Equation 4.5 are considered thermodynamic properties of the fluid and are directly computed by the open-source CoolProp library [24]. The "su" (supply) and "ex" (exhaust) subscripts denote the nodes variable of each cell, A_l is the lateral surface through which the heat flux $\dot{q}$ is exchanged with the metal wall and V is the constant volume of each cell. Specific enthalpy and pressure at the center of the control volume are considered as the state variables. The staggered discretization grid is used: the state variables are calculated at the center of the volume and the node values ("su","ex") are computed based on the selected

discretization scheme. Both central and upwind discretization schemes are supported by the model. Since the model accounts for flow reversal, a conditional statement is added depending on the flow rates at the inlet and outlet nodes. For the central difference scheme, h_{su} is expressed by 4.8 (an equivalent equation applies to h_{ex}):

$$h_{su} = \begin{cases} h^*_{ex} & \text{if } \dot{m}_{su} \geq 0 \\ 2 \cdot h - h_{ex} & \text{if } \dot{m}_{su} < 0 \text{ and } \dot{m}_{ex} < 0 \\ h & \text{if } \dot{m}_{su} < 0 \text{ and } \dot{m}_{ex} \geq 0 \end{cases} \tag{4.8}$$

where the flow rates are defined as positive when the fluid flows in the nominal direction (from "su" to "ex"), and where h^*_{ex} indicates the exhaust node enthalpy of the previous cell.
For the upwind scheme:

$$h_{su} = \begin{cases} h & \text{if } \dot{m}_{su} < 0 \\ h^*_{ex} & \text{if } \dot{m}_{su} \geq 0 \end{cases} \tag{4.9}$$

Thermal energy accumulation in the metal wall is expressed as:

$$\frac{M_{\mathrm{w}}}{N \cdot c_{\mathrm{w}}} \cdot \frac{dT_{\mathrm{w}}}{dt} = A_{\mathrm{ext}} \cdot \dot{q}_{\mathrm{ext}} + A_{\mathrm{int}} \cdot \dot{q}_{\mathrm{int}} \tag{4.10}$$

where M_{w} is the total mass of the metal wall, N is the number of cells and c_{w} is the metal wall specific heat capacity. The secondary fluid is modelled as an incompressible fluid whose density and specific heat capacity are assumed constant throughout the heat exchanger length. The secondary fluid mass and energy balance results in:

$$\dot{m}_{\mathrm{su}} = \dot{m}_{\mathrm{ex}} = \dot{m} \tag{4.11}$$

$$V \rho_{cst} c_{p,cst} \frac{dT}{dt} = \dot{m} \cdot (T_{\mathrm{su}} - T_{\mathrm{ex}}) + A_{\mathrm{l}} \cdot \dot{q} \tag{4.12}$$

where the abbreviation cst indicates a constant value over the heat exchanger length. The heat transfer problem between the two fluid components and the metal wall is solved with Newton's law of cooling.

4.3.3 Moving boundary method

The moving boundary model is developed following the object-oriented principles of abstraction, encapsulation and (limited) inheritance: two basic models are formulated simulating the fluid flow through a variable control volume in single and two-phase state. The connection of these two basic models allows building dry, flooded or general evaporator and condenser models. The moving boundary general evaporator structure is shown in Figure 4.4.
The enthalpy distribution of the fluid is assumed linear in each region of the tube (sub-cooled, two-phase, super-heated) and is computed as shown in Equation 4.13:

$$\overline{h} = \frac{1}{2} \cdot (h_{\mathrm{a}} + h_{\mathrm{b}}) \tag{4.13}$$

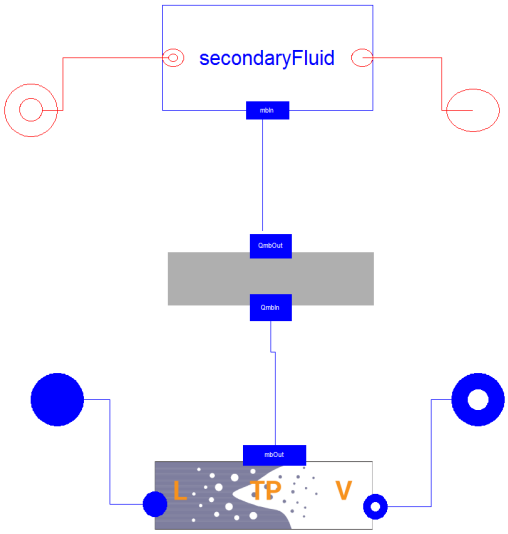

Figure 4.4 – Representation of the moving boundary general evaporator model from the Dymola graphical user interface (GUI).

where the a and b subscripts denote the left and right boundaries of the region. For a moving boundary control volume, the mass and energy balances are defined by integrating the general conservation laws of physics over the length of the zone, as shown in Equations 4.14 and 4.15.

$$A \cdot \int_{l_a}^{l_b} \frac{\partial \rho}{\partial t} \mathrm{d}z + \int_{l_a}^{l_b} \frac{\partial \dot{m}}{\partial z} \mathrm{d}z = 0 \tag{4.14}$$

$$A \cdot \int_{l_a}^{l_b} \frac{\partial (\rho \cdot h)}{\partial t} \mathrm{d}z - A \cdot l \cdot \frac{dp}{dt} + \int_{l_a}^{l_b} \frac{\partial (h \cdot \dot{m})}{\partial z} \mathrm{d}z = dl \cdot Y \cdot \dot{q} \tag{4.15}$$

where A is the cross sectional area, l_a and l_b are the lengths of the left and right boundaries of the region and Y is the channel perimeter. Assuming an homogeneous pressure, the momentum balance is given by Equation 4.7. As far as the one-phase region is concerned, the mass balance is derived in Equation 4.14 by applying Leibniz rule to the first term and using the mean-value theorem such that the rate of mass flow change results in:

$$\frac{d}{dt} \int_{l_a}^{l_b} \rho \, \mathrm{d}t = \frac{d}{dt} (\overline{\rho} \cdot l) \tag{4.16}$$

the mass balance for a one-phase region is equal to:

$$A \cdot \left[\overline{\rho} \cdot \frac{dl}{dt} + l \cdot \frac{d\overline{\rho}}{dt} - \rho_a \cdot \frac{dl_a}{dt} + \rho_b \cdot \frac{dl_b}{dt} \right] = \dot{m}_a - \dot{m}_b \tag{4.17}$$

where $\overline{\rho}$ is the average density of the region computed as a function of the pressure and of the average specific enthalpy, $\overline{\rho} \approx f\left(\overline{h}, p\right)$, l is the length of the region and $\frac{d\overline{\rho}}{dt}$ is calculated as:

$$\frac{d\overline{\rho}}{dt} = \frac{\partial\overline{\rho}}{\partial p}\cdot\frac{dp}{dt} + \frac{\partial\overline{\rho}}{\partial\overline{h}}\cdot\frac{d\overline{h}}{dt} = \frac{\partial\overline{\rho}}{\partial p}\cdot\frac{dp}{dt} + \frac{1}{2}\cdot\frac{\partial\overline{\rho}}{\partial\overline{h}}\cdot\left(\frac{dh_\mathrm{a}}{dt} + \frac{dh_\mathrm{b}}{dt}\right) \tag{4.18}$$

where $\frac{dh_{\mathrm{b/a}}}{dt}$ are defined based on Equations 4.19 to 4.22 reported in Table 4.1. The energy

Table 4.1 – Specific boundary enthalpy derivative depending on the heat transfer and control volume.

HE region	Evaporator	Condenser
Sub-cooled	$\frac{dh_\mathrm{b}}{dt} = \frac{\partial h_\mathrm{l}}{\partial p}\frac{dp}{dt}$ (4.19)	$\frac{dh_\mathrm{a}}{dt} = \frac{\partial h_\mathrm{l}}{\partial p}\frac{dp}{dt}$ (4.20)
Super-heated	$\frac{dh_\mathrm{a}}{dt} = \frac{\partial h_\mathrm{v}}{\partial p}\frac{dp}{dt}$ (4.21)	$\frac{dh_\mathrm{b}}{dt} = \frac{\partial h_\mathrm{v}}{\partial p}\frac{dp}{dt}$ (4.22)

balance is derived from equation Equation 4.15. Applying Leibniz rule to the first term and using the mean-value theorem allows to define the rate of energy change as:

$$\frac{d}{dt}\int_{l_\mathrm{a}}^{l_\mathrm{b}}\left(\rho\cdot h\right)\mathrm{d}z = \frac{d}{dt}\left(\overline{\rho h}\cdot l\right) \approx \frac{d}{dt}\left(\overline{\rho}\cdot\overline{h}\cdot l\right) \tag{4.23}$$

The energy balance for the one-phase region results in:

$$A\cdot\left[\overline{\rho}\overline{h}\frac{dl}{dt} + \overline{h}l\frac{d\overline{\rho}}{dt} + \overline{\rho}l\frac{d\overline{h}}{dt} + \left(\rho_\mathrm{a}h_\mathrm{a}\right)\cdot\frac{dl_\mathrm{a}}{dt} - \left(\rho_\mathrm{b}h_\mathrm{b}\right)\cdot\frac{dl_\mathrm{b}}{dt}\right] - A\cdot l_\mathrm{a}\cdot\frac{dp}{dt} = \dot{m}_\mathrm{a}\cdot h_\mathrm{a} - \dot{m}_\mathrm{b}\cdot h_\mathrm{b} + \dot{Q} \tag{4.24}$$

In the two-phase region, the assumption of homogeneous two-phase flow condition allows to express the mean density as a function of the average void fraction $\overline{\gamma}$ as:

$$\overline{\rho} = \left(1-\overline{\gamma}\right)\rho_\mathrm{l} + \overline{\gamma}\rho_\mathrm{v} \tag{4.25}$$

where the average void fraction is calculated integrating the local void fraction γ over the length of the region. $\overline{\gamma}$ is an indicator of the fraction of the total volume of the two-phase region occupied by fluid in vapour phase [126]. It is derived integrating the void fraction over the two-phase control volume as shown in Appendix A.1. Substituting Equation 4.25 into Equation 4.16 and solving Equation 4.14 results in the mass balance for the two phase region:

$$A\left[\left((1-\overline{\gamma})\rho_\mathrm{l} + \overline{\gamma}\rho_\mathrm{v}\right)\frac{dl}{dt} + l\left(\left(\rho_\mathrm{v}-\rho_\mathrm{l}\right)\frac{d\overline{\gamma}}{dt} + \overline{\gamma}\frac{d\rho_\mathrm{v}}{dp}\frac{dp}{dt} + \left(1-\overline{\gamma}\right)\frac{d\rho_\mathrm{l}}{dt}\right) - \rho_\mathrm{a}\frac{dl_\mathrm{a}}{dt} + \rho_\mathrm{b}\frac{dl_\mathrm{b}}{dt}\right] = \dot{m}_\mathrm{a} - \dot{m}_\mathrm{b} \tag{4.26}$$

The energy balance for the two phase region is obtained from Equation 4.15 using Equations 4.25 and 4.23:

$$A\Bigg[\left(\left(1-\overline{\gamma}\right)\rho_{\mathrm{l}}h_{\mathrm{l}}+\overline{\gamma}\rho_{\mathrm{v}}h_{\mathrm{v}}\right)\frac{dl}{dt}+l\Bigg(\left(\rho_{\mathrm{v}}h_{\mathrm{v}}-\rho_{\mathrm{l}}h_{\mathrm{l}}\right)\frac{d\overline{\gamma}}{dt}+\overline{\gamma}h_{\mathrm{v}}\frac{\partial\rho_{\mathrm{v}}}{\partial p}\frac{dp}{dt}+\overline{\gamma}\rho_{\mathrm{v}}\frac{\partial h_{\mathrm{v}}}{dp}\frac{dp}{dt}$$
$$+\left(1-\overline{\gamma}\right)h_{\mathrm{l}}\frac{\partial\rho_{\mathrm{l}}}{dp}\frac{dp}{dt}+\left(1-\gamma\right)\rho_{\mathrm{l}}\frac{\partial h_{\mathrm{l}}}{\partial p}\frac{dp}{dt}\Bigg)+\left(\rho_{\mathrm{a}}h_{\mathrm{a}}\right)\frac{dl_{\mathrm{a}}}{dt}-\left(\rho_{\mathrm{b}}h_{\mathrm{b}}\right)\frac{dl_{\mathrm{b}}}{dt}\Bigg]-A\cdot l\cdot\frac{dp}{dt} \tag{4.27}$$
$$=\dot{m}_{\mathrm{a}}h_{\mathrm{a}}-\dot{m}_{\mathrm{b}}h_{\mathrm{b}}+\dot{Q}$$

The void fraction time derivative is expressed as shown in equation 4.28, applying the chain rule, given that $\overline{\gamma}=f(p,h_{\mathrm{a}},h_{\mathrm{b}})$:

$$\frac{d\overline{\gamma}}{dt}=\frac{\partial\overline{\gamma}}{\partial p}\frac{dp}{dt}+\frac{\partial\overline{\gamma}}{\partial h_a}\frac{dh_a}{dt}+\frac{\partial\overline{\gamma}}{\partial h_b}\frac{dh_b}{dt} \tag{4.28}$$

The void fraction partial derivatives ($\frac{\partial\overline{\gamma}}{\partial p}$, $\frac{\partial\overline{\gamma}}{\partial h_a}$, $\frac{\partial\overline{\gamma}}{\partial h_b}$), are symbolically solved through the adoption of a technical computing software. Their final formulation is reported in Appendix A. The option of imposing a constant average void fraction, i.e. $\frac{d\overline{\gamma}}{dt}=0$, is supported by the model. The thermal energy balance in the metal wall for each control volume is expressed as:

$$\rho_{\mathrm{w}}c_{\mathrm{w}}A_{\mathbf{w}}\frac{\partial T_{\mathrm{w}}}{\partial t}=dl\cdot Y\cdot\dot{q}_{\mathrm{wf}}+dl\cdot Y\cdot\dot{q}_{\mathrm{sf}} \tag{4.29}$$

Integrating over the cell length and applying Leibniz rule:

$$\rho_{\mathrm{w}}c_{\mathrm{w}}A_{\mathrm{w}}\left[\frac{d}{dt}\int_{l_{\mathrm{a}}}^{l_{\mathrm{b}}}\partial T_{\mathrm{w}}\,\mathrm{d}z+T_{\mathrm{w}}\left(l_{\mathrm{b}}\right)\frac{dl_{\mathrm{b}}}{dt}-T_{\mathrm{w}}(l_{\mathrm{a}})\frac{dl_{\mathrm{a}}}{dt}\right]=\dot{Q}_{\mathrm{wf}}+\dot{Q}_{\mathrm{sf}} \tag{4.30}$$

Solving the integral results in:

$$\rho_{\mathrm{w}}c_{\mathrm{w}}A_{\mathrm{w}}[\frac{d(T_{\mathrm{w}}\cdot(l_{\mathrm{b}}-l_{\mathrm{a}}))}{dt}+T_{\mathrm{w}}(l_{\mathrm{b}})\frac{dl_{\mathrm{b}}}{\partial t}-T_{\mathrm{w}}(l_{\mathrm{a}})\frac{dl_{\mathrm{a}}}{\partial t}]=\dot{Q}_{\mathrm{wf}}-\dot{Q}_{\mathrm{sf}} \tag{4.31}$$

In order to simplify the resolution of the model, no energy, mass and momentum accumulation is considered in the secondary fluid side. The fluid is assumed incompressible with a constant density and specific heat capacity throughout the length of the heat exchanger. A linear temperature distribution is assumed and the thermal energy transfer with the metal wall is solved either with the semi-isothermal ϵ-NTU method or with Newton's law of cooling. For the sake of simplicity and model robustness, no switching mechanism is implemented in the proposed MB formulation. A constant heat transfer coefficient is set in the secondary fluid side and in each region of the working fluid side.

4.3.4 Lumped heat exchanger model

The L-HX is a simplified lumped-parameter heat exchanger model based on the LMTD method. The L-HX model is developed for single-phase working condition. Static mass, energy and momentum balances are assumed in the two fluid sides, i.e., the outlet flow rate is always

equal to the inlet flow rate for both sides of the heat exchanger. The heat transfer problem is solved using a modified robust version of the log mean temperature difference (RLMTD) method which is applied twice: between the wall and the working fluid temperature gradient and between the wall and the hot fluid temperature gradient. The RLMTD method is based on a set of causal heat transfer equations which allows the model to converge even if negative pinch points occur during the simulation process.
The two computed heat flow rates are not necessarily equal, the difference between them corresponding to the thermal energy accumulation or rejection of the metal wall, which is accounted for as:

$$M_{\mathrm{w}} \cdot c_{\mathrm{w}} \frac{dT_{\mathrm{w}}}{dt} = \dot{Q_{\mathrm{hf}}} - \dot{Q_{\mathrm{cf}}} \tag{4.32}$$

where M_{w} is the mass of the wall, $c_{\mathrm{p,w}}$ is the specific heat capacity of the wall, T_w is the mean temperature in the wall, and $\dot{Q_{\mathrm{hf}}}$ and $\dot{Q_{\mathrm{cf}}}$ are the heat power transferred by the hot fluid and received by the cold fluid respectively. The above equation allows computing the average wall temperature, but not the temperature gradient within the wall. In the absence of axial conduction in the wall, the evolutions of the temperatures in two infinitely small volumes at each extremity of the heat exchanger are given by:

$$dM_{\mathrm{w,0}} \cdot c_{\mathrm{w}} \frac{d\Delta T_{\mathrm{w,0}}}{dt} = dA \cdot [U_{\mathrm{hf}} \cdot (T_{\mathrm{hf,0}} - T_{\mathrm{w,0}}) - U_{\mathrm{cf}} \cdot (T_{\mathrm{w,0}} - T_{\mathrm{cf,0}}) \tag{4.33}$$

$$dM_{\mathrm{w,1}} \cdot c_{\mathrm{w}} \frac{d\Delta T_{\mathrm{w,1}}}{dt} = dA \cdot [U_{\mathrm{hf}} \cdot (T_{\mathrm{hf,1}} - T_{\mathrm{w,1}}) - U_{\mathrm{cf}} \cdot (T_{\mathrm{w,1}} - T_{\mathrm{cf,1}}) \tag{4.34}$$

where the subscript 0 and 1 indicate both extremities of the heat exchanger. The temperature evolutions are assumed to be linear with the axial distance. Integrating equations 4.33-4.34 from 0 to 1, the wall temperature gradient can be calculated as:

$$dM_{\mathrm{w,1}} \cdot c_{\mathrm{w}} \frac{d\Delta T_{\mathrm{w}}}{dt} = AU_{\mathrm{hf}} \cdot (T_{\mathrm{hf,su}} - T_{\mathrm{hf,ex}} - \Delta T_{\mathrm{w}}) + AU_{\mathrm{cf}} \cdot (T_{\mathrm{cf,ex}} - T_{\mathrm{cf,su}} - \Delta T_{\mathrm{w}}) \tag{4.35}$$

The wall temperature average value and its gradient are defined by equation 4.32 and 4.35 respectively.

4.4 Heat transfer coefficient modelling

The computation of the heat transfer coefficient (HTC) for the heat exchanger models is based on an inheritance structure taking advantage of the object-oriented Modelica language. The basic interface, called *'PartialHeatTransfer'*, define an ideal heat transfer element with no thermal resistance. The object takes as an input the bulk state of the fluid and computes the thermal energy flow per area. Two layers with different levels of details are built upon this base class. The first one is the *'PartialHeatTransferZones'* which extends *'PartialHeatTransfer'* and requires as additional inputs the nominal mass flow rate, $\dot{m}_{\mathrm{nom}}$, the actual mass flow rate, $\dot{m}$, the vapour quality, x, and the nominal values of the HTC of the working fluid for the liquid, α_{l}, the two-phase, α_{tp}, and the vapour, α_{v} region. These last values are normally obtained using

a simple steady-state model of the heat exchanger component. Based on this partial object two models are implemented modifying the HTC values as a function of the mass flow rate, *'MassFlowDependance'*-MFD:

$$\alpha = \alpha_{\text{nom}} \cdot \left(\frac{\dot{m}}{\dot{m}_{\text{nom}}} \right)^{0.8} \tag{4.36}$$

or as a function of the vapour quality, *'VapourQualityDependance'*-VQD:

$$\alpha = \begin{cases} \alpha_{\text{l}} & \text{if } x < -\Delta x/2 \\ \alpha_{\text{l}} + (\alpha_{\text{tp}} - \alpha_{\text{l}}) \cdot (1 + sin(x\pi/\Delta x))/2) & \text{if } x < \Delta x/2 \\ \alpha_{\text{tp}} & \text{if } x < 1 - \Delta x/2 \\ \alpha_{\text{tp}} + (\alpha_{\text{v}} - \alpha_{\text{tp}}) \cdot (1 + sin((x-1)\pi/\Delta x))/2) & \text{if } x < 1 + \Delta x/2 \\ \alpha_{\text{v}} & \text{if } x \geq 1 + \Delta x/2 \end{cases} \tag{4.37}$$

In order to add the possibility of computing the heat transfer coefficient based on detailed correlations a third partial object is defined called *'PartialHeatTransferSmoothed'*. This object includes the MFD and VQD functionalities and add the capability of computing the HTC for the different zones with correlations from the literature. The correlations implemented in the library are reported in Table 4.2. The definition of a replaceable model in the FV and MB cell

Table 4.2 – Heat transfer coefficient correlations available from the heat transfer ThermoCycle model.

Single phase	Two-phase
Dittus Boelter [127]	Gungor-Winterton [75]
Gnielinski [128]	Shah [72]
Muley-Manglik [30]	Cooper [76]
Martin [61]	DTU-HX 2016 eq. 3.47

allows to access the heat transfer object. The calculated heat flux and the temperature of the working fluid are exchanged between the cell and the heat transfer element through a thermal port connector.

4.5 Rotary machine modelling

A suite of rotational machine models characterized by different levels of detail are available in the ThermoCycle library. When modelling a whole power unit, since the time constants characterizing the expansion and compression processes are small compared to those of the heat exchangers, models based on empirically derived algebraic correlations where no dynamics is accounted for can be used. In the following only the lumped expander and pump models are described.

4.5.1 Expanders

If thermal energy losses to the environment are neglected, the expander can be modelled by its isentropic efficiency and its filling factor. These two variables are defined as reported in Equations 4.38 and 4.39.

$$\varepsilon_{\text{is,exp}} = \frac{\dot{W}_{\text{shaft}}}{\dot{m} \cdot (h_{\text{su}} - h_{\text{ex,s}})} \tag{4.38}$$

$$\phi = \frac{\dot{m}}{\rho_{\text{su,exp}} \cdot (V_{\text{s}} \cdot N_{\text{exp}})} \tag{4.39}$$

$$\tag{4.40}$$

The outlet enthalpy can then be computed as:

$$h_{\text{ex}} = h_{\text{su}} - \varepsilon_{\text{is,exp}} \cdot (h_{\text{su}} - h_{\text{ex,s}}) \tag{4.41}$$

The expander efficiency can be predicted as a function of selected boundary conditions of the machine, namely the expander inlet pressure, $p_{\text{su,exp}}$, the expander rotational speed, N_{exp}, and the expander pressure ratio, r_{p}. The expression originally proposed in [46] and inspired by Pacejka′s model [129] is reported in Equation 4.42:

$$\varepsilon_{\text{is,exp}} = y_{\max} \cdot \sin(\xi \cdot \arctan(B \cdot (r_{\text{p}} - r_{\text{p,0}}) - E \cdot (B \cdot (r_{\text{p}} - r_{\text{p,0}}) \arctan(B \cdot (r_{\text{p}} - r_{\text{p,0}}))))) \tag{4.42}$$

with:

$$B = \frac{\delta}{\xi \cdot y_{\max}} \tag{4.43}$$

$$E = \frac{B \cdot (r_{\text{p,max}} - r_{\text{p,0}}) - \tan\frac{\pi}{2\xi}}{B \cdot (r_{\text{p,max}} - r_{\text{p,0}}) - \arctan(B \cdot (r_{\text{p,max}} - r_{\text{p,0}}))} \tag{4.44}$$

Equation 4.42 is based on five parameters ($r_{\text{p,0}}, \delta, r_{\text{p,max}}, y_{\max}, \xi$), four of which are further expressed as a linear regression of the three selected input variables using seven empirical coefficients, a_{x}, as shown in equations 4.45 to 4.48:

$$r_{\text{p,0}} = r_{\text{p,0,n}} + a_0 \cdot N^*_{\text{exp}} \tag{4.45}$$

$$\delta = \delta_{\text{n}} + a_1 \cdot p^*_{\text{su,exp}} + a_2 \cdot N^*_{\text{exp}} \tag{4.46}$$

$$r_{\text{p,max}} = r_{\text{p,max,n}} + a_3 \cdot p^*_{\text{su,exp}} + a_4 \cdot N^*_{\text{exp}} \tag{4.47}$$

$$y_{\max} = y_{\max,\text{n}} + a_5 \cdot p^*_{\text{su,exp}} + a_6 \cdot (N^*_{\text{exp}} - N^*_{\text{exp,n}})^2 \tag{4.48}$$

where the "star" exponent indicates the non dimensional form expressed as:

$$X^* = \frac{X - X_n}{X_n} \tag{4.49}$$

The n subscripts indicates the selected reference conditions. Plotting the expander efficiency (y-axis) versus the pressure ratio (x-axis) for the reference conditions allows to identify the

mathematical meaning of some of the parameters used in Equations 4.45-4.48: $r_{p,0,n}$ is the intercept of the efficiency curve on the x-axis, δ_n is the slope of the efficiency curve close to the x-intercept, ξ is the shape of the efficiency curve, $y_{max,n}$ is the maximum efficiency, $r_{p,max,n}$ and $N_{exp,n}$ are the optimal pressure ratio and expander rotational speed respectively.
As far as the filling factor ϕ is concerned, in case the expander swept volume is not known, the group $\phi \cdot V_s$ can be considered as a single variable defined as:

$$\phi \cdot V_s = \frac{\dot{m}_{pred}}{N_{exp} \cdot \rho_{su,exp}} \tag{4.50}$$

where $\dot{m}_{pred}$ is the mass flow at expander inlet, predicted with a second order polynomial law with cross terms as a function of the non-dimensional expander inlet pressure $p^*_{su,exp}$ and expander rotational speed N^*_{exp} as shown in Equation 4.51:

$$\phi \cdot V_s = \frac{b_0 + b_1 \cdot p^*_{su,exp} + b_2 \cdot (p^*_{su,exp})^2 + b_3 \cdot N^*_{exp} + b_4 \cdot (N^*_{exp})^2 + b_5 \cdot p^*_{su,exp} \cdot N^*_{exp}}{N_{exp} \cdot \rho_{su,exp}} \tag{4.51}$$

It is characterized by two flow connectors for the fluid inlet and outlet and by a mechanical connector for the connection with the generator model. In this model, the user has the choice of providing a constant isentropic and volumetric efficiencies, or providing performance curves in the form of a Modelica function. The performance curves based on equation 4.51 and 4.42 can be selected through an enumeration tab from the general parameter window of the model.

4.5.2 Pump

The pump is modelled by two empirical correlations, one for the isentropic efficiency and one for the delivered mass flow rate. The isentropic efficiency is simulated with a second order polynomial with cross terms as a function of the non-dimensional pressure ratio, $r^*_{p,P}$, and the non-dimensional pump frequency, f^*_P, as shown in Equation 4.52:

$$\varepsilon_{is,P} = c_0 + c_1 \cdot f^*_P + c_2 \cdot (f^*_P)^2 + c_3 \cdot r^*_{p,P} + c_4 \cdot (r^*_{p,P})^2 + c_5 \cdot f^*_P \cdot r^*_{p,P} \tag{4.52}$$

The mass flow rate is expressed as a first order polynomial as a function of the non-dimensional pump frequency, f^*_P as shown in Equation 4.53:

$$\dot{m}_P = d_0 + d_1 \cdot f^*_P \tag{4.53}$$

The empirical coefficients (a_x, b_x, c_x, d_x) for the different performance curves need can be identified from the acquired measurements of the test unit under study.
It is characterized by two flow connectors for the fluid inlet and outlet and by a real input to set the frequency or the flow fraction depending on the requirements. In this model, the user has the choice of providing a constant isentropic efficiency, or providing a performance curve in the form of a Modelica function. The performance curve based on equation 4.52 can be selected through an enumeration tab from the general parameter window of the model.

4.6 Tanks

4.6.1 Liquid receiver

In small scale organic Rankine power systems, a tank is often placed at the outlet of the condenser to collect the refrigerant charge and avoid that the latter accumulates in the condenser increasing the condensing pressure. For this reason a liquid receiver model is included in the ThermoCycle library. The model is based on the assumption that the liquid and vapour phase are in thermodynamic equilibrium at all times, i.e. the vapour and liquid are assumed saturated at the given pressure. Accumulation of mass and energy is accounted for. The density is expressed as a function of the liquid level as:

$$\rho = \rho_l \cdot L + (1 - L) \cdot \rho_v \tag{4.54}$$

where L is the level of saturated liquid in the tank. Substituting Equation 4.54 in Equation 4.5 and after some algebraic manipulations the mass balance for the liquid receiver results as:

$$V \cdot \left((\rho_l - \rho_v) \cdot \frac{dL}{dt} + \frac{dp}{dt} \cdot \left(\frac{d\rho_l}{dp} \cdot L + (1 - L) \cdot \frac{d\rho_v}{dp} \right) \right) = \dot{m}_{su} - \dot{m}_{ex} \tag{4.55}$$

As far as the energy balance is concerned, the ρh term can be expressed as:

$$\rho h = L \cdot \rho_l h_l + (1 - L) \cdot \rho_v h_v \tag{4.56}$$

Substituting Equation 4.56 into Equation 4.6 and rearranging the terms yields the energy balance for the liquid receiver:

$$\begin{aligned} V \cdot \left(\frac{dL}{dt} \cdot (h_l \rho_l - h_v \rho_v) + \left(L \cdot (h_l \frac{d\rho_l}{dp} + \rho_l \frac{dh_l}{dp}) + (1 - L) \cdot (h_v \frac{d\rho_v}{dp} + \rho_v \frac{dh_v}{dp}) \right) \cdot \frac{dp}{dt} \right) = \\ = (\dot{m}h)_{su} - (\dot{m}h)_{ex} + V \frac{dp_{tot}}{dt} \end{aligned} \tag{4.57}$$

The effect of non-condensable gases is simulated by calculating the total pressure of the system, p_{tot}, as the sum of the pressure of the working fluid, p, plus a constant term accounting for the partial pressure of the gases. The model is developed in such way that it requires only one saturation call to the thermodynamic properties in order to avoid unnecessary computational efforts. Pressure, p, and liquid level, L, are defined as state variable.

4.6.2 Lumped Volume

In order to account for fluid stored in liquid phase in the pipes of a thermo-hydraulic system, a lumped volume model is developed and included in the ThermoCycle library. The model is based on a dynamic mass and energy balance, pressure is imposed as an input. The static pressure head due to the liquid level and possible thermal energy losses are taken into account.

The mass and energy balance are defined as follows:

$$M_{\mathrm{l}} \cdot \frac{dh}{dt} = \dot{m}_{\mathrm{su}} \cdot (h_{\mathrm{su}} - h) - \dot{m}_{\mathrm{ex}} \cdot (h_{\mathrm{ex}} - h) + A_{\mathrm{l}} \dot{q} \tag{4.58}$$

$$\tag{4.59}$$

The model comprises two flow connectors and one lumped thermal port connector. During normal operation the fluid flows from the InFlow connector and exits from the OutFlow connector. In case of flow reversal the fluid direction is inverted.

4.7 Pressure drop

In low capacity thermo-hydraulic systems, given the small length of the connection pipes pressure drops mainly occur in the vapour part of the heat exchangers. They can therefore be assumed lumped in the lowest vapour density part of both the low and the high pressure lines. This approach facilitates the convergence of the numerical iteration process and is valid when pressure drops are relatively small [125]. The proposed modelling formulation is also justified by the difficulty of accurately predicting pressure drop in two-phase plate heat exchangers: the available correlations usually provide divergent results, and a lumped pressure drop based on experimental data allows for an equivalent accuracy. The model is characterized by a linear and a quadratic term accounting for laminar and turbulent phenomena as shown in Equation 4.60:

$$\Delta p = \Delta p_{\mathrm{linear}} + \Delta p_{\mathrm{quadratic}}; \quad \Delta p_{linear} = k \cdot \dot{V}; \quad \Delta p_{\mathrm{quadratic}} = \frac{1}{A^2} \cdot \frac{\dot{m}^2}{2 \cdot \rho} \tag{4.60}$$

The parameters k and A can be experimentally identified. In case experimental data are not available, the model allows to compute the pressure drop based on nominal conditions provided by the user as parameters to the model.

4.8 Solar collector

Among concentrating solar power (CSP) technologies, parabolic trough collectors is the most appropriate technology for small-scale organic Rankine cycle systems [130]. Some CSP-ORC plants have been built since the 1950's [11] and in recent years ORC systems have been gaining popularity as a promising technology for this kind of application [26]. A set of parabolic trough models have been developed and included in the ThermoCycle library. The models represent the solar field, composed by a single or several loops of parabolic trough collectors. The large ratio between diameter and length allows a one dimensional (1D) discretization of the absorber tube. The SF model is composed by two sub-components: the $Flow1D$ model and the $SolAbs$ component. They are linked together through the thermal ports as shown in Figure 4.5.

The $Flow1D$ component models the heat transfer fluid flow in the heat collector element (HCE). It is based on one-dimensional (1D) dynamic mass and energy balance, discretized with the finite volume approach and static momentum balance as described in 4.3.2.

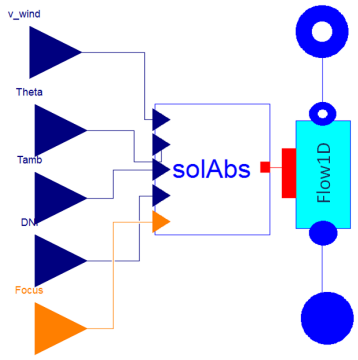

Figure 4.5 – Object diagram of the solar collector model from the GUI of Dymola.

The *SolAbs* component models the dynamic one dimentional radial energy balance around the HCE. Three different *SolAbs* models have been developed: the *SolAbsForristal*, the *SolAbsSchottSopo* and the *SolAbsSoltigua*.
The *SolAbsForristal* model is based on the steady-state model developed by Forristall [131] and represents the dynamic 1D radial energy balance around the HCE. It accounts for the conduction and thermal energy storage in the metal pipe, the convection and the radiation transfer in the vacuum chamber between the glass envelope and the metal pipe, the conduction and thermal energy storage in the glass envelope and the convection and the radiation transfer with the ambient air. The model implements the relations between the environmental parameters (DNI, Θ_{incid}, T_{amb}, v_{wind}) and the axial temperature distribution along the absorber. The thermal power transferred to the fluid ($\dot{q}_{conv,fl}$), the one discharged to the environment ($\dot{q}_{loss}$) and the temperatures of the metal pipe (T_t) and of the glass envelope (T_g), can then be evaluated. Two flags, *GlassUD* and *TubeUD*, allow setting the density, specific heat capacity and thermal conductivity of the glass and the metal tube as dependent on the glass and tube temperature respectively or as constant and user defined. A detailed description of the *SolAbs* model is reported in Appendix A.2.
The *SolAbsSoltigua* and the *SolAbsSchottSopo* solve the radial energy balance around the heat collector element based on correlations provided by the data sheet of existing parabolic through collectors. An empirically based correlations to compute the overall optical efficiency of the collector allows to compute the total heat flux absorbed by the tube in the *SolAbsSoltigua*, while a correlation defining the heat losses is used in the *SolAbsSchottSopo*. This approach eliminates any differential equations in the *SolAbs* component significantly increasing the computational efficiency of the overall parabolic through model. All the SolAbs models are characterized by an integer input *Focus*, which allows modelling the defocusing-focusing process of the solar collectors by changing the net collector area.

4.9 Handling of numerical problems

Dynamic modelling of thermodynamic cycles can be a challenging task, among others because of the numerous numerical issues arising both during initialization and during integration. In order to enhance the performance and the robustness of the ThermoCycle library, different numerical methods have been implemented. They are briefly presented and discussed in this section. A more detailed analysis can be found in A.5.

4.9.1 Initialization

The convergence of the Newton Solver during initialization is a key challenge when modelling complex system. Several strategies have been developed, such as the *homotopy* method [132]. In addition to this method, a slightly different approach is proposed in ThermoCycle: the system is initialized on a simplified system of equations, and the more complex non-linear equations, such as the computation of the heat transfer coefficients as a function of mass flow, are activated one by one during integration using an *initialization* component developed for that purpose.

4.9.2 Chattering and flow reversals

The phenomenon of chattering may occur when discontinuities in the model variables are present [126]. This phenomenon can lead to extremely slow simulation, or to simulation failures because the computed variables exceed acceptable boundaries. In discretized two-phase flow models, the main discontinuity often occurs in the density derivative on the liquid saturation curve. Simulation failures or stiff systems can occur if the cell-generated (and purely numerical) flow rate causes a flow reversal in one of the nodes due to this discontinuity. The computation of h_{su} and h_{ex} switches from one value to the other in equations 4.8 and 4.9. In addition to chattering, flow reversals can also result in a singular and non-solvable set of equations, as shown in [133]. A solvability criterion can be expressed as

$$h_{su} > h + \frac{\rho}{\frac{\partial \rho}{\partial h}}, \tag{4.61}$$

where $\partial\rho/\partial h$ is a negative term.
This inequality states that in cases of flow reversal, an unsolvable system of equations appears, if the enthalpy of the entering fluid is below a certain limit. A formal demonstration of this effect can be found in [133].
Therefore, to ensure the robustness of the simulation and to avoid chattering or unsolvable systems, two strategies can be employed:

1. Avoid flow reversals caused by the density derivative discontinuity, see equation 4.5.

2. If flow reversal occurs (it is physically possible), make sure that the backward flow enthalpy is higher than the limit described in equation 4.61.

The first strategy can be expressed by an inequality stating that purely numerical, cell-generated flow rates must be lower than the flow rate circulating through the cycle, which can be written

(for a single cell):

$$\dot{m}_{ext} \gg \frac{V}{N} \cdot \frac{d\rho}{dt} = \frac{V}{N} \cdot \left(\frac{\partial \rho}{\partial h} \cdot \frac{dh}{dt} + \frac{\partial \rho}{\partial p} \cdot \frac{dp}{dt} \right) \tag{4.62}$$

According to equation 4.62, flow reversals and thus chattering or simulation failures are likely to occur if:

- The number of cells (N) is low
- The working fluid flow rate ($\dot{m}_{ext}$) is low
- The internal volume (V) is high
- The working conditions are highly transient (i.e. dp/dt and dh/dt are high)

Different methods are implemented in ThermoCycle to avoid the simulation issues described above. Some are implemented at the Modelica level while others require a modification of the thermodynamic properties of the working fluid and are therefore implemented into CoolProp. It should also be noted that some of these methods have already been proposed in the literature, while some others are new. They are briefly described hereunder. A more comprehensive description of the different methods is reported in A.5.

- *Filtering method*: In this strategy, a first order filter is applied to the fast variations of the density with respect to time. This filter therefore acts as "mass damper" and avoids transmitting abrupt variations of the flow rate due the density derivative discontinuity.
- *Truncation method*: This strategy acts on the terms $\partial\rho/\partial p$ and $\partial\rho/\partial h$ of equation 4.62. The peak in the density derivative occurring after the transition from liquid to two-phase is truncated, reducing the numerical flow rate generated by the density derivative discontinuity.
- *Smoothing of the density derivative*: The idea behind this method is to smooth out the density derivative discontinuity using a spline function. Modifications of the thermo-physical properties are implemented at the level of the equation of state, i.e. inside the CoolProp database. The main drawback of this method is that the density function is still calculated with the original equation of state: the smoothed density derivative is not consistent with the density function provided by the EOS. This might cause a mass defect during the simulation.
- *Smoothing of the density function*: In order to avoid the mismatch between the density function and its derivative, one possible solution is to smooth the density for a range of vapour qualities (i.e. making it C1-continuous) and recalculating its partial derivatives in the smoothed area. In this situation, the density derivatives are continuous but not smooth, which should still be manageable for the solver.
- *Mean densities method*: The mean densities method was originally proposed by Casella [135] and successfully tested by Bonilla et al. [136]. It is also the method implemented in the ThermoPower Modelica library [37]. A mean density and its partial derivatives are computed in each cell as a function of the node densities, which eliminates the discontinuity in the partial derivatives.

- *The enthalpy limiter method*: Contrary to the previous methods, the enthalpy limiter method does not aim at avoiding flow reversals. Instead, it ensures that the system of equations remains solvable even in case of flow reversal. As indicated in equation 4.61, the enthalpy of the fluid entering a cell should have a minimum value, ensuring that the system of equations can be solved. The enthalpy limiter method is the practical implementation of this constraint in the cell model. It was originally proposed by Schulze et al. [133] and implemented in the TIL Modelica library.
- *Smooth Reversal Enthalpy*: In case of flow reversal a discontinuity appears in the computed node enthalpy. In this method, this is solved using a smooth transition function for the computation of the enthalpy as a function of the flow rate close to zero. The main drawback is the generation of a highly non-linear algebraic system that has to be solved by the simulator.

A comparison of these different methods, based on the simulation of a flow model with a high number of cells, in terms of simulation speed, simulation accuracy and mass and energy imbalance shows that adopting the proposed methods can dramatically improve the simulation performance and even allow to simulate flow reversals where traditional models generate simulation failures. The main concern is the error they introduce in the simulation results and the possible mass and energy unbalances they generate. In A.5, the methods have been tested on a test system submitted to highly transient conditions. Results have shown that although numerical artifacts are generated, the error remains of the same order of magnitude as the error linked to the standard finite volume model with a 10^{-4} tolerance. This is an important statement showing that the proposed models can ensure failure-free simulation even in highly transient conditions. It should also be noted that those transient conditions likely to generate chattering or stiff systems are usually concentrated in specific times of the simulation (e.g. start-up and shut-down), in which robustness is more important than accuracy.

4.10 Conclusions

In this chapter the structure and the main characteristics of the ThermoCycle Modelica library have been presented. The library has been built with a focus on small-scale thermo-hydraulic systems and its a fully open-source tool from the computation of the thermophysical fluid properties, using CoolProp [24], to the simulation of complex systems with their control strategies. The library design exploited the features of the open-source Modelica programming language, with a careful use of the inheritance, the class parametrization and the enumeration in order to avoid Matryoshka-type models and enhance model readability.
As the dynamics governing low capacity thermo-hydraulic systems are mainly concentrated in the heat exchanger (HE), particular care has been taken in the development of HE models. The two modelling approaches commonly adopted when modelling heat exchangers involving phase transitions, i.e., the finite volume and the moving boundary techniques, are developed together with a novel approach based on a robust logarithmic mean temperature difference. The HE model paradigms are described in details as they will be extensively used in the next

chapters of this thesis.
As far as rotary machines are concerned several models with different levels of details are available in ThermoCycle. In this chapter the ones based on a lumped approach and semi-empirical correlations with no dynamics are described as they are the most suited for system level simulations. A set of parabolic trough models have also been developed and included in the ThermoCycle library. Finally, the different numerical methods implemented in the library to increase model robustness have been described in the last section. The potential of these methods is analysed in detail in the next two chapter of the thesis.

Nomenclature

Acronyms	
LoD	level of detail
DAE	differential algebraic equation
EoS	equation of state
ORC	organic Rankine cycle
HE	heat exchanger
FV	finite volume
MB	moving boundary
GUI	graphical user interface
Subscripts	
P	pump
nom	nominal
n	reference
w	wall
hf	hot fluid
cf	cold fluid
int	internal
ext	external
pred	predicted
meas	measured
su	supply
el	electrical
ex	exit
sf	secondary fluid
wf	working fluid
s	isentropic

w	wall
l	lateral/saturated liquid
v	saturated vapour
exp	expander
Symbols	
p	pressure (bar)
T	temperature (°C)
s	specific entropy ($kJkg^{-1}K^{-1}$)
$\dot{V}$	volume flow rate ($m^3.s^{-1}$)
V_s	swept volume (m^3)
$\dot{q}$	heat flux ($kW.m^{-2}$)
M	mass (kg)
h	specific enthalpy ($kJ.kg^{-1}$)
ρ	density ($kg\,m^{-3}$)
A	area (m^2)
N	rotational speed (rpm)
Φ	filling factor
$\dot{W}$	electrical power (kW)
$\dot{m}$	mass flow rate ($kg.s^{-1}$)
L	liquid level (m)
U	heat transfer coefficient ($kJ.(kg.K)^{-1}$)
ε	efficiency
t	time

5 Validation of small-scale ORC systems based on the ThermoCycle Library

Abstract In this chapter the models presented in chapter 4 are validated at a component and at a system level against experimental results acquired on different facilities. The parabolic trough collector model is compared against a specific sets of dynamic experiments recorded at the Plataforma Solar de Almería. As for small-scale thermo-hydraulic systems the main dynamics are related to the physical phenomena characterizing the heat exchangers, the finite volume and the moving boundary ThermoCycle heat exchanger models are compared against transients experimental data recorded on the high pressure line of the test-rig presented in chapter 3. Finally a validation at a system level is presented. In particular measurements obtained from different operating conditions of the small-scale ORC system presented in chapter 2 are used to validate an ORC unit dynamic model. In light of the obtained results general guidelines for the dynamic modelling of thermo-hydraulic systems are outlined.

5.1 Introduction

The modular feature and simple layout make the ORC technology more adapted than traditional steam Rankine cycle units for the exploitation of distributed renewable energy sources which are often characterized by a temperature lower than that produced by the combustion of fossil fuels. Due to the non-constant nature generally characterizing renewable-based energy sources, specific control strategies ensuring safe and optimal operation of the ORC unit in any conditions are required. Before a control system can be designed the dynamic behaviour of the ORC unit needs to be well investigated [35, 37]. In this regard the adoption of dynamic models based on the first and second principles can play a fundamental role. Dynamic modelling can be adopted to evaluate and optimize the response time of a system under transient boundary conditions, to develop and test control strategies and to support the tuning of the controller.

In order to build the confidence for using a dynamic model, it is of paramount importance to ensure the model effectiveness in predicting the driving physical phenomena of the real system. This process is called Validation or Verification of the model and is a critical aspect in modelling and simulations. As no model is able to completely replicate the real system, specific validation test cases need to be designed in order to verify the model capability of predicting the transients of the real system it has been developed for. Two main aspects need

to be addressed during model validation:

- The suitability of the selected modelling structure, e.g. discretized, lumped etc.
- The identification of the model parameters

The two aspects are often approached simultaneously, i.e., parameters are optimized for different modelling structures which are then compared against data acquired on the real system. When comparing the simulation results against the experimental data of a real system, a reference simulation model needs to be defined. A model definition usually contains the declaration of variables, values that change with time in a continuous or discrete manner, and of parameters, values that are known a-priori and remain constant during the integration time. The variables of a model can be further classified in inputs and outputs. The former are provided by the external boundaries while the latter are endogenous to the model.
Small capacity ORC systems are characterized by faster dynamics compared to large power plants given the low volumes of the components. In particular the time constants characterizing the physical phenomena of the heat exchangers are the biggest and have the largest impact on the overall system transients [125, 137]. Properly predicting the heat exchanger dynamic trend is a crucial step towards the modelling of a whole ORC power unit.
Transient modelling of heat exchanger dates back to the late 70s [138] and mainly relied on the finite volume (FV) and the moving boundary (MB) modelling techniques [139] [140]. The first published work on transient modelling of heat exchanger in the Modelica language was proposed in 1997 by Mattsson [141]. He presented a shell and tube heat exchanger dynamic model for domestic hot water production based on the finite volume approach. Water at different temperatures was flowing in both side of the heat exchanger in liquid phase. A validation of the model for a transient consumption of the hot water was proposed. Bendapudi et al. [142] presented a comparison of the MB and FV modelling approaches against the experimental data of a 300 kW centrifugal chiller equipped with shell and tube heat exchangers working in transient conditions. It was concluded that, while the MB approach resulted 3 times faster than the FV one, the assumption of homogeneous flow in the two-phase region over-predicted the void fraction, leading to an under-prediction of the fluid charge. Comprehensive literature reviews on transient heat exchanger modelling can be found in [137, 143] and [144]. In general the moving boundary results in faster but sometimes less robust models [124] and remains a less common approach with respect to the finite volume one.
As far as dynamic modelling of the whole ORC system is concerned, most of the works available in literature focus on the application rather than the model validation. Quoilin et al. [145] developed a dynamic model of a small-scale ORC unit equipped with a volumetric expander, to analyse and compare different control strategies based on the regulation of the pump and expander rotational speed. A model based control strategy for ORC systems in automotive WHR was described in [146]. The control strategy was based on a reduced model of the evaporator and tested using an ORC dynamic model developed in Modelica as a reference. Rettig et al. [40] implemented a dynamic model of a low-capacity ORC system for stationary WHR in the Modelica language. The model was compared against experimental data and it was proposed as a starting point towards the implementation of a virtual test bed software

for design, analysis and virtual prototyping of ORC WHR systems. In the literature, other works underlined the advantages of adopting dynamic modelling for the development, the tuning and the comparison of different control strategies for WHR ORC systems [38, 39]. To the author's knowledge the only published work addressing the validation of a dynamic model of an ORC unit was presented by Casella et al. [118]. The dynamic, object-oriented model of a 150 kW_{el} commercial WHR ORC turbo-generator was compared against transient measurements, obtained while the plant was operating in closed loop. The shape of the response was therefore affected by the controller action. Recently in the applied thermo-hydraulic field, Qiao et al. [147] presented the validation of a Modelica model describing a flash tank vapour injection heat pump system. The model was able to replicate the major heat transfer and flow characteristic dynamics when compared against step change, start-up and shut-down transients.

Recent studies have envisaged the potential of small-capacity ORC-based CSP plants in case the future distributed energy scenario is considered [148, 149]. These power systems have been studied and prototypes were constructed in the 70's [12, 150]. Among CSP technologies, parabolic trough collectors allow reaching temperatures that perfectly fit the working conditions of ORC systems. In order to investigate the transients related to ORC-based CSP plants, it is fundamental to consider the transient related to the solar field. Dynamic models of parabolic trough collectors date back from the late '70s. Ray [151] presented in 1980 a non-linear dynamic model of a parabolic trough unit for direct steam generation. The finite volume modelling approach was adopted and the transient response of the model under different step disturbances was presented as typical results. Hirisch et al. [152] presented a finite volume based solar collector model of a DSG plant and a preliminary validation based on the first experimental results of the DISS facility at the plataforma solar the Almeria. A recent work from [144] reported a clear review of the major MB heat exchanger models capable of handling two-phase flows, and presented a moving boundary library developed in the Modelica language for the modelling of direct steam generation parabolic trough solar collectors.

Overall there is a lack of systematic work covering the validation of dynamic models for small-scale ORC power systems. This leads to the effort described in this chapter which focuses on the dynamic validation of some of the models included in the ThermoCycle Modelica library presented in chapter 4. One of the main assets of the experimental data presented in this work is its suitability for the validation of dynamic models: contrary to similar works in the same field, all measurements were performed in open-loop, which avoided the interferences of controller in the measured dynamic response. The shape of the transient responses is entirely determined by the intrinsic dynamics of each component, which could have been corrupted, e.g. by the slow response of a proportional-integral-derivative (PID) controller in the loop.

The structure of the chapter is as follows: section 5.2 presents a comparison of the solar collector model against experimental data collected on the PTTL facility of the Plataforma Solar de Almería, Spain. Section 5.3 deals with the dynamic validation of the finite volume and moving boundary heat exchanger models with a set of experimental data acquired on the heat exchanger test rig presented in chapter 3. In section 5.4 the dynamic model of an ORC

unit is validated against an experimental dataset of the stationary sub-critical 11 kW_{el} ORC test rig presented in chapter 2. Finally in light of the obtained results, the main conclusions are listed in section 5.5.

5.2 Dynamic validation of parabolic trough collector model

The validation of the parabolic trough solar field (SF) dynamic model described in section 4.8 and based on the Forristal model (see Appendix A.2) is presented in this section. The model is compared against experimental data acquired on the PTTL facility at the Plataforma Solar de Almería (PSA), Spain.

5.2.1 Measurements and experiments

Experimental facility

An aerial view of the PTTL system is shown in Figure 5.1. The solar field was characterized

Figure 5.1 – Aerial view of the PTTL facility at PSA, Almería

by three parallel lines of parabolic trough collectors (PTC) from different manufacturers AlbiasaTrough, EuroTrough and UrssaTrough. The system was a closed loop, with an East-West orientation and it is charged with the thermal oil Syltherm 800 [153]. The process flow diagram of the PTTL facility is shown in Figure 5.2. Looking at the bottom of Figure 5.2 it is possible to recognize the pump which drove the fluid, in liquid state, through one of the three parallel PTC lines of the solar field. The fluid was heated from (2) to (3) by absorbing the solar energy reflected by the collectors to the receiver tubes. At the outlet of the collectors the fluid was cooled down by air-cooler II characterized by a maximum thermal capacity of 400 kW_{th}. Once cooled down the oil reached the pump suction port (1). A 1 m^3 expansion vessel with Nitrogen, N_2, inertization placed in between the two air coolers was used to regulate the loop pressure which was limited to 18 bar. In the whole circuit the oil was maintained in liquid state. Two electric heaters installed at the outlet of the pump allowed controlling the temperature of the oil at the inlet of the PTC lines. A mass flow meter at the outlet of the pump was used to measure the oil mass flow rate. The temperatures at the inlet and at the outlet of the PTC were measured with temperature transmittance (TT) sensors. The direct normal irradiance (DNI) was measured with a pyrheliometer model CH1 by Kipp& Zonen [154]. A

weather station installed nearby the solar field was used to measure the ambient temperature and the wind speed. The sensors signal outputs were acquired by a data acquisition system with a sampling time of 5 seconds and LabView was used for data visualization. During the

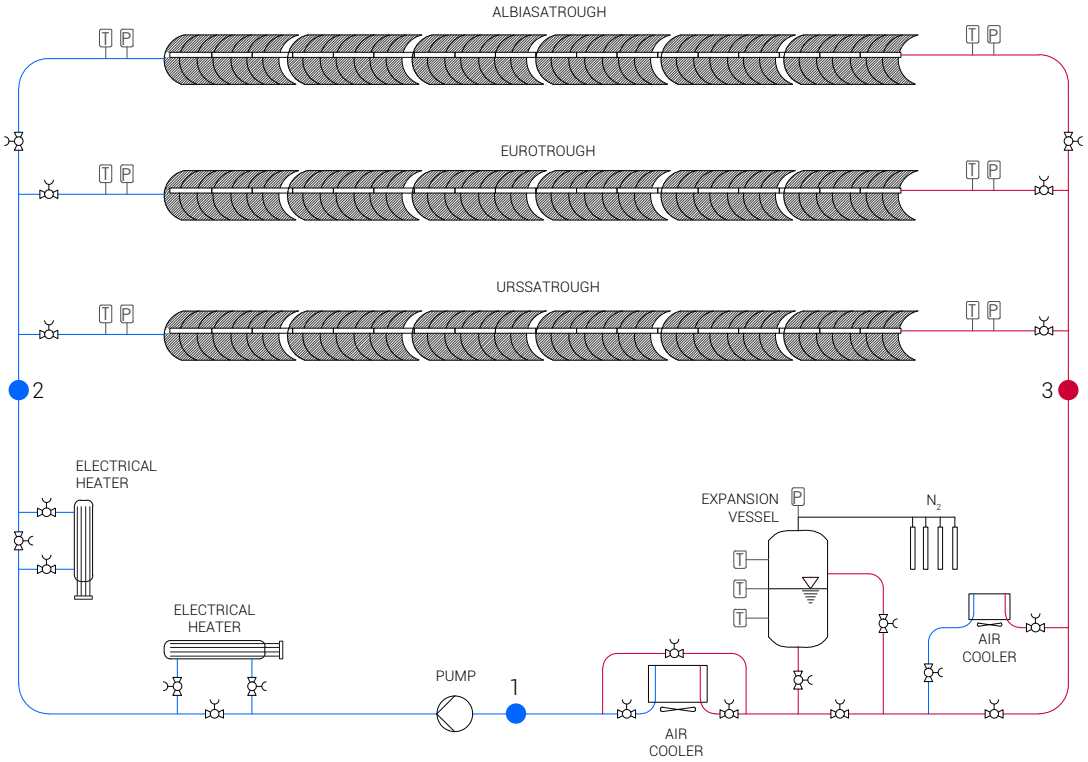

Figure 5.2 – Process flow diagram of the PTTL facility with the relative sensors positions.

experimental campaign on the PTTL facility, the EuroTrough collectors (ETC) line was tested. The ETC line was composed by 6 EuroTrough modules connected in series and 18 prototype receiver tubes from a Chinese manufacturer for a total length of 70.8 m and a net aperture area of 409.9 m^2.

Dynamic experiments

In order to characterize the dynamic performance of the ETC, the facility was run at different operating conditions by varying the pump speed velocity and the temperature at the inlet of the ETC for a total of 5 days of testing. In Table 5.1, the working conditions ranges of the main variables and of the external ambient conditions during the experimental campaign are reported. The dynamic validation was based on three specific sets of experiments:

- **MFE** - Oil mass flow change experiment: a step change was imposed to the oil mass flow rate at the inlet of the ETC by varying the pump speed velocity upwards or downwards starting from a steady-state condition.
- **TE** - Oil inlet temperature change experiment: the oil temperature at the inlet of the

Table 5.1 – Range of operation of the ETC main variable and of the external ambient condition during the experimental campaign.

Variable Unit	$\dot{m}_{oil,su}$ [kg s^{-1}]	$p_{SF,su}$ [bar]	$T_{oil,su}$ [°C]	$T_{oil,ex}$ [°C]	DNI [W m^{-2}]	T_{amb} [°C]	v_{wind} [m s^{-1}]
Min	1.55	12.96	150.05	170.21	593.95	26.23	0
Max	5.03	16.07	304.48	352.28	883.72	33.16	11.23

ETC was varied by shutting down the air cooler starting from a steady-state condition.

- **SBE** - Solar beam radiation change experiment: a step change to the solar beam radiations collected on the receiver was imposed downwards and upwards to the parabolic trough collectors by defocusing and focusing the parabolic trough collectors.

5.2.2 Initial conditions, model inputs and parameters

In order to compare the acquired dynamic experimental data with the modelling results a simulation framework was defined. A schematic representation of the system is shown in Figure 5.3. It comprised a mass flow source and a pressure sink connected to the fluid connectors of the SF model. The exogenous inputs (EI) imposed to the SF model and the

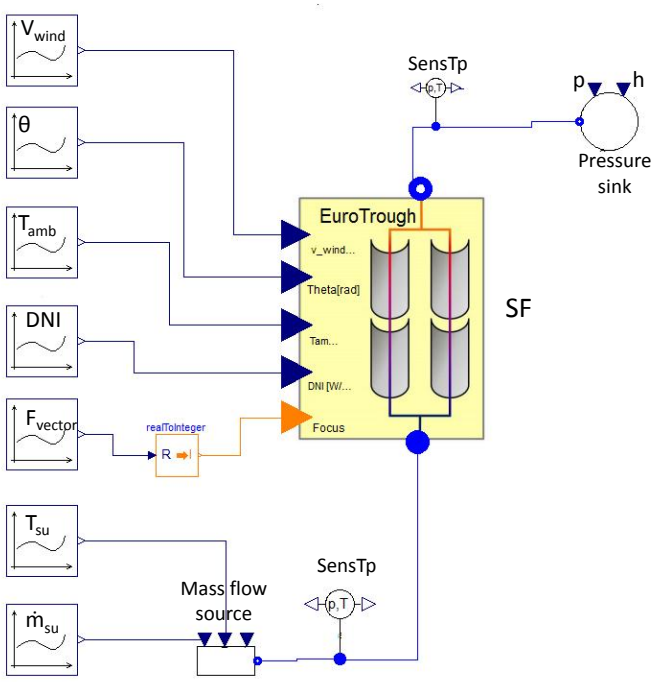

Figure 5.3 – Modelica model of the Eurotrough collector line installed in the PTTL facility from the Dymola graphical user interface (GUI).

relative unit are listed in Table 5.2. The SF model was parametrized based on the data-sheets of

Table 5.2 – List of exogenous inputs (EI) imposed to the SF model. v_{wind}: wind speed, Θ_{incid}: solar radiation incidence angle, T_{amb}: ambient temperature, DNI: direct normal irradiance, F_{vector}: vector for defocusing action, $\dot{m}_{oil,su}$: oil mass flow at SF inlet, $T_{oil,su}$: oil temperature at SF inlet, p_{ex}: oil pressure at SF outlet

EI	v_{wind}	Θ_{incid}	T_{amb}	DNI	F_{vector}	$\dot{m}_{oil,su}$	$T_{oil,su}$	p_{ex}
Unit	[m s^{-1}]	[Rad]	[°C]	[W m^{-2}]	[-]	[kg s^{-1}]	[°C]	[bar]

the EuroTrough collector and the receiver tubes. The incidence angle modifier (IAM), required for the optical efficiency calculation, was computed with an empirical equation as:

$$IAM = 1 - \frac{a_{I} \cdot \Theta_{incid} + a_{II} \cdot \Theta_{incid}^{2}}{\cos \Theta_{incid}} \tag{5.1}$$

where Θ_{incid} is the incidence angle of solar radiation and $a_{I} - a_{II}$ are two empirical parameters derived through an experimental campaign as described in [155] following the methodology presented in [156]. In order to consider unaccounted optical effects during testing, e.g., dirt on the parabolic mirrors and tube receivers, the parameter ϵ_{un} was included in the calculation of the optical efficiency. Its value was obtained through a least square optimization routine aimed at minimizing the error between the simulated SF outlet temperature and the measured one over a three minutes interval of the initial steady-state condition characterizing the first day of testing (see Figure 5.5). In Table 5.3 the values assigned to the parameters of the SF model are reported. The *GlassUD* and *TubeUD* options were set to false such that the density, specific heat capacity and thermal conductivity of the glass and the metal tube were computed as dependent on the glass and tube temperatures respectively. The heat transfer coefficient was computed based on the Gnielinski single phase correlation [128]. The thermal oil, Syltherm 800, flowing through the tube receivers was modelled as an incompressible fluid using the *TableBased* framework of the Modelica Standard library. As a consequence no mass accumulation was considered in the receiver tubes.

5.2.3 Results: dynamic validation

The SF Modelica model was run on Dymola2015. The Differential Algebraic System Solver (DASSL) [157] was selected as numerical solver, setting the relative tolerance to 10^{-4}. In order to increase the model robustness and decrease the computational time, the measured variables imposed as exogenous inputs to the SF model (see Table 5.2) are approximated by a spline function in the Modelica/Dymola simulation environment.
In Figure 5.4, the simulated ETC outlet temperature is plotted versus time and compared against the measured data for each of the three performed dynamic experiments. On the left abscissa the measured ETC inlet and outlet temperatures and the simulated ETC outlet temperature are plotted versus time. On the right abscissa the DNI and oil mass flow rate normalized with respect to the maximum value reached during the day are reported. For all the plots it is possible to see how the DNI was characterized by variation smaller than 2%. In

Table 5.3 – Values of the parameters for the SF Modelica model

Parameter	Units	Value
General parameters		
N - Number of discretized cells	[-]	20
L - PTC length	[m]	70.8
A_p - Parabola aperture	[m]	5.76
Optical properties		
ρ_{cl} - Mirror reflectivity	[-]	0.9388
τ_{gl} - Glass transmissivity	[-]	0.92
α_{gl} - Glass absorptivity	[-]	0.02
ϵ_{gl} - Glass emissivity	[-]	0.86
α_{tu} - Tube Absorptivity	[-]	0.7919
a_I - IAM coefficient I	[-]	$4.11e^{-3}$
a_{II} - IAM coefficient II	[-]	$5.513e^{-5}$
ϵ_{un} - Unaccounted	[-]	0.9437
Glass envelope geometries		
D_{gl} - External glass diameter	[m]	0.12
t_{gl} - Glass thickness	[m]	0.0025
Receiver tube geometries		
D_{tu} - External glass diameter	[m]	0.07
t_{tu} - Glass thickness	[m]	0.002
Vacuum properties		
p_{vacuum} - Vacuum pressure	[bar]	$1.333e^{-7}$
Γ - Ratio of specific heats for the annulus gas	[-]	1.39
Δ_{mol} - Molecular diameter for the annulus gas	[m]	$3.53e^{-10}$
k_{std} - Thermal conductivity at standard pressure and temperature	[W m^{-1}K^{-1}]	0.02551

Figure 5.4a the results for the MFE experiments and simulation results are reported. Starting from a steady-state condition two consecutive steps of the same magnitude upwards and downwards were imposed to the pump rotational speed at t=450 seconds and t=1430 seconds respectively. As the rotational speed increased at t=450 seconds, the velocity and pressure of the fluid in the high pressure line increased. This resulted in an oil mass flow rate, $\dot{m}_{oil,su}$, increment of about 40% in around 60 seconds. The increase in oil mass flow rate caused a drop in the temperature at the outlet of the ETC, $T_{oil,ex}$. The $T_{oil,ex}$ drop was registered at around t=500 seconds, 50 seconds after the oil mass flow rate started changing. This was due to the time required by the oil mass flow rate to reach the outlet of the 70.8 m long receiver tubes. During the experiments the ETC inlet temperature, $T_{oil,su}$, was maintained constant by manually manipulating the air cooler and electrical heaters power. When the oil mass flow rate was changed upwards, as $T_{oil,su}$ was expected to decrease the air cooler power was decreased and the electrical heaters power was increased manually, causing a small bump within 2 K in the temperature as it is shown in Figure 5.4a. The same phenomena in the opposite direction

took place when the pump speed was decreased. The ETC outlet temperature presented a symmetrical trend for the upwards and downwards oil mass flow rate change. The SF model was able to well predict the experimental trend both for the upward and downward steps and was characterized by a time constant slightly smaller than the real system.
In Figure 5.4b the TE experiments and simulation results are reported. Starting from a steady-state condition the air-cooler was turned off at t=900 seconds. This resulted in an increase of $T_{\text{oil,su}}$ and a consequently growth of $T_{\text{oil,ex}}$ delayed by around 100 seconds due to the time required by the oil mass flow to travel through the tube receiver. The shut-down of the oil-cooler did not allow to impose a step to $T_{\text{oil,su}}$ which increased with a slow first order trend. The large time constant characterizing $T_{\text{oil,su}}$ defined the change of the outlet ETC temperature. The SF model was able to correctly predict the experimental results including the delay characterizing the $T_{\text{oil,ex}}$ change.
Finally in Figure 5.4c the SBE experiments and simulation results are shown. Starting from a steady-state condition the ETCs were defocused at t=360 seconds, such that no solar radiation was reflected to the receiver tubes. This caused a sudden decrease of $T_{\text{oil,ex}}$ which reached the $T_{\text{oil,su}}$ value in about 200 seconds. The ETCs were focused again at t=650 bringing $T_{\text{oil,ex}}$ back to its initial value. During the experiment the oil mass flow rate and $T_{\text{oil,su}}$ were kept constant. The latter was maintained at its initial value by manually manipulating the power of the two electrical heaters installed after the pump. This resulted in a small bump of less then 4 K after the collectors were focused at t=700 seconds. The $T_{\text{oil,ex}}$ was characterized by a symmetrical behaviour during the focusing-defocusing experiments, as the thermal energy losses were relatively small. The SF model was able to replicate the trend and presented a slightly smaller time constant than the real system.
Overall it can be concluded that the SF Modelica model was capable of predicting the physical phenomena characterizing the real system behaviour during the three performed experiments and can be considered validated. In Figure 5.5 the simulation and experimental results for all of the five days of the experimental campaign are reported. In the first Figure, *Day I*, the three minutes time over which the ϵ_{un} parameter was optimized are highlighted by two vertical black dotted lines.

5.2.4 Results: number of tube receiver CVs parametric analysis

In order to investigate the effect of the level of discretization on the performance of the SF model when compared to the experimental results a parametric analysis was performed. The SF model, discretized with a number of control volumes (CVs) varying from 1 to 50, was simulated to replicate the experimental data of Day IV (see Figure 5.5). The results are displayed in Figure 5.6a where the simulated SF outlet temperature for the different levels of discretization is plotted versus time and compared against the measured experimental data on the left abscissa. On the right abscissa the nominal DNI and oil mass flow rate are plotted. Overall as the level of discretization increased the SF outlet temperature got closer to the measurements data. From 10 to 50 CVs the improvement in model accuracy was negligible. On the other hand the 5 CVs and 1 CVs SF model presented a slower time constant compared to the real system and were not able to properly predict the different undershoot and overshoot

characterizing the measured outlet ETC temperature when the boundary conditions where changed, e.g., step change in the mass flow or defocusing-focusing.
In Figure 5.6b the percentage computational effort (PCE) defined in equation 5.2 as the ratio of the computational time ($\text{Time}_{\text{Comp}}$) with respect to the simulated real time ($\text{Time}_{\text{Real}}$), is plotted for each simulation result. All the simulation results were characterized by a much shorter time compared to the real simulated time. This is related to the remarkably simple simulation framework on which the modelling results were based on (see section 5.2.2).

$$\text{PCE} = \frac{\text{Time}_{\text{Comp}}}{\text{Time}_{\text{Real}}} \cdot 100 \tag{5.2}$$

The computational time increased exponentially with the increase of number of CVs with the 1 and 5 CVs SF models being one order of magnitude faster than the higher discretized model. In order to assess the discrepancy between the different CVs discretization levels, the total energy absorbed by the thermal oil in the ETC collectors, E_{oil}, was computed as the integral of the thermal power over the simulated time, around 4 hours, and compared with respect to the 50 CVs model which was taken as a reference. The percentage relative error $\bar{\varepsilon}$ for each SF model was computed as:

$$\bar{\varepsilon}(k) = 100 \cdot \frac{|E_{\text{oil,50CVs}} - E_{\text{oil,k}}|}{E_{\text{oil,50CVs}}} \quad k \in [1,5,10,20]. \tag{5.3}$$

The results are reported in Table 5.4. As it possible to see, the overall percentage relative error

Table 5.4 – Total energy percentage relative error for the different levels of discretization of the SF model.

Model	$\bar{\varepsilon}$ [%]
SF CVs 1	0.5
SF CVs 5	0.18
SF CVs 10	0.08
SF CVs 20	0.03

on the total energy absorbed by the fluid over 4 hours of simulation with respect to the 50 CVs SF reference model was negligible for all the tested levels of discretization.

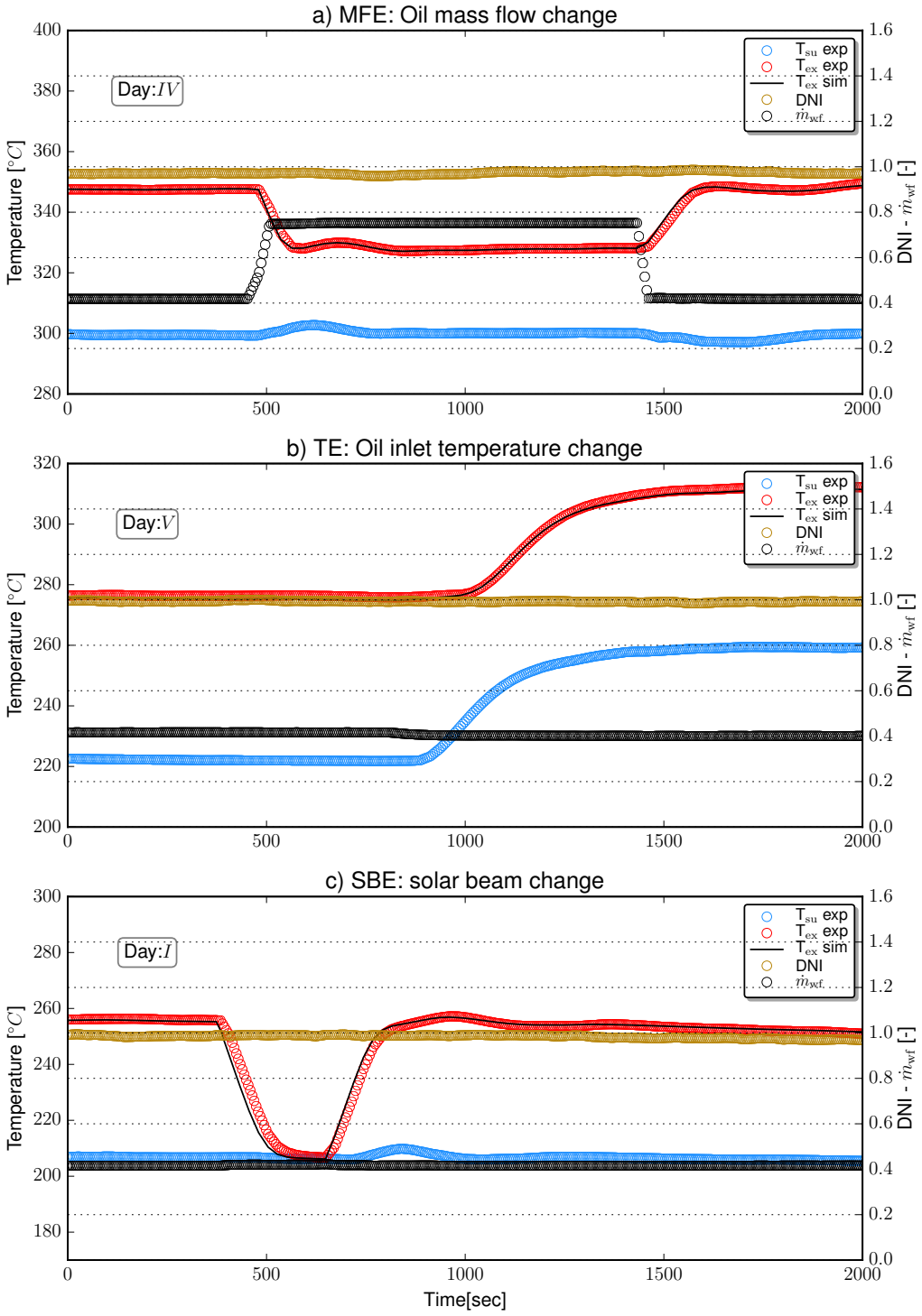

Figure 5.4 – Simulation and experimental results plotted versus time for: a) MFE - Mass flow change experiment b) TE - inlet ETC temperature change experiment c) SBE - solar beam radiation change experiment. The measured inlet and outlet ETC temperatures and the outlet SF model temperature are plotted on the left abscissa. The normalized DNI and oil mass flow rate values are plotted on the right abscissa.

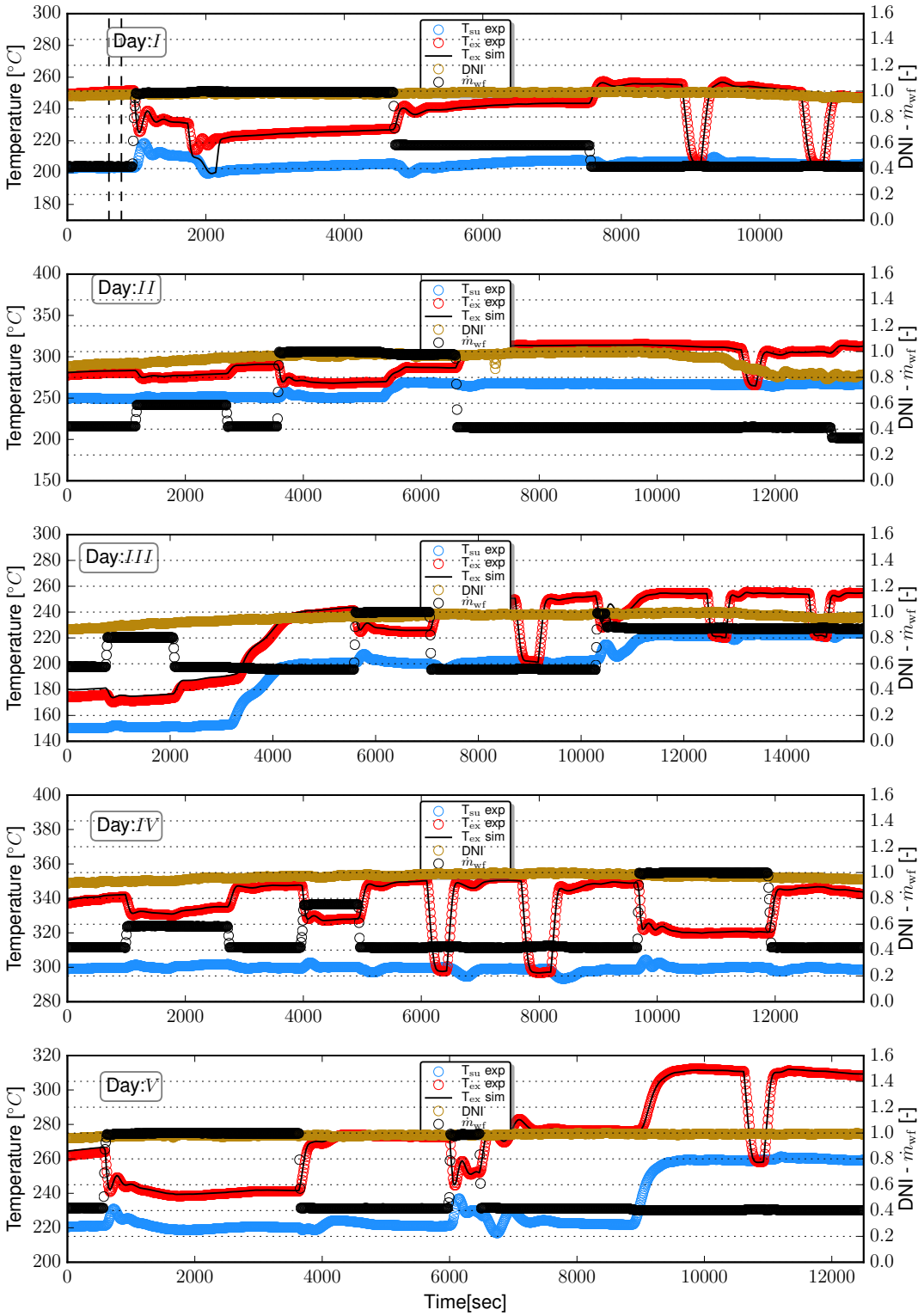

Figure 5.5 – Simulation versus experimental results for each full day of the experimental campaign plotted versus time.

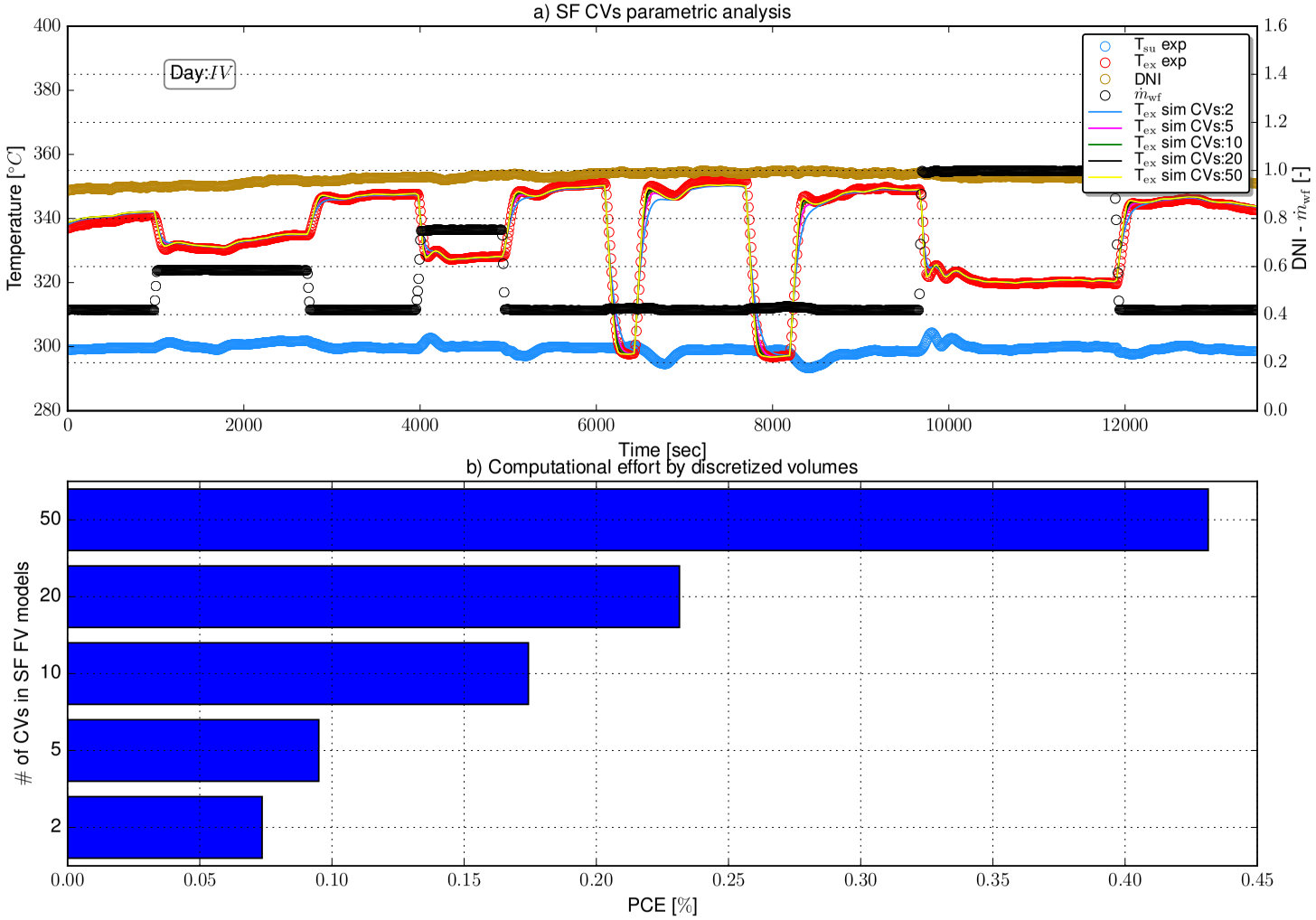

Figure 5.6 – Simulation results versus the experimental results for each full day of the experimental campaign. PCE: percentage computational effort.

5.3 Dynamic validation of heat exchanger models

In this section the finite volume (FV) and moving boundary (MB) dynamic heat exchanger models described in 4.3 are compared against a set of experimental dynamic data acquired on the heat exchanger test-rig described in Chapter 3.

5.3.1 Measurements and experiments

Experimental facility

The flow diagram of the high pressure section of the heat exchanger test rig presented in chapter 3 is shown in Figure 5.7. The oil and the refrigerant loops are depicted in red and

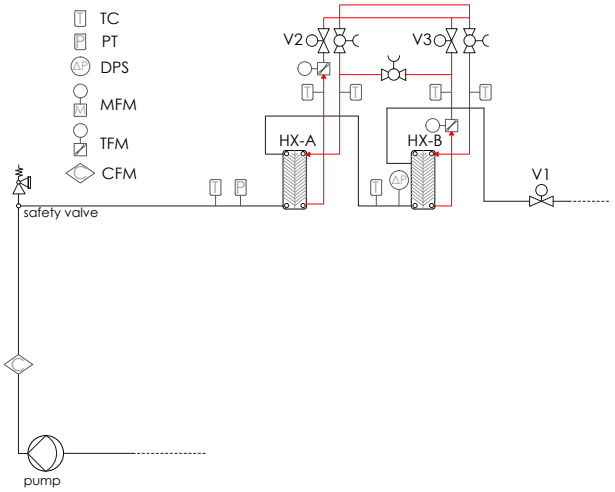

Figure 5.7 – Process flow diagram of the high pressure section of the HX-test rig with the relative sensors positions.

black respectively. The system was filled with HFC-245fa as working fluid. The refrigerant was pumped from the liquid receiver through the pre-heater, HX-A and the evaporator HX-B connected in series. The fluid exited HX-A in two-phase condition and got completely evaporated at the outlet of HX-B. The pre-heater and evaporator oil sides were arranged with a parallel configuration, i.e., the thermal oil inlet temperature was the same for both heat exchangers. The volumetric pump allowed to vary the mass flow while the valve, V1, was used to control the pressure. Type T thermocouples were used to measure the temperatures at the inlet and at the outlet of each components. A pressure transmitter measured the pressure at the inlet of HX-A. The refrigerant mass flow rate was measured with a coriolis flow meter installed at the outlet of the pump, while the oil volume flows at the outlet of HX-A and HX-B were measured by means of turbine flow meters. In Table 5.5, the uncertainties of the sensors are reported.

Dynamic experiments

A set of dynamic experiments was performed to investigate the transient phenomena characterizing the evaporation of the refrigerant through HX-A and HX-B. Starting from a steady-state

Table 5.5 – Range and precision of the measurement devices for the high pressure line of the HX test-rig. k: coverage factor. CFM: Coriolis flow meter. TFM: turbine flow meter.TC: thermocouple. PT: pressure transmitter.

Variable	Device type	Range	Uncertainty (k=2)
$\dot{m}_{wf}$	CFM	0-0.15 kg s^{-1}	± 0.06%
$\dot{V}_{oil}$	TFM	2-20 l min^{-1}	± 0.1 %
T	TC	20-180 °C	± 0.19 K
p_{wf}	PT	1-51 bar	± 0.45 %

condition, i.e., temperature oscillations below 0.5 K for 120 minutes, a step downwards was imposed to the volumetric pump rotational speed, causing a sudden decrease on the refrigerant mass flow rate. During the experiments on the oil side, the temperature and mass flow of the oil at the inlet of HX-A and HX-B were kept constant, on the refrigerant side the V1 valve aperture was fixed at a pre-defined value. The effect of the pump speed step change on the refrigerant and oil temperatures at the outlet of HX-A and HX-B was recorded with a sampling time of 0.1 seconds and compared against the finite volume (FV) and the moving boundary (MB) heat exchanger models from the ThermoCycle library.

5.3.2 Initial conditions, model inputs and parameters

Two simulation frameworks for the FV and MB modelling approaches were built in order to replicate the high pressure section of the HX test-rig. The layout of the models from the Dymola graphical user interface is shown in Figure 5.8. The system comprised two heat exchanger models connected via the fluid connectors to mass flow sources and pressure sinks. On the refrigerant side, one mass flow source imposed the mass flow sent by the volumetric pump through the heat exchangers, and a pressure sink was used to simulate the fixed aperture of the valve V1. On the oil side, two mass flow sources and two pressure sinks were connected to the inlets and to the outlets of the HXs models respectively. The former imposed the oil flow rate and temperature, the latter the pressure.

For the finite volume-based framework the same FV heat exchanger model was used to simulate HX-A and HX-B as the FV modelling technique is based on a spatial discretization where the same set of conservation equations can handle any states of the fluid. On the contrary, two different MB HX models were used as the MB approach is characterized by a discretization paradigm based on the number of fluid states. The flooded-evaporator and the dry-evaporator MB models were used for HX-A and HX-B respectively as shown in Figure 5.8b. The exogenous inputs (EI) imposed to the DTU test-rig models and the relative unit are listed in Table 5.2. The heat exchanger models were parametrized based on the SWEPT data-sheet. The parameters for the FV and MB HX-A and HX-B components are reported in Tables 5.7 and 5.8. As temperatures and mass flow of the oil side were kept stable during the experiments, the heat transfer coefficient of the oil side was calculated based on equation 3.32 at the oil average temperature for each HX and imposed as a constant to the model. On the working fluid side,

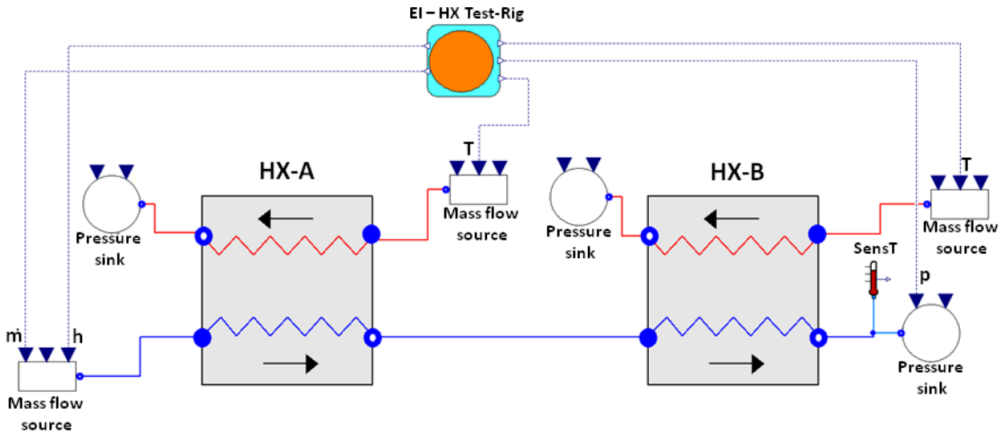

(a)

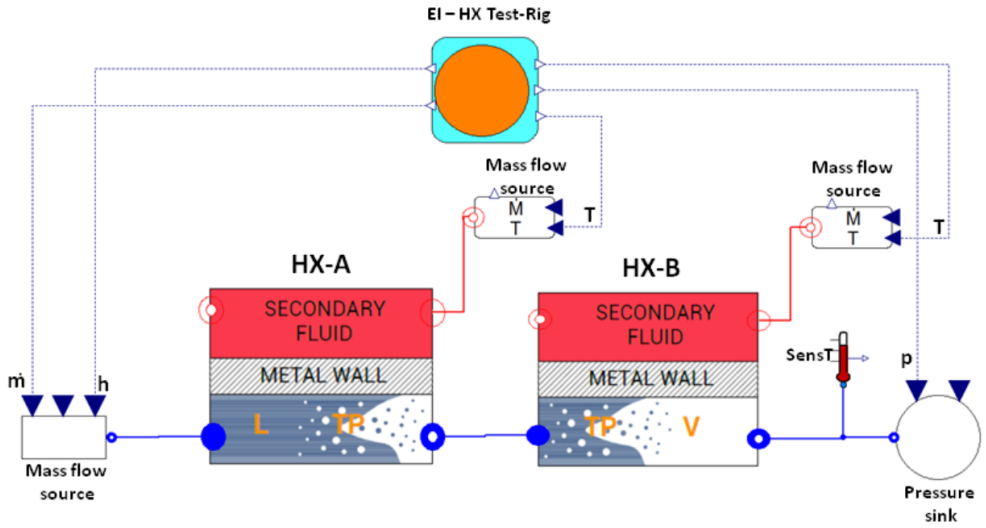

(b)

Figure 5.8 – Modelica model of the high pressure line of the HX-test rig from the Dymola graphical user. (a) Simulation framework based on the finite volume modelling approach. (b) Simulation framework based on the moving boundary modelling approach.

Muley and Mungley correlation [30] was used to compute the heat transfer coefficient of the liquid and vapour region, while the empirically derived correlation presented in chapter 3, equation 3.47, was used for the two-phase region. The models were initialized based on the values characterizing the steady-state condition before the step change was applied to the pump speed.

5.3.3 Results: dynamic validation

The HX test-rig models were run on Dymola2015. The Differential Algebraic System Solver (DASSL) [157] was selected as numerical solver, setting the relative tolerance to 10^{-4}. In order

Table 5.6 – List of exogenous inputs (EI) imposed to HX-A and HX-B models. $T_{oil,su}$: oil inlet temperature, $\dot{m}_{oil,su}$: oil inlet mass flow , $\dot{m}_{wf}$: refrigerant inlet mass flow , $h_{wf,su}$: refrigerant inlet enthalpy, p_{wf}: refrigerant outlet pressure.

EI	$T_{oil,su}$	$\dot{m}_{oil,su}$	$\dot{m}_{wf}$	$h_{wf,su}$	p_{wf}
Units	[°C]	[kg s^{-1}]	[kg s^{-1}]	[J kg^{-1}]	[bar]
HX-A	✓	✓	✓	✓	x
HX-B	✓	✓	x	x	✓

Table 5.7 – Parameters for the finite volume heat exchanger models.

Parameter	Units	Value HX-A	Value HX-B
Effective heat transfer area [wf,sf]	m^2	0.138	0.184
Total volume [wf,sf]	m^3	$7.2e^{-8}$	$1.2e^{-7}$
Metal wall mass	kg	1.41	1.56
Metal wall specific heat capacity	$J.(kg.K)^{-1}$	500	500
Nom. mass flow rate [wf]	$kg.s^{-1}$	0.06	0.06
Nom. mass flow rate [sf]	$kg.s^{-1}$	0.09	0.09

Table 5.8 – Parameters for the moving boundary heat exchanger models.

Parameter	Units	Value HX-A	Value HX-B
Channel cross section area [wf]	m^2	$4.56e^{-4}$	$6.08e^{-4}$
Channel perimeter [wf]	m	0.15	0.15
HX Total length	m	1.26	1.1
Metal wall mass	kg	1.41	1.56
Metal wall specific heat capacity	$J.(kg.K)^{-1}$	500	500
Nom. mass flow rate [wf]	$kg.s^{-1}$	0.06	0.06

to increase model robustness and simulation speed the exogenous inputs to the model are approximated as a spline function. The HX-A and HX-B FV models were discretized in 20 CVs respectively.

In Figure 5.9, the comparison between the measurements and the simulation results are reported. The refrigerant mass flow rate and temperature measured at the inlet of HX-A are shown in Figures 5.9a-b together with the relative spline function imposed as an input to the HX-test rig model. Starting from a steady-state condition, the pump speed step downwards was imposed at t=50 sec. As the pump speed was changed with a step signal, the refrigerant volume flow and thus the mass flow rate decreased. The refrigerant flow trend was characterized by a modest undershoot before reaching the second steady-state condition after around 100 seconds. The working fluid temperature at the inlet of HX-A slightly decreased by around 4 K. This transient, related to the heat exchangers installed on the low pressure side of the

test-rig (before the pump), was imposed to the model with a spline function as shown in Figure 5.9b.
In Figures 5.9c-d the oil temperatures at the outlet of HX-A and HX-B are depicted. The former resulted slightly affected by the pump speed step change and was characterized by a sharp peak of around 1.5 K when the refrigerant mass flow changed. The latter showed a distinct increase of around 5 K at the time the working fluid mass flow decreased. Both were characterized by a slow oscillation downwards of around 1 K between t=100 sec and t=500 sec, related to a variation of the oil inlet temperature and imposed to the model as an EI with a spline function (see Table 5.6).
As far as the working fluid HX-B outlet temperature is concerned, a fast increase of around 20 K was registered when the refrigerant mass flow changed, followed by a slow oscillations of less than 1 K related to the variation of the HX-B oil inlet temperature.
Overall the comparison between measured and simulated results showed a fair agreement for the MB and FV heat exchanger modelling approaches. Both models were able to correctly predict the oil and refrigerant outlet temperatures during the first 50 seconds of steady-state. After the pump speed was changed at t=50 sec, the main dynamics affecting the oil and refrigerant temperatures were properly predicted by the MB and the FV models. A larger off-set with respect to the experimental data characterized the MB simulation results compared to the FV ones. In particular, the MB-based model resulted slightly less precise in predicting the oil outlet temperatures. The simulated MB temperatures were in fact characterized by an offset of around 1 K with respect to the measured values after the pump speed step change was applied. In addition the MB model failed to predict the oil temperature peak registered at the outlet of HX-A. This can be explained by the simplified modelling approach characterizing the secondary fluid side of the MB models (see section 4.3.3). As the pump speed step change was applied, a downwards sharp peak of 1 K characterized the MB simulated HX-B oil and refrigerant outlet temperatures. This may be related to some numerical artefacts connected with the calculated two-phase heat transfer coefficient.
In terms of computational speed the MB-based model resulted three orders of magnitude faster than the FV-based model, characteristic that makes the MB approach an interesting solution despite the lower accuracy.

5.3.4 Results: Heat transfer coefficient analysis

In order to investigate the effect of employing detailed heat transfer correlations for simulating the thermal energy process in the 1-D FV and MB heat exchanger models additional simulations were run assuming a constant heat transfer coefficient (HTC) in the two phase region and the vapour quality dependance (VQD) heat transfer model (see section 4.4). The two-phase heat transfer coefficient was calculated based on equation 3.47 and imposed as a constant in the models. In Figure 5.10a-b-c the HX-A and HX-B oil and refrigerant outlet temperatures for the FV and MB models based on the VQD heat transfer coefficient ,α_{CONST}, are compared against the experimental data and the simulation results obtained with a correlation based heat transfer coefficient (α_{CORR}). Assuming a constant heat transfer coefficient led to slightly less precise results for the three predicted temperatures than adopting a correlation based HTC. The off-set between simulated and measured resulted increased with a maximum of around 1 K.

In Figure 5.10d the percentage computational effort computed with equation 5.2.2 is plotted for each of the four simulated models. The simulation time was within 10% of the real simulated time for all the simulated cases, being the HX-test rig model characterized by a simple structure composed by only two elements, i.e. HX-A and HX-B. As far as the MB models are concerned assuming a constant or a correlation based HTC didn't affect significantly the computational time. On the contrary the FV models employing the correlation based HTC resulted 1 order of magnitude slower than the FV model with a constant HTC and up to 3 orders of magnitude slower than the MB models.

These results led to the conclusion that for 1-D FV and MB based heat exchanger models designed to predict the temperatures at the outlet of the component employing correlation based HTC slightly increased the accuracy at the cost of a significant decrease of the simulation speed especially for the FV modelling approach. As for dynamic models of more complex systems, where several components are connected together, the simulation time is expected to increase considerably, it is recommended to employ constant based rather than correlation based HTC to avoid extremely low models and increase the overall robustness.

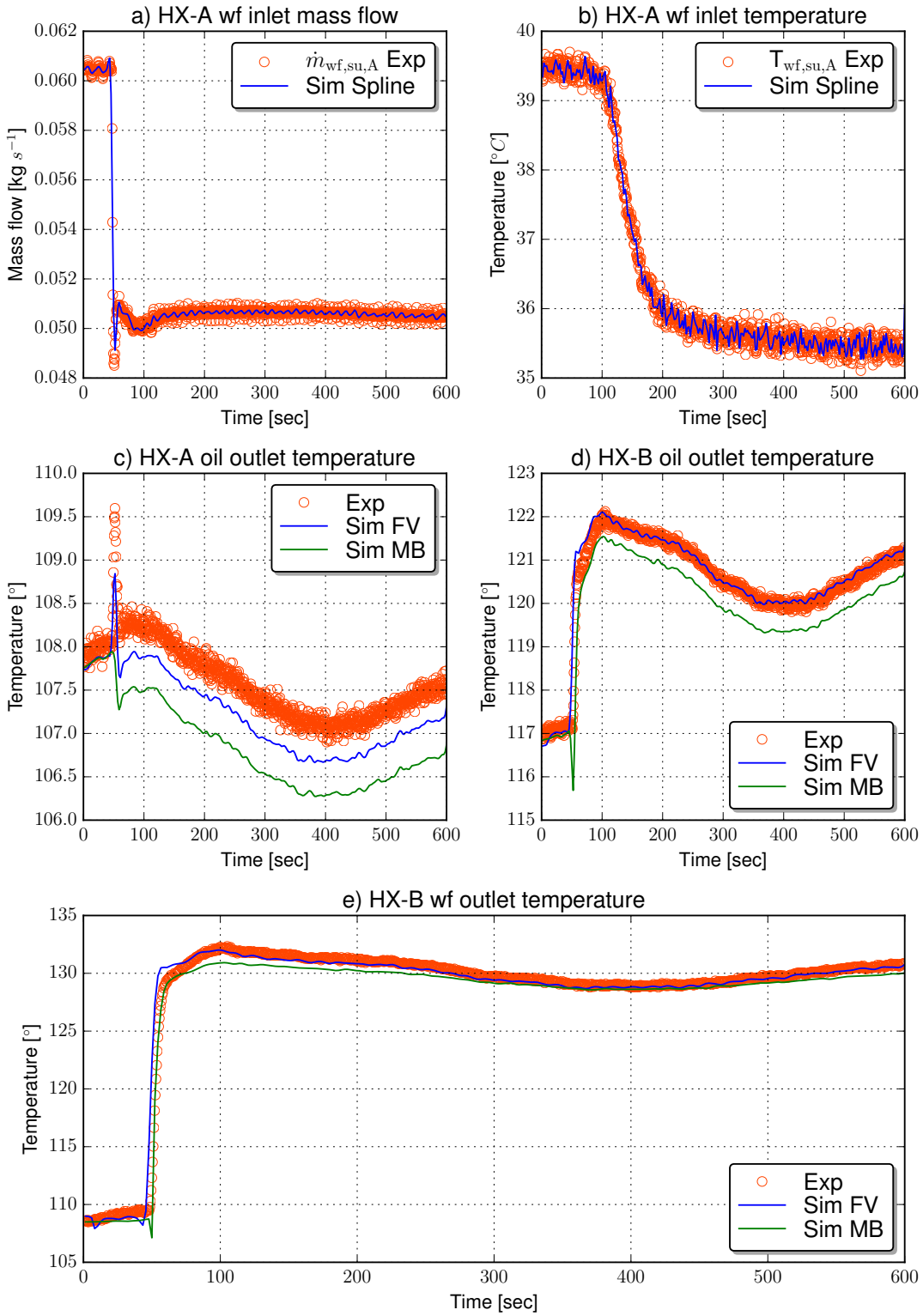

Figure 5.9 – Simulation and experimental results for the downward step change to the refrigerant volumetric pump plotted versus time.

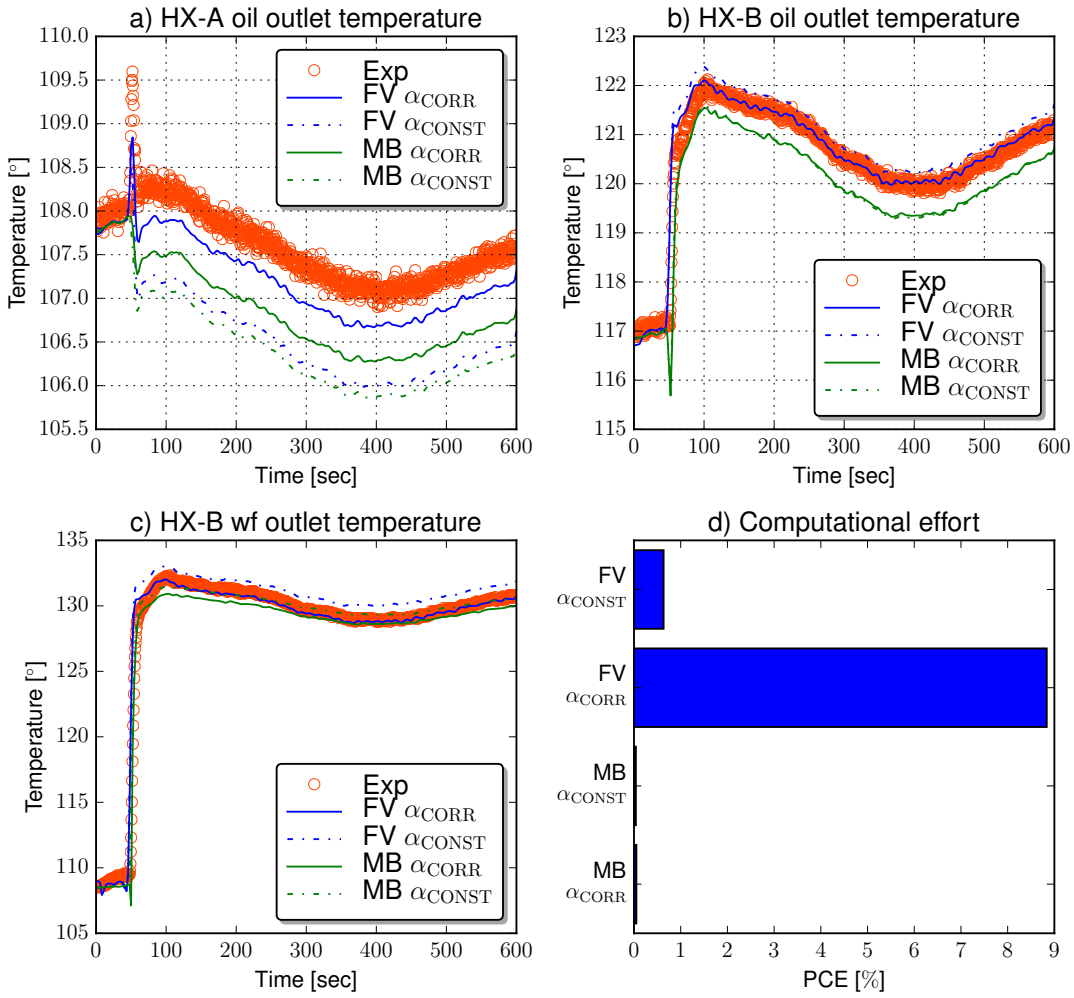

Figure 5.10 – Results of the heat transfer coefficient analysis on the FV and MB models. α_{CONST}: constant heat transfer coefficient , α_{CORR}: correlation based heat transfer coefficient, PCE: percentage computational effort.

5.4 Dynamic validation of a small-scale ORC unit dynamic model

In this section the dynamic validation of the Modelica model of a small-scale ORC unit is presented. The component models of the ThermoCycle Modelica library described in Chapter 4, are interconnected together to simulate the 11 kW_{el} ORC power unit presented in Chapter 2.

5.4.1 Measurements and experiments

Experimental facility

For the sake of readability the essential characteristics of the ORC power unit available at the laboratory of Ghent University campus Kortrijk are reported. Thermal oil Therminol66, pumped through an electrical boiler to temperatures of up to 125°C, serves as the energy

source of the ORC system. The front view of the ORC unit is depicted in figure 5.11a. A feed-forward controller in combination with a proportional integral (PI) controller ensured a constant oil temperature at the inlet of the evaporator when the ORC unit underwent transient conditions (e.g. change of the ORC pump rotational speed). Solkatherm (SES36) was used as the working fluid and it was cooled down in the condenser by means of a variable flow rate of glycol-water mixture. Oil was added to the working fluid (mass concentration of 3%) to lubricate the rotor while the bearings were lubricated through a by-pass pipe from the pump outlet to the expander. The expander was obtained by modifying a single-screw compressor to operate in expansion mode. The SWEP B200T SC-M brazed plate heat exchanger type was used for the evaporator, recuperator and condenser. The component counted 150 plates. The absolute pressure sensors (APS) and resistance temperature detectors (RTD) were placed at the inlet and at the outlet of each ORC unit component. The working fluid mass flow rate was measured by means of a Coriolis flow meter (CFM). An ultrasonic flow-meter (UFM) and pressure difference transmitter (DPS) were used to measure the volume flow rate of the heat sink and heat source respectively. The expander generator and the pump motor were connected to two inverters which allowed controlling the rotational speed of the machines. The generator electrical power was measured directly from the drive (DG). During the experimental campaign, the evaporator was insulated with a glass wool layer. The data acquisition was performed by means of a programmable logic controller (PLC) with a sampling time of one second. The range and the precision of the measurement devices are reported in Table 5.9.

Table 5.9 – Range and uncertainty of the measurement devices. k: coverage factor. The percentage errors are relative to the full scale.

Variable	Device type	Range	Uncertainty (k =2).
Mass flow (ORC)	CFM	0 kg s^{-1} to 1.8 kg s^{-1}	± 0.09%
Temperature (ORC)	RTD	50°C to 300°C	± 0.2 K
Temperature (heat sink)	RTD	0°C to 150°C	± 0.2 K
Temperature (heat source)	RTD	30°C to 350°C	± 0.2 K
pressure	APS	0 bar to 16 bar	± 0.016 bar
El. Power	DG	0 to 34.6 kW	± 0.1%
Volume flow (heat sink)	UFM	0.3 m^3 h^{-1} to 31.5 m^3 h^{-1}	± 0.9%
Volume flow (heat source)	DPS	0 m^3 h^{-1} to 18 m^3 h^{-1}	± 0.8%

Steady-state and dynamic experiments

In order to characterize the performance of the ORC test unit, 36 steady-state points were collected for different operating conditions, by varying the pump and expander rotational speeds, the heat source mass flow rate and the cooling fluid temperature at the condenser inlet. The system was run in stable conditions with temperature variations below 1 K for 10 minutes and the steady-state point was recorded by averaging the measurements over a period of 3 minutes. The acquired data were used to calibrate and to validate the model in steady-state.

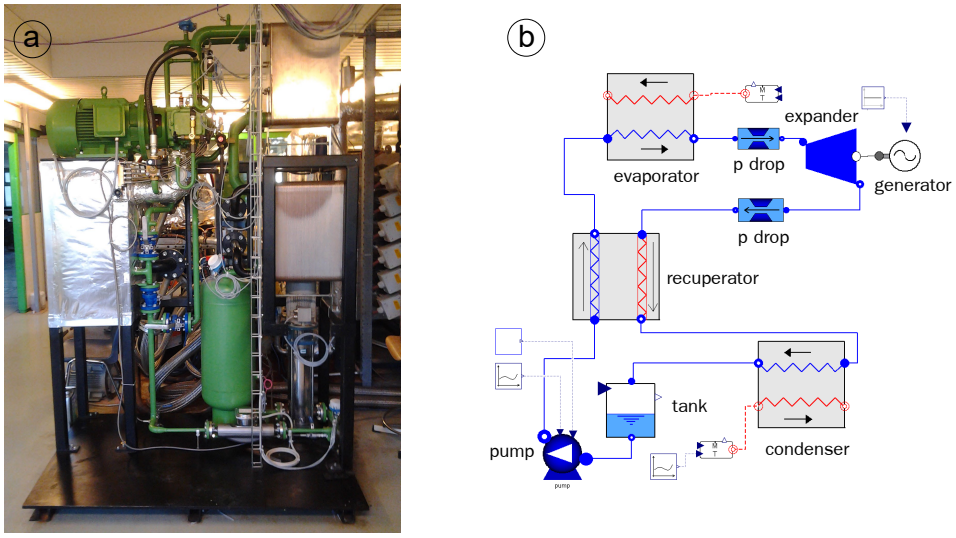

Figure 5.11 – (a) Front view of the ORC test-rig (b) ORC model from the Modelica-Dymola GUI.

The dynamic validation was based on two specific sets of experiments. In the first experiment, starting from a steady-state condition with an output power of 5.5 kW_{el}, two step changes of 5 Hz, one downwards and one upwards, were applied to the pump rotational speed through the drive signal. The amplitude of the step corresponded to the action that a PI controller would have imposed to the pump component to control the super-heating level in the evaporator. It should be noted that a step excitation is the worst-case scenario since it covers the whole frequency spectrum. In normal operation, lower frequencies are expected, which reduces the stress on the system. The goal of the experiment consisted in evaluating if the model was able to reproduce the system response when subjected to typical controller action. The successive upwards and downwards step signals allowed checking the symmetry of the system reaction. The second experiment aimed at analysing the dynamics characterizing the unit when the system was suddenly brought to a highly off-design operating condition. Starting from a steady-state condition, a downward step of 15 Hz was sent to the pump drive causing a decrease of the expander output power of around 90% and a significant increase of the super-heating. During the two sets of dynamic experiments, the ORC test rig was running in open-loop, such that the shape of the transients response was entirely determined by the time constants of the ORC components. In the oil loop, the mass flow rate was kept constant throughout the dynamic experiments. Furthermore, the controller allowed maintaining the Therminol66 evaporator inlet temperature close to a defined set-point acting on the boiler electrical heaters.

5.4.2 Initial conditions, model inputs and parameters

When modelling complex physical processes such as a whole power unit, the convergence of the solver during the initialization phase is not guaranteed. Initial conditions need to be user-specified in order to start the integration process. In the proposed model, steady-state

energy balances were set in the heat exchanger models to ensure robust initialization. The complete list of steady-state initial equations imposed to the system is reported in Table 5.10. Furthermore, initial guesses to the variables of each component were provided to the models

Table 5.10 – Initial equations imposed to the FV heat exchanger models. The subscript I refers to the working fluid in the evaporator/condenser and to the cold side in the recuperator. The subscript II refers to the secondary fluid in the evaporator/condenser and to the hot side in the recuperator.

Initial equations		Evaporator	Condenser	Recuperator
$\frac{dh_{\mathrm{I}}}{dt} = 0$	(5.4)	✓	✓	-
$\frac{dh_{\mathrm{II}}}{dt} = 0$	(5.5)	✓	✓	✓
$\frac{dT_{\mathrm{wall}}}{dt} = 0$	(5.6)	✓	✓	✓

using the built-in Modelica operator *start* [158]. The guess values were based on the operating conditions characterizing the system before the first 5 Hz step downwards was applied. The mass flow rates and inlet temperatures of the heat source and the heat sink were provided as external variables to the ORC unit model. The complete set of exogenous inputs imposed to the model is reported in Table 5.11.

The heat exchanger and liquid receiver models were parametrized based on the technical data-sheet and their values are reported in Table 5.12. In light of the results presented in section 5.3, the vapour quality dependance model was selected for the heat transfer coefficients whose nominal values were computed based on correlations available in the literature [30, 76, 92, 159]. The obtained HTC values were slightly modified to match the initial steady-state point of the 5-Hz and 15-Hz dynamic experiments. The parameters of the semi-empirical expander isentropic efficiency model, defined in Equations 4.42 - 4.48, are reported in Table 5.13. In Table 5.14 and 5.15 the parameters of the correlations describing the mass flow rate at the expander inlet, $\dot{m}_{\mathrm{pred}}$ (Eq. 4.51), and the pump efficiency, $\varepsilon_{\mathrm{is,P}}$ (Eq. 4.52), are respectively listed. The coefficients for pressure drop correlations in the high and low pressure lines are shown in Table 5.16. The empirical parameters were identified using robust regression methods [160] on the 36 steady-state points (see chapter 2). In Table 5.16, it can be noted that the coefficient of determination R^2 exhibited a low value for the pressure drop model. This is explained by the large cross-flow area characterizing the heat exchangers, resulting in low fluid velocity and low values of the pressure drop. The pressure difference being measured by two absolute pressure sensors, the accuracy was low and of the same order of magnitude as the measured value, resulting in a scarce prediction of the model. Furthermore, due to the low

repeatability of the pump performance measurements under the same boundary conditions, it was not possible to derive an accurate model to predict the working fluid mass flow rate in the form shown in Equation 4.53. The steady-state and transient simulations were therefore performed imposing the SES36 mass flow rate as an exogenous input (see Table 5.11). For all the performed simulations, the Modelica model was run on Dymola2015. The Differential Algebraic System Solver (DASSL) [157] was selected as numerical solver, setting the relative tolerance to 10^{-4}. The maximum simulation interval time was constrained to one second, equal to the sampling time of the PLC (see sub-section 5.4.1). The ExternalMedia package ensured the coupling between Modelica and the CoolProp software.

Table 5.11 – Exogenous inputs imposed to the ORC unit model.

Parameter	Units	Evaporator	Condenser	Expander	Pump
Secondary fluid mass flow rate	kg s^{-1}	✓	✓	-	-
Secondary fluid temperature	°C	✓	✓	-	-
Rotational speed	rpm - Hz	-	-	✓	✓
Working fluid mass flow rate	kg s^{-1}	-	-	-	✓

Table 5.12 – Parameters for the heat exchangers (evapoartor - recuperator - condenser) and the liquid receiver of the test-rig unit.

Parameter	Units	Value
Heat exchangers		
Effective heat transfer area [wf,sf]	m^2	16.18
Total volume [wf,sf]	m^3	0.0188
Metal wall mass	kg	69
Metal wall specific heat capacity	J.(kg.K)$^{-1}$	500
Liquid receiver		
Total Volume	m^3	0.06
Non-condensable gas pressure	Pa	34e3

5.4.3 Results: steady-state validation

The ORC model was compared against the 36 collected steady-state experimental points. The data were acquired for two different expander rotational speeds, 2000-3000 rpm, by varying the pump rotational speed and the temperatures and mass flow rates of the heat source and heat sink. In Figure 5.12, the model prediction for the expander inlet pressure and the net output power of the ORC unit model, as defined in Equation 5.7, are plotted versus the experimental values.

$$\dot{W}_{net} = \dot{W}_{el,exp} - \dot{W}_{P} \tag{5.7}$$

Table 5.13 – Empirical coefficients for the expander isentropic efficiency, R^2 = 91.3% (Eq.4.42 to 4.48).

Parameters	Description	Value
$r_{p,0,n}$	Intercept of the efficiency curve	3.076
δ_n	Slope of efficiency curve close to x-intercept	0.7924
ξ	Shape of the efficiency curve	1.213
$y_{max,n}$	Max efficiency for the reference conditions	0.592
$r_{p,max,n}$	Optimal pressure ratio for the reference conditions	10
$N_{exp,n}$	Optimal rotational speed for the reference conditions	3547
Empirical parameters:		
a_0 = 0; a_1 = 0.8411; a_2 = 8.347; a_3 = 3; a_4 = 3; a_5= 0.023383; a_6=0.4827		

Table 5.14 – Expander mass flow rate parameters, R^2 = 94.22% (Eq. 4.51)

Variable	Value
b_0	$4.13e^{-1}$
b_1	$5.53e^{-1}$
b_2	$2.02e^{-1}$
b_3	1.77^{-1}
b_4	-9.68^{-2}
b_5	1.66^{-1}

Table 5.15 – Pump efficiency parameters, R^2 = 79.8% (Eq.4.52).

Variable	Value
c_0	$1.64e^{-1}$
c_1	$2.61e^{-1}$
c_2	$3.93e^{-1}$
c_3	7.82^{-3}
c_4	1.91^{-5}
c_5	5.89^{-2}

Table 5.16 – Empirical coefficients for high (HP - R^2 = 47.4%) and low(LP - R^2 = 26.9%) pressure drop correlations (Eq. 4.60).

Parameters	Description	Unit	LP side	HP side
k	Linear term	[-]	1.782E07	0.000504
A	Quadratic term	[m^2]	0.000252	0.001508

The developed model was able to reproduce the measured data points with a good agreement. The pressure at the inlet of the expander was characterized by an accuracy within 5%. The electrical power output was reproduced with a 10% accuracy for most of the operating conditions. For extreme off-design conditions, the model predicted the experimental data with a maximum error of 30%. Such a low value is related to the inaccuracy of the derived semi-empirical expander, pressure drop and pump models to simulate the system operating conditions in the whole operational range of the ORC unit.

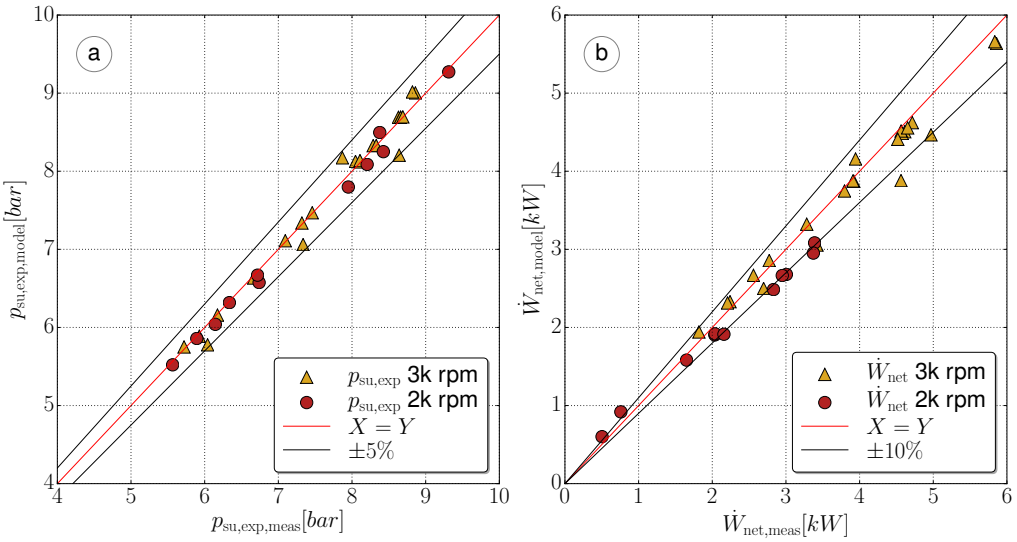

Figure 5.12 – (a) Parity plot for the expander inlet pressure and (b) the net output power of the ORC model compared against the experimental steady-state points. The squared and circular dots indicate an expander speed of 2000 and 3000 rpm respectively.

5.4.4 Results: dynamic validation

In this section, the simulation results are compared to the transient response of the ORC test unit. The finite volume (FV) recuperator model was discretized in 5 CVs as no phase transitions characterized the two fluid sides of the component. To handle the discontinuity characterizing the density in the regions around the saturation lines, the smooth density derivative method (SDD), described in [134], was activated in the CoolProp Solkatherm model and the condenser and evaporator heat exchanger models were discretized in 20 CVs. In section 5.4.6, a discussion investigating the reasons behind these choices is reported.

5-Hz step change

In figure 5.13, the comparison between the measurements and the simulations is shown for the 5 Hz step change experiments. The mass flow rate trend is reported in figure 5.13a. In order to increase the model robustness and computational efficiency, the measured mass flow rate was approximated by a spline function and imposed to the model [161]. Figure 5.13b shows the water-glycol temperature at the condenser inlet which is an exogenous input. For this specific dynamic experiment, in order to assess the transient response of the condenser two different modelling approaches were used to simulate the working fluid side of the condenser: the finite volume approach, described in section 4.3.2, and a simplified approach. In the latter a lumped model of the working fluid side was used, assuming steady-state mass and energy balances. The ORC models employing the simplified and FV approach for modelling the condenser are referred to as *ORC-LCond* and *ORC-FV*, respectively.

The steps downwards and upwards were imposed at t=300 seconds and t = 2061 seconds, respectively. When the pump speed was changed, the SES36 mass flow rate experienced an

overshoot which lasted a few seconds. As the pump speed was decreased and the expander rotational speed was kept constant, the velocity and pressure of the fluid in the high pressure line decreased. This resulted in a decrease of the vapour density at this point and consequently of the mass flow rate. The same phenomena in the opposite direction took place when the pump speed was increased. Despite the symmetrical characteristic of the upwards and downwards steps imposed to the pump rotational speed, the ORC unit response exhibited divergent trends due to the relations characterizing the thermodynamic cycle. The temperature at the expander inlet was fairly constant throughout the dynamic experiments. This was due to the oversizing of the evaporator heat exchange area which resulted in a very small pinch point, located at the outlet of the working fluid side (see Table 2.4). For this reason the evaporator outlet/expander inlet temperature is not plotted in Figure 5.13. The pressure at expander inlet and consequently the expander output power showed a very fast negative overshoot at t = 300 seconds, as depicted in Figures 5.13c-d. When the pump speed was increased, an overshoot of lower amplitude was registered for the same two variables. As far as the evaporator inlet temperature is concerned, a fast negative overshoot was registered when the pump speed was decreased, as shown in Figure 5.13e. The fast oscillation could be related to some disturbance in the temperature measurement device, as it was not visible in the next set point change.
On the low pressure side, as the pump speed changed, a sharp transient was recorded for the expander outlet pressure, followed by a much slower dynamics related to the temperature change of the cooling fluid at condenser inlet; as the working fluid mass flow decreased, the energy absorbed by the cooling fluid declined, since the thermal energy absorbed by the latter was rejected to the atmosphere by means of electric fans working at a fixed operating point. The temperature of the water-glycol mixture at the inlet of the condenser slowly reduced causing a decrease of the working fluid condensing pressure and thus temperature.
Overall, the comparison between measured and simulated trends showed a fair agreement for the *ORC-FV* model. On the low pressure side, it is interesting to note that the assumption of steady-state mass and energy balances in the condenser of the *ORC-LCond* model did not allow to capture the slow dynamics characterizing the expander outlet pressure, as shown in Figure 5.13f. The simplified condenser model also negatively affected the expander output power and the evaporator inlet temperature dynamics: the former was characterized by faster dynamics than the real system right after the step changes in the intervals t=400-500 seconds and t=2300-2500 seconds as shown in figure 5.13d, the latter exhibited a lower overshoot when the pump speed was changed and consequently higher off-set in the interval t=500-2000 seconds.

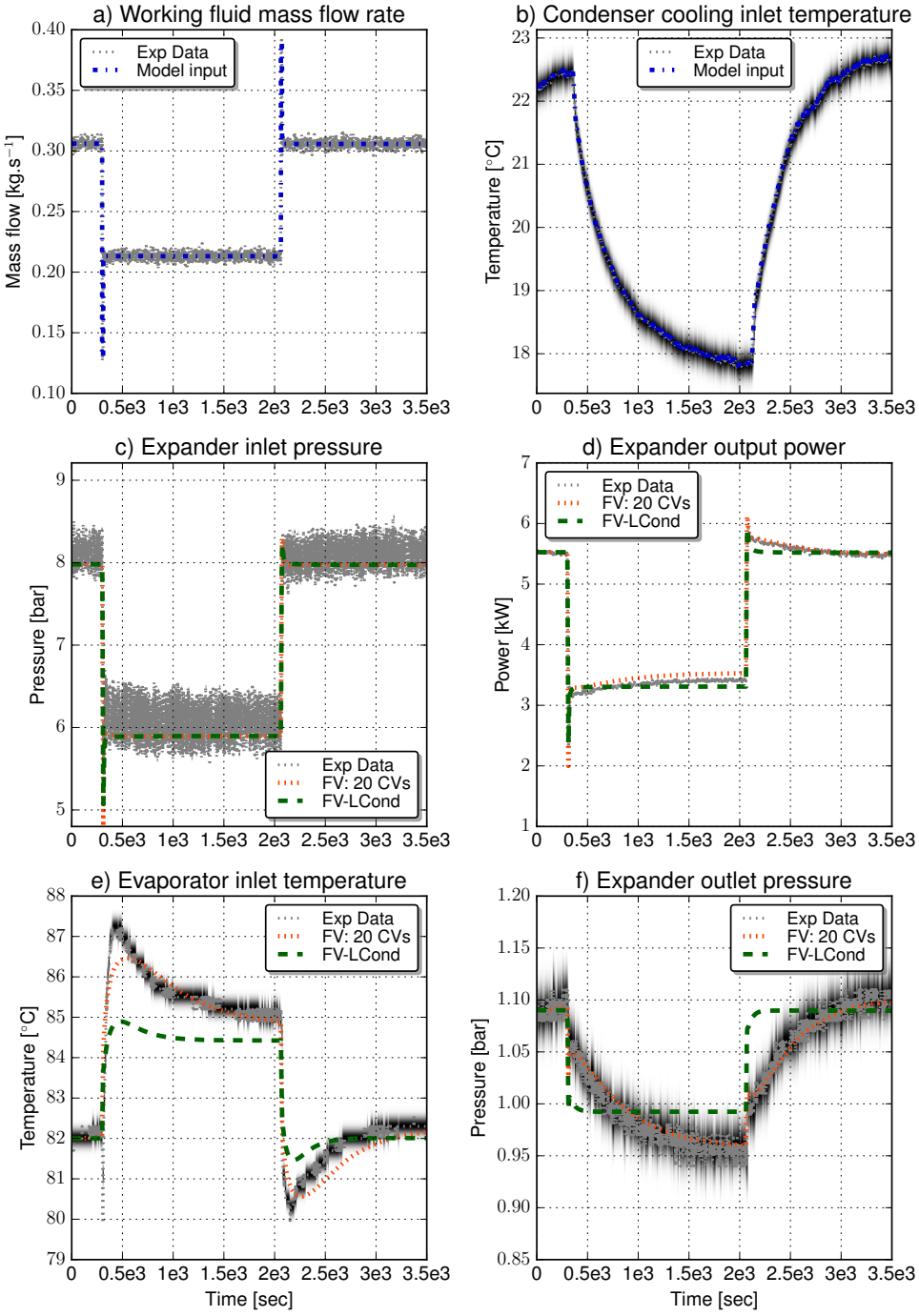

Figure 5.13 – Downward-Upward 5 Hz step change to the pump rotational speed, together with measurements uncertainty reported as a shade.

15-Hz step change

The experimental and simulated results for the 15-Hz step change in the pump rotational speed are displayed in Figure 5.14. The step was applied at t=300 seconds. The ORC unit was suddenly brought to a highly off-design condition experiencing an expander output power decrease by almost 90%. It is interesting to note that, despite the large step change imposed to the pump rotational speed, the pressure changes propagated through the test rig system at a fast pace, such that the trend of the pressure at the inlet of the expander and thus of the net output power was characterized by a very fast transient. The amplitude of the step change was such that a sudden decrease in mass flow rate was experienced on the recuperator cold side. This caused a sharp temperature increase at the evaporator inlet before it stabilized at a value slightly lower than the initial one. The model was able to capture this trend even tough it presented an offset once the system reached its second steady-state condition. It is interesting to note that, despite the steady-state error, the dynamic trends were correctly predicted by the model. The offset in the second steady-state condition can be explained by the low accuracy of the derived semi-empirical correlations used to simulate the pump, the expander and the pressure drop components at the edge of their calibration ranges.

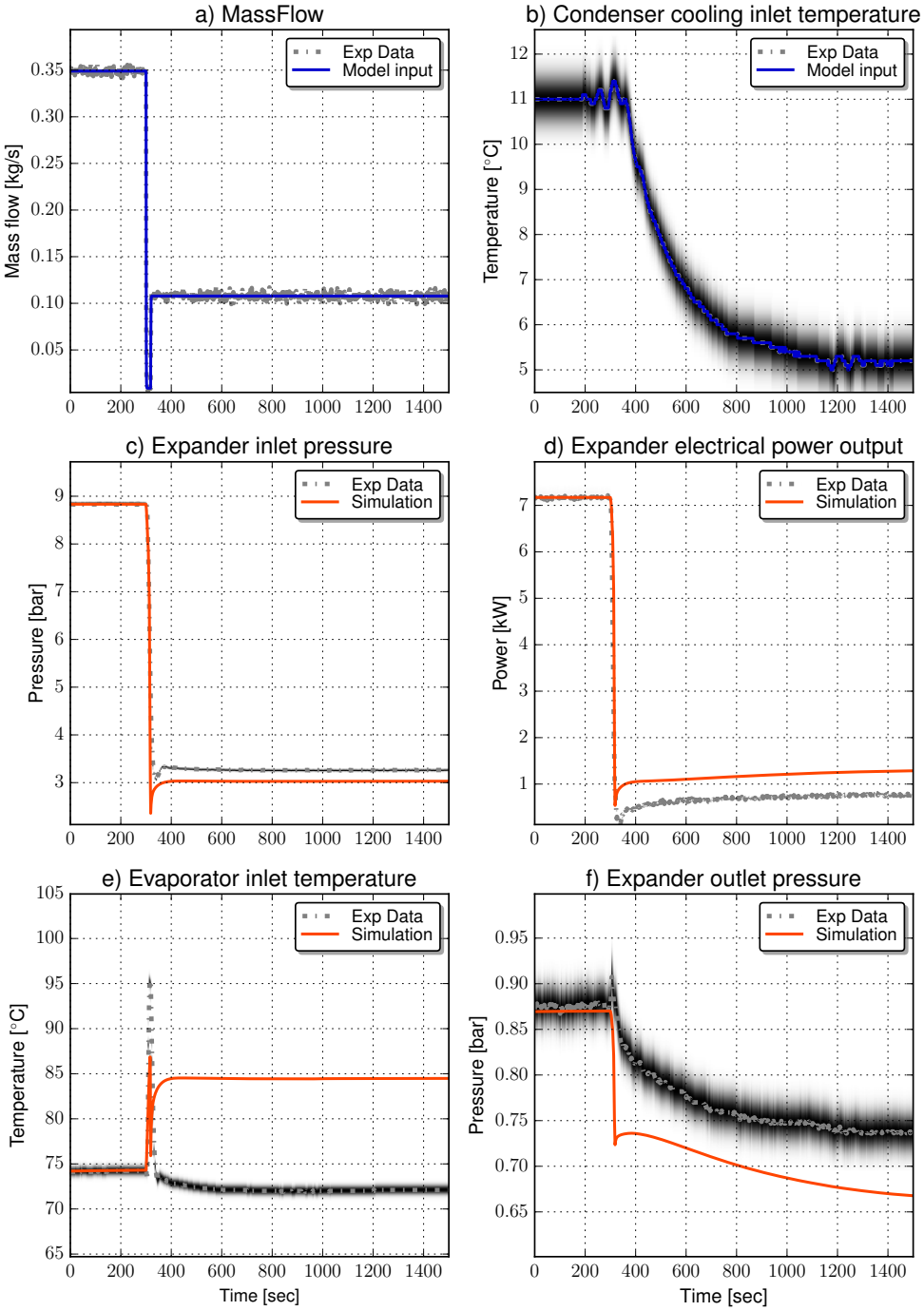

Figure 5.14 – Downward 15 Hz step change to the pump rotational speed, together with measurements uncertainty reported as a shade.

5.4.5 Finite volume and moving boundary evaporator model comparison

In order to compare the effectiveness of the finite volume (FV) and the moving boundary (MB) modelling approaches at a system level, an ORC unit model using the MB model for the evaporator was built. The FV and MB based ORC unit models were simulated to replicate the 5 Hz pump step change experiments. In particular the moving boundary model was simulated assuming a time varying and a constant void fraction value set to 0.9. The latter is referred to as MBConstVF. The FV evaporator model was discretized in 20 control volumes, which revealed to be a good compromise between model accuracy and computational time as explained in section 5.4.6. In Figure 5.15, the comparison between the measurements and the simulations results is reported. Figures 5.15a-b show the two dynamic inputs imposed to the model: the SES36 mass flow rate and the water-glycol temperature at condenser inlet. Both signals were smoothed with a spline in the modelling framework as described in section 5.4.4. The downwards and upwards steps were imposed at time t=300 seconds (sec) and t=2061 sec respectively. The physical phenomena defining the measured trends have been described in detail in section 5.4.4. The simulation results for the three models replicated with a good accuracy the main dynamics characterizing the system.

It is interesting to note that when the void fraction was kept constant in the MB model, MBConstVF, the response of the model was characterized by a larger time constant compared to that of the real unit. In particular the MBConstVF model was not able to replicate the fast overshoot/undershoot that characterized the pressure at the inlet of the expander and the expander output power when the pump speed was changed. This phenomenon was investigated and the results are explained in detail in 5.4.7.

In Table 5.17, the computational time required by the three different ORC unit models to complete the simulation is reported as a percentage of the real time simulated. The moving boundary model allowed to decrease the simulation speed by a factor of 10 while keeping high accuracy with respect to the experimental results. A comparison to test the integrity and

Table 5.17 – CPU time for integration in percentage of the total simulation time.

Model	CPU-time [%]
ORC unit model with FV	13.5
ORC unit model with MB	2.45
ORC unit model with MBConstFV	2.4

accuracy of the finite volume and moving boundary heat exchanger modelling approaches when no experimental data are available is presented in Appendix B.

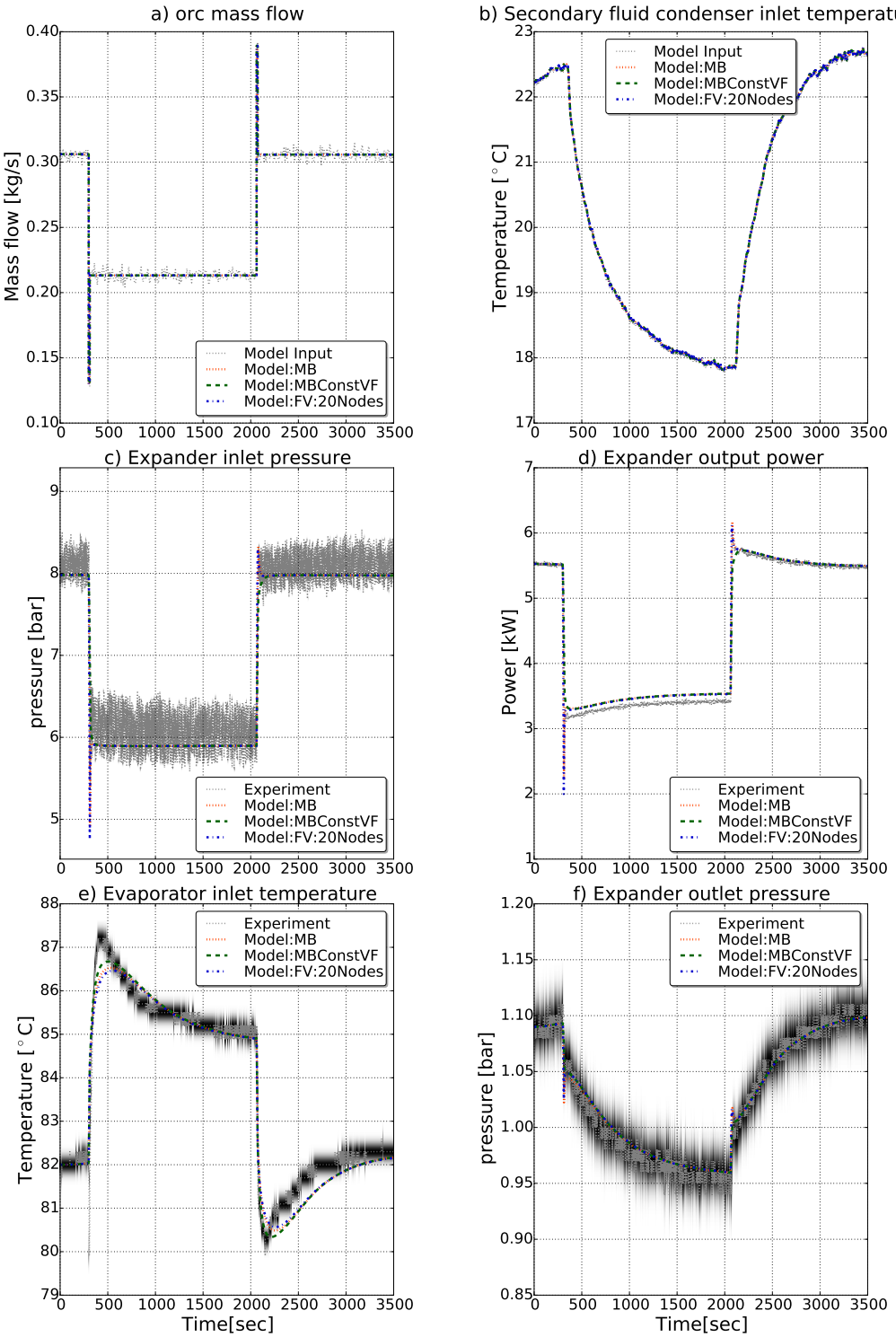

Figure 5.15 – Downward-Upward 5 Hz step change to the pump rotational speed simulation results for the FV and MB based ORC unit model compared against the experimental results. The measurement uncertainties are reported as a shade.

5.4.6 Finite volume model: Number of CVs parametric analysis

In case the FV based ORC model is considered, the modelling of the heat exchangers is based on the finite volume method, characterized by a trade-off between model accuracy and computational time: increasing the number of CVs leads to better accuracy but negatively affects the computational effort. Furthermore, the adoption of the FV approach for a heat exchanger involving a two-phase state can lead to simulation failure or erroneous results due to a discontinuity in the working fluid density derivative between the liquid and two-phase zones [134]. In particular, when the FV model is simulated under transient conditions, numerically-generated mass flow rate can occur as the working fluid phase boundary shifts from one cell to the next.

In order to investigate the effect of the discretization level for the FV evaporator and condenser

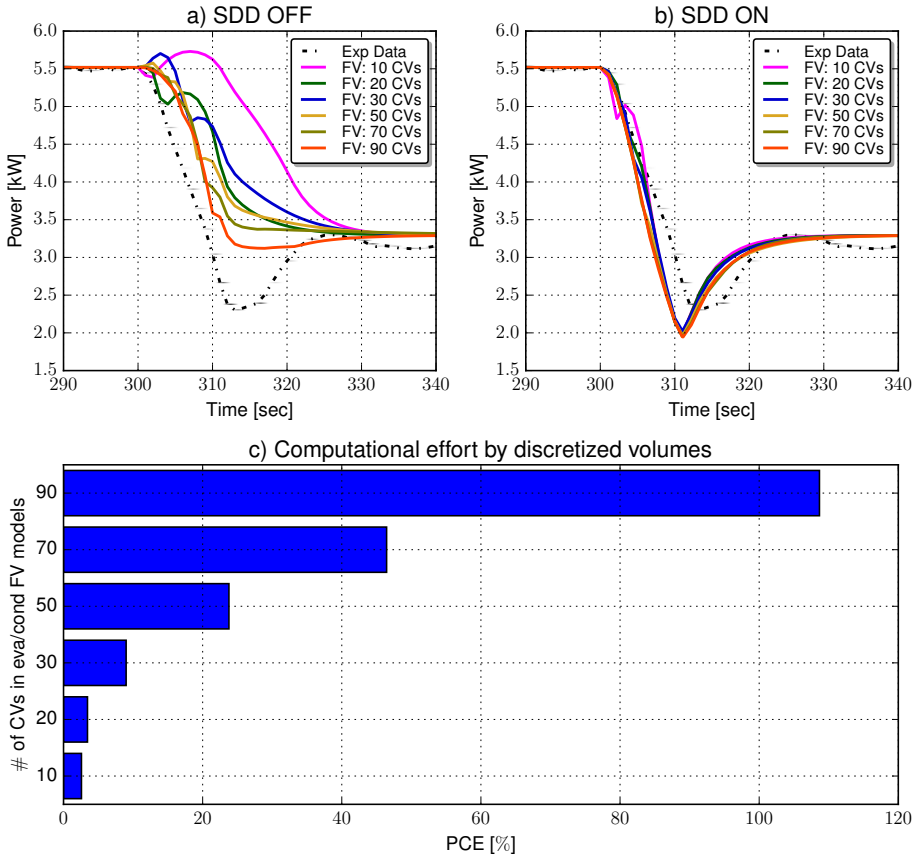

Figure 5.16 – Results of the number of CVs parametric analysis for the FV evaporator and condenser model. a) ORC expander output power when no numerical method is applied to the fluid model. b) ORC expander output power when the smooth density derivative (SSD) flag is activated in the fluid model c) Percentage computational effort (PCE) for the different discretization levels.

model on the simulation results a parametric analysis was performed. The number of CVs

was varied in a range from 10 to 90. The results are displayed in Figure 5.16 for the 5-Hz downwards pump speed change. In Figure 5.16a, the expander output power simulation results are compared with the experimental data. For all simulation results, a non-physical oscillation between time t=300-330 seconds was registered for the expander output power. The swing was related to the numerical mass flow generation described above. Because of the magnitude of this numerical flow rate depended on the cell size, the number of CVs reduced the effect of this phenomenon. However, the discretization in 90 CVs was not sufficient to properly predict the undershoot experienced by the expander output power and resulted in a much slower simulation. Increasing the discretization level would eventually have led to a suitable prediction of the experimental data at the price of a non-sustainable simulation speed for control-based analysis. In order to tackle this problem the smoothed density derivative method was presented and compared to alternative solutions by Quoilin et al. [134]. It was shown that this approach is recommended when simulation with fast transients are performed. The method consists in smoothing out the density derivative function at the interface between the liquid and two-phase regions with a spline function. It is directly implemented in the CoolProp library and can be triggered in the Modelica fluid model with a simple flag. In Figure 5.16b the simulation results when the smooth density derivative flag is active in the fluid model are plotted. For all the tested discretization levels, the ORC model was able to predict the undershoot in the electrical expander power output. No numerical oscillation was registered in the simulation results except for the 10 CVs model which was characterized by a narrow bump between time t=305-310 seconds. Although the equation of state of the fluid was modified around the saturated liquid state, the simulation results were improved because the non-physical flow-rate generation due to the finite discretization had been dampened by the smoothing of the density derivative [134]. As far as the model accuracy is concerned, it can be noted that increasing the level of discretization above 20 CVs leads to negligible differences. In Figure 5.16c the percentage computational effort (PCE), defined as reported in equation 5.2 is plotted for each simulation speed. As it is possible to see the simulation speed decreased exponentially as the CVs in the FV models increased with the 90 CVs model characterized by a simulation time longer than the real time simulated. From this analysis it can be concluded that with the smooth density derivative method and a level of discretization of 20 CVs it was possible to achieve a satisfactory result both in terms of accuracy and computational speed.

5.4.7 Moving boundary - mean void fraction parametric analysis

In order to further investigate the effect of the mean void fraction on the MB evaporator model performance, a parametric analysis was performed by replacing the endogenously-computed value of the mean void fraction, γ (see Eq. A.5), by 6 different constant values ranging from 0.2 to 0.99. The range upper limit was set as the highest void fraction value in the two phase region before the fluid got completely evaporated. The results are reported in Figure 5.17 for the pump speed step change downwards experiment. In Figure 5.17a, the expander output power simulation results for the different MB evaporator models are compared with the experimental data. As the void fraction value increased, the simulation results got closer to the measurements. In particular a value of 0.2 considerably overestimated the time constant

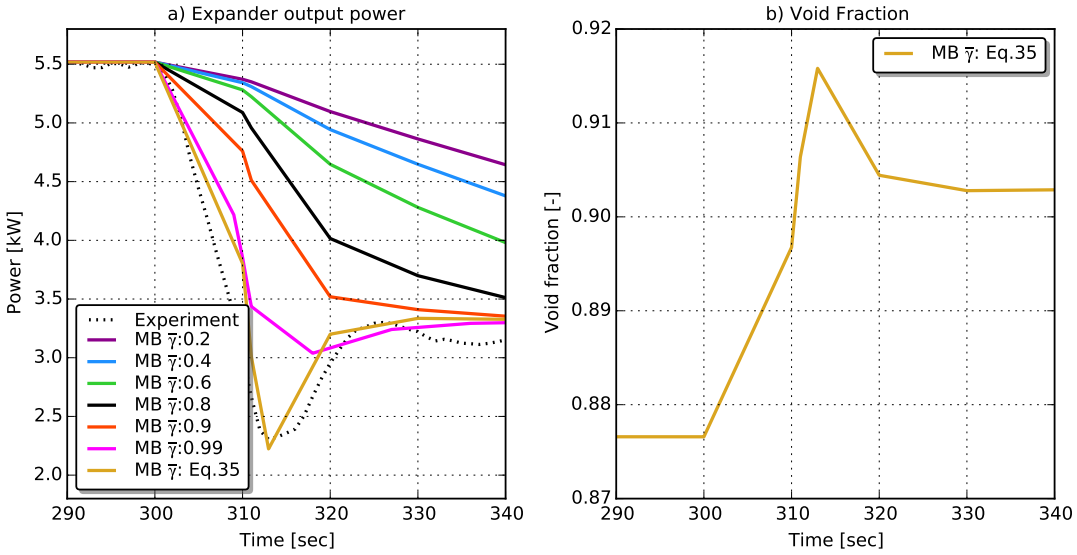

Figure 5.17 – Results of the void fraction parametric analysis for the MB evaporator model. a) Expander output power for different void fraction values in the MB evaporator model. b) Void fraction trend in the MB evaporator model when analytically computed.

while a value of 0.99 approached much better the experimental data. As it is clearly depicted in Figure 5.17a, an increase of the void fraction value in the evaporator MB model corresponded to a decrease of the expander output power time constant. This can be explained by the fact that a larger void fraction value resulted in an increased portion of the evaporator volume filled with gas which corresponded to a lower thermal inertia of the evaporator and therefore to a smaller time constant. None of the MB models with a constant void fraction were able to predict the overshoot characterizing the power output power trend. This is explained by the fact that when the mass flow decreased the void fraction increased, as shown in Figure 5.17b, as the portion of area occupied by the gas increased. As a consequence the thermal capacity decreased leading to faster transients. Keeping the mean void fraction constant neglected this phenomena and resulted in a too slow response. It also resulted in a poor prediction of the outlet flow rate variations during transients. To conclude, the void fraction needed to be computed analytically in order to follow the fast mass flow variation of the system, as shown in Figure 5.17b.

5.5 Conclusions

In this Chapter the models described in Chapter 4 were validated with experimental data based on open-loop step responses. It is argued that this kind of validation is more appropriate than the previously-proposed closed-loop validations. This is explained by the fact that the presence of a control unit might interfere with the dynamics of the components.
The ThermoCycle Modelica models were compared against experimental data acquired on the PTTL facility at the Plataforma Solar de Almería, on the heat exchanger test rig available at

the Mechanical Engineering Department of the Technical University of Denmark described in Chapter 3 and on the 11 kW_{el} ORC test rig available at the laboratory of Ghent University, campus Kortrijk described in chapter 2. The main outcomes of this study are reported hereunder:

- **Parabolic trough collector model validation** The parabolic trough ThermoCycle Modelica model was compared against experimental data acquired on the PTTL facility at the Plataforma Solar de Almería (PSA), Spain. Dynamic experiments were performed by varying the oil mass flow rate (MFE), the oil inlet temperature (TE) and the direct beam solar radiation (SBE) for different operating conditions.
  - The simulation results obtained for the oil mass flow change experiment(MFE), the oil inlet temperature change experiment (TE) and the solar incidence beam radiation experiment (SBE) showed a good overlap with the experimental results. The developed solar field model structure proves to be effective to predict the dynamic of a real solar field.
  - A minimum discretization level of 20 CVs was found to be a good compromise between model accuracy and simulation speed if the ETC outlet temperature had to be precisely predicted, e.g., the SF model is used as a reference to develop and test model based control strategies.
  - In light of the obtained results a lumped SF model is recommended if the performance of the ETC collectors are analysed on a daily or longer time frame. This approach allows to significantly decrease the computational time while maintaining a satisfying level of accuracy.
- **FV and MB heat exchanger model validation** The FV and MB heat exchanger models were compared against experimental data acquired on the high pressure line of the HX test rig presented in Chapter 3. The dynamic performance of the unit were analysed by applying a step downwards to the volumetric pump rotational speed. The two-phase heat transfer coefficient correlation derived in Chapter 3 was implemented in both the FV and the MB models.
  - The FV and MB heat exchanger models were able to correctly predict the experimental results. The FV model resulted more precise but up to three orders of magnitude slower than the MB model, in line with the results obtained by [142].
  - For 1-D FV and MB heat exchanger models designed to predict the overall dynamic performance of the component, employing detailed correlation for the modelling of the heat transfer coefficient lead to high accuracy at the cost of significantly increasing the computational time. As the computational effort is expected to increase significantly with the complexity of the dynamic model, when modelling complete power systems it is recommended to avoid employing specific HTC correlations and rather use simplified laws such as the vapour quality dependant (VQD) method.

- **Small-scale ORC unit model validation** The component models of the ThermoCycle library are interconnected together to simulate the 11 kW_{el} ORC unit presented in Chapter 2. The dynamic performance of the small-scale power unit was investigated by applying steps downwards and upwards to the centrifugal pump rotational speed. A first validation was performed with 36 steady-state data points. A second dynamic validation was performed by imposing relatively small steps on the boundary conditions of the open-loop system. A third dynamic validation was performed by applying a larger step to the boundary conditions. In light of the results obtained in section 5.3, the HTC of the heat exchanger models of the ORC unit were based on the VQD method.

    - The steady state validation showed a good overlap between experimental and simulation results. The expander inlet pressure and the net output power were reproduced with an accuracy below 5% and 10% respectively for most of the points. For extremely off-design conditions the expander output power was predicted with an accuracy of 30%.
    - The simulation results obtained for the downward-upward 5 Hz step changes in the pump rotational speed overlapped very well with the experimental results. It was demonstrated that the dynamic model was able to reproduce the system response when a typical control action was imposed to the pump rotational speed.
    - The developed ORC dynamic model was able to predict the main dynamics characterizing the test rig when a large change was imposed to the pump rotational speed as the results from the downward-15 Hz showed. On the other hand significant offsets were registered once the model had reached steady-state.
    - When modelling small power systems undergoing fast transient with the FV approach for the heat exchanger components, the discontinuity of the working fluid density derivative at the phase boundary can lead to erroneous results. Discretizing the FV model in a reasonable number of CVs and applying the smooth density derivative method in the working fluid model allows obtaining satisfactory results both in terms of accuracy and simulation time. In the presented case a total number of 20 CVs was sufficient to reproduce the measured transients, leading to a dynamic model suited for control strategies analysis. It is worth underlying that it was not possible to define a priori the minimum number of CVs required to avoid simulation errors related to the density discontinuity as the problem was dependent on the thermo-physical properties of the working fluid and the volume of the components of the modelled system.
    - The comparison against experimental transients of a small 11 kW_{el} ORC power unit demonstrates that both the FV and MV with an analytically calculated void fraction approaches were suitable for the dynamic modelling of the evaporator when integrated at a system level. The moving boundary model allowed to decrease significantly the simulation speed while keeping a good accuracy with the experimental data.

- In the proposed comparison the assumption of homogeneous two-phase flow did not lead to inaccurate estimation of the time constant characterizing the system; This result suggests that the homogeneous two-phase flow assumption can be considered appropriate for the modelling of small capacity ORC systems.
- Assuming a constant void fraction in the MB approach resulted in an overestimation of the dynamics (i.e. leads to slower response times) making it unsuitable for modelling small capacity heat exchangers. From the proposed parametric analysis it was clear that the average void fraction was inversely proportional to the time constant characterizing the evaporator model.
- Despite what is stated in the literature [142], the two modelling formulations were found to have a comparable level of robustness, i.e. both the FV and MB models were able to smoothly run the performed simulations. A wider range of simulation tests (e.g. start-up and shut-down of vapour compression cycles) are deemed necessary to further investigate on the robustness of the two modelling approaches.

It was proven that the modelling approaches adopted in the ThermoCycle library led to satisfactory results for the simulation of small capacity thermal systems.
The proposed solar collector model, MB and FV heat exchanger models and the ORC unit model together with the test cases are released as open-source and are available in the latest version of the ThermoCycle library.
The effectiveness of the proposed ORC model in studying and assessing the implementation of model-based control has been recently validated [162]. It should finally be noted that the models are not suitable for the simulation of cold start-up or shut-down conditions, mainly because the proposed finite volumes and moving boundary formulation cannot handle zero-flow conditions.

Nomenclature

Acronyms

WHR	Waste heat recovery
ORC	Organic Rankine cycle
FV	Finite volume
MB	Moving boundary
HX	Heat exchanger
MFE	Mass flow experiment
TE	Temperature experiment
CV	Control volume
PI	Proportional integer
APS	Absolute pressure sensor
RTD	Resistance temperature detector
CFM	Coriolis flow meter
UFM	Ultrasonic flow meter
DPS	Pressure difference transmitter
PLC	Programmable logic controller
VQD	Vapour quality dependence
DNI	Direct normal irradiation
PCE	Percentage computational effort
SF	Solar field
GUI	Graphical user interface

Subscripts

amb	ambient
incid	incidence
Comp	computational
ext	external
pred	predicted
meas	measured
su	supply
ex	exit
el	electrical
sf	secondary fluid
wf	working fluid
is	isentropic
w	wall
l	liquid
v	vapour

Symbols

$\bar{\varepsilon}$	relative error (-)
p	pressure (bar)
T	temperature (°C)
$\dot{V}$	volume flow rate ($m^3.s^{-1}$)
$\dot{q}$	heat flux ($kW.m^{-2}$)
$\bar{\gamma}$	mean void fraction (-)
h	specific enthalpy ($kJ.kg^{-1}$)
ρ	density ($kg\,m^{-3}$)
A	area (m^2)
$\dot{W}$	electrical power (kW)
$\dot{m}$	mass flow ($kg.s^{-1}$)
α	heat transfer coefficient ($kJ.(kg.K)^{-1}$)

6 Design of an organic Rankine Cycle-Based Trigeneration System

Abstract A techno economic-study of the trigeneration plant under development in the framework of the EU funded BRICKER project is presented employing the ThermoCycle Modelica library. The system is composed by four major units: biomass boiler, parabolic trough collector field, organic Rankine cycle power block and an adsorption chiller. The trigeneration plant together with heat recovery ventilation technology and novel insulation material has the aim of reducing the energy consumption of existing buildings by up to 50%. A methodology based on a simplified dynamic model of the system is proposed to investigate the system behaviour on a daily and an annual scale. The effectiveness in ensuring safe working conditions and in maximizing the sun power usage of two different solar field control approaches is investigated. An annual analysis to evaluate the economic viability of the trigeneration system is proposed.

6.1 Introduction

Over the past 30 years the electric industry has been characterized by a transition from a vertical production structure towards a horizontal one based on the deployment of intermittent renewable resources [163]. Among renewable energy technologies, concentrated solar power (CSP) systems have been increasingly considered worldwide as a key technology for meeting the renewable energy demand [164, 165]. Due to the high capital cost, the total CSP installed capacity is still low, with only 3.6 GW_{el} installed at the end of 2013 [166]. Research activities, with a focus on cost reduction, have been commissioned by leading research institute in Europe and in the US [163, 167], and significant reductions are expected especially for the thermal storage (TES) and the heat transfer fluid (HTF) components by the end of this decade. Another approach to achieve competitiveness in the current market consists in hybridization with fossil fuels [168]. Hybridizing these plants has not only the benefit of reducing the cost but it also enables the CSP unit to be dispatchable when the solar source is low. Several plants worldwide have demonstrated the advantages of this solution [166]. In recent years, the hybridization of CSP technology with biomass has gained attention and its potential has been investigated by several authors [169, 170]. The concept has been successfully demonstrated since the end of 2012 by the 22 MW_{el} Termosolar Borges plant in Catalonia, Spain [171, 172]. This solution allows to move CSP technology towards agricultural area, rich in biomass and waste material, enabling locations with lower levels of direct normal irradiance (DNI) com-

pared to DNI required by CSP standalone systems [173]. A technical economic assessment of a combined heat and power (CHP) system, using organic Rankine cycle (ORC) technology integrated with a hybrid CSP-biomass heat source, has been recently investigated [174]. The study compares, by means of a transient analysis, the economic profitability of a hybrid CSP system for three different locations in central Europe, concluding that the retrofit of biomass plants with CSP technology is a promising approach, to improve the economic performances. In this context the EU founded BRICKER project aims to develop a scalable, replicable, high energy efficient, zero emissions and cost effective CSP-biomass trigeneration system, based on ORC technology, to refurbish existing public-owned non-residential buildings. The trigeneration unit together with lightweight facades, and phase change material insulation technology, is expected to reduce the building energy consumption by at least 50%. Three systems are being developed in Spain, Belgium and Turkey to demonstrate the concept feasibility. In this chapter, a dynamic model of the CSP-biomass trigen system under development in Càceres, Spain is presented. The model is based on the ThermoCycle Modelica library presented in chapter 4. During the last years dynamic modelling has been increasingly recognized as a powerful tool to analyse the performance of CSP power systems under transient conditions. Casati et al. [130] developed a dynamic model of a novel ORC power block for a CSP system with a direct thermal storage, in order to investigate the controllability aspect under extreme critical conditions. Ireland et al. [175] investigated the transient performance of a micro CSP-ORC system, over four reference days, by means of a detailed dynamic model. More recently Dickes et al. [176] investigated model reduction methods for dynamic modelling of the solar field and the thermal storage of a micro CSP power unit, in order to increase the computational effectiveness of the models. In the presented work, a simplified modelling approach of the trigeneration BRICKER system is proposed. The presented modelling approach allows for a robust and efficient model capable of predicting the main time constants characterizing the overall system. Two analyses are performed. Firstly the model is employed to investigate the potential of different control logics of the system on a daily-basis. Secondly the capability of the model are exploited to analyse the economic viability of the project through annual-based simulations. The simulation results are analysed and discussed and guidelines for future work are drawn.

6.2 System description

The EU founded BRICKER project aims at demonstrating that retrofitting existing buildings with passive and active cutting edge technologies can lead to enormous energy savings. The project comprises the installation of a novel trigeneration (trigen) unit based on renewable energy sources to meet the thermal and electrical building demands, coupled with heat recovery ventilation system, lightweight facades and innovative insulation material to decrease the building energy consumption. The complete layout of the trigen system under development in Càceres, Spain is reported in Figure 6.1. The system is composed by two main loops. In the first loop the thermal energy collected by the parabolic trough collectors (SF) and generated by biomass combustion in the boiler (BMB) is transferred by a heat transfer fluid to the ORC power block for electricity production and to the second loop via a heat exchanger (HXI).

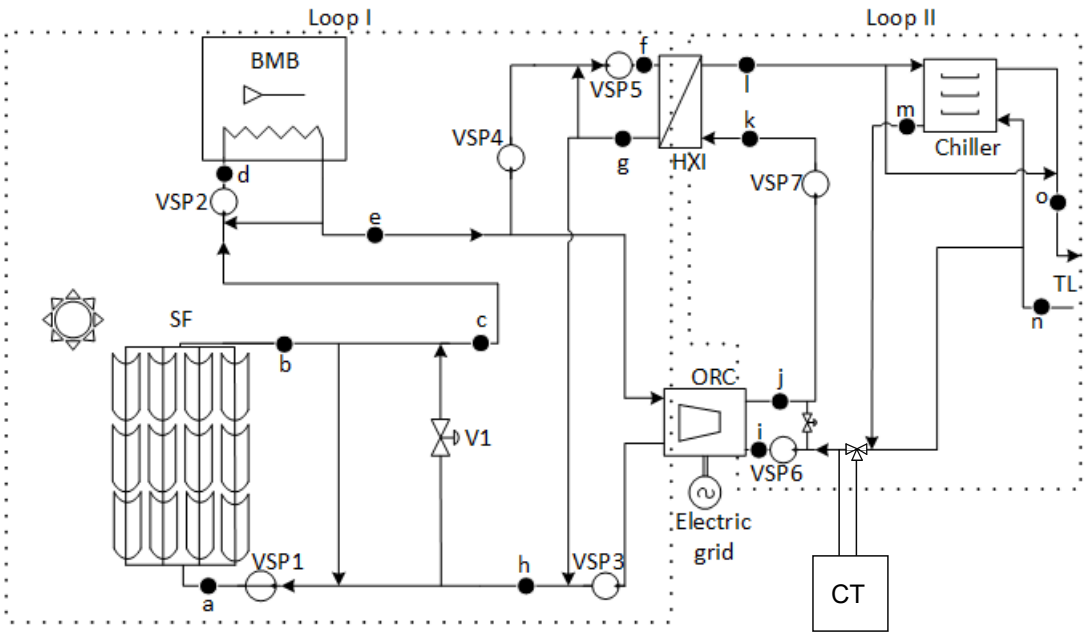

Figure 6.1 – Process flow diagram of the Trigeneration Bricker unit. BMB: biomass boiler. SF: solar field. ORC: organic Rankine cycle unit. VSP: pump. V: valve. TL: Thermal load. CT: cooling tower.

The synthetic thermal oil, TherminolSP, is selected as heat transfer fluid as it is widely used for CSP applications thanks to its low operating pressure, high thermal stability (up to 335 °C) and good heat transfer characteristics [177]. Starting from the bottom left of Figure 6.1 it is possible to recognize the solar field, where the HTF is pre-heated from (a) to (b) before entering the biomass system (d), reaching the maximum temperature at the outlet of the boiler (e). The fluid is then pumped through HXI from (f) to (g) and through the ORC power block which are connected in parallel. At the outlet of the ORC unit, the fluid mixes with the stream coming from HXI (h). Loop II comprises the adsorption chiller, the ORC condenser cooling side, the secondary side of HXI, the cooling tower and the connection to the thermal load of the building. A cooling tower is used to close the thermal balance in case of excessive thermal energy production from the oil loop. Looking at the right part of Figure 6.1 water gets pre-heated in the ORC condenser from (i) to (j), and then it is pumped through HXI from (k) to (l) where it reaches the maximum temperature of loop II. The fluid is then directed to the chiller or to the building depending on the thermal demand. The cooling tower is activated in case more thermal energy than the amount required by the building is generated. A description of the different components is reported in the list below.

- Parabolic trough collectors with evacuated tubular absorber are selected being the most reliable and proven technology in the CSP field [178]. In particular the selected collectors are characterized by a maximum temperature of 250°C that perfectly fits the nominal working temperature of the system. A total of 12 collectors are connected in 4

parallel loops of 3 collector each for a total nominal power of 250 KW_{th}. The solar field dimension results from a compromise between the available area on the demo building roof and on the seasonal thermal demand. The solar field works as a pre-heater for the biomass boiler, reducing the amount of biomass burnt during the day. Each solar collector is characterized by a net collecting surface of 54 m^2.

- The biomass boiler covers a fundamental role in the system as it provides together with the solar field the thermal power required by the ORC unit and by HX1. If there is a sudden demand of extra power, a larger amount of biomass is burnt to keep the outlet temperature close to the set point value. The boiler has a maximum power capacity of 500 kW_{th}.

- The thermal energy from the biomass and the solar field is converted into electrical energy by the ORC power block. The unit installed in the system can be operated in generation or cogeneration mode with an electrical power ranging between 100 and 70 kW_{el} respectively. The electrical power can be sent to the building or the national grid. In cogeneration mode the thermal energy dissipated at the condenser is used to meet the building energy thermal demand by heating up the water in the cooling circuit.

- A heat exchanger is used for thermal energy transfer between loop I and loop II. The brazed plate type is selected as it offers very good heat transfer performance in single phase with an extreme compact design [31]. The component can withstand a maximum thermal power load of 800 kW_{th}

- In order to satisfy the cooling demand during the summer season an adsorption chiller machine is included in Loop II. The selected chiller is of the silica gel-water type. This machine can be fed with a thermal input ranging between 60-90°C [179]. The chiller has a nominal cooling power of 300 $kW_{th,c}$

6.3 Control

6.3.1 Technical boundaries and operational logic

In this section a description of the control logic implemented on the presented system is described and discussed. The technical boundaries of the different components are listed hereunder:

- Solar field: a minimum mass flow rate must be guaranteed in the parabolic trough collectors to avoid high film temperature that could deteriorate the thermal oil. An autonomous warning control is provided by the manufacturer. When the outlet temperature of the solar field reaches a certain value, electrical motors are activated defocusing the collectors in order to decrease the temperature. A partial or total defocusing can be selected by the user.

- Biomass boiler: the boiler works in a range between 150 and 500 kW_{el}. The temperature gradient through the boiler is comprised between 5 K and 30 K. The system operates at

a constant mass flow of 9.5 kg.s^{-1} and is equipped with a recirculation circuit and an internal control which regulates the amount of biomass burnt to keep the temperature at the outlet at a user-defined set point. Power modulation is characterized by time constant between 30 seconds up to 2 minutes. This is mainly related to the kinetics limit of the combustion chemical process and to the air inflow adjustment. A limit of 1 daily start/stop is recommended by the manufacturer but it is preferably to maintain the biomass boiler at a minimum range in order to keep high efficiency, low pollutions and reduced maintenance. The boiler start-up is a slow process that can take up to 50 minute.

- ORC unit: it requires at the evaporator a constant thermal oil mass flow rate of 2.5 kg.s^{-1} and it is capable of handling heat source temperature deviation in the order of 20 K from the nominal value of 245°C.
- Adsorption chiller: it can handle temperature inlet variation in the order of plus minus 5 K from its nominal value. Proper control of HXI are required in order to respect these boundary limits.

Given the above mentioned technical boundaries, a correct operation of the system depends on finding the right balance between the solar field and the biomass boiler working condition. In particular, high controllability of the solar field is required in order to guarantee safe biomass boiler operation avoiding biomass shut-down. In order to achieve this goal the solar field is equipped with a recirculation and a by-pass stream as shown in Figure 6.1. A constant mass flow rate equal to the nominal value required by the ORC evaporator of 2.5 kg.s^{-1} is ensured to the solar field by running pump VSP1 at a fixed speed, avoiding high film temperature issues. A highly responsive control logic is developed by installing a PI controller (PI1) on the by-pass valve V1 to regulate the biomass inlet temperature T_d and by exploiting the solar field internal defocusing mechanism. In nominal condition the mass flow at the outlet of the ORC unit is pre-heated in the solar field and the by-pass valve V1 is closed. If the DNI overcomes its nominal value the solar field outlet temperature T_b increases and so does the biomass boiler inlet temperature T_d. The by-pass valve is opened by the PI controller to mitigate the temperature increase at biomass inlet T_d. As VSP1 runs at constant speed, mass flow rate equal to the one flowing through V1 is recirculated from SF outlet to the inlet, further increasing the solar field outlet temperature T_b. A chain mechanism is activated pushing T_b towards the defocusing set-point value. When T_b overpasses the set-point, automatic defocusing occurs, reducing the thermal power delivered by the collector fields and avoiding biomass shut down. On the other hand, sudden decrease of sun power are handled by the biomass internal control (PI2) which increases the biomass fed to the combustion chamber maintaining T_e at its nominal value. In case the heat rejected from the ORCs condenser is not sufficient to satisfy the thermal demand of the building, extra power has to be delivered to the water loop of the system via HXI. The heat exchange rate of HXI is controlled by a recirculation system with pump VSP4 and VSP5. The latter is kept constant at a fixed speed. As the adsorption chiller works at a constant inlet temperature, T_l, to guarantee high COP values, an increase in thermal demand corresponds to an increase in mass flow through HXI. A PI (PI3) controlling

the rotational speed of VSP4 is implemented to maintain the temperature, T_l, close to its set-point.

6.3.2 Control strategy

The thermal profile required by the building over the year is reported in Figure 6.2. The building hosts administrative offices of the Ministry of Agriculture, Rural Development, Environment and Energy of the Government of Extremadura, who is the owner of the building. The profiles are the results of measurements taken at the site over one year. The heating demand ranges from the end of November until the last days of April, while the cooling load starts from the middle of May to the end of September. The thermal demand of the building can thus be

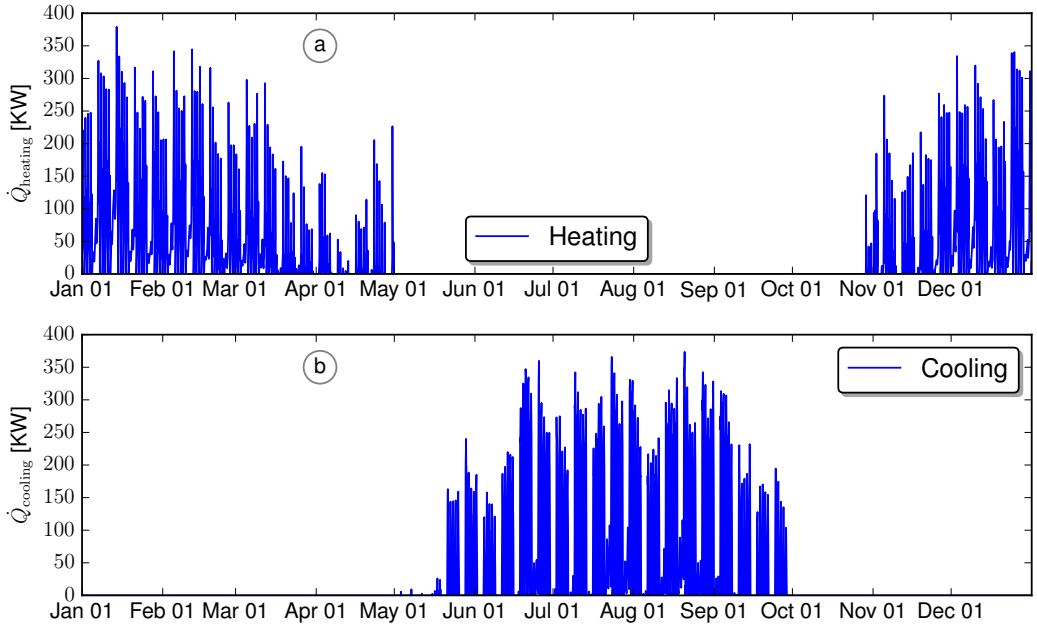

Figure 6.2 – Building thermal demand. a) heating load b) cooling load.

divided in three main sections: the summer time that ranges from the first of June to the 31st of September (17 weeks), the winter time that ranges from the first of November to the 31st of April (26 weeks) and a third section characterized by a thermal load lower than 10 kW_{th}, which covers May and October (9 weeks). During this third period the plant is switched off for maintenance. Based on the control logic reported in section 6.3.1 and the thermal load of the building, two control strategies regulating the start-up and shut-down of the ORC based on external conditions are developed.

- **Strategy I** In the summer time, as the thermal demand required by the chiller to supply the building cooling load can reach values higher than the nominal power provided by the biomass boiler (500 kW_{th}), the ORC unit is turned on only when the thermal power provided by the solar collector field is enough to cover together with the biomass boiler

and the thermal power at the ORC condenser the maximum thermal demand required by the building.
In winter time, the ORC is run in cogeneration mode during day-time from 7:00 to 20:00. In case there is not enough thermal power generated by the solar field and the biomass boiler, the power unit is switched off and turned on as soon as the building thermal demand decreases.

- **Strategy II** In summer time the ORC is run in cogeneration mode only when the thermal power provided by the solar field is enough to cover the thermal demand of the ORC evaporator, i.e. 472 kW_{th}.
  In winter time the ORC is always off-line and the biomass boiler is run to cover the thermal demand of the building.

The effect of the two strategies on the economic performance of the plant are investigated in section 6.5.

6.4 Simulation tool

In order to investigate the control logic on a daily basis and the control strategies on an annual basis a flexible dynamic model of the trigeneration system is implemented in Modelica using the ThermoCycle library. The thermal oil and the water flowing through loop I and II of the plant are always in liquid state and are assumed to behave as incompressible fluids. They are modelled following the table based approach proposed by the Modelica standard library. Temperature, T, is selected as the fluid model state variable. Density, ρ, and specific heat capacity, c_p, are computed fitting constant n-order polynomials on user-defined table data. Specific enthalpy, h, specific entropy, s, and the other thermodynamic properties are calculated from the integrals and derivatives of the derived polynomials, $\rho(T)$ – $c_p(T)$. As the presented dynamic models can be used for both compressible and incompressible fluids, pressure, p, and specific enthalpy, h, are selected as state variables. The Modelica table based media model uses an internal solver to retrieve the temperature value in order to compute the other thermodynamic properties. In Figure 6.3 the developed dynamic model of the system is shown. The model is used to investigate the effectiveness of the control logic in the oil loop which is considered the most critical aspect of the system and to analyse the performance of the whole system on an annual basis. Perfect ideal control is assumed in the coupling between the water loop the building and the cooling tower (CT). The building thermal demand (TL) is modelled by means of a negative source of thermal energy imposed to the water loop. In the following sub-sections, the dynamic models of the system components are briefly described.

6.4.1 Solar field

Assuming homogeneous pressure drop and equal ambient input data, the solar field can be modelled as a single row of 3 collectors in series with a forth (1/4) of the total mass flow flowing through it. The parabolic trough collector model of the ThermoCycle library is used. The radial energy balance between the HCE and the ambient is modelled with a semi-empirical correlation derived from typical values of solar collectors of comparable size. This approach

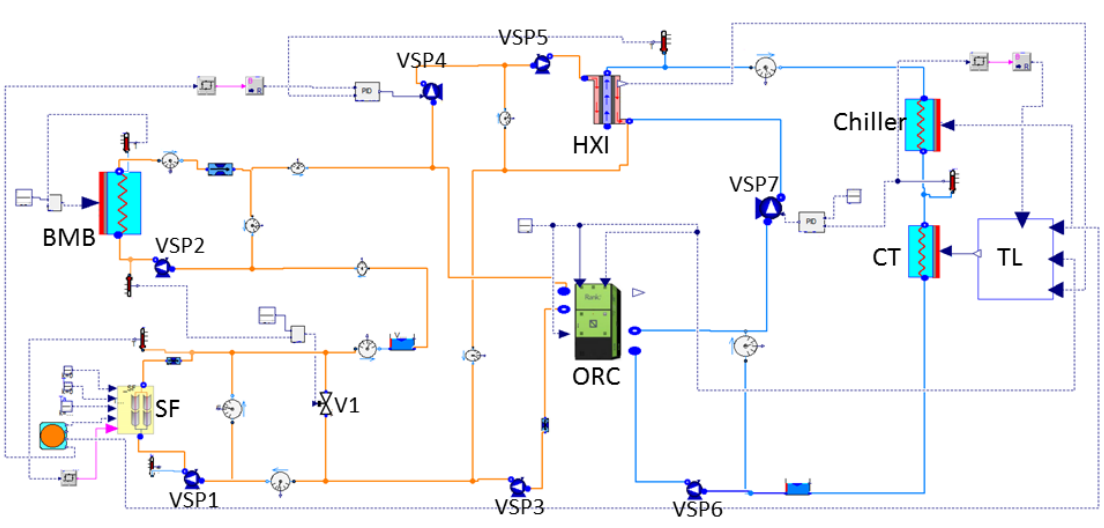

Figure 6.3 – Trigeneration Bricker system from the Dymola GUI. BMB: biomass boiler, SF: Solar field, CT: Cooling tower, TL: Thermal load.

allows reducing the number of equations increasing the computational time, while still modelling the main time constant characterizing the solar field dynamics. In light of the results obtained in chapter 5.2, a discretization of 20 nodes is employed for daily based simulation while a lumped approach is adopted for longer simulation.

6.4.2 Biomass boiler

No information were provided by the manufacturer on the biomass burning process. As a consequence a simplified approach is adopted to simulate the boiler. The biomass burning process is modelled as a zero-dimensional model where the power from the biomass combustion is imposed by the user, defining a value between 0, shut-down, and 1, maximum power. A first order model allows to account for the combustion dynamic with a fixed time constant. The oil side and the tube metal walls are modelled with a discretized one-dimensional approach. The oil flow through the boiler is modelled with a *Flow1Dim* component, accounting for energy accumulation, while the thermal energy capacity of the metal wall is modelled using the *MetalWall* component. The thermal inertia of the boiler is tuned in order to reproduce typical values that are found on boiler of the same size (500 kW_{el}). The dynamic is checked by simulating the warm up of the boiler, and verifying that the period of time required to reach the desired set point in temperature is close to realistic values (1 to 2 hours). A more detailed description is available in Appendix A.4.

6.4.3 Oil-Water heat exchanger

The oil-water heat exchanger is modelled using the lumped heat exchanger model of the ThermoCycle library. It models a counter-current plate heat exchanger based on the LMTD approach.

6.4.4 ORC power unit

In a small capacity ORC unit, the dynamic is mainly defined by energy and mass transfer phenomena characterizing the heat exchanger components, as the expansion and compression processes are characterized by very small time constants. Two *Flow1Dim* models are used to simulate the evaporator and condenser secondary side. The thermal power absorbed and rejected by the ORC working fluid is imposed to the *Flow1Dim* as an exogenous inputs. A semi-empirical curve based on experimental data is used to predict the net electrical output power as a function of the heat source temperature at the evaporator inlet and the heat sink temperature at condenser inlet. A more detailed description is available in Appendix A.3.

6.4.5 Piping

In order to account for the volume of the piping system the *PipeV* component is used in both loops. The model is a lumped one dimensional model accounting for mass accumulation in liquid phase in a defined constant volume. A constant pressure is imposed by the model, allowing for a robust resolution of the system of equations of the overall plant model.

6.4.6 Building thermal demand

A simplified approach is employed in order to solve the thermal coupling between the water loop and the building. The thermal energy required by the building is extracted from the water loop through a *Flow1Dim* model with an exogenous input. A second *Flow1Dim* model, TC, simulates the cooling tower. The BD model computes the thermal energy dissipated by the tower through a thermal balance accounting for the thermal power from the ORC unit condenser, from the oil/water heat exchanger and the one required by the building. The result is imposed as a negative exogenous input to the TC model.

6.4.7 Balance of the plant

The *Pump* model is used to simulate the pump units installed on the system. Pressure drop through the solar field, the ORC evaporator and the biomass boiler are modelled with the lumped Δp model. The model computes a punctual pressure drop assuming fluid incompressibility and no thermal energy losses to the ambient. A linear and quadratic pressure drop terms are used to compute the total pressure drop. The homotopy function [180] is used during initialization to set the pressure drop to zero, facilitating the convergence of the solver. The expansion of the fluid through the by-pass valve of the solar field system is modelled with the *Valve* model. It is a lumped model where no dynamic and thermal energy losses to the ambient are considered. Four *PID* models for the different simulated controller units are used.

6.5 Results and discussion

6.5.1 Control logic analysis

The dynamic model of the Bricker system controlled according to the control logic described in section 6.3 is simulated under daily transient conditions. The main goal of this study is to investigate if the whole system can be safely and efficiently operated with the proposed automated control logic. From the safety point of view, the main concern is related to the biomass boiler,

the ORC system and the adsorption chiller, which need to be operated respecting the technical boundaries described in section 6.3. From the efficiency point of view, maximum exploitation of the solar resources should be ensured in order to minimize the biomass combustion rate. At the same time keeping the oil temperature at the ORC evaporator inlet (T_e) and the water temperature to the adsorption machine (T_l) close to their nominal values, allows for on-design working conditions maximizing the overall system efficiency. The dynamic model of the whole plant is simulated under a transient condition representative of an extreme reference situation characterized by a periodically sharp drop of the solar input due to the passage of a series of clouds [148]. The thermal load at the oil-water heat exchanger is assumed constant over the simulation time imposing a constant mass flow rate on the secondary side of the HXI component. The results are shown in Figure 6.4. The solar input drop is modeled by applying

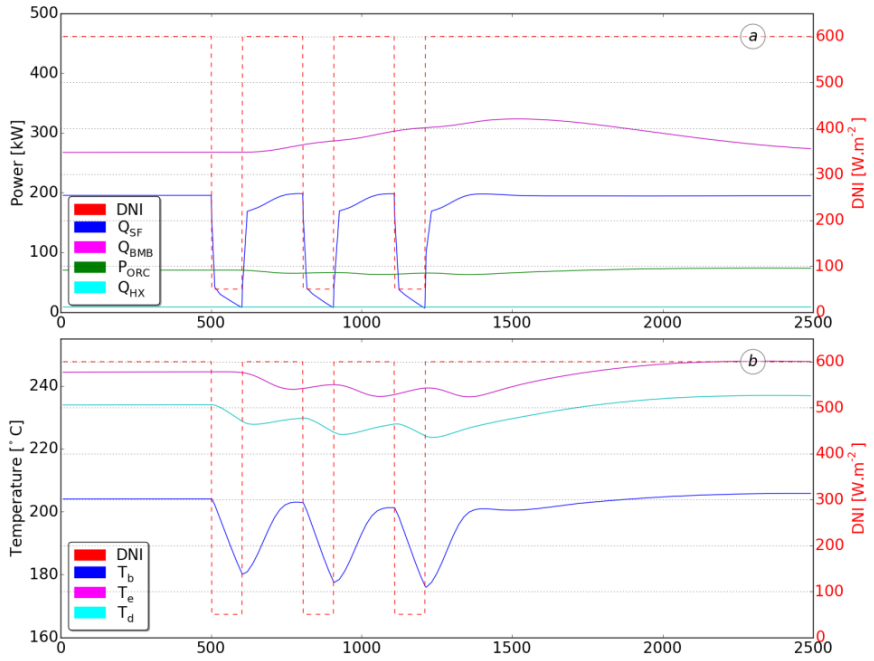

Figure 6.4 – Dynamic simulation results of the whole plant model as shown in Figure 2. The red dotted represents the DNI: it drops by 100% of its nominal value in 2 s, remain constant for 200 s then returns to its nominal value in 2 s. the interval between two subsequent drop is 200 s. a) Thermal power delivered by the solar field, the biomass, the ORC evaporator and the HX oil/water evaporator b) Temperature values in key points of the system.

a signal with three subsequent ramps to the DNI input of the solar field model. The DNI drops by 90% of its nominal value, perturbing the initial steady state condition. From the results, it appears that the time constants characterizing the biomass system are large enough to cause an overlapping effect of the disturbances. The variation of the controlled biomass thermal power, $\dot{Q}_{BMB}$, is shown in Figure 6.4a. Despite the sharp drop of the power absorbed in the solar field, $\dot{Q}_{SF}$, the ORC electrical power, P_{ORC}, is maintained close to its nominal value with a maximum deviation of 10%. The temperature variations are reported in Figure 6.4b. The

significant oscillations of the temperature at solar field outlet, T_b, are dumped by the biomass boiler recirculation system and the temperature at the boiler inlet, T_d, results characterized by much lower variations maintaining the biomass boiler temperature gradient between 9 and 15 K. The results show that through a mild regulation of the biomass boiler the system is able to run the ORC unit close to its nominal working condition despite the sharp drop of sun power. The effectiveness of the biomass system in decoupling the solar field from the ORC unit is assessed. In order to investigate and compare the performance of partial and total defocusing control logic implemented on the solar field, the dynamic model is simulated during a reference summer day in Càceres, Spain. The high value of the DNI is expected to trigger the defocusing mechanism. Two different simulations are run, one considering a constant negligible building thermal demand and one considering a variable thermal load based on available empirical data. In Figure 4 the simulation results for a partial (PD) and a total (TD) solar field defocusing are compared when a constant low building thermal demand is assumed. The simulation starts at 5:00 am and last for 17 hours. During the night the DNI is zero and the biomass is assumed to run close to its maximum power to provide the thermal energy required by the ORC power block. When the sun rises, at around 6:00 am, the thermal power provided by the solar field, $\dot{Q}_{SF}$, starts increasing and the biomass power, $\dot{Q}_{BMB}$, is consequently decreased by the control as the thermal power demand stays constant as shown in Figure 6.5a. Looking at Figure 6.5b, the increase of T_b causes the temperature at biomass inlet, T_d, to rise. As a consequence PI1 starts opening V1 to bypass the solar field and keep T_d close to its nominal point. The mass flow through the solar field by-pass valve and the solar field recirculation circuit increases proportionally as shown in Figure 6.5c. This mechanism boosts T_b towards its upper limit value, pushing the solar field into the defocusing mode and avoiding the shut-down of the biomass boiler. As the defocusing mode is activated, the system behaviour changes significantly depending on the adopted defocusing approach. In the PD case, solid lines, one forth of the solar field is defocused. The partial decrease in the solar collector effective surface allows for a smooth decrease of the solar field outlet temperature, T_b, bringing the system in a second steady working condition. In the TD case, dashed lines, the total defocusing of the solar collector causes a sharp decrease of the evaporator outlet temperature down to its minimum value which consequently triggers the solar field to exit the defocusing mode. As the DNI is roughly constant during the simulated reference day, the focusing-defocusing control runs continuously. A continuous control of the biomass system to overcome the sharp changes of the solar field thermal power is deemed necessary. As a consequence the overall system is characterized by an oscillatory trend. When the sun starts to set between 17:00 and 18:00, T_b reaches its lowest value that triggers the solar field to exit the defocusing mode. The drop of solar energy at the end of the day is compensated by the biomass power which is increased to meet the required thermal power demand. Overall both defocusing methods are able to maintain the system in safe working conditions during the simulated reference day. The temperature gradient at the biomass boiler is kept between 18 and 8 K. The ORC power block is run continuously with a maximum power deviation of 12.6% and 14% in the PD and the TD case respectively. At the cost of a continuous regulation of the solar field inclination, the TD approach allows a reduction of the total thermal energy

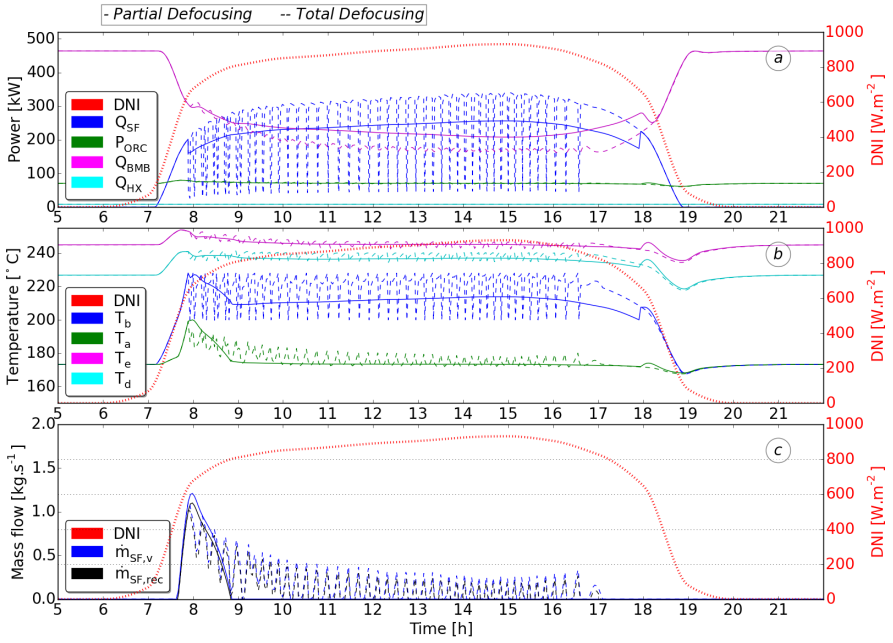

Figure 6.5 – Dynamic simulation results of the whole plant model during a reference summer day in Càceres, Spain. The dashed line represents the results for a solar field control strategy based on a total defocusing, the solid line for a partial defocusing. a) Thermal power delivered by the solar field, the biomass, the ORC evaporator and the HX oil/water evaporator b) Temperature values in key points of the system c) Mass flows of the solar field bypass and recirculation system.

delivered by the biomass boiler of 8% with respect to the PD mode consuming a smaller amount of biomass. Defining the solar fraction, $E_{SF,r}$ as:

$$E_{SF,r} = \frac{E_{SF}}{E_{BM}} = \frac{\int \dot{Q}_{SF} dt}{\int \dot{Q}_{BM}} \tag{6.1}$$

where E_{SF} is the total energy delivered by the solar field and E_{BM} is the total energy delivered by the biomass over a period of 17h from 5:00 to 22:00. The TD approach results in a solar fraction of 59% while the PD in a solar fraction of 47%. The simulation results for the same reference day considering a variable thermal load demand are reported in Figure 6.6. As in the previous simulation, the DNI increase triggers the defocusing mechanism around 8:00 am. The PD approach brings the system to a steady condition while the TD approach causes an oscillatory behaviour in the system. As shown in Figure 6.6a, around 9:00 am the building thermal demand starts increasing and more power is required by HX1, Q_{HX}. As more thermal energy is required, the solar field inlet temperature T_a decreases and so does T_b reaching its lowest value which causes the solar field to exit its defocusing mode around 9:30 am. For the rest of the day the TD and PD approaches lead to the same results. As the thermal demand keeps increasing during the day, the biomass boiler power is regulated to meet the thermal

needs. From a safety point of view the control logic is able to maintain the biomass boiler temperature gradient between the required limit with a minimum of 9 K and a maximum of 20 K. The ORC power block inlet temperature experience the biggest drop around 19:00 and 21:00 when the sun goes down and the biomass is brought close to its maximum value to provide the requested thermal power. The ORC evaporator inlet temperature smoothly decreases reaching a minimum value of 233°C which corresponds to an electrical power drop of 17% with respect to the nominal power. Overall the TD case allows a reduction of the biomass boiler of only 0.5% with respect to the PD case as the two approaches lead to the same plant trend for most of the time. As a consequence a solar fraction of 53% and 54% is found for the PD and the TD case respectively.

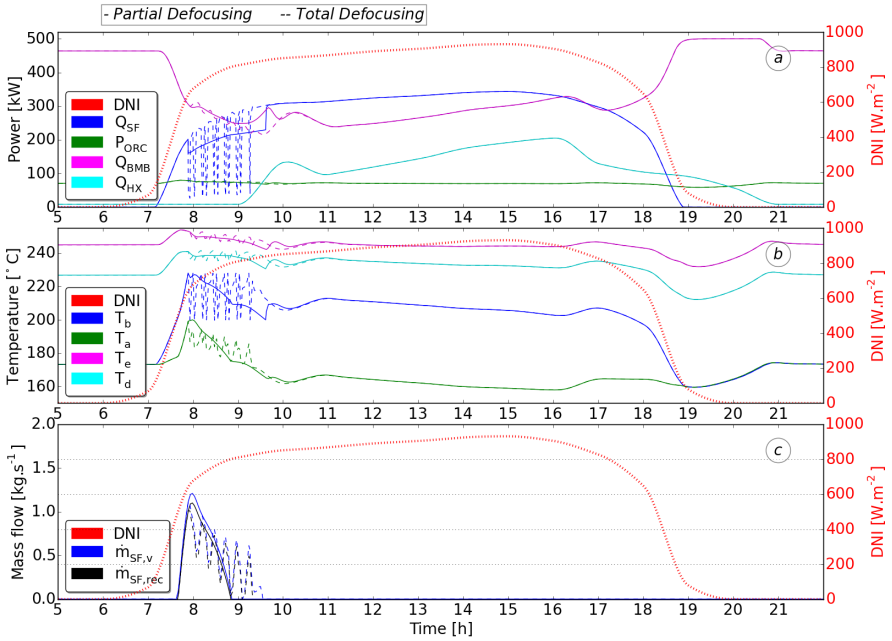

Figure 6.6 – Dynamic simulation results of the whole plant model during a reference summer day in Càceres, Spain with variable thermal power load. The dashed line represents the results for a solar field control strategy based on a total defocusing (TD) , the solid line for a partial defocusing (PD). a) Thermal power delivered by the solar field, the biomass, the ORC evaporator and the HX oil/water evaporator b) Temperature values in key points of the system c) Mass flows of the solar field bypass and recirculation system.

6.5.2 Economic analysis

In order to investigate the effect of the different control strategies, reported in sub-section 6.3, on the economic profitability of the BRICKER system an annual analysis is performed using the developed dynamic model. In particular rather then simulating the model for a complete year, weekly simulations are performed on reference weeks for the summer and winter time period and the results are extended over a full year. This approach allows to obtain preliminary

annual performance of the system by significantly decrease the computational time, while still accounting for the main dynamics. The payback time (PBT) and the net present value (NPV) are selected as the two indexes to compare the effect of the different control strategies on the economic performance of the system [181].
The payback time is computed as:

$$PBT = \frac{IC}{AS} \tag{6.2}$$

where IC is the total investment cost of the unit and AS accounts for the annual savings and it is defined as:

$$AS = ElSav + ThSav_h + ThSav_c + Sub \tag{6.3}$$

where $ElSav$ are the electrical savings, $ThSav_h$ and $ThSav_c$ are the heating and cooling thermal savings respectively and Sub stands for possible subsidies from the government. The electrical savings are defined as:

$$ElSav = E_{\text{ORC}} \cdot C_{\text{el}} \tag{6.4}$$

where E_{ORC} is the annual electrical energy produced by the ORC unit and C_{el} is the cost of electricity. The heating thermal savings are computed as as if the whole required thermal energy was generated with a gas burner with an efficiency, η_b, of 0.9. The heating thermal savings are computed as:

$$ThSav_h = \frac{Eth/\eta_b}{LHV_{gas}} \cdot C_{gas} \tag{6.5}$$

where Eth is the annual heating demand of the building, LHV_{gas} is the low gas heating value and C_{gas} is the cost of gas. The cooling savings are computed as as if the whole cooling demand was generated with an electric chiller with a COP of 2.5:

$$ThSav_c = C_{el} \cdot E_{el,chiller} \tag{6.6}$$

where $E_{el,c}$ is the total energy required to run the electric chiller to supply the cooling demand and it is calculated as the integral over the year of the electrical power absorbed by the chiller:

$$E_{el,c} = \int P_{el,chiller}\, dt = \frac{1}{COP} \cdot \int \dot{Q}_c\, dt \tag{6.7}$$

where $\dot{Q}_c$ is the cooling thermal power required by the building. The net present value (NPV) allows to determine the overall value of the project. It represents the value in today's Euro of all future cash flows. A plant lifetime of 25 years is assumed. Electricity generation and the building thermal demand over the lifetime are considered invariant with respect to the first

year. The NPV is computed as:

$$NPV = -IC + (PDB - PDC) + Sub \tag{6.8}$$

where PDB is the present discount benefit and PDC is the present discount cost. The PDB accounts for the electricity generated by the ORC and sold to the grid and the thermal and cooling savings which are translated to benefit. As the electricity is generated only during day-time a constant tariff of 0.1 €kWh^{-1} is assumed. The PDC accounts for the annual consumption of biomass and the maintenance cost. The discount rate is set at 3%.
The costs for the different components of BRICKER plant are reported in Table 6.1. The costs

Table 6.1 – Cost for the different components of the Trigen system.

Item	Cost
CSP field	600 €m^{-2}
ORC unit	2.5e3 €kW$_{el}^{-1}$
Adsorption Chiller	400 €kW$_{th,c}^{-1}$
Biomass Boiler	8e2 €kW^{-1}

of the biomass crops and of the gas are reported in Table 6.2. The maintenance costs are estimated to make up 0.5 % of the total investment costs. Based on the ministerial order

Table 6.2 – Price for biomass and gas

Item	Cost
Biomass crops	0.07 €kg^{-1}
Gas	0.0236 €m^{-3}

IET/1045/2014 [182], an annual subsidy of 557.011 €MW^{-1} is provided for cogeneration unit based on renewable energy technology for a minimum number of nominal operational hours (NOP) of 1632 per year. As the ORC unit has a gross nominal power of 100 kW$_{el}$ an annual subsidy of 55.701 €MW^{-1} is considered. In order to further assess the benefit of the BRICKER unit from an environmental point of view, the reduction of greenhouse gas (GHG) emission is computed assuming that the emission of CO2 per GJ of gas equals to 51.33 kg/GJ [183].
In Table 6.3, the annual results for the two strategies are reported. Running the plant following

Table 6.3 – Indexes assessing the annual performances of the two proposed control strategies.

Strategy	NOP [hours]	PBT [years]	NPV [€]	GHG savings [ton of CO2]
I	2770	12	369e3	145
II	236	54	-1e6	144

Strategy I allows to run the ORC for a number of hours higher than the threshold set by the Spanish government to access the subsidy. This allows to reach a payback time of 12 years and a positive net present value of around 370 €. On the contrary applying Strategy II leads to under-exploit the ORC power block cutting off the access to the subsidy. This leads to an entirely non-sustainable situation characterized by a payback time of 54 years and a negative net present value. As the burning of biomass has a limited impact on the final ton of CO2 saved by the plant the GHG savings of the two strategies are characterized by a very similar value.
From these results it is evident that the proposed system is not economically viable unless subsidies from the government are provided. A drastic decrease of the cost of the technologies employed in the system or a more advanced system architecture leading to lower investment cost and higher efficiency could lead to economic viability.

6.6 Conclusions

The performance of the CSP-biomass trigeneration system based on the ORC technology developed in the framework of the EU founded BRICKER project is investigated by means of a dynamic model. The system has the goal of meeting the electricity, heating and cooling demands of a non-residential building in Càceres, Spain. The dynamic model is based on the ThermoCycle library described in Chapter 4, adopting a simplified approach which allows to account only for the main dynamics. Firstly the model is employed to investigate the performance of the different control logics on a daily basis. Secondly weekly based simulations are performed to assess the effect of two proposed control strategies on the economic performance of the system. The following conclusions can be drawn:

- The dynamic simulations allowed to assess the effectiveness of the biomass boiler to decouple the solar field to the HXI and ORC units. The system is able to withstand fast variation of the sun power as demonstrated by the results of the simulations reported in Figures 6.4-6.6. Variation in solar field outlet temperature of 30 K results in variation at the evaporator ORC inlet temperature of 8 K causing a decrease in electrical power of 8% with respect to its nominal power.

- The two solar field defocusing approaches are investigated during different working conditions, one with constant thermal power and one with variable thermal power. In both situations the two approaches allow to operate the system within the safety limits imposed by the ORC unit and the biomass boiler. The effectiveness of the two approaches in exploiting the sun power is assessed in terms of the solar fraction. The TD approach allow to increase the solar fraction of up to 12 percentage point compared to the PD case at the cost of continuously running the electric motor of the solar field.

- A preliminary investigation of the annual performance of the BRICKER system is performed with the developed dynamic model. The results allow to conclude that the system is economically viable only if public funds are available for support. A significant decrease of the cost of the technology employed or a more advanced system architecture could lead to economic viability.

In this work a methodology based on dynamic simulations to investigate the performance of a novel trigeneration system on a daily and annual basis is proposed. The developed dynamic model is based on a simplified modelling approach which allows to analyse the system at different levels of details.

Nomenclature

Acronyms

EU	European Union
CSP	Concentrated solar power
ORC	Organic Rankine cycle
TES	Thermal energy storage
HTF	Heat transfer fluid
DNI	Direct normal irradiation
CHP	Combined heat and power
SF	Solar field
HX	Heat exchanger
BMB	Biomass boiler
CT	Cooling tower
TL	Thermal load
GUI	Graphical user interface
IC	Investment cost
AS	Annual savings
C	Cost

Subscripts

th	Thermal
el	Electrical
h	Heating
c	Cooling

Symbols

T	Temperature (°C)
$\dot{Q}$	Thermal power (W)
P	Electrical power (W)
E	Energy (J)

7 Conclusions

In this thesis the original results related to experimental and numerical research carried out by the author and his colleagues, aimed at developing a reliable, flexible and validated methodology to investigate the dynamics of low-capacity, organic Rankine cycle systems with a focus on low quality heat recovery applications are outlined. The content of this manuscript constitutes the base of several conference papers and peer-reviewed journals which have been listed in the Papers and Presentations section. The thesis is composed by five main chapters. The main outcomes and future prospectives related to each chapter are considered below defined with the * and ♢ symbols respectively.

Chapter 2 presented an experimental investigation of a small capacity ORC system equipped with a single screw expander using SES36 and R245fa as working fluid.

* The expander was obtained by modifying a screw compressor to work in expansion mode. Maximum electrical isentropic efficiencies of 62% and of 52% were measured at 3000 rpm and at pressure ratio of 6.8 and 7.7 for SES36 and R245fa respectively. A maximum power of 7.3 kW_{el} was reached with R245fa at a pressure ratio of 6.2 at 3000 rpm while a value of 7.1 kW_{el} was reached using SES36 with a pressure ratio of 8.5 at 3000 rpm. These results highlighted the potential of the single screw machine as an interesting solution for small capacity ORC unit for low temperature applications.

* The experimental analysis at a system level led to the conclusion that the fluid characterized by the lowest critical temperature allowed higher power generation in line with the numerical study presented in [59].

* In light of the obtained experimental results, it followed that for low temperature waste heat recovery applications with an intermediate oil loop, an optimally designed SES36 ORC system would perform better than an R245fa one. On the other hand, the SES36 system will be characterized by bigger components (e.g. expander with higher swept volume) resulting in a more costly system compared to an R245fa one. This analysis experimentally proved that accounting for parameters related to the system components characteristics from the early design stage can add significant benefit to the final power system layout, in particular the expansion machine characteristic.

- ♢ This work is meant to serve as a reference for setting up experimental investigation of small ORC-systems at a component and at a system level. Furthermore to the author's knowledge it is the first to propose open source data opening a broad range of possibilities for further investigation, such as model calibration or validation, cycle analysis or fluid comparison.

Chapter 3 reported the experimental campaign results obtained by investigating the vaporization phenomena of HFC-245fa and HFO-1233zd in small brazed plate heat exchangers at typical evaporating conditions for ORC power systems for low temperature applications. The refrigerant experimental results were analysed in terms of average heat transfer coefficient and frictional pressure drop

- * The Wilson plot technique employed to derive the secondary fluid single phase heat transfer coefficient led to Nusselt values up to two times higher than the ones predicted with existing correlations. This result underlined the limit of most of the standard water-based single phase correlations available in the literature, and call for an effort towards the development of up to date single-phase correlations.

- * The refrigerants heat transfer coefficient showed an increasing trend with respect to the mean vapour quality up to a certain value when dry-out occurred. The Thonon method results suggested that nucleate boiling was predominant during the tests.

- * Six heat transfer and four frictional pressure drop correlations available in the literature were compared against the acquired experimental results. For the tested conditions, only the Cooper heat transfer correlation was capable of delivering satisfying results. All the pressure drop correlations considerably over-predicted the experimental results.

- * A heat transfer and a pressure drop correlations were derived from the experimental data. The correlations were characterized by a fairly good accuracy and can be used for modelling the tested test-rig unit.

- ♢ A first step towards the investigation of the physical phenomena driving the vaporization of low temperature organic fluids in small-scale brazed plate heat exchangers for ORC application has been set. Further work is necessary to enlarge the database, making it as comprehensive as possible. Experimental campaigns comprising the study of mixture vaporization and the investigation of the heat exchanger geometrical parameters are suggested as next steps.

Chapter 4 described the main characteristics of the ThermoCycle Modelica library. The library is an open-source tool for the modelling of small scale thermo-hydraulic systems.

- * The library has been designed exploiting the feature of the Modelica programming language. Particular care has been taken to avoid an extensive use of the inheritance feature, in order to maximise model readability.

* As the time constants characterizing small-scale thermo-hydraulic systems are predominantly defined by the physical phenomena characterizing the heat exchangers, these have been modelled based on accumulation of mass and energy and on a steady-state momentum balance following the finite volume (FV), the moving boundary (MB) and a novel lumped approach (L-HX). When developing model based control, the FV and MB are recommended as they allow for an high level of details. The simple paradigm characterizing the L-HX model can significantly boost simulation time and robustness of the simulation and should be used when simulating complex system models over long time periods.

* An inheritance structure has been implemented in the finite volume and moving boundary heat exchanger models to handle the computation of the convective heat transfer coefficients on the two fluid sides. The object allows the user to select detailed heat transfer correlations from the literature or simplified laws based on the mass flow rate or the fluid vapour quality.

* Models of rotary machines and balance of plants components are available in the library with different levels of details. For simulation at a component level, detailed dynamic models accounting for the inertia of the different mechanical elements are recommended. For thermo-hydraulic system model simulations, semi-empirical models with no dynamics are suggested.

* In order to increase the performance and robustness of the ThermoCycle library different numerical methods have been implemented and are available in the library. In particular, in discretized two-phase flow models, special care must be taken to handle the discontinuity in the density derivative on the liquid saturation curve.

◇ The library is thought as a work in progress project. During the last years several universities started using it for the modelling of thermal systems. Development towards models of large systems for annual based simulations is foreseen as the next step.

Chapter 5 reported the dynamic validation of the models presented in Chapter 4 at a component and at a system level against experimental data acquired on different facilities. In order to build the confidence for using a dynamic model, it is of paramount importance to ensure the model effectiveness in predicting the driving physical phenomena of the real system. This process is called Validation.

* A dynamic validation of the parabolic trough collector model was performed against experimental data obtained at the Plataforma Solar the Almería, Spain. The measured data were based on heat transfer fluid mass flow rate variation, heat transfer fluid inlet temperature variation and solar beam radiation changes were carried out. The Modelica model was able to predict with good accuracy the measured data.

* A dynamic validation of the finite volume (FV) and the moving boundary (MB) heat exchanger models was performed against experimental data acquired on the high pressure line of the test rig presented in Chapter 3. The dynamic of the units were analysed

by applying a step downwards in the pump rotational speed. Both approaches were able to correctly predict the data. The FV results were characterized by an absolute error of the simulated working fluid outlet temperature up to 0.8 °C closer to the experimental data than the MB models. The higher precision of the FV model came at the cost of a simulation speed up to three orders of magnitude slower than the MB approach in line with the results obtained by [142].

* A dynamic validation of a complete ORC model against the experimental data acquired on the 11 kW_{el} ORC unit presented in Chapter 2 was performed. Two ORC unit models employing a FV and MB based evaporator were developed. The dynamic validation was performed by imposing downwards and upwards step changes to the centrifugal pump rotational speed. The validation showed a good overlap between the experimental data and the two ORC unit models.

♢ In light of the obtained results for the parabolic trough model validation, a lumped model is recommended if the performance of the collectors is analysed on a daily or longer time frame. A minimum level of discretization of 20 nodes is suggested if more detailed analysis needs to be performed e.g. model based control strategy investigations.

♢ In light of the obtained results for the heat exchangers validation, when modelling complete power systems it is recommended to avoid employing specific heat transfer correlations and rather use simplified laws such as the vapour quality dependant (VQD) method. Detailed heat transfer correlations increase significantly the computational time of the simulation while slightly improving the model accuracy.

♢ In light of the obtained results for the ORC unit validation, constant void fraction in the MB modelling approach should be avoided as it overestimates the dynamics of the system. Furthermore the implementation of numerical methods such as the smooth density derivative method is recommended to properly handle the discontinuity of the density derivative at the fluid phase boundary.

♢ It was proven that the modelling approaches adopted in the ThermoCycle library led to satisfactory results for the simulation of small capacity thermal systems. Further developments should focus on implementing models capable of handling the simulation of cold start-up or shut-down conditions, i.e. zero flow rate in the tubes.

Chapter 6 presents a methodology based on a simplified dynamic modelling approach to investigate the daily and annual performance of the trigeneration CSP-biomass system based on the ORC technology developed in the framework of the EU founded project BRICKER.

* The Modelica ThermoCycle library coupled to the CoolProp package for the computational of fluid properties provided a robust and efficient framework for the development of a simplified modelling approach for the simulation of the trigeneration CSP-biomass BRICKER system.

* The developed system model allowed to successfully assess the capability of different control logics to maintain safe working conditions during fast solar variations and to investigate their effects on the performance of the overall system. For this type of analysis lumped models are recommended.

* The model capabilities were exploited to investigate the economic viability of the system when different control strategies are applied. Weekly simulations were performed on reference weeks and the results were extended over a full year. This approach allowed to obtain preliminary annual performance of the system by significantly decreasing the computational time, while still accounting for the main dynamics.

* The annual results allowed to derive a preliminary conclusions on how to organize the control strategy of the system and led to the conclusions that the proposed trigeneration unit required government subsidies to reach economic viability.

◇ The presented simplified modelling approach allowed to build a reliable simulation tool for predicting the performance of the trigeneration BRICKER unit, demonstrating the capability of dynamic model-based technique in helping identifying the economically successful operation in an early project phase. The proposed methodology and tool are virtually applicable to any combined heat and power systems.

Bibliography

[1] J. Hansen, M. Sato, P. Hearty, R. Ruedy, M. Kelley, V. Masson-Delmotte, G. Russell, G. Tselioudis, J. Cao, E. Rignot, I. Velicogna, E. Kandiano, K. von Schuckmann, P. Kharecha, a. N. Legrande, M. Bauer, and K.-W. Lo. Ice melt, sea level rise and superstorms: evidence from paleoclimate data, climate modeling, and modern observations that 2 °C global warming is highly dangerous. *Atmospheric Chemistry and Physics Discussions*, 15(14): 20059–20179, 2015. ISSN 1680-7375. doi: 10.5194/acpd-15-20059-2015.

[2] RasmusE. Benestad, Dana Nuccitelli, Stephan Lewandowsky, Katharine Hayhoe, HansOlav Hygen, Rob van Dorland, and John Cook. Learning from mistakes in climate research. *Theoretical and Applied Climatology*, pages 1–5, 2015. ISSN 0177-798X. doi: 10.1007/s00704-015-1597-5.

[3] John Cook, Naomi Oreskes, Peter T Doran, William R L Anderegg, Bart Verheggen, Ed W Maibach, J Stuart Carlton, Stephan Lewandowsky, Andrew G Skuce, and A Sarah. Consensus on consensus : a synthesis of consensus estimates on human caused global warming. *Environmental Research Letters*, 11(2016):1–24, 2016. ISSN 1748-9326. doi: 10.1088/1748-9326/11/4/048002.

[4] UNFCCC. Conference of the Parties (COP). Adoption of the Paris Agreement. Proposal by the President. *Paris Climate Change Conference - November 2015, COP 21*, 21932 (December):32, 2015. doi: FCCC/CP/2015/L.9/Rev.1.

[5] IEA. Energy and Climate Change. *World Energy Outlook Special Report*, pages 1–200, 2015. ISSN 1476-4687. doi: 10.1038/479267b.

[6] Costante M. Invernizzi. *Closed power cycles*. 2013. ISBN 9781447151395.

[7] F.W. Ofeldt. Frank w, January 18 1887. URL http://www.google.com/patents/US356420. US Patent 356,420.

[8] L. D'Amelio. *L'impiego di vapori ad alto peso molecolare in piccole turbine e l'utilizzazione del calore solare per energia motrice*. INAG, 1935. URL https://books.google.be/books?id=87PWoAEACAAJ.

[9] Cesare Silvi. STORIA DELLA POMPA SOLARE SOMOR E DEI SUOI INVENTORI, 2000.

[10] H M Curran. Use of Organic Working Fluids in Rankine Engines. *Journal of Energy*, 5(4): 218–223, 1981. ISSN 0146-0412. doi: 10.2514/3.62532. URL http://dx.doi.org/10.2514/3.62532.

[11] L. C. Spencer. A comprehensive review of small solar-powered heat engines: Part II. Research since 1950-"conventional" engines up to 100 kW. *Solar Energy*, 43(4):197–210, 1989. ISSN 0038092X. doi: 10.1016/0038-092X(89)90020-0.

[12] G. Angelino, M. Gaia, and E. Macchi. A review of italian activity in the field of organic Rankine cycles. *Verein Deutscher Ingenieure Berichte 539*, pages 465–482, 1984.

[13] Thomas Tartière, 2016. URL http://orc-world-map.org/index.html. Online; accessed 2016-07-29.

[14] Elsevier B.V., 2016. URL https://www.scopus.com/.

[15] Aleksandra Borsukiewicz-Gozdur and Wladyslaw Nowak. Comparative analysis of natural and synthetic refrigerants in application to low temperature Clausius-Rankine cycle. *Energy*, 32(4):344–352, 2007. ISSN 03605442. doi: 10.1016/j.energy.2006.07.012.

[16] Bahaa Saleh, Gerald Koglbauer, Martin Wendland, and Johann Fischer. Working fluids for low-temperature organic Rankine cycles. *Energy*, 32(7):1210–1221, 2007. ISSN 03605442. doi: 10.1016/j.energy.2006.07.001.

[17] Florian Heberle and Dieter Brüggemann. Exergy based fluid selection for a geothermal Organic Rankine Cycle for combined heat and power generation. *Applied Thermal Engineering*, 30(11-12):1326–1332, 2010. ISSN 13594311. doi: 10.1016/j.applthermaleng.2010.02.012.

[18] J. G. Andreasen, U. Larsen, T. Knudsen, L. Pierobon, and F. Haglind. Selection and optimization of pure and mixed working fluids for low grade heat utilization using organic rankine cycles. *Energy*, 73:204–213, 2014. ISSN 03605442. doi: 10.1016/j.energy.2014.06.012. URL http://dx.doi.org/10.1016/j.energy.2014.06.012.

[19] Patrick Linke, Athanasios Papadopoulos, and Panos Seferlis. Systematic Methods for Working Fluid Selection and the Design, Integration and Control of Organic Rankine Cycles—A Review. *Energies*, 8(6):4755–4801, 2015. ISSN 1996-1073. doi: 10.3390/en8064755.

[20] E.W. Lemmon, Mark O Mclinden, and M.L. Huber. Reference Fluid Thermodynamic and Transport Properties-REFPROP Version 9.1. Technical report, National Institute of Standards and Technology (NIST), 2013.

[21] FluidProp v3.0. Asimptote, 2014. URL http://www.asimptote.nl/software/fluidprop. Online; accessed 2016-07-29.

[22] TLK Thermo GmbH. TIL Suite - Simulates Thermal Systems, April 4th 2013. URL http://www.tlk-thermo.com.

[23] F. J.Wagner M. Otter M. Tiller H. Elmqvist H. Tummescheit, J. Eborn. Modelica.Media v3.1. Modelica Association, 2013.

[24] I.H. Bell, J. Wronski, S. Quoilin, and V. Lemort. Pure- and Pseudo-Pure Fluid Thermophysical Property Evaluation and the Open-Source Thermophysical Property Library CoolProp. *Industrial & Engineering Chemistry Research*, 53:2498–2508, 2014. doi: 10.1021/ie4033999.

[25] Piero Colonna, Emiliano Casati, Carsten Trapp, Tiemo Mathijssen, Jaakko Larjola, Teemu Turunen-Saaresti, and Antti Uusitalo. Organic Rankine Cycle Power Systems: From the Concept to Current Technology, Applications, and an Outlook to the Future. *Journal of Engineering for Gas Turbines and Power*, 137(10):100801, 2015. ISSN 0742-4795. doi: 10.1115/1.4029884. URL http://gasturbinespower.asmedigitalcollection.asme.org/article.aspx?doi=10.1115/1.4029884.

[26] S. Quoilin, M. van den Broek, S. Declaye, P. Dewallef, and V. Lemort. Techno-economic survey of organic Rankine cycle ORC systems. *Renewable and Sustainable Energy Reviews*, 22:168–186, 2013. doi: 10.1016/j.rser.2013.01.028.

[27] Hubertus Tummescheit. *Design and Implementation of Object-Oriented Model Libraries using Modelica*. PhD thesis, Department of Automatic Control Lund Institute of Technology, 2002.

[28] Francesco Casella, Francesco Pretolani, Politecnico Milano, and Piazza Leonardo. Fast Start-up of a Combined-Cycle Power Plant : a Simulation Study with Modelica. In *In proceedings of the 5th International Modelica Conference*, pages 3–10, 2006.

[29] Sylvain Quoilin. *Sustainable energy conversion through the use of organic Rankine cycles for waste heat recovery and solar applications*. PhD thesis, University of Liege, 2011.

[30] a. Muley and R. M. Manglik. Experimental Study of Turbulent Flow Heat Transfer and Pressure Drop in a Plate Heat Exchanger With Chevron Plates. *Journal of Heat Transfer*, 121(1):110, 1999. ISSN 00221481. doi: 10.1115/1.2825923.

[31] Björn Palm and Joachim Claesson. Plate Heat Exchangers: Calculation Methods for Singleand Two-Phase Flow. *Heat Transfer Engineering*, 27(4):88–98, 2006. ISSN 0145-7632. doi: 10.1080/01457630500523949.

[32] G. Longo and A. Gasparella. Heat transfer and pressure drop during HFC refrigerant vaporisation inside a brazed plate heat exchanger. *International Journal of Heat and Mass Transfer*, 50(25-26):5194–5203, 2007. ISSN 00179310. doi: 10.1016/j.ijheatmasstransfer.2007.07.001.

[33] Giovanni a. Longo. Hydrocarbon Refrigerant Vaporization Inside a Brazed Plate Heat Exchanger. *Journal of Heat Transfer*, 134(10):101801, 2012. ISSN 00221481. doi: 10.1115/1.4006817.

[34] Sadashiva S. Godbole. MMS Simulation of RSG/FW Train of a nuclear power plant for developing a RSG level control system. Technical report, B&W Nuclear Service Company, 1990.

[35] P. Colonna and H. van Putten. Dynamic modeling of steam power cycles. Part I-Modeling paradigm and validation. *Applied Thermal Engineering*, 27(2-3):467–480, 2007. ISSN 13594311. doi: 10.1016/j.applthermaleng.2006.06.011.

[36] Modelica Association, July 2016. URL https://www.modelica.org/. Online; accessed 2016-07-29.

[37] F. Casella and A. Leva. Modelica open library for power plant simulation: design and experimental validation. *Proceedings of the 3rd International Modelica Conference*, pages 41–50, 2003. URL http://scholar.google.com/scholar?hl=en{&}btnG=Search{&}q=intitle:Modelica+open+library+for+power+plant+simulation+:+design+and+experimental+validation{#}0.

[38] Jianhua Zhang, Wenfang Zhang, Guolian Hou, and Fang Fang. Dynamic modeling and multivariable control of organic Rankine cycles in waste heat utilizing processes. *Computers & Mathematics with Applications*, 64(5):908 – 921, 2012. ISSN 0898-1221. doi: http://dx.doi.org/10.1016/j.camwa.2012.01.054. Advanced Technologies in Computer, Consumer and Control.

[39] Jianhua Zhang, Yeli Zhou, Rui Wang, Jinliang Xu, and Fang Fang. Modeling and constrained multivariable predictive control for {ORC} (rganic Rankine cycle) based waste heat energy conversion systems. *Energy*, 66(0):128 – 138, 2014. ISSN 0360-5442. doi: http://dx.doi.org/10.1016/j.energy.2014.01.068.

[40] Adrian Rettig and Ulf Christian Müller. A Performance Prediction Tool for Orc Applications Based on Modelica. *3RD International Seminar on ORC Power Systems, October 12-14, 2015, Brussels, Belgium*, (2009):1–10, 2015.

[41] Junjiang Bao and Li Zhao. A review of working fluid and expander selections for organic rankine cycle. *Renewable and Sustainable Energy Reviews*, 24(0):325 – 342, 2013. ISSN 1364-0321. doi: http://dx.doi.org/10.1016/j.rser.2013.03.040.

[42] Daniel Maraver, Javier Royo, Vincent Lemort, and Sylvain Quoilin. Systematic optimization of subcritical and transcritical organic Rankine cycles (ORCs) constrained by technical parameters in multiple applications. *Applied Energy*, 117(0):11 – 29, 2014. ISSN 0306-2619. doi: http://dx.doi.org/10.1016/j.apenergy.2013.11.076.

[43] J.G. Persson. Performance mapping vs design parameters for screw compressors and other displacement compressor types. *Verein Deutscher Ingenieure Berichte 539*, 859:15 – 31, 1990.

[44] Liu H. Qiu, G. and Riffat; S. Expanders for micro-CHP systems with organic rankine cycle. *Applied Thermal Engineering*, 31(16):3301 – 3307, 2011. ISSN 1359-4311. doi: http://dx.doi.org/10.1016/j.applthermaleng.2011.06.008.

[45] V. Lemort, S. Declaye, and S. Quoilin. Experimental characterization of a hermetic scroll expander for use in a micro-scale Rankine cycle. *Proccedings of the Institution of Mechanical Engineers, Part A: Journal of Power and Energy*, 226(1), 2011.

[46] Sébastien Declaye, Sylvain Quoilin, Ludovic Guillaume, and Vincent Lemort. Experimental study on an open-drive scroll expander integrated into an ORC (organic Rankine cycle) system with R245fa as working fluid. *Energy*, 55(0):173 – 183, 2013. ISSN 0360-5442. doi: http://dx.doi.org/10.1016/j.energy.2013.04.003.

[47] H. Leibowitz, I.K. Smith, and N. Stosic. Cost effective small scale ORC systems for power recovery from low grade heat sources. In *Proceedings of IMEC2006*, 2006.

[48] Henrik Öhman. Implementation and evaluation of a low temperature waste heat recovery power cycle using NH3 in an organic Rankine cycle. *Energy*, 48(1):227 – 232, 2012. ISSN 0360-5442. doi: http://dx.doi.org/10.1016/j.energy.2012.02.074.

[49] Henrik Öhman and Per Lundqvist. Experimental investigation of a lysholm turbine operating with superheated, saturated and 2-phase inlet conditions. *Applied Thermal Engineering*, 50(1):1211 – 1218, 2012. ISSN 1359-4311. doi: http://dx.doi.org/10.1016/j.applthermaleng.2012.08.035.

[50] D. Ziviani, I. Bell, De Paepe, and M. v. d. Broek. Comprehensive model of a single screw expander for ORC-systems applications. In *Proceedings of the 22nd International compressor engineering conference at Purdue*, 2014.

[51] Wei Wang, Yu ting Wu, Chong fang Ma, Lin ding Liu, and Jian Yu. Preliminary experimental study of single screw expander prototype. *Applied Thermal Engineering*, 31(17–18): 3684 – 3688, 2011. ISSN 1359-4311. doi: http://dx.doi.org/10.1016/j.applthermaleng.2011.01.019. {SET} 2010 Special Issue.

[52] Wei He, Yuting Wu, Yanhai Peng, Yeqiang Zhang, Chongfang Ma, and Guoyuan Ma. Influence of intake pressure on the performance of single screw expander working with compressed air. *Applied Thermal Engineering*, 51(1–2):662 – 669, 2013. ISSN 1359-4311. doi: http://dx.doi.org/10.1016/j.applthermaleng.2012.10.013.

[53] Wei Wang, Yu ting Wu, Chong fang Ma, Guo dong Xia, and Jing fu Wang. Experimental study on the performance of single screw expanders by gap adjustment. *Energy*, 62(0): 379 – 384, 2013. ISSN 0360-5442. doi: http://dx.doi.org/10.1016/j.energy.2013.09.031.

[54] S. Gusev, D. Ziviani, I. Bell, M. De Paepe, and M. van den Broek. Experimental comparison of working fluids for organic Rankine cycle with single screw expander. In *Proceedings of the 15th International refrigeration and air conditioning conference Purdue*, 2014.

[55] A. Desideri, M. v. d. Broek, S. Gusev, V. Lemort, and S. Quoilin. Experimental campaign and modeling of a low-capacity waste heat recovery system based on a single screw expander. In *Proceedings of the 22nd International compressor engineering conference at Purdue*, 2014.

[56] Theodore L. Bergman, Adrienne S. Lavine, Frank P. Incropera, and David P. Dewitt. *Fundamentals of Heat and Mass Transfer*. John Wiley and Sons, 2011.

[57] E.J. Bala, P.W. O Callaghan, and S.D. Probert. Influence of organic working fluids on the performance of a positive-displacement pump with sliding vanes. *Applied Energy*, 20(2): 153 – 159, 1985. ISSN 0306-2619. doi: http://dx.doi.org/10.1016/0306-2619(85)90031-5.

[58] Costante Mario Invernizzi. *Closed power Cycles*. Springer, 2013.

[59] Chien K.H. Liu, B.T. and C.C. Wang. Effect of working fluids on organic rankine cycle for waste heat recovery. *Energy*, pages 1207–17, 2004. doi: http://dx.doi.org/10.1016/j.energy.2004.01.004.

[60] S. Quoilin, S. Declaye, A. Legros, L. Guillaume, and L. Vincent. Working fluid selection and operating maps for organic rankine cycle expansion machines. In *Proceedings of the 21st International Compressor Conference at Purdue*, 2012.

[61] Holger Martin. Pressure Drop and Heat Transfer in Plate Heat Exchangers. *VDI Heat Atlas*, page 1609, 2010. doi: 10.1007/978-3-540-77877-6.

[62] Sotirios Karellas, Andreas Schuster, and Aris-Dimitrios Leontaritis. Influence of supercritical ORC parameters on plate heat exchanger design. *Applied Thermal Engineering*, 33-34:70–76, feb 2012. ISSN 13594311. doi: 10.1016/j.applthermaleng.2011.09.013.

[63] Bala V Datla, Joost J Brasz, Syracuse Turbo, and Machinery Llc. Comparing R1233zd and R245fa for Low Temperature ORC Applications. In *15th International Refrigeration and Air Conditioning Conference at Purdue*, pages 1–7, Purdue, 2014.

[64] Ludovic Guillaume, Arnaud Legros, Adriano Desideri, and Vincent Lemort. Performance of a radial-inflow turbine integrated in an ORC system and designed for a WHR on truck application: An experimental comparison between R245fa and R1233zd. *Applied Energy*, (March), 2016. ISSN 03062619. doi: 10.1016/j.apenergy.2016.03.012.

[65] A. Desideri, T.S. Ommen, J. Wronski, S. Quoilin, V. Lemort, and Haglind F. Experimental results for hydrocarbon refrigerant vaporization in brazed plate heat exchangers at high pressure. In *16th International Refrigeration and Air Conditioning Conference at Purdue*, 2016.

[66] J. Zhang, A. Desideri, M. Ryhl Kaern, and Fredrik H. Flow boiling heat transfer and pressure drop characteristics of r134a, r1234yf and r1234ze in a plate heat exchanger with conditions prevailing in the evaporator of organic rankine cycle units. *Submitted for publication*, 2016.

[67] Zahid H. Ayub. Plate Heat Exchanger Literature Survey and New Heat Transfer and Pressure Drop Correlations for Refrigerant Evaporators. *Heat Transfer Engineering*, 24 (5):3–16, 2003. ISSN 0145-7632. doi: 10.1080/01457630304056.

[68] B Thonon, R Vidil, and C Marvillet. Recent research and developments in Plate Heat Exchangers. *Journal of Enhanced heat transfer*, 2:149–155, 1995.

[69] RALPH L. WEBB and NEELKANTH S. GUPTE. A Critical Review of Correlations for Convective Vaporization in Tubes and Tube Banks. *Heat Transfer Engineering*, 13(3): 58–81, 1992. ISSN 0145-7632. doi: 10.1080/01457639208939782.

[70] J C Chen. Correlation for boiling heat transfer to saturated fluids in convective flow. *Industrial & Engineering Chemistry Process Design and development*, 5(3):322–329, 1966. ISSN 01964305. doi: 10.1021/i260019a023.

[71] S.S. Kutateladze. Boiling Heat Transfer. *Heat transfer conference*, pages 1–39, 1961.

[72] M Mohammed Shah. Chart correlation for saturated boiling heat transfer equations and further study. 1982.

[73] D.Chisholm. Lockhart-Martinelli Basis for the Correlation Flow for Two-Phase. *International Communications in Heat and Mass Transfer*, 10(18):1767–1778, 1967.

[74] E. W. Jassim, T. A. Newell, and J. C. Chato. Refrigerant pressure drop in chevron and bumpy style flat plate heat exchangers. *Experimental Thermal and Fluid Science*, 30(3): 213–222, 2006. ISSN 08941777. doi: 10.1016/j.expthermflusci.2005.05.008.

[75] K.E. Gungor and R.H.S. Winterton. A general correlation for flow boiling in tubes and annuli. *International Journal of Heat and Mass Transfer*, 29(3):351–358, mar 1986. ISSN 00179310. doi: 10.1016/0017-9310(86)90205-X.

[76] M.G. Cooper. Heat Flow Rates in Saturated Nucleate Pool Boiling-A Wide-Ranging Examination Using Reduced Properties. *Advances in Heat Transfer*, 16:157–239, 1984. ISSN 00652717. doi: 10.1016/S0065-2717(08)70205-3.

[77] D. Gorenflo. Pool boiling. *VDI Heat Atlas*, 1993.

[78] Dong Hyouck Han, Kyu Jung Lee, and Yoon Ho Kim. Experiments on the characteristics of evaporation of R410A in brazed plate heat exchangers with different geometric configurations. *Applied Thermal Engineering*, 23(10):1209–1225, 2003. ISSN 13594311. doi: 10.1016/S1359-4311(03)00061-9.

[79] Raffaele L. Amalfi, Farzad Vakili-Farahani, and John R. Thome. Flow boiling and frictional pressure gradients in plate heat exchangers: part 1, review and experimental database. *International Journal of Refrigeration*, jul 2015. ISSN 01407007. doi: 10.1016/j.ijrefrig.2015.07.010.

[80] Radia Eldeeb, Vikrant Aute, and Reinhard Radermacher. A Model for Performance Prediction of Brazed Plate Condensers with Conventional and Alternative Lower GWP Refrigerants. In *International refrigeration and air conditioning Conference*, pages 1–10, Purdue University, 2014. ISBN 3014058726.

[81] Raffaele L. Amalfi, Farzad Vakili-Farahani, and John R. Thome. Flow boiling and frictional pressure gradients in plate heat exchangers. Part 2: Comparison of literature methods to database and new prediction methods. *International Journal of Refrigeration*, 61:185–203, 2016. ISSN 01407007. doi: 10.1016/j.ijrefrig.2015.07.009. URL http://dx.doi.org/10.1016/j.ijrefrig.2015.07.009.

[82] Mohammad S. Khan, Tariq S. Khan, Ming-C. Chyu, and Zahid H. Ayub. Experimental investigation of evaporation heat transfer and pressure drop of ammonia in a 30° chevron plate heat exchanger. *International Journal of Refrigeration*, 35(6):1757–1765, sep 2012. ISSN 01407007. doi: 10.1016/j.ijrefrig.2012.05.019.

[83] F Vakili-Farahani, R L Amalfi, and J R Thome. Two-Phase Flow and boiling of R-245fa in a 1 mm pressing depth plate heat exchanger — Part I : Adiabatic pressure Drop. *Interfacial Phenomena and Heat Transfer*, 2(4):325–342, 2014.

[84] R. K. Shah. Assessment of modified wilson plot techniques for obtaining heat exchanger design data. In *The Ninth international heat transfer Conference*, 1990. ISBN 0891169091.

[85] CEPSA. http://www.cepsa.com/. Online; accessed 2016-04-13.

[86] Aie Sherbini, a Joardar, and Am Jacobi. Modified Wilson-Plot Technique for Heat Exchanger Performance: Strategies for Minimizing Uncertainty in Data Reduction. *International Refrigeration and Air Conditioning Conference*, pages 1–8, 2004. URL http://docs.lib.purdue.edu/cgi/viewcontent.cgi?article=1626{&}context=iracc.

[87] Eric Jones, Travis Oliphant, Pearu Peterson, et al. SciPy: Open source scientific tools for Python, 2001. URL http://www.scipy.org/. Online; accessed 2016-07-29.

[88] A. Maslov and M. Kovalenko. Hydraulic resistance and heat transfer in plate heat exchangers. *Molochnuya Promyshlennost*, (10):20–22, 1972.

[89] G. Rosenblad and A. Kullendroff. Estimating heat transfer from mass transfer studies on plate heat exchanger surfaces. *Warme-und Stoffubertragung*, 8(3):187–191, 1975.

[90] A. C. Talik, L. S. Fletcher, N. K. Anand, and L. W. Swanson. Heat transfer and pressure drop characteristics of a plate heat exchanger. In *Proceedings of the ASME/JSME Thermal Engineering Conference*, volume 4, pages 321–329, New York, 1995. ASME.

[91] A. C. Talik, L. S. Fletcher, N. K. Anand, and L. W. Swanson. Heat transfer and pressure drop characteristics of a plate heat exchanger using a propylene-glycol/water mixture as the working fluid. In *30th National Heat Transfer Con- ference*, volume 12, pages 83–88, New York, 1995. ASME.

[92] A.S. Wanniarachchi, U. Ratman, B.E. Tilton, and K. Dutta-Roy. Approximate correlations for chevron-type plate heat exchangers. In *National Heat Transfer Conference*, volume 12, pages 145–151. ASME, 1995.

[93] R. Bogaerts and A. Bolcs. Global performance of a prototype brazed plate heat exchanger in a large reynolds number range. *Experimental Heat transfer*, pages 293–311, 1995.

[94] Joachim Claesson. *Thermal and Hydraulic Performance of Compact Brazed Plate Heat Exchangers Operating as Evaporators in Domestic Heat Pumps*. Doctoral thesis, Royal Institute of Technology, KTH, 2004.

[95] S.J. Kline and F.A. McClintock. Describing uncertainties in single sample experiments.pdf. *Mechanical Engineering*, 1953.

[96] Dieter Steiner. Flow boiling heat transfer in vertical tubes correlated by an asymptotic model. *Heat transfer engineering*, 1982.

[97] D. Shiferaw, T.G. Karayiannis, and D.B.R. Kenning. Flow boiling in a 1.1 mm tube with R134a: Experimental results and comparison with model. *International Journal of Thermal Sciences*, 48(2):331–341, feb 2009. ISSN 12900729. doi: 10.1016/j.ijthermalsci.2008.02.009.

[98] Jacqueline B. Copetti, Mario H. Macagnan, Flávia Zinani, and Nicole L.F. Kunsler. Flow boiling heat transfer and pressure drop of R-134a in a mini tube: an experimental investigation. *Experimental Thermal and Fluid Science*, 35(4):636–644, may 2011. ISSN 08941777. doi: 10.1016/j.expthermflusci.2010.12.013.

[99] Y.-Y. Yan and T.-F. Lin. Evaporation Heat Transfer and Pressure Drop of Refrigerant R-134a in a Plate Heat Exchanger. *Journal of Heat Transfer*, 121(1):118, 1999. ISSN 00221481. doi: 10.1115/1.2825924.

[100] D.E. Briggs and E.H. Young. Modified wilson plot techniques for obtaining heat transfer corre- lations for shell and tube heat exchangers. *Chel. Eng. Progr. Symp. Ser.*, 65(92): 35–45, 1969.

[101] Hilding Elmqvist. *A Structured Model Language for Large Continous Systems*. PhD thesis, Lund Institute of Technology, 1978.

[102] P K M Pherson, G B Collins, C B Guppy, and A Sumner. Dynamics analysis of a nuclear boiler. In *Institution of Mechanical Engineers*, volume 180, pages 417–449, 1965.

[103] K. J. Åström and R. D. Bell. Drum-boiler dynamics. *Automatica*, 36(3):363–378, 2000. ISSN 00051098. doi: 10.1016/S0005-1098(99)00171-5.

[104] Girish Ghatikar, Salman Mashayekh, Michael Stadler, Rongxin Yin, and Zhenhua Liu. Distributed energy systems integration and demand optimization for autonomous operations and electric grid transactions. *Applied Energy*, pages 1–17, 2015. ISSN 03062619. doi: 10.1016/j.apenergy.2015.10.117.

[105] Wikipedia. Comparison of system dynamics software. URL https://en.wikipedia.org/wiki/Comparison_of_system_dynamics_software. Online; accessed 2016-07-29.

[106] J. Bonilla, L. J. Yebra, and S. Dormido. Chattering in dynamic mathematical two-phase flow models. *Applied Mathematical Modelling*, 36(5):2067–2081, 2012. ISSN 0307904X. doi: 10.1016/j.apm.2011.08.013.

[107] Volker Mehrmann and Lena Wunderlich. Hybrid systems of differential-algebraic equations – Analysis and numerical solution. *Journal of Process Control*, 19(8):1218–1228, sep 2009. ISSN 09591524. doi: 10.1016/j.jprocont.2009.05.002. URL http://www.sciencedirect.com/science/article/pii/S0959152409000985.

[108] Francois E. Cellier. *Continuous system modeling*. Springer-Verlag New York, 1991. ISBN 9788578110796. doi: 10.1017/CBO9781107415324.004.

[109] S.E. Mattsson and H. Elmqvist. Modelica - an international effort to design the next generation modeling language. In *7th IFAC Symposium on Computer Aided Control Systems Design, CACSD'97*, April 28-30, 1997.

[110] Modelon. Dymola, 2000. URL http://www.modelon.com/products/dymola/. Online; accessed 2016-07-29.

[111] Open Source Modelica Consortium (OSMC). Open modelica. URL https://openmodelica.org/. Online; accessed 2016-07-29.

[112] F. Casella and A. Leva. Object-oriented modelling & simulation of power plants with modelica. In *Proceedings of the 44th IEEE Conference on Decision and Control, and the European Control Conference*, 2005.

[113] H. Tummescheit, J. Ebron, and F.J. Wagner. Development of a Modelica base Library for Modeling of Thermo-Hydraulic Systems. In *Proceedings of the Modelica Workshop*, 2000.

[114] Baligh El Hefni. Dynamic modeling of concentrated solar power plants with the ThermoSysPro library (Parabolic Trough collectors, Fresnel reflector and Solar-Hybrid). *Energy Procedia*, 49:1127–1137, 2013. ISSN 18766102. doi: 10.1016/j.egypro.2014.03.122. URL http://dx.doi.org/10.1016/j.egypro.2014.03.122.

[115] Modelon. Thermal power library. URL http://www.modelon.com/products/modelica-libraries/thermal-power-library/. Online; accessed 2016-07-29.

[116] TLK-ThermoGmbH. URL http://www.tlk-thermo.com/index.php/en/software-products/til-suite. Online; accessed 2016-07-29.

[117] Michael Wetter. Modelica Library for Building Heating , Ventilation and Air-Conditioning Systems. pages 20–22, 2009. doi: 10.3384/ecp09430042.

[118] Francesco Casella, Tiemo Mathijssen, Piero Colonna, and Jos van Buijtenen. Dynamic modeling of organic rankine cycle power systems. *Journal of Engineering for Gas Turbines and Power*, 135(4):042310, March 2013.

[119] Francesco Casella and Christoph Richter. External media: A library for easy re-use of external fluid property code in madelica. In *In proceeding of the 6th International Modelica Conference*, 2008.

[120] S. Quoilin, A. Desideri, J. Wronski, I. H. Bell, and V. Lemort. ThermoCycle: A Modelica library for the simulation of thermodynamic systems. In *Proceedings of the 10th International Modelica Conference*, 2014.

[121] Bernard P. Zeigler. Towards a Formal Theory of Modeling and Simulation: Structure Preserving Morphisms. *Journal of the Assocation for Computing Machinery*, 19(4): 742–764, 1972. ISSN 00045411. doi: 10.1145/321724.321737.

[122] B.P. Zeigler, P. Herbert, and T. G. Kim. *Theory of Modeling and Simulation*. Academic Press, 2nd edition edition, 2000.

[123] Marvin Lee Minsky. Matter, Minds and Models. In *Proceedings of IFIP Congress*, pages 45–49, 1965. doi: http://hdl.handle.net/1721.1/6119.

[124] S. Bendapudi, J. Braun, E. Groll, and A. Eckhard. Dynamic model of a centrifugal chiller system–model development, numerical study and validation. *ASHRAE*, 2005.

[125] S. Quoilin. *Sustainable Energy Conversion Through the Use of Organic Rankine Cycles for Waste Heat Recovery and Solar Applications*. PhD thesis, University of Liege, October 2011.

[126] Jakob Munch Jensen. *Dynamic Modeling of Thermo-Fluid Systems*. PhD thesis, Technical University of Denmark, 2003.

[127] F. W. Dittus and L. M K Boelter. Heat transfer in automobile radiators of the tubular type. *International Communications in Heat and Mass Transfer*, 12(1):3–22, 1985. ISSN 07351933. doi: 10.1016/0735-1933(85)90003-X.

[128] Volker Gnielinski. Heat Transfer in Pipe Flow. *VDI Heat Atlas*, pages 691–700, 2010. doi: 10.1007/978-3-540-77877-6_34. URL http://dx.doi.org/10.1007/978-3-540-77877-6{_}34.

[129] Hans B. Pacejka. *Tyre and Vehicle Dynamics*. SAE International, second edition edition, 2005.

[130] E. Casati, a. Galli, and P. Colonna. Thermal energy storage for solar-powered organic Rankine cycle engines. *Solar Energy*, 96:205–219, 2013. ISSN 0038092X. doi: 10.1016/j.solener.2013.07.013.

[131] R Forristall. Heat Transfer Analysis and Modeling of a Parabolic Trough Solar Receiver Implemented in Engineering Equation Solver. Technical Report October, National Renewable Energy Laboratory, 2003.

[132] Michael Sielemann, Francesco Casella, Martin Otter, Christoph Clauß, Jonas Eborn, Sven Erik Mattsson, and Hans Olsson. Robust initialization of differential-algebraic equations using homotopy. In *Proceedings of the 8th Modelica Conference*, pages 21–22, Dresden, 2011.

[133] Christian Schulze, Manuel Graber, and Wilhelm Tegethoff. A limiter for preventing singularity in simplified finite volume methods. In *Mathematical Modelling*, 2012.

[134] Sylvain Quoilin, Ian Bell, Adriano Desideri, and Vincent Lemort. Methods to increase the robustness of finite-volume flow models in thermodynamic systems. *Energies*, 2014.

[135] F. Casella. Object-oriented modelling of two-phase fluid flows by the finite volume method. *Proceedings 5th Mathmod Vienna, Austria, Sep*, 2006.

[136] J. Bonilla, L. J. Yebra, and S. Dormido. Mean densities in dynamic mathematical two-phase flow models. *Computer Modeling in Engineering and Sciences (CMES)*, 67(1):13, 2010.

[137] S. Bendapudi. A literature review of dynamic models of vapor compression equipment. Technical report, Herrick Laboratories, Purdue University, 2002.

[138] G. L. Wedekind, B. L. Bhatt, and B. T. Beck. A system mean void fraction model for predicting various transient phenomena associated with two-phase evaporating and condensing flows. *International Journal of Multiphase Flow*, 4(1):97–114, 1978. ISSN 03019322. doi: 10.1016/0301-9322(78)90029-0.

[139] M. Dhar and W. Soedel. Transient analysis of a vapor compression refrigeration system. In *In proceedings of the XV International Congress of Refrigeration*, Venice, 1979.

[140] J.W. MacArtur and E.W. Grald. Prediction of cyclic heat pump performance with a fully distributed model and a comparison with experimental data. *ASHRAE Transactions*, 93(2):1159–1178, 1987.

[141] S Mattsson. On modelling of heat exchangers in modelica. *ESS97-European Simulation Symposium*, pages 1–7, 1997. URL http://citeseerx.ist.psu.edu/viewdoc/download?doi=10.1.1.16.5210{&}rep=rep1{&}type=pdf.

[142] Satyam Bendapudi, James E. Braun, and Eckhard a. Groll. A comparison of moving-boundary and finite-volume formulations for transients in centrifugal chillers. *International Journal of Refrigeration*, 31(8):1437–1452, 2008. ISSN 01407007. doi: 10.1016/j.ijrefrig.2008.03.006. URL http://dx.doi.org/10.1016/j.ijrefrig.2008.03.006.

[143] S. Bendapudi. Development and validation of a mechanistic dynamic model for a vapor compression centrifugal liquid chiller. Technical report, Herrick Laboratories, Purdue University, 2002.

[144] Javier Bonilla, Sebastian Dormido, and Francois E. Cellier. Switching moving boundary models for two-phase flow evaporators and condensers. *Communications in Nonlinear Science and Numerical Simulation*, 20(3):743–768, 2015. ISSN 1007-5704.

[145] Sylvain Quoilin, Richard Aumann, Andreas Grill, Andreas Schuster, Vincent Lemort, and Hartmut Spliethoff. Dynamic modeling and optimal control strategy of waste heat recovery organic Rankine cycles. *Applied Energy*, 88(6):2183 – 2190, 2011. ISSN 0306-2619. doi: http://dx.doi.org/10.1016/j.apenergy.2011.01.015.

[146] J. Peralez, T. Paolino, A. Sciarretta, P. Dufour, and M. Nadri. Towards model-based control of a steam Rankine process for engine waste heat recovery. In *IEEE Vehicle Power and Propulsion Conference (VPPC), Republic Of Korea*, 2012.

[147] Hongtao Qiao, Vikrant Aute, and Reinhard Radermacher. Transient modeling of a flash tank vapor injection heat pump system – part i: Model development. *International Journal of Refrigeration*, 49(0):169 – 182, 2015. ISSN 0140-7007. doi: http://dx.doi.org/10.1016/j.ijrefrig.2014.06.019.

[148] Emiliano Casati, Adriano Desideri, Francesco Casella, and Piero Colonna. Preliminary Assessment of a Novel Small CSP Plant Based on Linear Collectors , ORC and Direct Thermal Storage. *SolarPaces Conference*, 2012.

[149] E Prabhu. Solar Trough Organic Rankine Electricity System (STORES) Stage 1 : Power Plant Optimization and Economics. Technical Report March, 2006.

[150] Alain Verneau. L'emploi des fluides organiques dans les turbines solaires. *Entropie*, pages 9 – 18, 1978.

[151] A. Ray. Nonlinear dynamic model of a solar steam generator. *Solar Energy*, 26(4):297 – 306, 1981.

[152] Hirsch T., Eck M., and Steinmann W.D. Simulation of transient two-phase flow in parabolic trough collectors using Modelica. In *Proceedings of the 4th International Modelica Conference*, March 2005.

[153] Dow Oil and Gas. Syltherm 800 Heat Transfer Fluid. Technical report, DOW, 1997.

[154] Kipp and Zonen. *CH1 NIO (normal incidence pyrhelimeter) manual*, 1997. URL http://www.kippzonen.com.

[155] Fabienne Sallaberry, Loreto Valenzuela, Alberto García de Jalón, Javier Leon, and Ignacio David Bernad. Towards standardization of in-site parabolic trough collector testing in solar thermal power plants. *AIP Conference Proceedings*, 1734:130019–1–130019–8,

2016. doi: 10.1063/1.4949229. URL http://scitation.aip.org/content/aip/proceeding/aipcp/10.1063/1.4949229.

[156] Loreto Valenzuela, Rafael López-Martín, and Eduardo Zarza. Optical and thermal performance of large-size parabolic-trough solar collectors from outdoor experiments: A test method and a case study. *Energy*, 70:456–464, 2014. ISSN 03605442. doi: 10.1016/j.energy.2014.04.016.

[157] Linda R Petzold. A description of DASSL: a differential-algebraic system solver. *Scientific computing*, 94550:65–68, 1983.

[158] Dynasim AB. Dymola User's Manual. Technical report, 2014.

[159] Yi-Yie Yan, Hsiang-Chao Lio, and Tsing-Fa Lin. Condensation heat transfer and pressure drop of refrigerant R-134a in a plate heat exchanger. *International Journal of Heat and Mass Transfer*, 42(6):993–1006, 1999. ISSN 00179310. doi: 10.1016/S0017-9310(98)00217-8.

[160] P.J. Huber. *Robust Statistics*. John Viley and Sons, 1992.

[161] Jörg Ungethüm and Dirk Hülsebusch. Implementation of a Modelica Library for Smooth Spline Approximation. *Interfaces*, pages 669–675, 2009. doi: 10.3384/ecp09430013.

[162] Andres Hernandez, Adriano Desideri, Clara Ionescu, Robin De Keyser, Vincent Lemort, and Sylvain Quoilin. Real-time optimization of organic Rankine cycle systems by Extremum-Seeking control. *energies*, 2016. doi: 10.3390/en9050334.

[163] Jim Hinkley, Bryan Curtin, Jenny Hayward, Alex Wonhas, Rod Boyd, Charles Grima, Amir Tadros, Ross Hall, Kevin Naicker, and Adeeb Mikhail. Concentrating solar power - drivers and opportunities for cost-competitive electricity. (March):1–32, 2011. URL www.csiro.au.

[164] Resnick Institute. Grid 2020 Towards a Policy of Renewable and Distributed Energy Resources. Technical Report September, Resnick Institute, 2012.

[165] Margarita Mediavilla, Carlos de Castro, Iñigo Capellán, Luis Javier Miguel, Iñaki Arto, and Fernando Frechoso. The transition towards renewable energies: Physical limits and temporal conditions. *Energy Policy*, 52:297–311, jan 2013. ISSN 03014215. doi: 10.1016/j.enpol.2012.09.033. URL http://www.sciencedirect.com/science/article/pii/S0301421512008087.

[166] IEA. Technology Roadmap Solar Thermal Electricity - 2014 edition. Technical report, INternational Energy Agency, 2014.

[167] Robert Pitz-Paal, Jurgen Dersch, Barbara Milow, Felix Tellez, Alain Ferriere, Ulrich Langnickel, Aldo Steinfeld, Jacob Karni, Eduardo Zarza, and Oleg Popel. Development Steps for Parabolic Trough Solar Power Technologies With Maximum Impact on Cost

Reduction. *Journal of Solar Energy Engineering*, 129(4):371, 2007. ISSN 01996231. doi: 10.1115/1.2769697.

[168] Juergen H. Peterseim, Stuart White, Amir Tadros, and Udo Hellwig. Concentrated solar power hybrid plants, which technologies are best suited for hybridisation? *Renewable Energy*, 57:520–532, 2013. ISSN 09601481. doi: 10.1016/j.renene.2013.02.014. URL http://dx.doi.org/10.1016/j.renene.2013.02.014.

[169] Juergen H. Peterseim, Udo Hellwig, Amir Tadros, and Stuart White. Hybridisation optimization of concentrating solar thermal and biomass power generation facilities. *Solar Energy*, 99:203–214, 2014. ISSN 0038092X. doi: 10.1016/j.solener.2013.10.041. URL http://dx.doi.org/10.1016/j.solener.2013.10.041.

[170] Rafael Soria, Joana Portugal-Pereira, Alexandre Szklo, Rodrigo Milani, and Roberto Schaeffer. Hybrid concentrated solar power (CSP)-biomass plants in a semiarid region: A strategy for CSP deployment in Brazil. *Energy Policy*, 86:57–72, nov 2015. ISSN 03014215. doi: 10.1016/j.enpol.2015.06.028. URL http://www.sciencedirect.com/science/article/pii/S0301421515002463.

[171] A Cot, A Amettler, J Vall-Llovera, J Aguilo, and J M Arque. Termosolar Borges: A Thermosolar Hybrid Plant with Biomass. In *Third International Symposium on Energy from Biomass and Waste*, number November, 2010.

[172] Abantia Csp. TERMOSOLAR BORGES THE FIRST COMMERCIAL CSP HYBRIDIZED WITH BIOMASS IN THE WORLD, 2012.

[173] Juergen H. Peterseim, Amir Tadros, Udo Hellwig, and Stuart White. Increasing the efficiency of parabolic trough plants using thermal oil through external superheating with biomass. *Energy Conversion and Management*, 77:784–793, 2014. ISSN 01968904. doi: 10.1016/j.enconman.2013.10.022. URL http://dx.doi.org/10.1016/j.enconman.2013.10.022.

[174] R. Sterrer, S. Schidler, O. Schwandt, P. Franz, and A. Hammerschmid. Theoretical Analysis of the Combination of CSP with a Biomass CHP-plant Using ORC-technology in Central Europe. *Energy Procedia*, 49:1218–1227, 2014. ISSN 18766102. doi: 10.1016/j.egypro.2014.03.131. URL http://www.sciencedirect.com/science/article/pii/S1876610214005852.

[175] Melissa Ireland, Matthew Orsoz, Adriano Desideri, Sylvain Quoilin, and J. G. DesuBrisson. Dynamic modeling and control system definition for a micro-CSP plant coupled with thermal storage unit. In *Proceedings of ASME Turbo Expo 2014: Turbine Technical Conference and Exposition*, 2014.

[176] Rémi Dickes, Adriano Desideri, Vincent Lemort, and Sylvain Quoilin. Model reduction for simulating the dynamic behavior of parabolic troughs and a thermocline energy storage in a micro-solar power unit. In *THE 28TH INTERNATIONAL CONFERENCE ON*

EFFICIENCY, COST, OPTIMIZATION, SIMULATION AND ENVIRONMENTAL IMPACT OF ENERGY SYSTEMS, 2015.

[177] F. Alberti, L Crema, and A Bozzoli. Heat Transfer Analysis for a Small-Size Direct-Flow Coaxial Concentrating Collector. *Solar Energy Engineering*, 2012. doi: 10.1115/1.4007297.

[178] J. M. Cabello, J. M. Cejudo, M. Luque, F. Ruiz, K. Deb, and R. Tewari. Optimization of the size of a solar thermal electricity plant by means of genetic algorithms. *Renewable Energy*, 36(11):3146–3153, 2011. ISSN 09601481. doi: 10.1016/j.renene.2011.03.018. URL http://dx.doi.org/10.1016/j.renene.2011.03.018.

[179] By Kai Wang and Edward a Vineyard. Adsorption Refrigeration. *Ashrae*, (September), 2011.

[180] Francesco Casella, Michael Sielemann, and Luca Savoldelli. Steady-state initialization of object-oriented thermo-fluid models by homotopy methods. *8th Modelica Conference*, pages 86–96, 2011.

[181] NSW. Cogeneration feasibility guide. Technical report, Office of Environment and Heritage NSW, 2013. URL http://www.environment.nsw.gov.au/.

[182] Agencia Estatal Boletin Oficial del Estado. URL https://www.boe.es/diario_boe/txt.php?id=BOE-A-2014-6495. Online; accessed 2016-07-29.

[183] ICF Consulting Canada. Life Cycle Greenhouse Gas Emissions of Natural Gas A LITERATURE REVIEW OF KEY STUDIES COMPARING EMISSIONS. Technical report, ICF International, 2012. URL http://www.capp.ca/getdoc.aspx?DocId=215278.

A ThermoCycle Modelica models

A.1 Heat exchanger Moving boundary model

A.1.1 Mean void fraction

In this section the process to derive the mean void fraction is reported. The regularly used quantities at the phase boundaries at constant pressure are denoted with $'$ for the liquid phase and $''$ for the vapour phase. The area average void fraction , which is the most adopted definition of the void fraction γ [126], and the static quality are defined as shown in Equations A.1 and A.2.

$$\gamma = \frac{A^{''}}{A} \tag{A.1}$$

$$x = \frac{M^{''}}{M} \tag{A.2}$$

where $M^{''}$ is the mass of vapour in the two phase volume, M is the total mass flow of the fluid, $A^{''}$ and A are the pipe cross section occupied by the vapour and the total cross section respectively. From Equations A.1-A.2, it follows that:

$$x = \frac{\gamma V \rho^{''}}{V(\gamma\rho^{''} + (1-\gamma)\rho^{'})} = \frac{\gamma\rho^{''}}{(\gamma\rho^{''} + (1-\gamma)\rho^{'})} \tag{A.3}$$

Rearranging Equation A.3, the void fraction can be expressed as:

$$\gamma(p,h) = \frac{x\rho^{'}}{x\rho^{'} + (1-x)\,\rho^{''}} \tag{A.4}$$

Defining the enthalpy at the boundary of the two-phase control volume as h_a and h_b, the average void fraction, $\overline{\gamma}$, can be computed integrating Eq. A.4 over the enthalpy range $\Delta h = h_b - h_a$ as a function of pressure and the two boundary enthalpies:

$$\overline{\gamma}(p,h_a,h_b) = \int_{h_a}^{h_b} \gamma(p,h)\,dh = \frac{\rho^{'2}(h_a - h_b) + \rho^{'}\rho^{''}\left(h_b - h_a + (h^{'} - h^{''})\left(\frac{\Gamma(h_a)}{\Gamma(h_b)}\right)\right)}{(h_a - h_b)\left(\rho^{'} - \rho^{''}\right)^2} \tag{A.5}$$

$$\text{with } \Gamma(h) = \rho^{'}(h - h^{'}) + \rho^{''}(h^{''} - h) \tag{A.6}$$

A.1.2 Average void fraction partial derivatives

In this section the formulation of the average void fraction partial derivatives adopted in the two-phase cell of the moving boundary model are reported. The average void fraction time derivative is expressed as:

$$\frac{d\overline{\gamma}}{dt} = + \frac{\partial \overline{\gamma}}{\partial p}\frac{dp}{dt} + \frac{\partial \overline{\gamma}}{\partial h_a}\frac{dh_a}{dt} + \frac{\partial \overline{\gamma}}{\partial h_b}\frac{dh_b}{dt} \tag{A.7}$$

The partial derivative with respect to pressure is reported in equation A.8.

$$\begin{aligned}
\frac{\partial \overline{\gamma}}{\partial p} = &+ \frac{\frac{d\rho'}{dp}}{\Delta h_{ab}\Delta\rho_{tp}^2}\left\{\Delta h_{ab}\rho' + \rho''\Delta h_{ab,tp}\right\} \\
&- \frac{2\rho'\left(\frac{d\rho'}{dp} - \frac{d\rho''}{dp}\right)}{\Delta h_{ab}\Delta\rho_{tp}^3}\left\{\Delta h_{ab}\rho' + \rho''\Delta h_{ab,tp}\right\} \\
&+ \frac{\rho'}{\Delta h_{ab}\Delta\rho_{tp}^2}\left\{\Delta h_{ab}\frac{d\rho'}{dp} + \frac{d\rho''}{dp}\Delta h_{ab,tp}\right. \\
&\left. + \rho''\left[\left(\frac{dh'}{dp} - \frac{dh''}{dp}\right)\ln(G) + \frac{\Delta h_{tp}}{\Gamma(h_a)}\left(\Theta(h_a) - G\Theta(h_b)\right)\right]\right\}
\end{aligned} \tag{A.8}$$

The partial derivative with respect to h_a and h_b are reported in equation A.9 and A.10 respectively

$$\begin{aligned}
\frac{\partial \overline{\gamma}}{\partial h_a} = &- \frac{\rho'}{\Delta h_{ab}^2\Delta\rho_{tp}^2}\left\{\Delta h_{ab}\rho' + \rho''\Delta h_{ab,tp}\right\} \\
&+ \frac{\rho'}{\Delta h_{ab}\Delta\rho_{tp}^2}\left\{+\rho' + \rho''\left(-1 + \frac{\Delta h_{tp}\Delta\rho_{tp}}{\Gamma(h_a)}\right)\right\}
\end{aligned} \tag{A.9}$$

$$\begin{aligned}
\frac{\partial \overline{\gamma}}{\partial h_b} = &+ \frac{\rho'}{\Delta h_{ab}^2\Delta\rho_{tp}^2}\left\{\Delta h_{ab}\rho' + \rho''\Delta h_{ab,tp}\right\} \\
&+ \frac{\rho'}{\Delta h_{ab}\Delta\rho_{tp}^2}\left\{-\rho' + \rho''\left(+1 - \frac{\Delta h_{tp}\Delta\rho_{tp}}{\Gamma(h_b)}\right)\right\}
\end{aligned} \tag{A.10}$$

$$\text{with } \Delta h_{tp} = h' - h'', \quad \Delta\rho_{tp} = \rho' - \rho'', \quad \Delta h_{ab} = h_a - h_b,$$

$$\Theta(h) = \left(h - h'\right)\frac{d\rho'}{dp} - \rho'\frac{dh'}{dp} + \left(h'' - h\right)\frac{d\rho''}{dp} + \rho''\frac{dh''}{dp},$$

$$\Delta h_{ab,tp} = -\Delta h_{ab} + \Delta h_{tp}\ln(G), \text{ and } G = \Gamma(h_a)/\Gamma(h_b), \tag{A.11}$$

(A.12)

with $\Gamma(h)$ as defined in equation A.6.

A.2 Solar collector Forristal model

The equations defining the *SolAbsForristal* introduced in section 4.8 are reported. The model solves the one-dimensional radial energy balance between the heat collector element (HCE) and the atmosphere. The terms in the energy balance depends on the collector type, the HCE condition, the optical properties and the ambient conditions. The modelled physical phenomena are:

- Convection in the heat transfer fluid.
- Conduction and thermal energy accumulation in the metal pipe.
- Convection and radiation transfer in the vacuum between the glass envelope and the metal pipe.
- Conduction and thermal energy accumulation in the glass envelope.
- Radiation and convection to the environment.

The assumptions are:

- Temperatures, thermal energy flux and thermodynamic properties are considered uniform around the circumference of the HCE.
- Solar absorption is treated as a linear phenomenon.

The energy conservation equations for the metal wall and the glass envelope are defined as:

$$\rho_{\mathrm{g}} \cdot C_{\mathrm{p,g}} \cdot \frac{dT_{\mathrm{g}}}{dt} = \dot{q}_{\mathrm{int,g}} \cdot \mathrm{D}_{\mathrm{int,g}} \cdot \pi + \dot{q}_{\mathrm{ext,g}} \cdot \mathrm{D}_{\mathrm{ext,g}} \cdot \pi \tag{A.13}$$

$$\rho_{\mathrm{t}} \cdot C_{\mathrm{p,t}} \cdot \frac{dT_{\mathrm{t}}}{dt} = \dot{q}_{\mathrm{int,t}} \cdot \mathrm{D}_{\mathrm{int,t}} \cdot \pi + \dot{q}_{\mathrm{ext,t}} \cdot \mathrm{D}_{\mathrm{ext,t}} \cdot \pi \tag{A.14}$$

The equations defining the thermal energy transfer from the sun energy concentrated on the heat collector element to the the heat transfer fluid are listed below. Thermal energy transfer from the sun to the metal wall:

$$\dot{q}_{\mathrm{tot,t}} = \frac{DNI \cdot \eta_{\mathrm{opt,t}} \cdot A_{\mathrm{ref}}}{A_{\mathrm{ext,t}}} \tag{A.15}$$

Thermal energy transfer from the sun to the glass envelope:

$$\dot{q}_{\mathrm{tot,g}} = \frac{DNI \cdot \eta_{\mathrm{opt,g}} \cdot A_{\mathrm{ref}}}{A_{\mathrm{ext,g}}} \tag{A.16}$$

Radiation to the ambient air:

$$\dot{q}_{\mathrm{rad,air}} = \epsilon_{\mathrm{g}} \cdot \sigma \cdot (T_{\mathrm{ext,g}}^4 - T_{\mathrm{sky}}^4) \tag{A.17}$$

Convection to the ambient air:

$$\phi_{\text{conv,air}} = U_{\text{air}} \cdot (T_{\text{ext,g}} - T_{\text{amb}}) \tag{A.18}$$

Conduction through the external half-thickness of the glass envelope:

$$\dot{q}_{\text{ext,g}} = \frac{\lambda_{\text{g}}}{r_{\text{ext,g}} \cdot \log((2 \cdot r_{\text{ext,g}})/(r_{\text{int,g}} + r_{\text{ext,g}}))} \cdot (T_{\text{ext,g}} - T_{\text{g}}) \tag{A.19}$$

Conduction through the internal half-thickness of the glass envelope:

$$\dot{q}_{\text{int,g}} = \frac{\lambda_{\text{g}}}{r_{\text{int,g}} \cdot \log((2 \cdot r_{\text{int,g}})/(r_{\text{int,g}} + r_{\text{ext,g}}))} \cdot (T_{\text{int,g}} - T_{\text{g}}) \tag{A.20}$$

Radiation transfer in the vacuum:

$$\dot{q}_{\text{rad,gas}} = \sigma \cdot \frac{(T_{\text{ext,t}}^4 - T_{\text{int,g}}^4)}{1/\epsilon_{\text{t}} + D_{\text{ext,t}}/D_{\text{ext,g}} \cdot (1/\epsilon_{\text{g}} - 1)} \tag{A.21}$$

Convection transfer in the vacuum:

$$\dot{q}_{\text{conv,gas}} = U_{\text{gas}} \cdot (T_{\text{ext,t}} - T_{\text{int,g}}) \tag{A.22}$$

Conduction through the external half-thickness of the absorber metal wall:

$$\dot{q}_{\text{ext,t}} = \frac{\lambda_{\text{t}}}{r_{\text{ext,t}} \cdot \log((2 \cdot r_{\text{ext,t}})/(r_{\text{int,t}} + r_{\text{ext,t}}))} \cdot (T_{\text{ext,t}} - T_{\text{t}}) \tag{A.23}$$

Conduction through the internal half-thickness of the absorber metal wall:

$$\dot{q}_{\text{int,t}} = \frac{\lambda_{\text{t}}}{r_{\text{int,t}} \cdot \log((2 \cdot r_{\text{int,t}})/(r_{\text{int,t}} + r_{\text{ext,t}}))} \cdot (T_{\text{int,t}} - T_{\text{t}}) \tag{A.24}$$

Convection transfer in the fluid:

$$\dot{q}_{\text{conv,fluid}} = U_{\text{fluid}} \cdot (T_{\text{int,t}} - T_{\text{fluid}}) \tag{A.25}$$

The constitutive equations are reported from equation A.26 to equation A.39. The glass optical efficiency corresponds to:

$$\eta_{\text{opt,g}} = \eta_{\text{opt}} \cdot \alpha_{\text{g}} \tag{A.26}$$

The tube optical efficiency corresponds to:

$$\eta_{\text{opt,t}} = \eta_{\text{opt}} \cdot \alpha_{\text{t}} \cdot \tau_{\text{g}} \tag{A.27}$$

where η_{opt} is defined as:

$$\eta_{opt} = \epsilon_1 \cdot \epsilon_2 \cdot \epsilon_3 \cdot \epsilon_4 \cdot \epsilon_5 \cdot \epsilon_6 \cdot \rho_{cl} \cdot IAM \tag{A.28}$$

The temperature of the sky is calculated as:

$$T_{sky} = T_{amb} - 8 \tag{A.29}$$

The area of the reflectors is defined as:

$$A_{ref} = L \cdot A_P \tag{A.30}$$

The lateral area of the tube and of the glass envelope is calculated with eq. A.31 and A.32 respectively:

$$A_{ext,t} = \pi \cdot D_{ext,t} \cdot L \tag{A.31}$$

$$A_{ext,g} = \pi \cdot D_{ext,g} \cdot L \tag{A.32}$$

The heat transfer coefficient of ambient air is calculated as:

$$U_{air} = \frac{Nu \cdot k_{air}}{D_{ext,g}} \tag{A.33}$$

with Nu:

$$Nu_{air} = C_{air} \cdot Re_{air}^{n_{air}} \cdot Pr_{air}^{m_{air}} \tag{A.34}$$

where C_{air} , m_{air} and n_{air} assume different values depending on the Reynolds and Prandtl number [131]. The Reynolds number is calculated as

$$Re_{air} = V_{wind} \cdot \rho_{air} \cdot D_{ext,g} / \mu_{air} \tag{A.35}$$

The heat transfer coefficient in the vacuum is calculated as:

$$U_{gas} = \frac{k_{gas}}{\mathrm{D}_{ext,t}/2 \cdot \log(r_{int,g}/r_{ext,t} + B \cdot \lambda_{gas} \cdot (r_{ext,t}/r_{int,g}) + 1)} \tag{A.36}$$

where λ_{gas} is defined as

$$\lambda_{gas} = \frac{2.33E^{-20} \cdot T_{g,t}}{p_{gas} \cdot \delta_{gas}} \tag{A.37}$$

with $T_{g,t}$:

$$T_{g,t} = \frac{T_{int,g} + T_{ext,t}}{2} \tag{A.38}$$

The tube emissivity is calculated with the following equations assuming the PTR70 heat collector element is used:

$$\epsilon_t = 0.062 + 2E^{-7} \cdot (T_{\text{ext,t}} - 273.15)^2 \tag{A.39}$$

The following constraining equations are required to solve the system of equations:

$$\dot{q}_{\text{ext,g}} = \dot{q}_{\text{tot,g}} - \dot{q}_{\text{rad,air}} - \dot{q}_{\text{conv,air}} \tag{A.40}$$

$$\dot{q}_{\text{int,g}} = \dot{q}_{\text{conv,gas}} + \dot{q}_{\text{rad,gas}} \tag{A.41}$$

$$\dot{q}_{\text{ext,t}} = \dot{q}_{\text{tot,t}} - \dot{q}_{\text{rad,air}} - \dot{q}_{\text{conv,air}} \tag{A.42}$$

$$\dot{q}_{\text{int,t}} = -\dot{q}_{\text{conv,fluid}} \tag{A.43}$$

The parameters of the model with the relative definition and unit are reported in Table A.1.

Parameter	Description
Optical	
ϵ_1	Shadowing error
ϵ_2	Tracking error
ϵ_3	Geometry error
ρ_{cl}	Mirror reflectivity
ϵ_4	Dirt on mirror
ϵ_5	Dirt on HCE
ϵ_6	Unaccounted losses
τ_{g}	Glass transmissivity
α_{g}	Glass absorptivitiy
ϵ_{g}	Glass emissivity
α_{t}	tube absorptivity
Geometrical	
L	receiver length [m]
$\mathrm{A_P}$	parabola aperture [m]
$\mathrm{D_{ext,g}}$	Envelope outer diameter [m]
$\mathrm{th_g}$	Envelope thickness [m]
$\mathrm{D_{ext,t}}$	Absorber tube outer diameter [m]
$\mathrm{th_t}$	Absorber tube thickness [m]
Glass, Metalwall, Annulus, Atm.	
ρ_{g}	glass density [kg/m^3]
$C_{\mathrm{p,g}}$	glass heat capacity [J/kgK]
λ_{g}	glass thermal conductivity [W/mk]
ρ_{t}	metal density[kg/m^3]
$C_{\mathrm{p,t}}$	metal heat capacity [J/kgK]
λ_{t}	metal thermal conductivity[W/mk]
p_{gas}	pressure in the vacuum [bar]
γ_{gas}	ratio of specific heat for the vacuum gas [-]
δ_{gas}	Molecular diameter for annulus gas [cm]
B	Molecular interaction coefficient [-]
k_{gas}	Thermal conductivity in the annulus gas [W/mk]
$\mathrm{p_{atm}}$	Atmospheric pressure [bar]
$\mathrm{k_{air}}$	Ambient air thermal conductivity [W/mk]
ρ_{air}	Ambient air density [kg/m^3]
μ_{air}	Ambient air dynamic viscosity [Pa.s]
Pr	Prandtl number [-]

Table A.1 – Parameters of the *SolAbs* model

The inputs to the model are reported in table A.2.
The main outputs computed by the model are reported in table A.3.

Inputs	Description
DNI	direct normal incidence [W/m^2]
v_{wind}	Wind velocity [m/s]
T_{amb}	Ambient temperature [° C]
Θ_{incid}	Incident angle [°]
T_{fluid}	HTF inlet temperature from the $Flow1Dim$ model [° C]
U_{fluid}	HTF heat transfer coefficient from the $Flow1Dim$ model [W/m^{2}K]

Table A.2 – Inputs to the $SolAbs$ model

In the initialization phase both the Steady state and the Start value initialization can be

Inputs	Description
$T_{ext,g}$	External temperature of the glass envelope [° C]
T_g	Temperature at the half-thickness of the glass envelope [° C]
$T_{int,g}$	Internal temperature of the glass envelope [° C]
$T_{ext,t}$	External temperature of the absorber metal wall [° C]
T_t	Temperature at the half-thickness of the absorber metal wall [° C]
$T_{int,t}$	Internal temperature of the absorber metal wall [° C]
$\dot{q}_{conv,fl}$	Thermal energy transfer to the HTF [° C]
$\dot{q}_{rad,air}$	Thermal energy transfer by radiation to ambient air [W/m^2]
$\dot{q}_{conv,air}$	Thermal energy transfer by convection to ambient air [W/m^2]
$\dot{q}_{rad,gas}$	Thermal energy transfer by radiation in the annulus [W/m^2]
$\dot{q}_{conv,gas}$	Thermal energy transfer by convection in the annulus [W/m^2]

Table A.3 – Inputs to the $SolAbs$ model

adopted. In case the Start value initialization is selected a defined value is assigned to the glass and tube temperature, assuming a linear distribution along the absorber. In detail the inlet and outlet temperature of the glass envelope ($T_{start,g,in}$, $T_{start,g,out}$) and of the absorber metal wall ($T_{start,t,in}$, $T_{start,t,out}$) are imposed and the built-in linspace function from the Modelica Standard library is used to linearly distribute the values among the cells. Note that Inputs and Outputs have been defined only to present the model in a clear scheme to the readers. In fact the a-casual approach of the Modelica programming language does not require that Inputs and Outputs of the model are explicitly defined in the code.

A.3 ORC unit simplified model

The *ORCunit* model allows to simulate an ORC power block assuming perfect control of the unit, while still accounting for mass and energy accumulation in the evaporator and condenser secondary side. The model is not suitable to analyse in detail the dynamic of the ORC power block, but it can be very useful when the integration of the ORC unit in a more complex thermo-hydraulic system needs to be assessed. The model as shown from the graphical user interface of Dymola is reported in figure A.1. It is composed by two *Flow1Dim* models to simulate

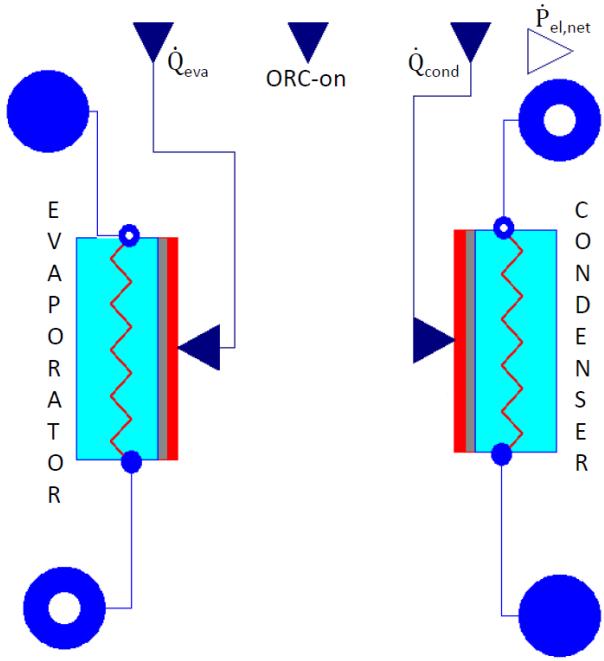

Figure A.1 – Schematic layout of the *ORCunit* model from the Dymola graphical user interface.

the evaporator and condenser secondary side. The thermal power absorbed and rejected by the ORC working fluid is imposed to the *Flow1Dim* models as an exogenous inputs. A real input *ORC-on* triggers the start-up and shut-down of the unit. The electrical power output is computed based on the temperature of the secondary fluids at the inlet of the evaporator and condenser as:

$$P_{\text{el,net}} = a_1 + a_2 \cdot T_{\text{eva,su}} + a_3 \cdot T_{\text{cond,su}} + a_4 \cdot T_{\text{eva,su}}^2 + a_5 \cdot T_{\text{cond,su}}^2 \tag{A.44}$$

where a_x are empirically derived parameters and $T_{\text{cond,su}}$ and $T_{\text{eva,su}}$ are the secondary fluid condenser and evaporator inlet temperatures respectively. The parameters required by the model are reported in table A.4.

Parameter	Description
A_{eva}	Evaporator area, secondary side [m^2]
V_{eva}	Evaporator volume, secondary side [m^3]
$U_{nom,eva}$	Evaporator nominal heat transfer coefficient
A_{cond}	Condenser area, secondary side [m^2]
V_{cond}	Condenser volume, secondary side [m^3]
$U_{nom,cond}$	Condenser nominal heat transfer coefficient [W/m^2K]

Table A.4 – Parameters of the $ORCunit$ model

A.4 Boiler simplified model

The *Boiler* model can be used to simulate the process of thermal energy absorption by a fluid when flowing through any type of boiler. The model is based on the connection of four different components: one *Flow1Dim* model, one *MetalWall* model, one *sourceQ* model and a *CombustionDynamic* model. The thermal power absorbed by the fluid in the boiler is set as an exogenous input. The *CombustionDynamic* model imposes a linear or first order delay to the imposed thermal power. The *sourceQ* model transforms the thermal power set as a real input into a signal compatible with the Modelica *ThermalPort* interface. The *MetalWall* model accounts for energy accumulation in the metal walls of the boiler, while the *Flow1Dim* model accounts for mass and energy accumulation of the fluid which is heated in the boiler. The parameters required by the model are reported in table A.5. The model as shown from the graphical user interface of Dymola is reported in figure A.2.

Parameter	Description
N	Number of nodes for $Flow1Dim$ discretization
V_{int}	Evaporator volume, secondary side [m^3]
A_{int}	Evaporator nominal heat transfer coefficient [m^2]
A_{ext}	Condenser area, secondary side [m^2]
$t_{startup}$	Condenser volume, secondary side [s]
M_{wall}	Boiler metal mass [kg]
$c_{p,wall}$	Condenser volume, secondary side [J/kg.K]
U_{nom}	Condenser nominal heat transfer coefficient [W/m^2.K]

Table A.5 – Parameters of the $Boiler$ model

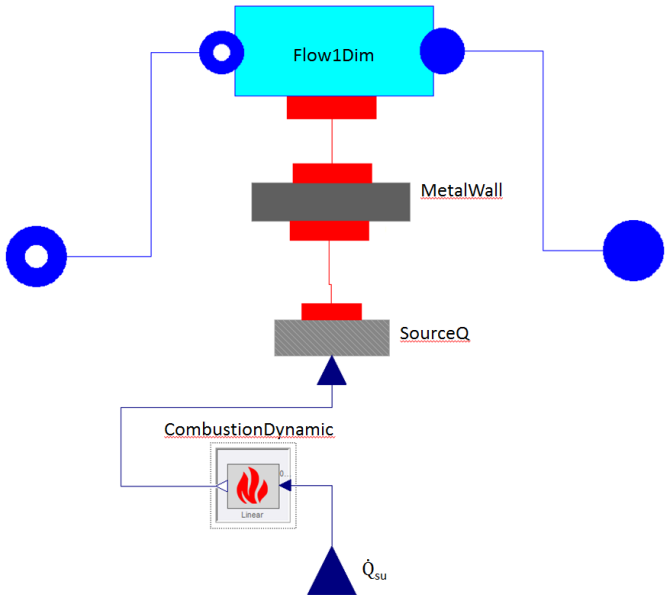

Figure A.2 – Schematic layout of the *Boiler* model from the Dymola graphical user interface.

A.5 Numerical methods to increase robustness of finite volume flow models

This section describes the different numerical methods implemented to avoid the simulation issues described in Chapter 4, section 4.9. These methods aim at avoiding numerical flow reversal or avoiding unsolvable systems in case a flow reversal occurs. They have been developed for one dimensional discretized models, i.e. the $Flow1D$ model of the ThermoCycle library, described in section 4.3.2. For the sake of clarity the mass, energy and momentum balance defining each cell of the model are reported hereunder:

$$\frac{dM}{dt} = \dot{m}_{su} - \dot{m}_{ex} \quad \text{with} \quad \frac{dM}{dt} = V \cdot \left(\frac{\partial \rho}{\partial h} \cdot \frac{dh}{dt} + \frac{\partial \rho}{\partial p} \cdot \frac{dp}{dt} \right) \tag{A.45}$$

$$V \rho \frac{dh}{dt} = \dot{m}_{su} \cdot (h_{su} - h) - \dot{m}_{ex} \cdot (h_{ex} - h) + V \frac{dp}{dt} + A_l \cdot \dot{q} \tag{A.46}$$

$$p_{su} = p_{ex} \tag{A.47}$$

Some can be implemented at the Modelica level, while others require a modification of the thermodynamic properties of the working fluid. It should also be noted that some of these methods have already been proposed in the literature, while some others are new.

A.5.1 Filtering Method

A first-order filter is applied to smooth the fast variations of the density with respect with time:

$$\frac{dy}{dt} = \frac{u - y}{T_{\text{filter}}} \tag{A.48}$$

where u and y are the input and output signals, respectively. In this case, u is the mass variation calculated via the equation of state, and y is the filtered mass derivative. This filter therefore acts as a "mass damper" and avoids the transmission transferring abrupt variations of the flow rate due to the density derivative discontinuity. The filtered mass accumulation in each cell is written:

$$\frac{d^2\dot{M}}{d^2t} = \frac{V \cdot [\frac{\partial \rho}{\partial h} \cdot \frac{dh}{dt} + \frac{\partial \rho}{\partial p} \cdot \frac{dp}{dt}] - \frac{dM}{dt}}{T_{\text{filter}}} \tag{A.49}$$

where T_{filter} is the filter time constant, set as a model parameter. This approach allows displacing the mass variations in time without generating mass defects. On the contrary as the cell density does not corresponds to the one of the actual node flow rates, the energy balance is affected. Furthermore, the number of time states is doubled since the second-order derivative of the working fluid mass in the cell is required. The method can be implemented at a model level.

A.5.2 Truncation method

In this approach, the peaks characterizing the partial density derivatives with respect to pressure and enthalpy during the fluid transition from saturated liquid to two-phase are truncated as a function of the vapour quality (defined as $x = (h - h_l)/(h_v - h_l)$, see Figure A.3. The maximum time derivative of the density is a model parameter, and the maximum partial derivatives are calculated using the following equation:

$$\frac{\partial \rho^{max}}{\partial h} = \frac{d\rho^{max}}{dt} / \frac{dh^{ref}}{dt} \tag{A.50}$$

$$\frac{\partial \rho^{max}}{\partial p} = \frac{d\rho^{max}}{dt} / \frac{dp^{ref}}{dt} \tag{A.51}$$

The reference values denoted with the superscript, ref, are set to typical values. This allows using one single parameter to compute the two maximum values of the partial derivatives. This strategy conserves the mass balance in each cell, except when a phase transition occurs. In this case, a fictitious creation or destruction of mass appears. In Figure A.3 it is shown that the truncated area is relatively limited, which should keep the mass unbalance within acceptable limits. The underlying idea is that a mass defect is acceptable for the simulation if its value is limited and if it significantly increases the robustness of the model. The approach can be easily implemented at a model level with no modification of the working fluid equation of state.

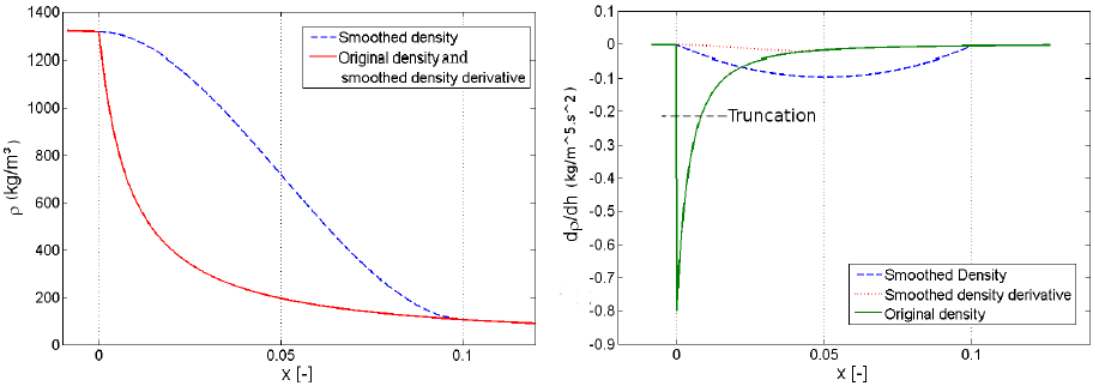

Figure A.3 – Original and modified density and density derivative functions *vs.* vapour quality.

A.5.3 Smoothing of the density derivative

This method allows to smooth out the density derivative discontinuity using a spline function, as shown in Figure A.3. A modification of the equation of state, , i.e., in the thermophysical properties database, is therefore necessary. The method has been implemented in the main code of the open-source CoolProp library. The main drawback of this approach is that the density function is still calculated with the original equation of state, i.e., the smoothed density derivative is not consistent with the density function provided by the equation of state. This might cause a mass balance defect during the simulation.

A.5.4 Smoothing of the density function

In order to avoid the mismatch between the density function and its derivative, one possible solution consists in smoothing the density for a range of vapour qualities (i.e., making it C1-continuous) and recalculating its partial derivatives in the smoothed area. In this situation, the density derivatives are continuous, but not smooth, which should still be manageable for the solver. The density is smoothed using a spline function with respect to the enthalpy between the liquid saturation line and a constant vapour quality line (hereunder referred to by the subscript "x"), as shown in Figure A.3. Note that in the equations below, the two independent variables are p and h. For the sake of conciseness, partial derivatives as a function of one of these variables is always assumed to be performed with the other one being constant, although this is not explicitly indicated in the equations.

$$\rho_{\text{smooth}} = a \cdot \Delta^3 + b \cdot \Delta^2 + c \cdot \Delta + d \quad \text{for} \quad 0 < \delta < \Delta_x \tag{A.52}$$

where Δ is the difference between the cell enthalpy and the saturated liquid enthalpy at the given pressure:

$$\Delta = h - h_l \qquad \Delta_x = x \cdot (h_v - h_l) \tag{A.53}$$

The spline coefficients a, b, c, d are reported below:

$$a = \frac{1}{\Delta_x^3} \cdot \left[2\rho_l - 2\rho_x + \Delta_x \cdot (\frac{\partial \rho}{\partial h}|_l + \frac{\partial \rho}{\partial h}|_x) \right] \tag{A.54}$$

$$b = \frac{3}{\Delta_x^3} \cdot (\rho_x - \rho_l) - \frac{1}{\Delta_x} \cdot (2 \cdot \frac{\partial \rho}{\partial h}|_l + \frac{\partial \rho}{\partial h}|_x) \tag{A.55}$$

$$c = \frac{\partial \rho}{\partial h}|_l \tag{A.56}$$

$$d = \rho_l \tag{A.57}$$

Since the partial derivative of Δ with respect to h is equal to one, the partial derivative of the smoothed density function with respect to h is straightforward:

$$\frac{\partial \rho_{\text{smooth}}}{\partial h} = 3a\Delta^2 + 2b\Delta + c \tag{A.58}$$

The partial derivative with respect to p requires more terms, since the spline coefficients depend on p and must also be differentiated:

$$\frac{\partial \rho_{\text{smooth}}}{\partial p} = (3a\Delta^2 + 2b\Delta + c) \cdot \frac{\partial \Delta}{\partial p} + \frac{da}{dp} \cdot \Delta^3 + \frac{db}{dp} \cdot \Delta^2 + \frac{dc}{dp} \cdot \Delta + \frac{dd}{dp} \tag{A.59}$$

with:

$$\begin{aligned} \frac{da}{dp} = {} & \frac{6}{\Delta_x^4} \cdot \frac{d\Delta_x}{dp} \cdot (\rho_x - \rho_l) + \frac{2}{\Delta_x^3} \cdot (\frac{d\rho_l}{dp} - \frac{d\rho_x}{dp}) + \frac{1}{\Delta_x^2} \cdot (\frac{\partial^2 \rho}{\partial h \partial p}|_l + \frac{\partial^2 \rho}{\partial h \partial p}|_x) - \\ & - \frac{2}{\Delta_x^3} \cdot (\frac{d\rho_l}{dh} + \frac{d\rho_x}{dh}) \cdot \frac{d\Delta_x}{dp} \end{aligned} \tag{A.60}$$

$$\begin{aligned} \frac{db}{dp} = {} & \frac{6}{\Delta_x^3} \cdot \frac{d\Delta_x}{dp} \cdot (\rho_x - \rho_l) + \frac{3}{\Delta_x^2} \cdot (\frac{d\rho_x}{dp} - \frac{d\rho_l}{dp}) + \frac{1}{\Delta_x^2} \cdot \frac{d\Delta_x}{dp} \cdot (2 \cdot \frac{\partial \rho}{\partial h}|_l + \frac{\partial \rho}{\partial h}|_x) - \\ & - \frac{1}{\Delta_x} \cdot (\frac{\partial^2 \rho}{\partial h \partial p}|_x + 2 \cdot \frac{\partial^2 \rho}{\partial h \partial p}|_l) \end{aligned} \tag{A.61}$$

$$\frac{dc}{dp} = \frac{\partial^2 \rho}{\partial h \partial p}|_l \tag{A.62}$$

$$\frac{dd}{dp} = \frac{d\rho_l}{dp} \tag{A.63}$$

and:

$$\frac{d\Delta_x}{dp} = x \cdot (\frac{dh_v}{dp} - \frac{dh_l}{dp}) \tag{A.64}$$

$$\frac{\partial \Delta}{\partial p} = -\frac{dh_l}{dp} \tag{A.65}$$

$$\frac{d\rho_x}{dp} = \rho_x^2 \cdot (\frac{x}{\rho_v^2} \cdot \frac{d\rho_v}{dp} + \frac{1-x}{\rho_l^2} \cdot \frac{d\rho_l}{dp}) \tag{A.66}$$

All the other partial or total derivatives can be obtained from the Bridgeman Tables. They are implemented in the standard distribution of CoolProp [24] and are summarized in [**?**]. Equations A.52–A.58-A.59 are therefore used instead of the original equation of state in the area of the thermodynamic diagram characterized by a vapour quality varying between zero and x. x is a parameter of the model and can be set by the user, values ranging between 0.1 and 0.15 are normally selected.

A.5.5 Mean densities method

The mean densities method was originally proposed by Casella [135] and successfully tested by Bonilla et al. [136]. The goal is to avoid the numerical artefact, due to the density derivative discontinuity crossing one of the finite volumes boundaries. To that end, a mean density and its partial derivatives are computed in each cell as a function of the node densities. The main advantage is that the discontinuity in the partial derivatives disappears. Nine different equations of the mean density are proposed, corresponding to nine possible situations: h_{su} and h_{ex} can both either be liquid, two-phase or vapour. The total number of combinations is therefore equal to nine. As an example, in the case where h_{su} is liquid and h_{ex} is two-phase, the mean density is computed by:

$$\bar{\rho} = \frac{1}{h_{ex} - h_{su}} \left[\frac{\rho_{su} + \rho_l}{2} \cdot (h_l - h_{su}) + \frac{h_v - h_l}{v_v - v_l} \cdot ln\left(\frac{\rho_l}{\rho_{ex}}\right) \right] \tag{A.67}$$

$$\frac{\partial \bar{\rho}}{\partial h} = \frac{\rho_{ex} - \rho_{su}}{h_{ex} - h_{su}} \tag{A.68}$$

$$\frac{\partial \bar{\rho}}{\partial p} = \frac{1}{h_{ex} - h_{su}} \left[\frac{1}{2} \left(\frac{\partial \rho_{su}}{\partial p} + \frac{\partial \rho_l}{\partial p} \right) (h_l - h_{su}) + A \cdot ln\left(\frac{\rho_l}{\rho_{ex}}\right) + B(\rho_l - \rho_e x) \right] \tag{A.69}$$

where A and B are functions of the fluid thermodynamic properties on the liquid and vapour saturation lines. The equations for the eight other cases, as well as the analytical expression of A and B are available in [135, 136]. It should be noted that this approach requires the computation of the node densities. As a consequence, a staggered grid should not be used, since it would require twice as many thermodynamic state computations (in the cells and in the nodes), which would considerably increase the simulation time. Therefore, to implement this method, the staggered grid described in the previous section was changed to a collocated grid (i.e., the thermodynamic states are only computed at the nodes).

A.5.6 The enthalpy limiter method

Contrary to the previous methods, the enthalpy limiter method does not aim at avoiding flow reversals. Instead, it ensures that the system of equations remains solvable even in case of flow reversal. As indicated in equation 4.61, the enthalpy of the fluid entering a cell should have a minimum value, ensuring that the system of equations can be solved. The enthalpy limiter method is the practical implementation of this constraint in the cell model. It was originally proposed by Schulze et al. [133] and implemented in the TIL Modelica library. The idea is to make profit of the "Stream" connector type available in Modelica to propagate the minimum enthalpy limitation: in this manner, a cell can communicate with its two neighbouring cells

and propagate the minimum enthalpy of an incoming flow according to Equation 4.61. The incoming flow is limited to this minimum value:

$$h_{\text{limit},i} = h_i + 0.9 \cdot \frac{\rho_i}{\frac{\partial \rho_i}{\partial h}} \tag{A.70}$$

In the two adjacent cells, the enthalpy of the outlet flow is given by (example for i-1):

$$h_{\text{ex},i-1} = max(h_{\text{limit,i}}, h_{i-1}) \tag{A.71}$$

A security factor of 0.9 is taken to ensure a minimum distance between the outlet enthalpy and the theoretical limit.

A.5.7 Smooth Reversal Enthalpy

In equation 4.9, a discontinuity arises in the computed node enthalpy in the case of flow reversal. This can be solved using a smooth transition between both parts of the equation. Equation 4.9 is therefore transformed into:

$$h_{\text{su}} = \begin{cases} h & \text{if } \dot{m}_{\text{su}} \leq -\frac{\dot{m}_{\text{nom}}}{10} \\ h + \frac{h^*_{\text{ex}} - h}{2} \cdot \left[1 + \sin(\frac{5 \cdot \pi}{\dot{m}_{\text{nom}}} \dot{m})\right] & \\ h^*_{\text{ex}} & \text{if } \dot{m}_{\text{su}} \geq \frac{\dot{m}_{\text{nom}}}{10} \end{cases} \tag{A.72}$$

The smooth transition is a C1-continuous sinusoidal transition function varying from zero to one between $-\dot{m}_{\text{nom}} = 10$ and $-\dot{m}_{\text{nom}} = 10$ and available in ThermoCycle. $\dot{m}_{\text{nom}}$ is a user-defined model parameter.

B Finite volume and moving boundary heat exchanger model integrity

In this section a comparison between the FV and the MB heat exchanger modelling approaches when no experimental data are available is presented. The comparison aimed at testing the model accuracy and integrity. The accuracy is defined as the agreement of the model-predicted output values with respect to a reference system. A 100-CVs FV model was selected as standard reference as proposed in [134]. Such a large number of discretized volumes ensured small mass and energy mismatch and increased the robustness of the finite volume approach. The integrity is defined as the capacity of the model to respect the conservation of energy and mass. The FV and MB models were parametrized based on the evaporator installed in the low capacity 11 kW_{el} ORC unit described in chapter 2. The models were subjected to inlet enthalpy and pressure variations, whose value was limited to avoid any back-flow or phase change at the working fluid side outlet. The boundary conditions for pressure and enthalpy are defined in Equations B.1 and B.2.

$$p = 8.04 + 0.2 \cdot \sin(0.1 \cdot 2\pi \cdot t) \text{ [bar]} \tag{B.1}$$

$$h_{su} = 0.11 \cdot 10^5 + 0.2 \cdot 10^5 \cdot sin(0.2 \cdot 2\pi \cdot t) \text{ [J/kg]} \tag{B.2}$$

The FV heat exchanger model was discretized using the upwind method and simulations were performed considering 10, 20, 40 and 100 CVs. The medium selected for these simulations was solkatherm (SES36). The simulation was initialized in steady-state and lasts 625 seconds. The numerical solver was the DASSL and the relative tolerance was set to 10^{-4} [**?**]. The integrity of the models was investigated by calculating the energy and mass balances over the whole simulation time for the complete models. The energy balance over each heat exchanger model was computed as:

$$\epsilon_{ener} = \frac{(E_{ext} + E_{su} - E_{ex} - \Delta U)_{wf} + (E_{ext} + E_{su} - E_{ex} - \Delta U)_{sf} + (E_{su} - E_{ex} - \Delta U)_{wall}}{E_{ext,sf}} \tag{B.3}$$

where E_{ext} is the overall thermal energy exchanged due to heat convection through the lateral surface, $E_{ex/su}$ is the total energy into/out of the system due to leaving/entering mass flow rate

and ΔU is the total net increase of energy. They were calculated in Equation B.4.

$$E_{\text{ext}} = \int_0^t \dot{Q}\,\mathrm{d}t, \quad E_{\text{ex/su}} = \int_0^t \dot{m}_{\text{ex/su}} \cdot h_{\text{ex/su}}\,\mathrm{d}t, \quad \Delta U = \sum_{i=1}^{N} \left(U_{\text{i,final}} - U_{\text{i,init}}\right) \tag{B.4}$$

where the $final$ and $init$ subscripts refer to the values the variable has at the end and at the start of the simulation and N indicates the number of CVs. The conservation of mass was checked on the working fluid side as:

$$\epsilon_{\text{mass}} = \sum_{i=1}^{n} \frac{M_{\text{ex}} - M_{\text{su}} - \Delta M}{M_{\text{su}}} \tag{B.5}$$

where $M_{\text{ex/su}}$ is the overall mass leaving/entering the system and ΔM is the net change in mass. Their values were computed using Equation B.6.

$$M_{\text{ex/su}} = \int_0^t \dot{m}_{\text{ex,su}}\,\mathrm{d}t \quad \Delta M = \sum_{i=1}^{N} V_i \left(\rho_{\text{i,final}} - \rho_{\text{i,init}}\right) \tag{B.6}$$

The accuracy of the models was investigated by comparing the model output enthalpy and mass flow rate with respect to a reference system, using as mathematical indicator the mean percentage relative error, $\overline{\varepsilon}$, defined in Equation B.7. In this case the finite volume model with 100 CVs was taken as a reference.

$$\varepsilon\left(j\right) = 100 \cdot \frac{\left|X_{\text{s}}\left(j\right) - X_{\text{ref}}\left(j\right)\right|}{X_{\text{ref}}\left(j\right)} \quad \varepsilon = \sum_{j=1}^{n} \varepsilon\left(j\right) \quad \overline{\varepsilon} = \frac{\varepsilon}{n} \quad j \in [1, n]. \tag{B.7}$$

where $X_{\text{s}}\left(j\right)$ and $X_{\text{ref}}\left(j\right)$ are the $\mathrm{j}th$ sampled simulation and reference value of the selected variable and n is the number of samples. Table B.1 reports the simulated benchmarking

Table B.1 – Benchmarking indicators for the integrity and accuracy test for the moving boundary and the finite volume models.

Model	MBConstVF	MB	FV 10 CVs	FV 20 CVs	FV 40 CVs	FV 100 CVs
ϵ_{mass} [%]	$2.33 \cdot 10^{-13}$	$1.08 \cdot 10^{-12}$	$1.72 \cdot 10^{-13}$	$6.33 \cdot 10^{-13}$	$3.06 \cdot 10^{-14}$	$1.01 \cdot 10^{-12}$
ϵ_{ener} [%]	$6.67 \cdot 10^{-12}$	$9.51 \cdot 10^{-12}$	$5.28 \cdot 10^{-12}$	$2.89 \cdot 10^{-12}$	$4.64 \cdot 10^{-12}$	$1.04 \cdot 10^{-12}$
$\overline{\varepsilon}\ h_{\text{ex}}$ [%]	0.55	0.69	3.16	1.06	0.31	0.0
$\overline{\varepsilon}\ \dot{m}_{\text{ex}}$ [%]	3.88	1.40	5.52	1.85	0.53	0.0
Time [s]	0.65	0.73	2.89	13.7	34.8	147

indicators. The mass and energy unbalances were negligible in all the considered models. The lack of a clear trend in the error values as the number of CVs increased in the FV models can be explained by small inaccuracies of the numerical method used for solving the integrals of equations B.4 and B.6. As expected the computational time increased exponentially with the increase of the number of CVs in the FV model. The MB approach was three order of magnitude faster than the finite volume with 100 CVs, allowing to maintain a good accuracy

with respect to the 100 CVs FV model in terms of outlet mass flow and outlet enthalpy as the $\bar{\varepsilon}$ values reported in Table B.1 show. In Figure B.1, the temperature profile for heat transfer calculation for the MB and FV model is depicted.

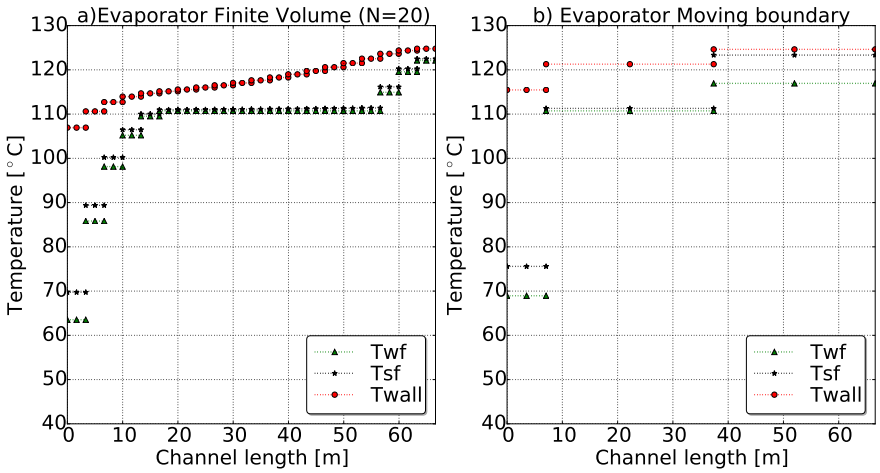

Figure B.1 – Temperature profiles of the finite volume (a) and the moving boundary (b) evaporator models as they are assumed by the application of Newton's law of cooling to solve the heat transfer problem. Each segment corresponds to one control volume.

The goal of the future is full unemployment,
so we can play.

ARTHUR C. CLARKE (1917 - 2008)